The Distribution of Water in the Lunar Magmatic Ocean

Dissertation

for the award of the degree

"Doctor rerum naturalium" (Dr.rer.nat.)

of the Georg-August-Universität Göttingen
within the doctoral program Geoscience

of the Georg-August University School of Science (GAUSS)

submitted by

Matthias Christian Alexander Nieuwenhuis

from Münster

Göttingen, 2023

Thesis Committee

Prof. Dr. Sharon Webb, Experimental Mineralogy, GZG

Dr. Urs Mall, Planets Department, MPI for Solar System Research

Prof. Dr. Bernd Lehmann, Mineral Resources, TU Clausthal

Dr. Burkhard Schmidt, Experimental Mineralogy, GZG

Members of the Examination Board

Reviewer: Prof. Dr. Sharon Webb, Experimental Mineralogy, GZG

Second Reviewer: Prof. Dr. Andreas Pack, Isotope Geology, GZG

Further members of the Examination Board

Prof. Dr. Geoffrey Bromiley, School of GeoSciences, University of Edinburgh

Dr. Urs Mall, Planets Department, MPI for Solar System Research

Prof. Dr. Bernd Lehmann, Mineral Resources, TU Clausthal

Dr. Burkhard Schmidt, Experimental Mineralogy, GZG

Date of the oral examination: May 10, 2023

I. Contents

I.I Table of contents

I. Contents I

I.I **Table of contents** I

I.II **List of Figures** V

I.III **List of Tables** IX

I.IV **List of Equations** IX

II. Acknowledgements XI

III. Abstract XIII

1 Introduction 1

1.1 **Origin of the solar system** 1

1.2 **Origin of water on Earth** 3

1.3 **Theories of the lunar formation** 5

1.4 **Background and previous research** 8

1.4.1 The composition of the lunar interior 8

1.4.2 Lunar Magmatic Ocean (LMO) 9

1.4.3 The structural composition of the Moon 13

1.5 **Water in lunar materials** 17

1.5.1 Water-bearing minerals 18

1.5.2 Nominally dry minerals: 19

1.5.3 Water in lunar rocks and glasses 20

1.5.4 Water in melt inclusions 21

1.5.5 Water on the lunar Surface 23

1.6 **Is the lunar water distribution homogeneous?** 25

1.6.1 What is the lunar water content? 28

1.7 **Aim of this study** 29

2 Material and Methods 31

2.1 **Experimental approach** 32

2.1.1 Functionality of an end-load piston cylinder press 33

2.1.2 Composition of the water-inhibiting assembly 38

2.1.3 The Internally Heated Pressure Vessel (IHPV) 42

2.2 **Carrying out the calibration experiments** 44

2.2.1 Why does the assembly need to be calibrated? 44

2.2.2 Calibration by the conversion of α-quartz to coestite 46
2.2.3 Calibration by the decomposition of albite to jadeite and quartz 47
2.2.4 Phase determination by means of powder diffraction 48
2.2.5 Crystallisation problems and pseudo-friction of BN assemblies 50
2.2.6 Reaction of anorthite, gehlenite and corundum to Kushiroite 53
2.3 **Development of a stable assembly** 55
2.4 **Experimental crystallisation of the LMO** 66
2.4.1 Pressure 66
2.4.2 Temperature 69
2.4.3 Crystallisation progress (PCS) 72
2.4.4 Oxygen fugacity 74
2.4.5 Chemical composition 77
2.4.6 Characterisation of the starting melts 80
2.4.7 Water 82
2.4.8 Melting tests in a graphite furnace under Argon atmosphere 82
2.5 **Carrying out the experiments** 86
2.5.1 Sample preparation 88
2.6 **Analytical Methods** 90
2.6.1 Scanning electron microscope JEOL JSM-IT500 90
2.6.2 µ-XRF Bruker "M4" Tornado 92
2.6.3 IR-spectrometer Hyperion 3000 with ATR unit Bruker Vertex 70 94
2.6.4 Raman spectrometer Horiba Jabin-Yvon HR800UV 96
2.6.5 Melt fraction determination with MATLAB 98
3 Results 103
3.1 **LPUM 300-1 // 680 km depth** 104
3.2 **LPUM 285-2 // 435 km depth** 110
3.3 **LPUM 210-2 // 435 km depth** 116
3.4 **LPUM 150-1 // 294 km depth** 122
3.5 **LPUM 150-3 // 294 km depth** 128
3.6 **LPUM 100-1 // 186 km depth** 134
3.7 **LPUM 075-1 // 137 km depth** 140
3.8 **LPUM 050-1 // 90 km depth** 146
3.9 **LPUM 030-1 // 53 km depth** 154
3.10 **LPUM 020-1 // 35 km depth** 160
3.11 **Summary of the mineral compositions** 165

3.12 **Buffer development** ... 168
3.13 **Estimating the redox conditions** ... 171
4 Discussion ... 175
4.1 **The lunar interior as shown by the run products** ... 176
4.2 **Fe-nuggets - Result of the conditions?** ... 183
4.2.1 $F(O_2)$ of the pressurising medium ... 184
4.2.2 Dependencies on Iron content, pressure and temperature ... 184
4.2.3 The capsule material as cause - composition of the residual melt ... 184
4.2.4 The capsule material as cause - bulk composition ... 186
4.3 **Simulation of LMO crystallisation using MELTS** ... 191
4.3.1 MELTS - LMO composition and mineral stack (1) ... 193
4.3.2 LPUM-M-120-1 ... 194
4.3.3 MELTS - LMO composition and mineral stack (2) ... 201
4.4 **The distribution of water inside the Moon** ... 208
5 Summary ... 211
5.1.1 Conclusions and future work ... 212
6 Appendix ... 215
6.1.1 LPUM Starting Glasses ... 216
6.1.2 LPUM 300-1 OPX and Olivine ... 217
6.1.3 LPUM 285-2 OPX ... 218
6.1.4 LPUM 285-2 Olivine ... 219
6.1.5 LPUM 210-2 OPX and CPX ... 220
6.1.6 LPUM 150-1 OPX Part 1 ... 221
6.1.7 LPUM 150-1 OPX Part 2 ... 222
6.1.8 LPUM 150-3 OPX Part 1 ... 223
6.1.9 LPUM 150-3 OPX Part 2 ... 224
6.1.10 LPUM 100-1 Olivine ... 225
6.1.11 LPUM 100-1 OPX Part 1 ... 226
6.1.12 LPUM 100-1 OPX Part 2 ... 227
6.1.13 LPUM 100-1 OPX Part 3 ... 228
6.1.14 LPUM 075-1 Olivine ... 229
6.1.15 LPUM 075-1 OPX Part 1 ... 230
6.1.16 LPUM 075-1 OPX Part 2 ... 231
6.1.17 LPUM 075-1 Spinel ... 232
6.1.18 LPUM 050-1 Olivine ... 233

6.1.19 LPUM 050-1 CPX 234
6.1.20 LPUM 050-1 FSP 235
6.1.21 LPUM 030-1 CPX, FSP and Quartz 236
6.1.22 LPUM 030-1 Spinel 237
6.1.23 LPUM 020-1 FSP 238
6.1.24 LPUM 020-1 CPX and Quartz 239
6.1.25 LPUM-M 120-1 OPX and Olivine 240
6.1.26 LPUM residual melts – Part 1 241
6.1.27 LPUM residual melts – Part 2 242
6.1.28 LPUM residual melts – Part 3 243
6.1.29 LPUM residual melts – Part 4 244
6.1.30 LPUM residual melts – Part 5 245
6.1.31 MELTS – IW-2 and IW0 Conditions and Runproducts 246
6.1.32 MELTS – IW-2 and IW0 Melt Compositions 247
6.2 **MATLAB – Source Code used for Image Separation** 248
6.3 **References** 249
6.4 **List of Tools** 266

I.II List of Figures

Figure 1: Approximate position of the Snow Line at 2.7 Au 2
Figure 2: Composition of the inner, middle and outer asteroid belts (DeMeo & Carry, 2014) 2
Figure 3: Possible origins of terrestrial water 3
Figure 4: Proportion of Earth mass present after the formation of the solar system 7
Figure 5: Modelled or experimental results of different authors on the crystallisation of LMO 11
Figure 6: Cross-section of the Moon before (c) and after (d) the cumulate overturn 12
Figure 7: Location of Apollo-era lunar seismometer measurement sites 14
Figure 8: Wave velocities and density of the Moon with depth 15
Figure 9: Examples of melt inclusions 22
Figure 10: Compilation of water contents in lunar melt inclusions as a function of titanium content 25
Figure 11: H_2O in melt inclusions of terrestrial and lunar samples as a function of fluorine content 27
Figure 12: H_2O content of lunar melt inclusions against cerium 27
Figure 13: Estimated pressure and temperature conditions for the experimental crystallisation of the LMO 32
Figure 14: Components of a piston-cylinder assembly 34
Figure 15: End-load piston cylinder press of the GZG and schematic structure 35
Figure 16: Components of a piston cylinder press 36
Figure 17: S-type thermosensor 37
Figure 18: Temperature distribution in a simulation by Schilling and Wunder (2004) 38
Figure 19: Thermal behaviour of diamond and CBN regarding to hardness and temperature 39
Figure 20: Design of a water-inhibiting assembly made of BN 41
Figure 21: Internally Heated Pressure Vessel (IHPV) of the GZG 43
Figure 22: Schematic of the furnace system of the IHPV and position of thermocouples relative to the sample 43
Figure 23: Phase diagram of quartz as a function of ambient pressure and temperature 45
Figure 24: Material failure of the piston due to the high loads during the experiments 46
Figure 25: Decomposition of albite into jadeite and quartz as a function of pressure and temperature 47
Figure 26: X-ray diffractogram of one of the calibration experiments 49
Figure 27: Results of calibration using Ab = Jd + Qz between 600 and 1000°C 52
Figure 28: Phase diagram of Kushiroite as a function of temperature and pressure 53
Figure 29: Original assembly design for the LMO experiments with high BN content 55
Figure 30: BN assembly with Al_2O_3 guide for the thermosensor 56
Figure 31 Talk-Pyrex Assembly of the GZG with BN sample chamber. 57
Figure 32: Microscopic image after an experiment and schematic representation of an intact thermosensor 58
Figure 33: Element distribution map of a thermosensor (EDX) 59
Figure 34: Assembly design 4 with NaCl as mantle material 60
Figure 35: Furnace material around the thermocouple bearing (Al_2O_3) 61
Figure 36: Assembly 5 with extended steel guide on the thermosensor 62
Figure 37: Assembly 6 with MgO as a guide for the thermosensor 63
Figure 38: Schematic representation of the thermocouples in top view and cross-section 64
Figure 39: Thermocouple with recessed weld bead and after cementing 64
Figure 40: Pressure as a function of depth in the Moon according to Garcia et al. (2011) 67
Figure 41: Internal structure of the Moon according to Weber et al., 2011 68
Figure 42: Schematic representation of LMO cooling at three arbitrary times 70
Figure 43: Relationship between pressure (P) and temperature (T) in the LMO 71
Figure 44: Oxygen fugacity of buffer reactions as a function of temperature 75
Figure 45: Capsule design with Cr-Cr_2O_3 buffer and SEM image of a successful experiment 76
Figure 46: Composition of the starting materials for the indexed experiments 79
Figure 47: Initial compositions of the experiments in the TAS diagram 81
Figure 48: Initial compositions of the experiments in the AFM plot 81
Figure 49: Structure of the Geochemistry Graphite Furnace (GZG) 83

Figure 50: Graphite furnace of the geochemistry department at the GZG 84
Figure 51: Mo-loop with sample after the experiment 84
Figure 52: IR spectrum of the OH band of a sample with known water content 85
Figure 53: Relationship between PCS and pressure 86
Figure 54: Specimen capsule, sawing process, split specimen capsules before polishingand in the SEM 89
Figure 55: JSM-IT500 InTouchScope™ SEM of the GoeLem Laboratory of the GZG 90
Figure 56: Schematic representation of the internal structure of an SEM 91
Figure 57: Micro X-ray fluorescence spectrometry (Micro-XRF) Bruker M4 TORNADO 92
Figure 58: Schematic representation of the X-ray optics of a Bruker M4 "Tornado" 93
Figure 59: Infrared spectrometer Bruker "Hyperion 3000" with ATR unit "Vertex 70" 94
Figure 60: Schematic representation of the evanescent wave by total internal reflection in the ATR crystal 95
Figure 61: Raman spectroscopy: Horiba Jobin-Yvon Labram HR800UV 96
Figure 62: Original image of sample LPUM 050-1, already prepared for segmentation 99
Figure 63: Capsule and holes of sample LPUM 050-1 (grey values 0 - 1) 100
Figure 64: Olivine of sample LPUM 050-1 (grey values 2 - 21) 100
Figure 65: Plagioclase of sample LPUM 050-1 (grey values 22 - 90) 101
Figure 66: Orthopyroxene of sample LPUM 050-1 (grey values 91- 120) 101
Figure 67: Melt of sample LPUM 050-1 (grey values 121- 254) 102
Figure 68: Fe spheres of sample LPUM 050-1 (grey values 255-256) 102
Figure 69: Overview image of sample LPUM 300-1 105
Figure 70: Close-up of sample LPUM 300-1 106
Figure 71: Close-up of the carbon buffer of sample LPUM 300-1 106
Figure 72: Forsterite content of olivine in sample LPUM 300-1 107
Figure 73: Composition of orthopyroxenes in the sample LPUM-300-1 107
Figure 74: Separation by grey values of sample 300-1 using MATLAB 108
Figure 75: Separation by grey values of sample 300-1 using MATLAB (2) 109
Figure 76: General view of sample LPUM 285-2 111
Figure 77: Close-up of sample LPUM 285-2 112
Figure 78: Close-up of sample LPUM 285-2 (2) 112
Figure 79: Composition of orthopyroxenes in the sample LPUM-285-2 113
Figure 80: Forsterite content of olivine in sample LPUM 285-2 113
Figure 81: Separation by grey values of sample 285-2 using MATLAB 114
Figure 82: General view of sample LPUM 210-2 117
Figure 83: Close-up of sample LPUM 210-2 118
Figure 84: Close-up of sample LPUM 210-2 (2) 118
Figure 85: Forsterite content of olivine in sample LPUM 210-2 119
Figure 86: Mineral composition of the Pyroxenes in sample LPUM 210-2 119
Figure 87: Separation by grey values of sample 210-2 using MATLAB 120
Figure 88: Area measurement of sample LPUM 210-2 121
Figure 89: Elemental distribution map of Cr , Pt, Mg, Al, Fe and Si and photograph of sample LPUM 150-1 122
Figure 90: General view of sample LPUM 150-1 123
Figure 91: Close-up of sample LPUM 150-1 124
Figure 92: Mineral composition of the orthopyroxenes in sample LPUM 150-1 125
Figure 93: Separation by grey values of sample 210-2 using MATLAB 126
Figure 94: General view of sample LPUM 150-3 129
Figure 95: Close-up 1 of sample LPUM 150-3 130
Figure 96: Close-up 2 of sample LPUM 150-3 130
Figure 97: Composition of orthopyroxenes in sample LPUM 150-3 131
Figure 98: Separation by grey values of sample 150-3 using MATLAB 132
Figure 99: General view of sample LPUM 100-1 135
Figure 100: Close-up of sample LPUM 100-1 with pyroxene, olivine and melt 136
Figure 101: Close-up of sample LPUM 100-1 with Fe-nuggets inside the melt 136

Figure 102: Mineral composition of the orthopyroxenes in sample LPUM 100-1 137
Figure 103: Mineral composition of the Pyroxenes in sample LPUM 100-1 137
Figure 104: Separation by grey values of sample 100-1 using MATLAB 138
Figure 105: General view of sample LPUM 075-1 141
Figure 106: Close-up of sample LPUM 075-1 142
Figure 107: Close-up of sample LPUM 075-1 143
Figure 108: Mineral composition of the pyroxenes in sample LPUM 075-1 143
Figure 109: Mineral composition of the Pyroxenes in sample LPUM 075-1 144
Figure 110: Mineral composition of the spinels in sample LPUM 075-1. 144
Figure 111: Separation by grey values of sample 075-1 using MATLAB 145
Figure 112: General view of sample LPUM 050-1 147
Figure 113: Detailed image of sample LPUM 050-1 148
Figure 114: Close-up of sample LPUM 050-1 148
Figure 115: SEM image of the area of chemical separation in sample LPUM 050-1 149
Figure 116: Mineral composition of the clinopyroxenes in sample LPUM 050-1 150
Figure 117: Mineral composition of the Pyroxenes in sample LPUM 050-1 150
Figure 118: Mineral composition of the plagioclase in sample LPUM 050-1 151
Figure 119: Separation by grey values of sample 050-1 using MATLAB 152
Figure 120: General view of sample LPUM 030-1 155
Figure 121: Close-up of sample LPUM 030-1 156
Figure 122: Close-up of sample LPUM 030-1(2) 156
Figure 123: Mineral composition of clinopyroxene in sample LPUM 030-1 157
Figure 124: Mineral composition of the plagioclase in sample LPUM 030-1 157
Figure 125: Separation by grey values of sample 030-1 using MATLAB 158
Figure 126: General view of sample LPUM 020-1 161
Figure 127: Detail image 1 of sample LPUM 020-1 162
Figure 128: Close-up 1 of sample LPUM 020-1 162
Figure 129: Mineral composition of clinopyroxene in sample LPUM 020-1 163
Figure 130: Mineral composition of the plagioclase in sample LPUM 020-1. 163
Figure 131: Separation by grey values of sample 020-1 using MATLAB 164
Figure 132: Classification of the pyroxene in all applicable experiments 165
Figure 133: Forsterite content of olivine across all applicable experiments 166
Figure 134: Classification of feldspar for alll applicable experiments 167
Figure 135: Difference in the ratio of Cr and Cr_2O_3 to the calculated volume in the starting material 169
Figure 136: Buffer state in the electron microscope image after the experiments 170
Figure 137: Estimated values of oxygen fugacity for all samples with iron nuggets present 172
Figure 138: LMO mineral composition as a result of our study vs. the degree of crystallisation 176
Figure 139: LMO mineral composition as given in Rapp and Draper versus the degree of crystallisation 177
Figure 140: Composition of the LMO in the overall result of the experiments individually 178
Figure 141: Composition of the LMO of the individual experiments as given in Rapp and Draper (2018). 179
Figure 142: Pressure versus crystallisation progress of the experiments 181
Figure 143: Phase diagram of platinum and iron 186
Figure 144: Area measurement on sample LPUM 050-1 187
Figure 145: Area measurement on sample LPUM-M 120-1 188
Figure 146: SEM image of the experiments LPUM-30-1 and LPUM 30-2 190
Figure 147: Overview of sample LPUM-M120-1 with capsule materials in white. 195
Figure 148: Close-up 1 of sample LPUM-M 120-1 196
Figure 149: Close-up 2 of sample LPUM-M 120-1 196
Figure 150: Original Image of sample LPUM-M 120-1 197
Figure 151: Platinum distribution in sample LPUM-M 120-1 197
Figure 152: Forsterite content of olivine in sample LPUM-M 120-1. 198
Figure 153: Mineral composition of orthopyroxenes in sample LPUM-M 120-1. 198

Figure 154: Separation by gray values of sample 120-1 using MATLAB _____ *199*
Figure 155: Results of MELTS, the LPUM-M-120-1 sample and the adjusted MELTS simulation _____ *200*
Figure 156: Modal crystal fractions of LMO crystallisation versus degree of crystallisation _____ *202*
Figure 157: Modal crystal fractions of LMO crystallisation versus degree of crystallisation (2) _____ *203*
Figure 158: Volume fractions of minerals in Rapp and Draper (2018) and simulations at IW0 and IW-2 _____ *205*
Figure 159: Crust thickness as a result of experimental LMO crystallisation at different water contents _____ *207*
Figure 160: Water content of LMO versus crystallisation progress _____ *209*
Figure 161: Solid phase water content versus crystallisation progress _____ *209*

I.III List of Tables

Table 1: Number and type of lunar Earthquakes during the recording period of the Apollo experiments 15
Table 2: Estimates for the volatile content of mantle, KREEP and BSM 18
Table 3: H_2O in lunar materials 19
Table 4: Overview of the calibration experiments 51
Table 5: Calculation of the average pressure loss due to friction 54
Table 6: Relationship between depth, pressure, temperature and degree of crystallisation of LMO 73
Table 7: Compositions of the experiments of Rapp and Draper (2018) compared to our study 78
Table 8: Molybdenum and tungsten contamination of the samples 83
Table 9: Experimental conditions of the experiments by Rapp and Draper (2018) 86
Table 10: Overview of the successful LPUM experiments 87
Table 11: Characteristics of the experiments with and without the appearance of Fe-nuggets 183
Table 12: Initial iron content and iron content of the residual melt LPUM and LPUM-M experiments 185
Table 13: Composition of area measurements at LPUM 50-1 as shown in Figure 144. 187
Table 14: Composition of area measurements at LPUM-M-120-1 as shown in Figure 145. 188
Table 15: Starting compositon forboth of the MELTS simulations 192
Table 16: Most important parameters of the simulations IW0 and IW-2 with MELTS 192
Table 17: Results of the MELTS simulation, LPUM-M-120-1 and the adjusted simulation 200
Table 18: Plagioclase volume and the crustal thickness calculated from it 206
Table 19: Partition coefficients between olivine, OPX, CPX, plagioclase, quartz and apatite to melt 208

I.IV List of Equations

Equation 1: Bragg condition 48
Equation 2: Pressure-depth relation for the LMO 67
Equation 3: Temperature-pressure relation for the LMO 70
Equation 4: PCS-depth relation for the LMO 72
Equation 5: Crystallised volume of the LMO at depth D 72
Equation 6: Total volume of the LMO with maximum depth D_0 72
Equation 7: Simplified PCS-depth relation for a 1400 km deep LMO 72
Equation 8: Buffer reaction of chromium and chromium(III) oxide 76
Equation 9: Iron-wüstite reaction 76
Equation 10: Lambert-Beer-law 94
Equation 11: Phase fraction of phase n of the separated image 98
Equation 12: Reaction between iron, hematite and water 168
Equation 13: Buffer reaction of chromium and chromium(III) oxide 168
Equation 14: Exchange reaction of iron between melt and metallic iron nuggets 171
Equation 15: The equilibrium constant K of Equation 14 171
Equation 16: Equation 15 transformed 171
Equation 17: Equation 16 rewritten for the iron-wüstite reaction 171
Equation 18: Calculation of oxygen fugacity from iron-melt partitioning 171

II. Acknowledgements

A dissertation is never the result of the efforts of a single person, but only becomes possible through the collaboration of many. These people should be thanked here, regardless of whether they have contributed officially or quietly in the background to the success of this dissertation.

First of all, I would like to thank the International Max Planck Research School (IMPRS) and the Max Planck Institute for Solar System Research in Göttingen for making it possible for me to write this thesis. I would also like to thank Dr. Sonja Schuh and Johanna Wagner-Farsi for organising and promoting the professional and private exchange between PhD students from all over the world.

For the professional supervision of my work, I would like to express my sincere thanks to my supervisors, Sharon Webb, Urs Mall, Bernd Lehmann and Burkhard Schmidt, who have always supported this work with advice, but also with supervision in the laboratory, as well as Sharon Webb and Andreas Pack, who kindly took over the refereeing of this work.

I would like to express special thanks to Geoffrey Bromiley, who took time for me without any benefit to himself and contributed significantly to solving our experimental problems with his extremely helpful advice.

Thanks also goes to my colleagues in the Department of Mineralogy and Petrology. I would like to make a special mention of Jochen Gätjen for his great help at the electron microscope and analytics, as well as the other staff members of the GoeLEM laboratory.

For technical help, I would like to thank Alexander Masurowski as well as Lothar Laake and the staff of the central workshop for the numerous small and large repairs of the experimental equipment.

I would also like to sincerely thank my sisters, Michaela and Claudia, who contributed to the formulation of this thesis with their numerous linguistic comments.

For her continuous support in all phases of this work, I would like to thank my partner Heidrun, who at the same time gave me the greatest gift during this time with the birth of our son Arne. I could not have done it without both of you.

III. Abstract

Water plays an important role for many geological and organic processes. Nevertheless, it is still unclear why our Earth has such large quantities of it. Either it has been part of the building blocks of our planet or was delivered to it very early after its formation. The lunar formation took place simultaneously and therefore offers unaltered insights into the early history of the Earth where information was constantly lost by active processes like weathering for billions of years.

The assumed Moon forming giant impact caused magma oceans on Earth and Moon. In this study, experiments have been made which simulate the conditions of the lunar magma ocean in the pressure range between 3 and 0.2 GPa. One of the goals was the investigation of the crystallisation process to derive the partitioning of water between melt and minerals at realistic lunar conditions. This results in a model distribution of the lunar interior water prior a possible mantle inversion.

The experimental results predict olivine and orthopyroxenes as mantle phases followed by clinopyroxene at 81% solidification. The onset of crustal formation by precipitation of plagioclase has been found for the last 9% of solidification accompanied by metal oxides and quartz. The performed runs have shown the challenges of generating reliably the dry and reducing lunar conditions two log-units below the iron-wüstite buffer. We noticed precipitation of elemental iron in our series considered to be indicative of reducing conditions. Nevertheless, it has not been clearly demonstrated whether the Fe-nuggets found are a result of the conditions or an artifact caused by the use of iron capsules.

To investigate these experimental findings, additional thermodynamic simulations were performed with MELTS. These predict a strong loss of iron in the deep Moon for the envisaged oxygen fugacity indicating ongoing core formation. The results of the simulations were combined with partitioning coefficients that have since been published for lunar conditions by another group to model the distribution of water in the interior of the Moon. The results predict a minor role of the actual mineral abundances for the water content of the residual melt. With an initial water content of 100 ppm in the LMO composition, the minerals show an increase in water content above 10 ppm only from a depth of 60-90 km. This predicts very dry mantle conditions for the previous 1300 km depth and a significant increase in water content of the uppermost clinopyroxene and plagioclase layers. To match the measured water content of lunar samples to our results, extensive degassing must have taken place for the late stages of the LMO crystallisation.

1 Introduction

1.1 Origin of the solar system

By dating of the oldest known material in the solar system – the calcium-aluminium rich inclusions (CAI) in chondritic meteorites - it has been determined that our solar system formed about 4.568 billion years ago. This process began with a rotating disk of gas and dust with the Sun at its centre (Bouvier & Wadhwa, 2010) and gradually, through a series of collisions and accretions of larger and larger objects, all the celestial bodies in the solar system formed, eventually resulting in the solar system as it is known to us today.

In such disks gases are driven outwards until the temperature has fallen below their condensation temperature causing the formation of solids. As a result, gas planets are found in the outer region of the solar system while rocky planets, including Earth, are forming in the interior. The boundary between these areas is called the "snow line" which is located at approximately 2.7 AU (Figure 1), i.e. within the asteroid belt between Mars and Jupiter (Martin & Livio, 2012). This assumption is based, among other things, on the fact that the outer asteroid belt (>2.7 AU) contains many icy C-class asteroids, while the inner asteroid belt (<2.7 AU) is almost devoid of water (Figure 2) (Abe et al., 2000, Morbidelli et al., 2000).

The formation of the gas giants Jupiter, Saturn, Uranus and Neptune was already completed after 0.1 Ma (Walsh et al., 2011) while the formation of the inner rocky planets - Mercury, Venus, Earth and Mars - required considerably more time. For Earth, it is assumed that it may have reached two-thirds of its present mass after 10 Ma (Rudge et al., 2010) with its formation completed between 38 Ma (König et al., 2011) and 100 Ma (Rudge et al., 2010).

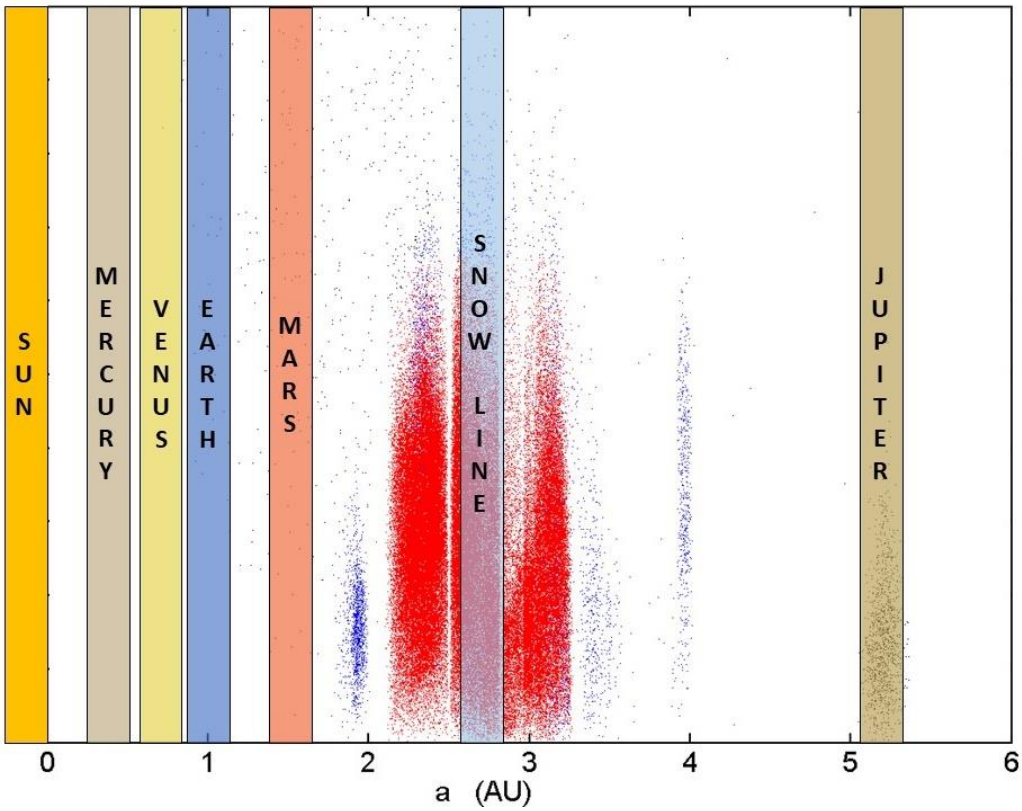


Figure 1: Approximate position of the Snow Line at 2.7 Au and mean positions of the planets Earth, Mars and Jupiter relative to the asteroid belt (original image: Piotr Deuar, modified).

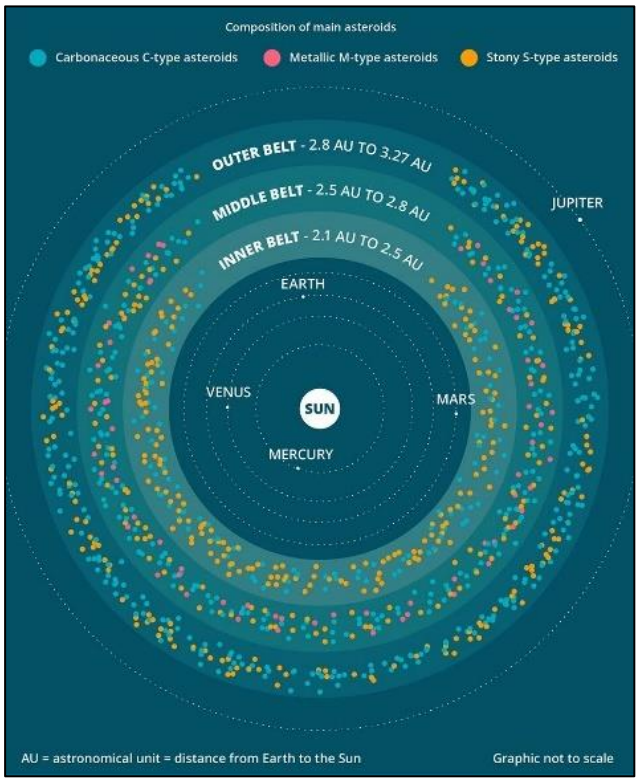


Figure 2: Composition of the inner, middle and outer asteroid belts (DeMeo & Carry, 2014).

1.2 Origin of water on Earth

Despite its location within the snow line, which suggests that the Earth should hardly carry any water, we detect numerous oceans on our planet with even more water being stored within the Earth's mantle (Peslier et al., 2017). The earliest evidence of liquid water on Earth was found in overprinted pillow basalts from Canada which are between 4.28 Ga and 3.8 Ga (O'Neil et al., 2012; Cates & Mojzsis, 2007). However, the source of Earth's water is still up to debate.

Figure 3 suggests that there are two main possibilities regarding the origin of water on Earth which have yet to be distinguished:

1) Water was already present in the building blocks that formed the Earth and thus it has been part of the planet since its inception.

2 & 3) Water was delivered to Earth after its formation by impacts of water-rich comets and asteroids.

These two options do not necessarily contradict each other, but their relative contributions to the Earth's overall terrestrial water budget is unclear. While both processes may have contributed equally, it could have been possible that one of them had a negligible impact.

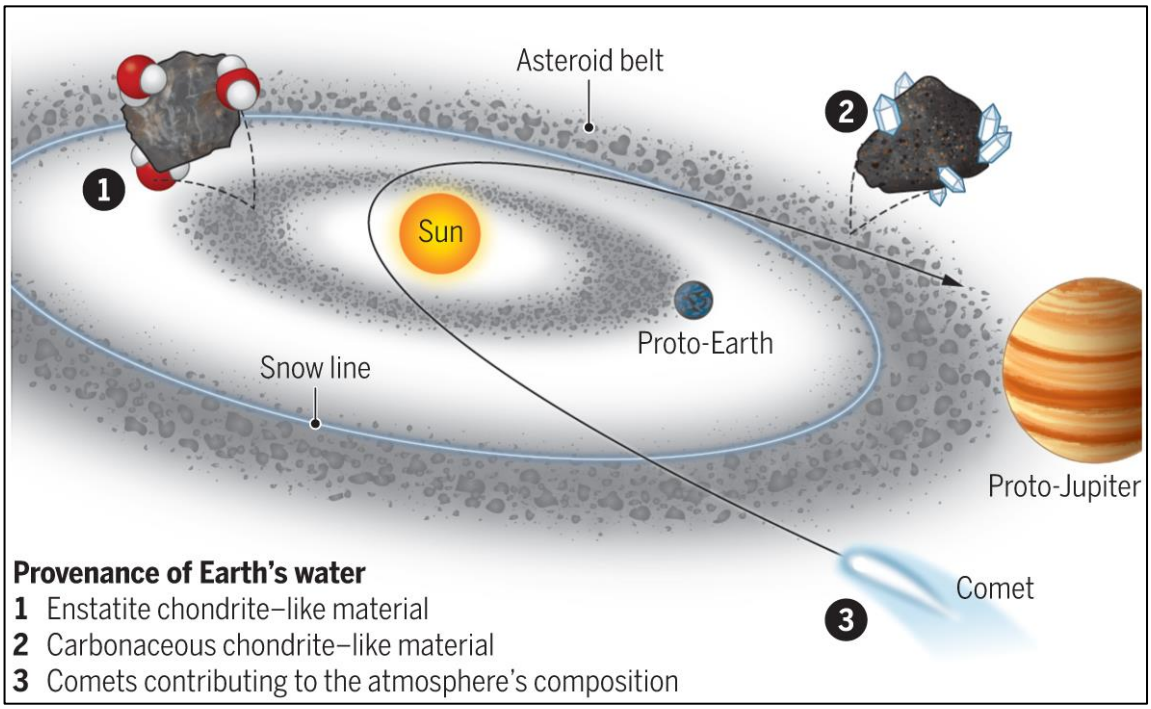


Figure 3: Possible origins of terrestrial water (Peslier, 2020)

Enstatite chondrites (EC) are among the most reduced silicates in the solar system and are considered rather rare. They are characterised by the almost exclusive presence of pure iron or in the form of sulphides rather than oxides. This chemical composition suggests that ECs may have formed close to the sun (Norton & Chitwood, 2008). They are believed to be the most likely building blocks of the Earth and Moon, as their isotopic signature can hardly be distinguished from EC meteorites (Young et al., 2016; Zhang et al., 2012; Dauphas et al., 2015; Qin et al., 2010; Javoy et al., 2010; Warren, 2011; Dauphas & Schauble, 2016). However, until recently, it was assumed that material formed close to the Sun and thus inside the snow line, where temperatures are high, could hardly contain water. Moreover, the expected H_2 concentrations in these materials are believed to be very low. Hence very sensitive techniques are required to measure while ruling out contamination with terrestrial water. Only in 2020, Piani et al. (2020) were able to successfully measure the water content of ECs revealing that they contain between 0.08 to 0.54 wt% water. Combining this with models of Earth accretion suggests that the Earth may have absorbed up to three ocean equivalents of water from this source alone, without even considering the contribution of water-rich impacts. Another theory regarding the source of terrestrial water suggests that it originated from beyond the snow line where water can condense into ice. According to this model, the material must have left its original orbit and come close to the inner planets, such as Earth. This movement could have been caused by the formation and rapid growth of the large gas giants, destabilising the orbits of water-bearing planetesimals (Raymond & Izidoro, 2017). As a result, these may have entered the terrestrial regions of the solar system (Raymond & Izidoro, 2017). While some of these theories provide plausible explanations for the origin of terrestrial water, they must also account for the existence of heterogeneous isotope ratios in the solar system and simultaneously describe how the D/H ratio of the Earth can be explained.

Several other theories have also been proposed to explain the origin of terrestrial water, including a shift of the snow line towards the inner regions of the solar system during the advanced stages of accretion (Hartmann et al., 2017) or the adsorption of H_2 on dust particles in the early days of the solar system (Drake, 2005). Despite these existing theories, the origin of terrestrial water remains unclear with no profound proof to support any one theory.

However, a key to understanding the origin of our planet's water may be found very close to us: the formation of our Moon is closely linked with the early evolution of the Earth. The Moon's lack of active geology also means that it preserves information about the early history of our solar system that is no longer present on Earth. Hence the Moon represents

a valuable source of information for scientists who seek a better understanding not only of its history and inner structure but also of the origins of water on our planet.

1.3 Theories of the lunar formation

Understanding the formation of the Moon is a crucial aspect of investigating the origin of terrestrial water. One important question in this context is why the Earth has a satellite at all and how it was formed. Scientists believe that the Moon was formed by a collision event between the early Earth and another protoplanet. However, the underlying reasons for this event remain an open question.

Our understanding of the Moon's chemical and physical properties has grown significantly requiring good explanations to account for them comprehensively. Key properties that must be taken into account are the angular momentum of the Earth-Moon system, the small core size of the Moon - if it has one - and the chemical similarities between the two bodies. The similarities in isotopic signatures of the Moon and the Earth for example in oxygen, tungsten and silicon (Wiechert, 2001; Touboul et al., 2007; Georg et al., 2007), are highly unlikely to be coincidental and rather show that both bodies must be linked by a common history of formation.

For centuries scientists have long attempted to explain the scientific origins of the Moon. One of the earliest proposals was that the Moon may have formed at the same time as the Earth (Thompson, 1862). However, this hypothesis fails to account for the significant angular momentum of the Earth-Moon system. Therefore, alternative theories have been proposed instead.

Darwin, for example, chose a different approach. He was aware of the fact that the rotation of the Earth must have been much faster in the past - in early times, a day corresponded to only about 2.5 hours - and that this rotation has slowed down since. According to his theory, the Moon was formed by the resulting high centrifugal forces generated by the fast rotation of the Earth. This process ejected material from the Earth's crust with the gaps left behind becoming our ocean basins (Darwin & Glashier, 1879; Jeans, 1928). However, as we know now, they are the result of plate tectonics (e.g. Wright & Rothery, 1998).

Scientists have also considered the possibility that the Moon may have formed elsewhere in the solar system. According to this theory the moon has later been captured by the Earth's gravitation (Urey, 1952). However, this explanation seems rather unlikely for the Earth and Moon – having formed at different locations in the Solar System – to carry the same isotope ratios.

The various previously mentioned theories have each been limited in their ability to account for all observed properties. The only theory so far that has sufficiently linked all of these properties is the Giant Impact Theory. According to this theory, the Earth collided early in its formation with a protoplanet of the size of Mars ejecting material that eventually coalesced to form the Moon (Safronov, 1964, 1978; Weidenschilling et al., 1997; Wetherill, 1975, 1985, 1990; Daly, 1946; Canup & Asphaug, 2001). Various variations and extensions of this theory have been formulated, e.g. the collision of two bodies of the same size (Canup et al., 2014) or the collision of many small bodies that gradually formed the Moon (Rufu et al., 2017). The Giant Impact Theory explains the angular momentum of the Earth-Moon system, the chemical similarities between the Earth and the Moon as well as the isotope ratios of both bodies.

Despite of variations in the specific details of the event, scientists believe that it has occurred between 30 Ma and 100 Ma after the formation of the solar system. According to Halliday (2008) this impact provided the final 10% of our Earth's mass and thus also marks the completion of its formation (Figure 4).

Such an impact dissipates large amounts of kinetic energy, which leads to the deformation of the bodies and to extreme heating. According to calculations, the temperature of Earth and Moon was increased through this to 2,000°K - 10,000°K (Flasar & Birch, 1973; Melosh, 1990; Pierazzo et al., 1997; Tonks & Melosh, 1993). However, the melting temperature of the rocks at the core-mantle boundary of the Earth is only 4,000°K to 5,000°K. Therefore, it is believed that the Earth could have been at least partially molten and the Moon was potentially completely molten. Hence the theory of a large, moon-forming impact is therefore closely linked to the existence of a magma ocean on both bodies.

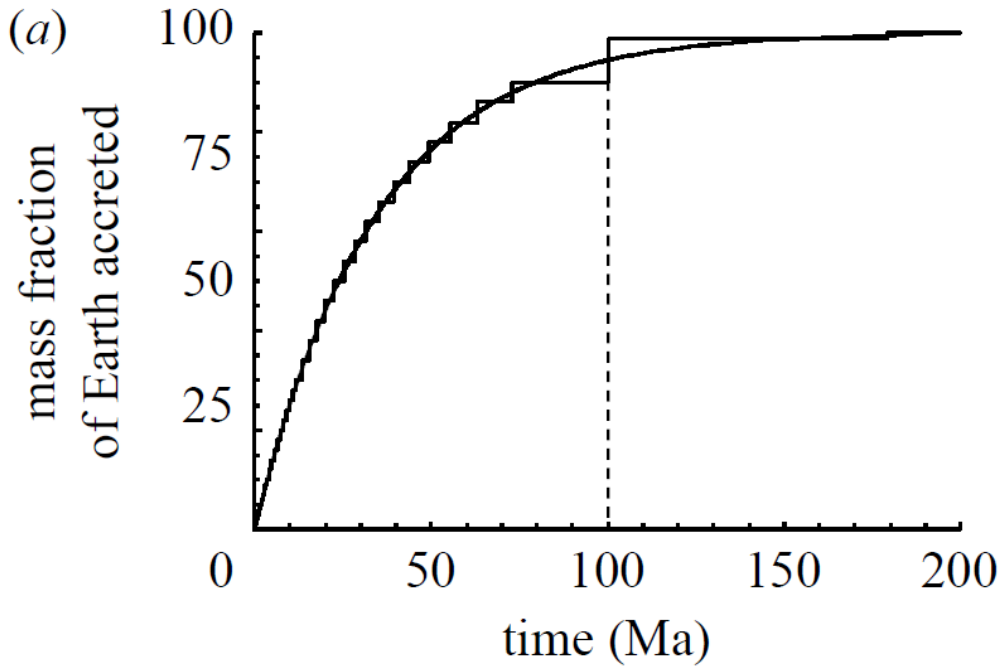


Figure 4: Proportion of Earth mass already present in millions of years after the formation of the solar system. The moon-forming impact is thought to have provided the last 10% of the Earth's mass (Halliday, 2008)

The immense thermal energy presumably evaporated any volatiles that existed on the young Earth up to that point. These initially formed a dense, CO_2-dominated atmosphere on Earth, from which oceans condensed (Sleep et al., 2001). The Moon's gravity is too low to be able to maintain an atmosphere, which is why until now, it was assumed that any volatiles were degassed from the debris disc forming the Moon. According to simulations by Nakajima and Stevenson (2018), this process is inhibited by the slow diffusion of volatiles through the debris disk. This may have allowed the Moon to retain some volatiles. Where these originally came from is still unclear. The Moon is considered one of the most likely places to find information about this early period.

1.4 Background and previous research

1.4.1 The composition of the lunar interior

Besides the question of how the Moon was formed, it is equally important to understand its composition. Most of the information we have comes from the US Apollo programme (1961-1975). Among the returned specimens are crustal rocks which are predominantly anorthosites, a plutonic rock that is composed of 90 - 100% plagioclase (a feldspar), as the analyses of the rocks showed. On Earth, this rock forms in large magma bodies when the plagioclase, which is less dense than the magma, rises and accumulates at the roof of such a batholith. This indicates that the Moon might also once have been a “magma chamber” itself. This information thus supports the theory of a large impact as the cause of the lunar formation.

Based on the assumption that the Moon eventually formed from debris ejected by Earth as well as the impacting protoplanet named Theia, Canup et. al. (2004) ran simulations to investigate the processes involved in the formation of the moon. They identified that the Moon is composed primarily of material from Theia which is therefore assumed to have had a very similar composition to Earth. In the past, this problem was countered with the idea that a larger proportion of Theia could have been ice, thus diluting its influence on the chemical signature (Reufer et al., 2012). Other ideas assume that the Earth was surrounded by a disk of vaporised material after the impact, which had sufficient time to equilibrate with the moon-forming material. This would explain the measured similarities (Pahlevan & Stevenson, 2007).

However, the question why the Moon and the Earth show such similarities in their chemical compositions remains the subject of ongoing debate. Derived from the Apollo-specimens, two compositional endmembers of the Moon could be defined: On the one hand, the approach of John Longhi (Lunar Primitive Upper Mantle (LPUM), Longhi, 2006), which assumes a similar composition to Bulk Silicate Earth (BSE). On the other hand the view of the ‘Taylor^3’ (Taylor Whole Moon (TWM); Taylor, Taylor & Taylor, 2006), who also take the BSE as a starting point, but add an enrichment of the refractory elements by 50%. Both groups justify their theses with analyses of the Apollo samples, whereby Longhi refers to the aluminium in the crust and mantle, while ‘Taylor^3’ refers to aluminium and thorium. Both arguments are preceded by assumptions, e.g. about the crustal thickness of the Moon, which according to the latest investigation of data from the GRAIL mission is thinner than previously thought (35 km instead of 50 - 70 km) (Wieczorek et al., 2013). Hence, the exact composition of the Moon and its similarities with the earth remain an area of active research.

1.4.2 Lunar Magmatic Ocean (LMO)

It is widely accepted that the Moon was once covered by a global magma ocean, and scientists have since developed several theories about its composition. In 1992, Snyder et al. (1992) used this information to model the lunar magmatic ocean (LMO) and thermodynamically calculated which minerals would crystallise at which depth, deriving an initial framework for understanding of the basic structure of the lunar interior (Snyder et al., 1992). To this day, this study forms the basis for all considerations surrounding the LMO and the internal structure of the Moon. To complement theoretical calculations, many experimental studies have also been conducted. In these, the estimated lunar mantle composition is studied in the laboratory under the physical conditions of the LMO and the crystallisation is quenched after a certain time by rapid cooling. This makes it possible to recreate the conditions at any depth of the LMO. It allows one to study the minerals crystallising in this particular layer and their compositions and relative proportions.

Nevertheless, these experiments can only depict a simplified image of the real LMO. A fundamental problem of such experimental series is the question how one incorporates convection. For the LMO, the convection was characterised early on as turbulent and it is assumed that it is capable of keeping minerals up to a size of one millimetre in suspension (Castaing et al., 1989; Grossmann & Lohse, 1992; Shraiman & Siggia, 1990; Siggia, 1994). As a result, newly formed minerals do not necessarily fractionate (i.e. sinking to the bottom of the magma ocean). Instead, they remain in contact with the surrounding melt leading to an equilibrium crystallisation process. During this process, melt and crystal can continue to interact with each other and changes in the melt chemistry are transferred to the crystals.

As soon as the Moon is about 50% crystallised, it is assumed that convection slows down to such an extent that it is no longer able to keep crystals in suspension (e.g. Snyder et al.,1992). These fractionate immediately after formation and are thus no longer available to the melt for exchange reactions. In experimental studies, one must therefore decide whether to consider fractional or equilibrium crystallisation. Both variants have been investigated by various authors in the past. Figure 5 gives an overview of existing studies and their outcome regarding the mineral composition from the deep LMO (0 percent solidified) to the surface (100 percent solidified) under varying assumptions for the initial composition, pressure, water content and crystallisation regime. The results hardly differ in the basic sequence.

According to these results, magnesium-rich olivine (Fo# ~85) crystallises at the beginning of the LMO until about 50% of the LMO is solidified. This is followed by magnesium-rich

orthopyroxene (OPX) (Elardo et al., 2011; Elkins-Tanton et al., 2002; Snyder et al., 1992). The crystallisation of these minerals removes elements from the melt; thus, it becomes depleted in certain chemical components while others are enriched. For the LMO, the heavy melt components in the form of iron and titanium are of particular importance. Neither olivine nor the pyroxenes incorporate those into the crystal structure to any appreciable extent up to this point. The density of the residual melt therefore increases steadily.

At 78% solidification, the first plagioclase forms. Due to its lower density compared to the the iron-titanium rich melt, the newly formed plagioclase rises to the surface of the LMO forming a primitive lunar crust of anorthosite, which is the only structural unit of the Moon that has been sampled directly by the Apollo missions so far (Ringwood and Kesson,1976; Smith et al., 1970; Taylor and Jakes, 1974; Wood et al., 1975).

The last crystallising layer is therefore below the Moon's crust instead of on the surface and consists of iron-rich minerals such as ilmenite as well as an accumulation of all those elements that are not or difficult to incorporate into the crystal lattice of the previously crystallised minerals. This results in the formation of a layer who is known as KREEP (K for potassium, REE for rare earth elements and P for phosphorus) (Warren 1988a,b; Warren & Wasson, 1979).

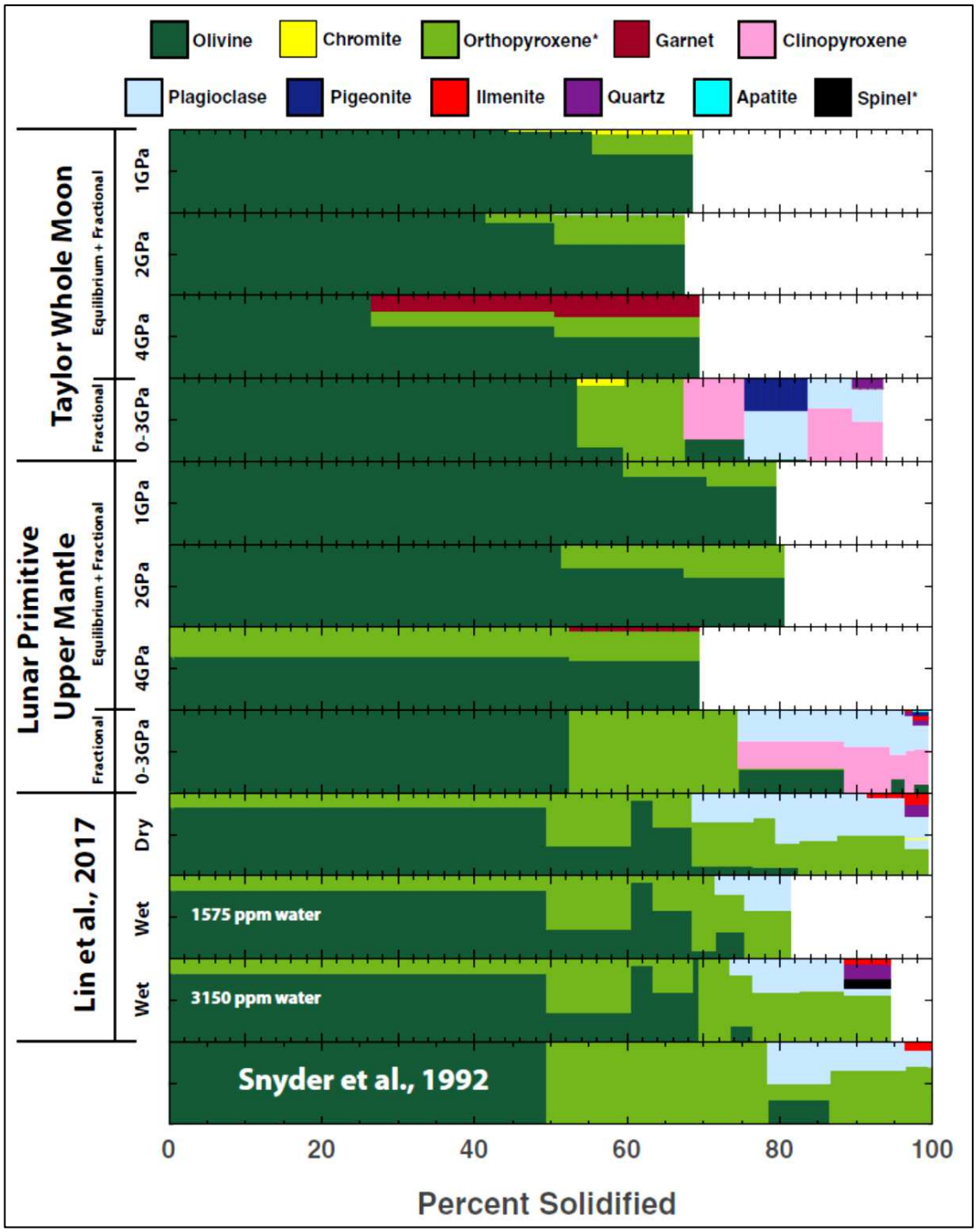


Figure 5: Modelled or experimental results of different authors on the crystallisation of LMO under the given conditions. (Rapp & Draper, 2018)

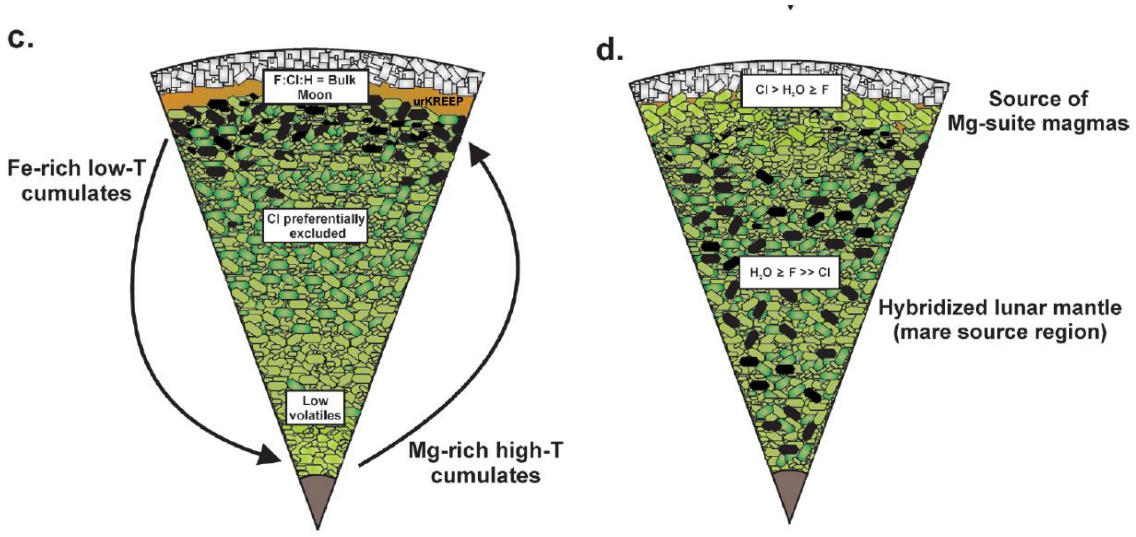


Figure 6: Cross-section of the Moon before (c) and after (d) the cumulate overturn. The putative sources of Mare and Mg-suite magmatism are described in the figure on the right. (McCubbin et al., 2015)

The Moon's mantle is thus simplistically composed of olivine and pyroxene and is rich in iron oxides in the upper mantle, while the anorthositic curst is separated from the mantle by the KREEP layer.

However, it turns out that the magma ocean formed in this process is gravitationally unstable: The ilmenite-rich cumulates are significantly denser than the underlying olivine-pyroxene mixtures due to the high iron and titanium content. In theory, this leads to what is known as a mantle overturn: the ilmenite-rich cumulates sink, while hot, magnesium-rich olivines and pyroxenes rise (Figure 6) (Elkins-Tanton et al., 2002; Hess & Parmentier, 1995; Neal & Taylor, 1992; Ryder, 1991).

This process is thought to be responsible for two types of magmatism: The first type is the formation of titanium- and iron-rich mare basalts which fill the many impact basins on the lunar surface. These basalts are believed to originate from the partial melting of the submerged ilmenite cumulates in interaction with the hot mantle material. The second type is the magnesium highland suite, which is believed to have formed from a mixture of the upwelling magenisum rich olivines, the anorthositic crust and the KREEP layer, which begin to melt when pressure is released (Shearer et al., 2015, Longhi, 1992).

1.4.3 The structural composition of the Moon

The previously mentioned theories and models provide us with a good idea of the Moon's mineralogical composition. However, is there any empirical evidence about the internal lunar structure? Earth seismology is a crucial tool providing valuable insights into the Earth's interior through the measurements of the speed and type of shock waves that cross our planet triggered by earthquakes or other events. There are hundreds of measuring points deployed worldwide. According to the Federal Institute for Geosciences and Natural Resources (*Bundesanstalt für Geowissenschaften und Rohstoffe*, BGR), 250 measuring stations are operated in Germany alone, some of which have been recording continuously since 1976. On the Moon, there are 6 measuring stations from the Apollo era (Figure 7), one of which (Apollo 11) was only active for three weeks. The measuring stations from Apollo 12, 14, 15, 16 and 17 were switched off in 1977 (Nunn et al., 2020).

Unlike on Earth, where seismometers can strategically be placed in ideal locations, the lunar seismometers are restricted to the landing site of the module and are therefore only located on the front side of the Moon. Additionally, the signal transmission is limited by hundreds of meters of thick layers of dust and impact debris (regolith) that scatters seismic waves. Despite these limitations, the six stations were able to record 13058 different events (Table 1).

Using the recorded data of these events, various researchers have developed physical models to reproduce the lunar interior (Nakamura, 1983; Lognonné et al., 2003; Weber et al., 2011; Garcia et al., 2011, 2012). Figure 8 depicts the wave velocities of shear and compression waves with the depth of the Moon, as well as the derived density of the material (Weber et al., 2011).

The interpretation of data suggests that the moon likely has a core with a radius of 330 km. However, due to the limited amount of data, this conclusion is not certain and remains the subject of active research. Additionally, other theories suggest the presence of a lunar core based on the fact that there were hardly any events recorded from the backside of the Moon (Weber et al., 2011) and electromagnetic observations are consistent with a core of 4% of the lunar mass (Weber, 2014).

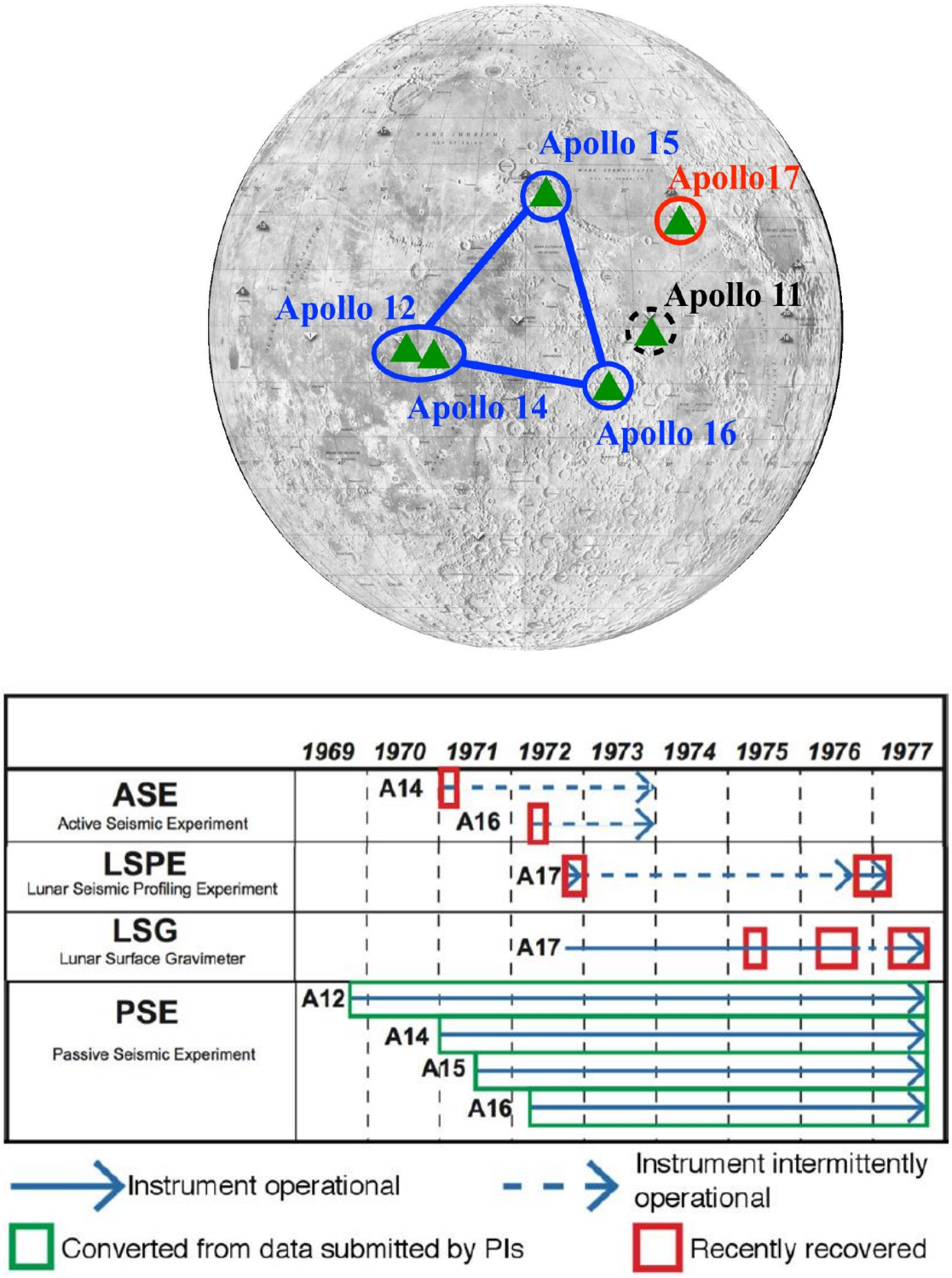


Figure 7: Location of Apollo-era lunar seismometer measurement sites (top) and period of data recording (bottom) (Nunn et al., 2020).

Table 1: Number and type of lunar earthquakes during the recording period of the Apollo experiments (Nunn et al., 2020, catalogued by Nakamura et al., 1981, revised 2008).

Type of moonquake	No.
Artificial impacts	9
Meteoroid impacts	1743
Shallow moonquakes	28
Deep moonquakes (assigned to nests)	7083
Deep moonquakes (not assigned to nests)	317
Other types (including thermal quakes)	555
Unclassified	3323
Total	**13058**

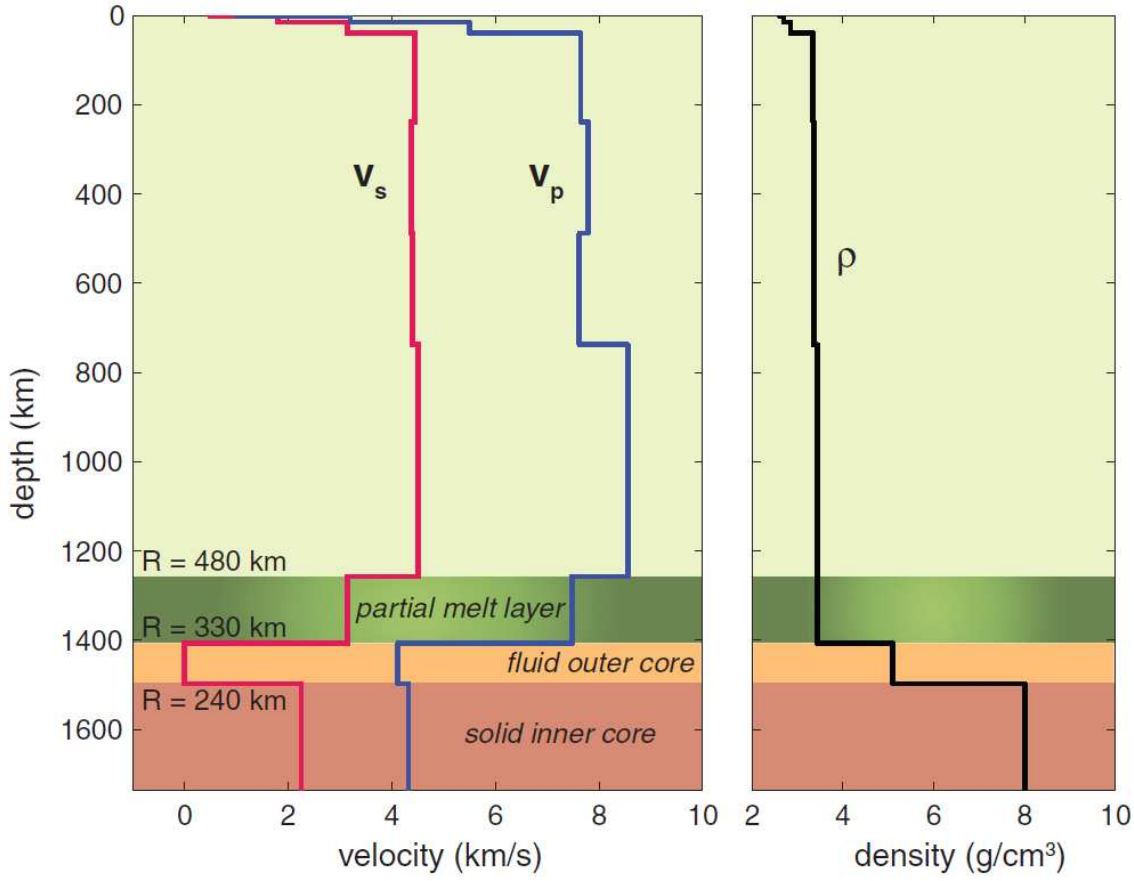


Figure 8: Wave velocities (left) and density (right) of the Moon with depth (Weber et al., 2011).

Due to the limited amount and the low quality of data on the Moon's mantle, definitive conclusions can hardly be drawn. However, calculations based on the moon's moment of inertia suggest a homogeneous mantle in terms of density. The evaluation of the seismograms from the Apollo missions is complex and does not provide a detailed picture. It is striking that the wave velocities hardly weaken. This is an indication of very dry conditions and suggest that mantle convection is unlikely (Weber, 2014). The source region of deep lunar earthquakes (800-1000km depth) is located in the mantle, but the cause of these earthquakes is not yet understood. Below 800km depth, wave velocities weaken, indicating the presence of partial melts. While the seismic data are broadly consistent with the assumed mineralogical structure of the Moon, there is still considerable uncertainty (Weber, 2014).

To address these open questions, several nations are currently planning a network of seismic stations on the Moon which is expected to provide a much better understanding of the lunar interior (Nunn et al., 2020). For more information on past and planned seismological missions, see Lognonné & Johnson (2015).

1.5 Water in lunar materials

During the Apollo missions, the astronauts collected samples of volcanic effusive rocks from the Moon, which were subsequently analysed for their volatile content. Volatiles, such as water, play a critical role in the development and evolution of planets. Water is of particular interest, as it can lower melting points, affect the viscosity of melts, serve as a lubricant for geodynamic processes such as plate tectonics or take on transport functions for exchange reactions. Additionally, water is fundamental to all known forms of life, making it a crucial prerequisite. Therefore, understanding the quantity of water within a planetary body or moon is of great interest to be able to model their development.

The lunar crust and core make up only a small fraction of the Moon's overall volume. Analogous to Earth, understanding the water balance of the Moon requires examining the water content in its mantle. However, since mantle rocks are very rarely exposed directly on the surface, we rely on melts that originate in the mantle to provide us with information about its water content. Unfortunately, simply measuring the water content in magmatic rocks is not sufficient because the solubility of water and other volatiles in melts is significantly affected by pressure (Hamilton et al., 1964; Silver et al., 1990; Blank et al., 1993; Dixon et al., 1995; Zhang, 1999; Yamashita, 1999; Behrens & Jantos, 2001; Tamic et al., 2001). If a magma rises to the surface, the pressure gradually decreases and with it the solubility of the volatiles. If the solubility falls below the volatile content, the magma degasses. As a result, gas bubbles form, which continue to grow through diffusive transport until they finally escape at the surface during eruption.

For a long time, scientists assumed that the Moon had lost a substantial proportion of its volatiles and water due to its hot formation history. However, this assumption was challenged after samples of magmatic rocks brought back by the Apollo missions were analysed, but since the analytical methods were not sensitive enough at that time, there were initially only estimated values for the primitive water content (<1ppb).

In 2008, a paradigm shift finally followed when Alberto Saal and his team were able to detect primitive water contents in basaltic glasses of the Moon using advanced analytical methods. The measured water contents were in the range of 10s of ppm, indicating that the region of origin likely had primary water contents between 260 to 750 ppm (Saal et al., 2008). These values are comparable to the dry middle oceanic ridge basalts (MORB) on Earth.

Following the discovery that there is a primitive water content in basaltic glasses of the moon, further samples were analysed and water was found in apatite (up to 7000 ppm, McCubbin et al., 2010), melt inclusions (up to 1,200 ppm, Hauri et al., 2011) and plagioclase (up to 6 ppm, Hui et al., 2013). These measurements clearly indicate that the Moon contains a much larger, primitive water content than previously thought. However, the extent of the water content of the entire Moon remains an open question. Various attempts have been made to estimate general values of the water content of the mantle, the crust or KREEP based on measurements of respective samples (e.g. McCubbin et al., 2015). However, the estimates differ significantly, which could indicate a heterogeneous water distribution ("wet spots", e.g. Mills et al., 2017). Table 2 shows a range of estimates for the volatiles of the mantle, bulkmoon and urKreep.

Table 2: Estimates for the volatile content of mantle, KREEP and BSM based on measurements of lunar samples (from McCubbin et al., 2015).

Lunar reservoir	Basis of estimate	H_2O	F	Cl	C	S
Mantle						
	74220: Olivine-hosted melt inclusion within orange glass	9–130	2–11	0.034–0.24	0.014–0.57	57–250
	Bulk rock mare basalts	0.3–11	1.1–12	0.009–2.8	–	38–924
	10058: Apatite	9–28	4–20	–	–	–
	12039: Apatite	16–51	4–10	–	–	–
	15058: Apatite	1–4	2–12	0.9–3	–	–
	15555: Apatite	10–30	2–10	–	–	–
	MIL 05035: Apatite	8–26	0.56–6	–	–	–
	LAP 04841: Apatite	53–166	4.5–19	2–6	–	–
	10044: Apatite	5–15	2–13	–	–	–
	75055: Apatite	4–13	3–9	–	–	–
	14053: Apatite	8–26	4.5–15	–	–	–
	12064: Apatite	2–7	1–6	–	–	–
	Bulk lunar mantle from CFHA & 0.5% ILTc	1.2–5.3	4.5	2.3–2.9	-	-
	Bulk lunar mantle from LSHA & 0.5% ILTc	0.15–0.61	0.54	0.26–0.32	-	-
urKREEP						
	Lunar soils	–	660	150	–	–
	Lunar soils and highland apatite (LSHA)	300–1250	660	1100–1350	–	–
	Ferroan amorthosite	1.4 wt%	–	–	–	–
	Chondritic F and highlands apatite (CFHA)	0.26–1.09 wt%	5548	0.98–1.20 wt%	–	–
Bulk silicate Moon						
	Primordial bulk silicate moon CFHA	27–114	60	100–123	0.014–0.57	78.9
	Primordial bulk silicate moon LSHA	3.1–13.1	7.1	11.3–13.8	0.014–0.57	78.9

1.5.1 Water-bearing minerals

In the incredibly dry environment of the lunar mantle, the occurrence of nominally hydrous minerals is severely limited. Among the volatile-bearing minerals found in lunar rocks, apatite is the most common. It has been identified in all rocks of the Moon except for ferroan anorthosites (FANs) of the lunar crust and the volcanic glass beads, with sizes ranging from <1 µm to 2 mm and should therefore be considered a trace mineral (McCubbin et al., 2011; Treiman et al., 2014). Despite its limited presence, apatite is an essential mineral because

it holds the largest reservoir of rare earth elements and phosphorus (Hughes et al., 2006; Jolliff et al.,1993 & 2006). Notably, almost all lunar apatite is fluorapatite (McCubbin et al., 2011).

The composition of apatites varies depending on the type of rock in which they have been discovered. In Mare basalts, for example, apatites tend to have low chlorine and water contents ranging from 100 ppm (sample 12040) to 7000 ppm (sample 12039) (Greenwood et al., 2011; Tartèse et al., 2013). In contrast, rocks from the magnesium and alkali suite and KREEP-rich impact melts tend to have higher levels of chlorine (McCubbin et al., 2011) as well as lower water contents, ranging from less than 100 ppm (Troctolite 76535) to 1612 ppm (norite 77215) (Barnes et al., 2014). On the other hand, apatites in KREEP-rich basalt tend to have water contents that fall roughly in between, ranging from less than 40 ppm (sample 72275) up to 2500 ppm (NWA 772). The research results gathered by McCubbin et al. (2015) also show the broad variety of volatile contents in lunar apatite and other materials, as indicated in Table 3.

Table 3: H_2O in lunar materials (from McCubbin et al., 2015)

Volatile (ppm[a])	H_2O	C	N	F	S	Cl
Interior of orange glass	5–13	–	–	9–17	282–490	0.02–0.14
Interior of green glass	0.4–30	–	–	2–10	114–270	0.03–0.50
Interior of yellow glass	17–46	–	–	29–40	518–576	1.3–2.0
Mare basalts	9–98	3–70	0.3–20	18–78	300–3300	0.3–28
Olivine hosted melt inclusions in orange glass	270–1200	–	–	37–72	450–880	1.5–2.4
Apatites in mare basalts	Up to 7600	–	–	18600–37900	Up to 463	Up to 15700
Apatites in Mg- and alkali-suite rocks	Up to 530	–	–	27000–36300	–	2400–17800
Apatites in breccias and impact melt rocks	Up to 16744	–	–	19900–36800	–	1500–36200
Mineralized coatings on lunar glasses	–	–	–	Up to 3000	Up to 650	~100
Agglutinates	13–488	–	–	–	–	–
Lunar soil and regolith breccias	4	Up to 280 (average 100–150)	4–209	9–520	60–600	0.6–270

1.5.2 Nominally dry minerals:

Nominally anhydrous minerals (NAMs) are minerals that do not incorporate water as a necessary component in their crystal lattice structure. However, they can still incorporate volatiles such as H, F and Cl at defects in their crystal lattice to balance the charge (Bell & Rossman, 1992; Libowitzky & Beran, 2006; Smyth, 2006; Wright, 2006). The most common representatives of NAMs found in lunar rocks are olivine, pyroxenes, garnet and plagioclase. While the volatile content of NAMs in lunar rocks has only been determined for feldspars (Hui et al., 2013; Mills et al., 2014), measurements show that plagioclases in ferroan anorthosites can contain up to 6 ppm H_2O, those from Mg-suite troctolites contain

up to 2.7 ppm H_2O (Hui et al., 2013). Furthermore, measurements on alkali feldspars in a granitoid clast (Breccia 15405) reached 1000 ppm H_2O (Mills et al., 2014). Research conducted by Liu et al. (2013) also suggests that olivine could have water contents in the ppm range.

It is essential to note, however, that it is difficult to draw conclusions for the water content of the entire Moon solely based on measurements of the water contents in individual minerals such as apatite (McCubbin et al., 2010) and plagioclase (Hui et al., 2013). Instead, the water content of the moon is usually determined using partitioning coefficients of water which describe the ratio of water in the mineral to the melt at the crystallisation conditions. The calculation of partitioning coefficients allow estimates on how much water was present in the original melt before degassing occurred. The water content of the melt itself depends on the water content of the mantle source and its degree of melting.

Water is known to behave incompatibly, meaning that it tends to preferentially change into the liquid phase during a melting process. As a result, the water content of the first melt will therefore have a high water content which decreases towards increasing degrees of melting due to dilution. If the degree of melting in the mantle is 10%, for example, the resulting melt contains 10 times more water than the mantle source originally had. If one now knows the approximate degree of melting during the formation of the melt, conclusions can be drawn about the source region. However, in case of apatite, it does not crystallise from the original melt, but from the last 1-3% of the melt before it has cooled down completely. At this stage, the melts already segregate into iron- and silicate-rich melt components in small, unconnected pockets, making it difficult to draw conclusions about the region of origin (e.g. Potts et al., 2016).

1.5.3 Water in lunar rocks and glasses

Bulk analyses for mare basalts are limited with the available data suggesting a hydrogen content ranging from 1 to 11 ppm (Haskin & Warren, 1991). However, the origin of this hydrogen is assumed to be from sources such as the solar wind or spallation reactions, i.e. subsequent alterations to the content that have no relation to the primitive water on the Moon.

Significantly more data for magmatic water contents from the Moon are found in glass beads (Saal et al., 2008). The classification of these lunar glasses follows the titanium content and at the same time the colour. Furthermore, a distinction must be made between glasses formed by impacts and volcanic glasses. Here, only volcanic glasses will be considered, as

only these provide information about primitive water contents from the lunar interior. Various such glasses from the lunar surface were analysed for their volatile content. The *High*-Ti Orange Glasses contain 5-13 ppm H_2O, 9-17 ppm F, 0.02-0.14 ppm Cl, and 282-490 ppm S. Very *low-Ti Green Glasses* reach values of 0.4-30 ppm H_2O, 2-10 ppm F, 0.03-0.50 ppm Cl, and 114-270 ppm S. The highest measured values are reached by *low-Ti Yellow Glasses* with 17-46 ppm H_2O, 29-40 ppm F, 1.3-2.0 ppm Cl, and 518-576 ppm S. Of these, only two samples were measured. (Saal et al., 2008; McCubbin et al., 2015).

It is assumed that those glasses were formed by fire fountains. These are gas-driven magmatic eruptions in which the melt is ejected at the surface and falls back to the ground, quenched into glass beads. In the process, the beads degas, but the process is not exhaustive. A characteristic degassing profile develops in the bead, i.e. the contents drop from the centre to the edge of the bead.

By analysing and understanding these processes, the water content in the melt can be estimated before degassing. It is still unclear which kind of gas drove these eruptions. Suggestions in the literature range from sulphide-rich gas (Butler & Meyer, 1976; Meyer et al., 1975), carbon rich gas (Fogel & Rutherford, 1995; Nicholis & Rutherford, 2009; Rutherford & Papale, 2009; Sato, 1979), fluorine and chlorine rich gas (Elkins- Tanton et al., 2003; Goldberg et al., 1976) as well as H_2 rich gas (Sharp et al. 2013; Vander Kaaden et al., 2015). These results are primarily based on the analysis of the glass beads as well as their surface coatings (McCubbin et al., 2015). The presence of volcanic activity of this kind on the Moon is often considered to be a strong indication for the hypothesis that the Moon has or must have had primitive volatiles to some extent.

1.5.4 Water in melt inclusions

Melt inclusions are particularly valuable in providing insight into the lunar mantle. These are small, trapped melt fractions which are able to avoid degassing by becoming encased in minerals during crystallisation (Sorby, 1858; Roedder, 1979, 1984; Metrich & Wallace, 2008; Moore 2008; Blundy & Cashman, 2008). This happens when a crystal is subjected to a selective growth inhibition, such as a lattice defect or a smaller crystal that must be grown around (Faure & Schiano, 2005; Kent, 2008; Nakamura & Shimakita, 1998; Kohut & Nielsen, 2004; Goldstein & Luth, 2006; Baker, 2008). Due to this protective effect of the host crystal lattice, the melt inclusion is largely shielded from a pressure drop during the ascent of the melt and thus from degassing in the remainder of the melt.

The internal pressure of an enclosure depends largely on its temperature which decreases during the cooling process. As a result, the melt inclusion contracts while the surrounding

crystal lattice is rigid and cannot follow. This negative pressure causes the formation of a gas bubble, filled with volatiles (Roedder, 1984). These gas bubbles can contain up to 90% of the volatiles of a melt inclusion (Sobolev et al., 1990; Anderson & Brown, 1993) and as they are retained by the surrounding crystal lattice of the host mineral, the information about the volatile content of the melt is preserved. Melt inclusions are therefore a valuable source of information for our understanding of the water content in the interior of a planet or moon.

However, several problems with melt inclusions are known. For example, melt inclusions need to be a closed system that maintains original information, which is not always the case. A pressure gradient is created by the fact that an inclusion maintains the pressure inside while the pressure outside the host mineral drops during ascent. Minerals are mostly robust against compression, but much weaker when faced with extension forces. The result is a possible formation of microcracks creating a path for volatiles to escape or even other substances to enter (Tait, 1992). These cracks are sometimes difficult to detect (Figure 9).

Furthermore, it is worth noting that the host mineral does not form an impenetrable barrier, allowing both outward and inward diffusion within the inclusion. As a result, the confined melt crystallises to varying degrees depending on the rate of cooling, changing the melt chemistry (Figure 9). This process can be partially reversed by reheating and re-quenching the inclusion to its glassy state (Roedder, 1979, 1984).

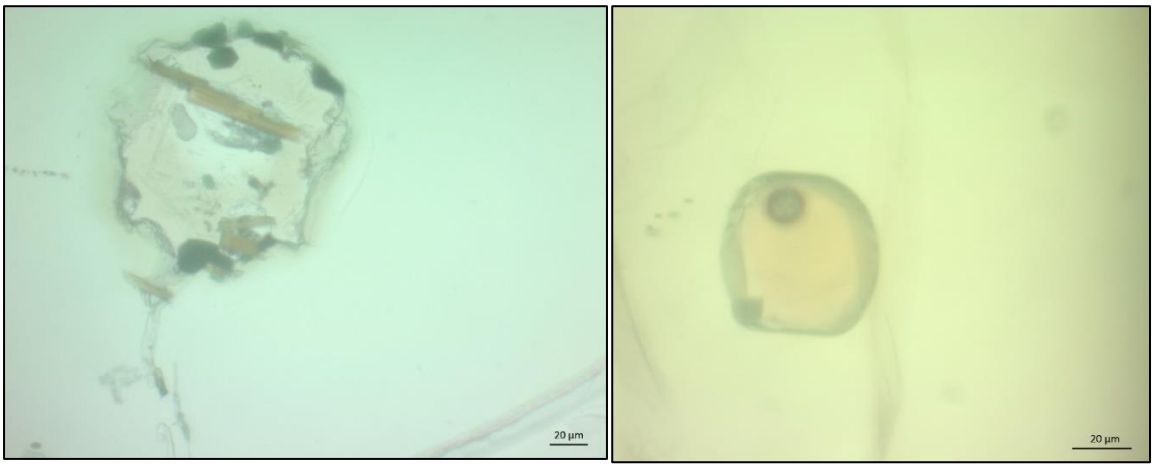


Figure 9: Examples of melt inclusions. Left: Melt inclusion with clear crystallisation of minerals as well as a connection to the crystal edge. Right: Melt inclusion with gas bubble. (Sample material: Laacher See, G. Wörner)

Even if an inclusion fulfils the condition of a closed system, it is important to consider which melt was trapped inside. As crystals grow, they extract the necessary components for growth from their immediate surroundings. This process is creating a concentration gradient within the melt which must be balanced by diffusion. However, if the growth rate exceeds the diffusion rate and a melt inclusion is formed at the same time, its chemistry may differ compared from that of the actual primary melt. This effect is mainly relevant for very small inclusions and does significantly impact larger ones (Faure & Schiano, 2005; Kuzmin & Sobolev, 2004; Nielsen et al., 1995, 1998).

Magmatic systems are not composed of a single magma but of many individual melts that mix with each other until eruption. Siliciclastic melt inclusions can provide insight into this diversity as well as different magmatic processes involved. It is thus essential to exercise caution when interpreting these inclusions (e.g. Anderson & Brown, 1993; Sobolev et al., 1983a,b, 1991; Sinton et al., 1993; Sobolev & Danyushevsky, 1994; Gurenko & Chaussidon, 1995).

Finally, it is worth noting that the water contents of lunar melt inclusions can vary significantly, ranging from a few ppm up to 1200 ppm (Hauri et al., 2011).

1.5.5 Water on the lunar Surface

Aside from primitive water, other sources of water can also occur on the lunar surface. One of the first discoveries was made for water in the form of ice which was found in the craters that lie permanently in the shade of the polar regions (Arnold 1979; Watson et al., 1961). While earlier missions could not confirm this beyond doubt, radar data from Clementine (Nozette et al., 1996) and spectroscopic data from the Lunar Reconnaissance Orbiter (LRO) and Chandrayaan-1 have lent support to this hypothesis (Spudis et al., 2010; 2013).

More robust evidence of water on the lunar surface has been provided by the Lunar Prospector Neutron Spectrometer (LP-NS), with average concentrations of 100 to 150 ppm for the polar regions of the Moon (Feldman et al., 1998, 2000, 2001; Lawrence et al., 2006). In craters that are permanently in the shadow, the water content can range from 1 to 3 Wt% (Eke et al., 2009; Elphic et al., 2007; Feldman et al., 1998, 2000, 2001; Lawrence et al., 2006; Teodoro et al., 2010). However, for equatorial regions, only 50 ppm are found (Lawrence et al., 2006).

In 2009, NASA conducted an experiment where a stage segment of a Saturn V rocket was dropped into the Cabeus crater at the South Pole (Schultz et al., 2010). The spectroscopic data of the regolith revealed that it contained 5% water ice (Colaprete et al., 2010).

NIR data of magmatic rocks on the lunar surface show that mare basalts contain significantly fewer hydroxyl groups than the lunar highlands (Clark, 2009; Pieters et al., 2009; Sunshine et al., 2009). The highest contents are found in pyroclastic deposits of a region called the Procellarum KREEP Terrane (PKT). This area on the Earth-facing side of the Moon is notable for high trace element concentrations (Jolliff et al., 2000). Hydroxyl contents of these pyroclastics reach 500 to 1500 ppm (Li & Milliken, 2013, 2014).

1.6 Is the lunar water distribution homogeneous?

Although spectroscopic data from the lunar surface allow us to examine considerable areas, there is the fundamental challenge of distinguishing between primitive water from the lunar interior and water formed by external processes such as solar wind, sputtering and impacts. Primitive water is water that was already stored in the interior of the Moon during its formation and solidification. To study primitive water, it is therefore important to analyse water within crystal structures, as, for example, in the case of melt inclusions.

The water contents of melt inclusions in Apollo samples have shown significant variations, with the highest values being found in sample 74220 "Orange Soil" containing up to 1200 ppm water, Figure 10). However, it is important to consider whether these samples, which were only taken at a single site, have any significance for the global water balance of the moon or can be neglected as a purely local phenomenon.

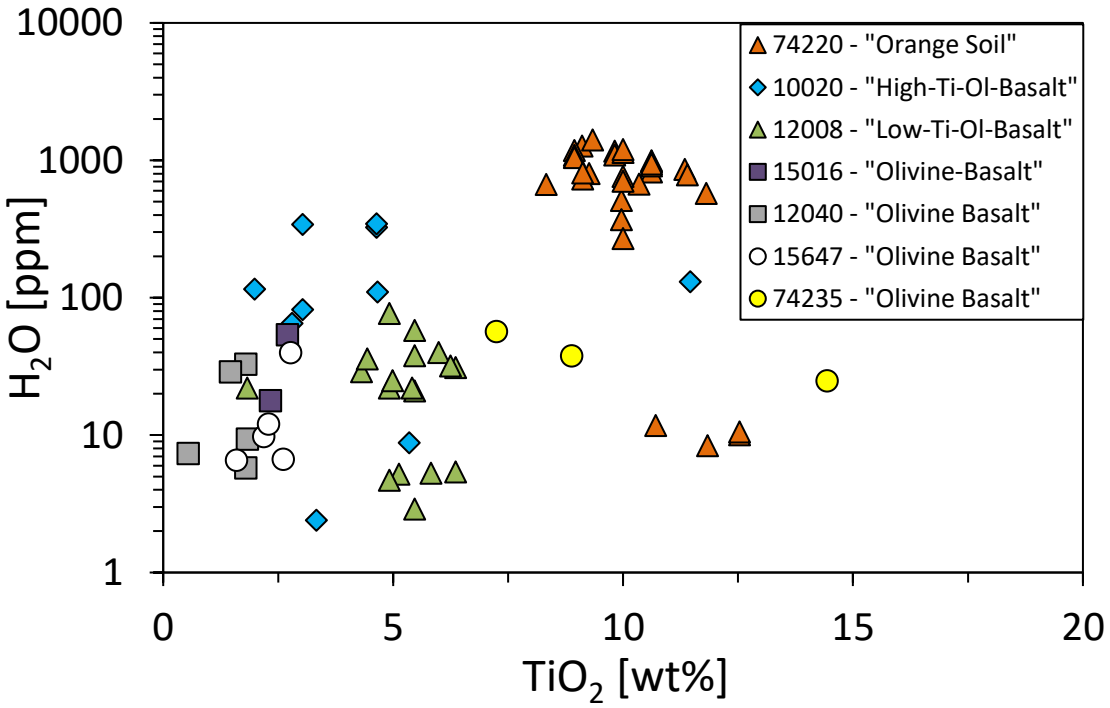


Figure 10: Compilation of water contents in lunar melt inclusions as a function of titanium content (for better readability, the classification of lunar glasses follows the Titanium content)

Morphologically, the sample comprises small glass beads that were rapidly quenched during the volcanic eruption with isolated melt inclusion-bearing olivine crystals dispersed throughout (Figure 10). The other samples in Figure 10, mainlyconsisting of melt inclusions in olivine-bearing basalt, have water contents one to two orders of magnitude lower. The

basalt from which they originated likely cooled much more slowly, allowing more time for the water to degas from the melt inclusions.

To gain a better understanding of the significance of sample 74220 for the estimation of the water content of the Moon, it is important to distinguish whether it is only a local anomaly or representative for the entire Moon. A helpful comparison can be made with Earth. Sample 74220 (orange squares, Figure 11) shows a similar H_2O - fluorine ratio to that found in depleted MORB and in melt inclusions of oceanic island basalts (20:1 trend line in Figure 11, Chen et al., 2015).

The lunar melt inclusions in basalt (red squares) have similar fluorine contents, but significantly lower water contents and lie on the same trend line as the degassed glass beads of sample 74220 (orange crosses) and the matrix glass from Hawaii (purple crosses, trend line 1:1). The melt inclusions of sample 74220 thus appear to be degassed in the same way as the melt inclusions of oceanic island basalts on Earth (e.g. from Hawaii). The shift to a lower trend line can be explained by the fact that water is somewhat more volatile than fluorine and therefore volatilizes first in the event of degassing.

The same picture emerges when the measured values for water are compared with those for a refractory element (Chen et al., 2015, Figure 12). Cerium is a good choice because it is just as incompatible as water but does not degas. During melting and crystallisation processes, cerium and water thus behave similarly. However, during the process of degassing, only the water content changes, and the refractory cerium can be considered constant. The melt inclusions in MORB from Earth hardly degas because they cool deep in the ocean. Hence their values only reflect the different geological processes, but remain on the same trend line (black circles, Figure 12). In contrast, sample 74220 from the Moon (orange circles) and the lunar melt inclusions in basalt (red rectangles), show a degassing process.

It can also be assumed that sample 74220 would certainly also have degassed if it had not been a particularly fast-cooling eruption in which the material was ejected in a gas-driven fountain of fire. The water contents of these samples thus appear to be closest to the original water content of the Moon. The slower-cooling basalt apparently lost its water, but the cerium contents suggest that the original contents were those of sample 74220.

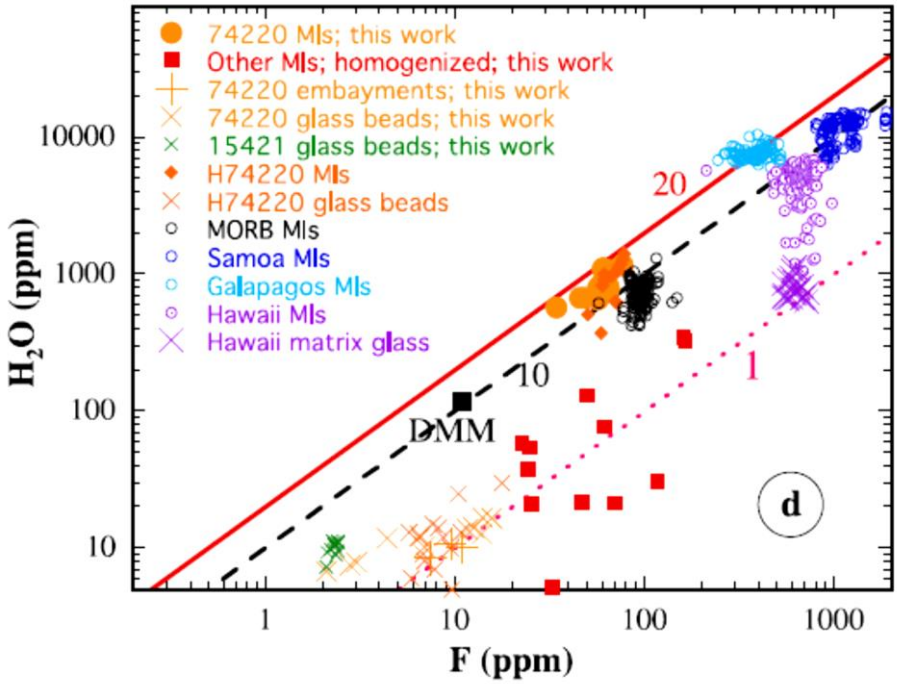


Figure 11: H_2O in melt inclusions and associated glasses of terrestrial and lunar samples as a function of fluorine content in ppm. The straight lines shown correspond to the water-fluorine ratio indicated in each case (1:1, 10:1, 20:1). (Chen et al., 2015)

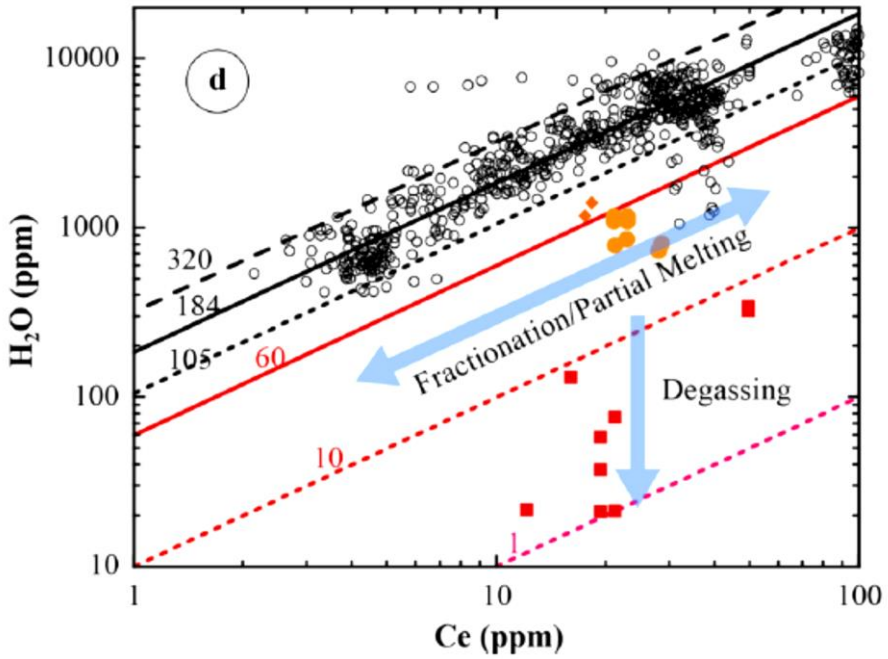


Figure 12: H_2O content of lunar melt inclusions against cerium as a refractory element (orange = 74220; red = basaltic MIs, black = MORB). The straight lines again indicate the element ratios, the blue arrows the behaviour of the ratio during melt formation and degassing, respectively. (Chen et al., 201*5)*

For terrestrial samples, it is common to consider the highest measured water content in melt inclusions as the original value of the melt. All lower values are considered as water loss due to degassing and/or other processes. For the lunar melt inclusions, this results in a maximum water content of ~1200 ppm. However, the other contents, which are lower by a factor of 5 to 100, show the same cerium contents. As a result, it can be deduced that sample 74220 "Orange Glass" is by no means a local anomaly, but rather indicates that the moon is "wet" overall (Chen et al. (2015)).

1.6.1 What is the lunar water content?

According to estimates by Chen et al. (2015), the cerium content of the lunar mantle yields a total water content of 111 ppm, which agrees well with the estimates of Hauri et al. (2015) (133-292 ppm) and Hui et al. (2013) (130 ppm). For comparison, the depleted MORB mantle on Earth is estimated to contain around 116 ppm of water (Salters & Stracke, 2004), which matches the lunar values quite well. The water content estimates for the lunar mantle from Chen et al. (2015), Hauri et al. (2015) and Hui et al. (2013) are also in similar orders of magnitude (100-300 ppm) and thus conclusive.

1.7 Aim of this study

Based on the analysis of the melt inclusions from sample 74220 and other olivine-bearing samples collected from various locations on the lunar surface, we may deduce that their water contents are probably not a local anomaly, but rather representative of the broader lunar water distribution. Hence, we may assume that the moon is not only locally “wet” but that its water is probably distributed globally. While various approaches for the quantification of the exact values for the amount of water present exist, their orders of magnitude are comparable. In any case, it remains unclear where this water on the Moon comes from and how it is distributed. These questions have not even conclusively been clarified for the Earth, where an overwhelming number of samples has been collected. One advantage in case of the moon is, however, that does not seem to have any active geodynamics anymore and is therefore hardly subject to changes.

The aim of this study is to investigate how the water must have been distributed inside the Moon immediately after its formation. What storage possibilities exist at different depths in its interior? Is it particularly wet or dry at certain depths? Can a model distribution obtained in this way be reproduced using the measured values from the Apollo samples?

To answer these questions, it is essential to understand how the LMO has developed in terms of its volatiles. Past studies such as the one by Rapp et al. (2018) indicate which minerals crystallised in the lunar magma ocean and the timing of these events. However, it is important to note that these assumptions are based on simplifications about the lunar magma ocean such as the total fractionation of minerals, LPUM as the initial composition and an initial depth of 1400 km. Altering these assumptions can result to different outcomes. For example, a higher aluminium content in the initial composition, could lead to a thicker crust, as more plagioclase can be formed. In contrast, assuming a shallower magma ocean could result in a lower crustal thickness due to its lower mass. Therefore, it is essential to note that the respective results of such studies can only represent a model of the magma ocean and may not necessarily have to correspond to the geological reality of the Moon’s magma ocean.

The role of volatiles was previously only studied by Lin et al. (2017), who explored the thickness of the lunar crust as a function of the water content of the LMO. Their findings suggest that a lunar crust of 30 km can only be explained by the presence of water, as it reduces plagioclase crystallisation.

Building upon the experimental approach developed by Rapp et al. (2018), this study aims to repeat selected step-by-step experiments at similar conditions (composition, pressure, temperature, and f(O_2) conditions are known). However, a new component will be added to the sample material which is a fixed and well-documented fraction of water (e.g. 100-1000 ppm, estimated mantle value). In addition to the minerals that form, it is possible to study the partitioning of water between minerals and melt in each step of the crystallisation process of the LMO from the core-mantle boundary to the crust.

The sequence of minerals obtained in the result will be compared to that of Rapp and Draper (2018), but with the additional information of the water content in each mineral phase and thus, the partitioning of water between melt and all LMO relevant minerals.

This study will overall investigate the question how the water is distributed for all LMO-relevant minerals at any time of the LMO crystallisation process under lunar conditions. It also provides insights into the distribution of water on the Moon prior to the Cumulate Overturn. The findings should deepen our understanding of the water distribution and history of the Moon's formation and provide valuable information for future work and studies on the lunar interior.

2 Material and Methods

2.1 Experimental approach

The recreation of the conditions present in the LMO 4.5 Ga ago is a central part of this study. The most relevant parameters are melt chemistry, pressure, temperature and oxygen fugacity ($f(O_2)$). To adjust these correctly, physical and chemical properties of the melt, the apparatus and the pressure medium must also be taken into account, as well as the kinetics of the desired and undesired reactions.

This chapter deals with the design and calibration of an assembly for the piston-cylinder-press (PCP) followed by a description of the necessary conditions to be generated for the LMO experimental series. The general P-T-range for the experiments is shown in Figure 13.

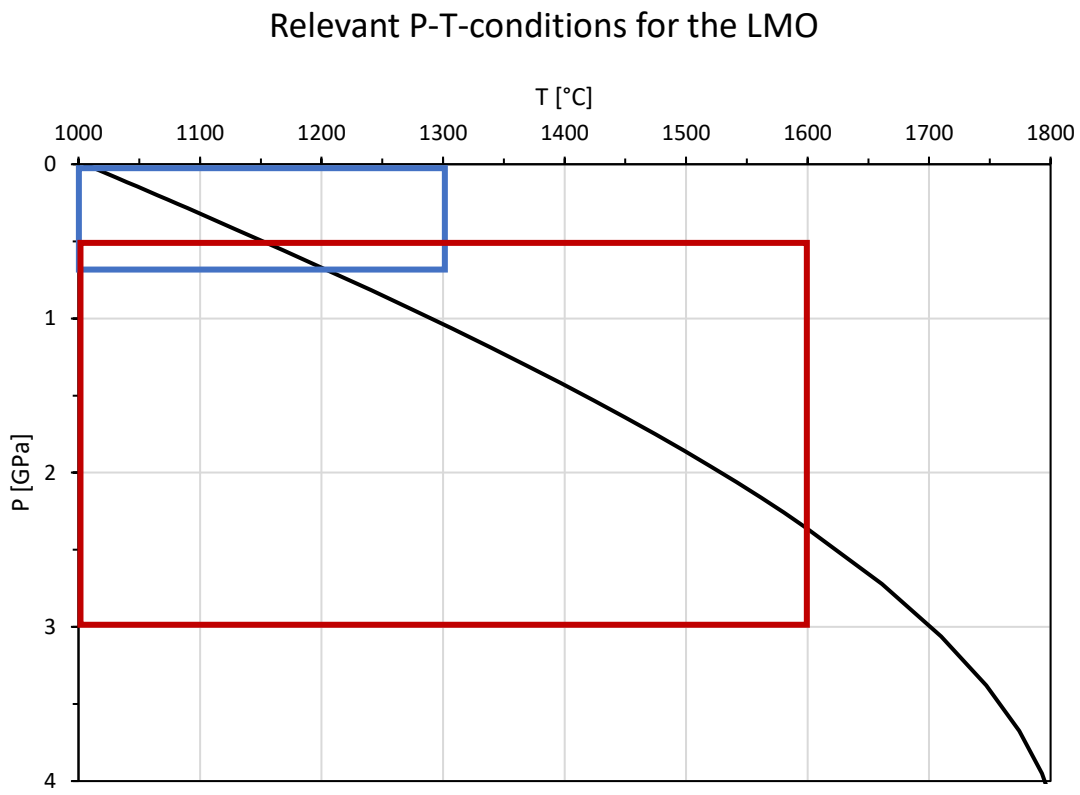


Figure 13: Estimated pressure and temperature conditions required for the experimental crystallisation of the LMO. The boxes indicate the capabilities of the Internally heated pressure vessel (IHPV), blue, and the piston-cylinder-press (PCP), red, used in this study.

2.1.1 Functionality of an end-load piston cylinder press

Investigations of processes in the Earth' crust, mantle and core require methods to generate the appropriate pressure and temperature conditions. For this purpose, authors in the past developed various instruments of which each is specialized for a given area of use. Among the most common are the internally heated pressure vessel (IHPV, up to 1 GPa, processes of the upper Earth's crust), the piston-cylinder-press (0.5 to 5 GPa, e.g. Boyd & England, 1960, processes of the Earth's crust and a small part of the upper mantle), the multi-anvil press (up to 65 GPa, processes of the upper Earth's mantle (e.g. Ishii et al., 2017) and the diamond anvil press (up to 770 GPa, e.g. Dubrovinsky et al., 2015, processes of the Earth's mantle, core and beyond). The limit of these methods always depends on the available design and can deviate significantly from the upper limits given here. Generally, a higher maximum pressure of a method usually is accompanied by a smaller possible sample volume as a downside.

Best suited for the pressure distribution of the lunar interior of 0 to 5 GPa is the piston-cylinder-press (Figure 15 & Figure 16). This method uses a simple force-per-area principle in which a system of pistons with a 1:100 pressure transmission is pressed into a hard metal casing called bomb. Due to the ratio, easily generated 100 bar oil pressure at the master ram result in 1 GPa at the uppermost piston and thus the sample. The resulting forces impose a great strain even on hardened materials such as tungsten carbide. To prevent damage to the casing, it is loaded with 72 t by the end load ram (Figure 16) causing the materials to expand. By this, a counterpressure on the piston allows the material to withstand a significantly higher pressure without failure. The original design of this method was invented by F.R. Boyd and J.L. England (Boyd & England, 1960).

To ensure an ideal transmission of force from the piston to the specimen, the sample capsule is located in an assembly, a composite of ceramic, graphite and metal tubes that is inserted into the tungsten carbide core of the bomb (Figure 15). The tubing holds the sample in place and distributes the pressure almost hydrostatically in the sample chamber. Furthermore, it is designed with a system of graphite parts, which can be heated up through strong electrical currents (1 - 10 V, 1 - 500 A). By that, theoretical temperatures of more than 2000°C can be achieved, but the melting and weakening points of the used assembly material is a limiting parameter.



Figure 14: Components of a piston-cylinder assembly with sample capsule (top) and fully assembled assembly (bottom)

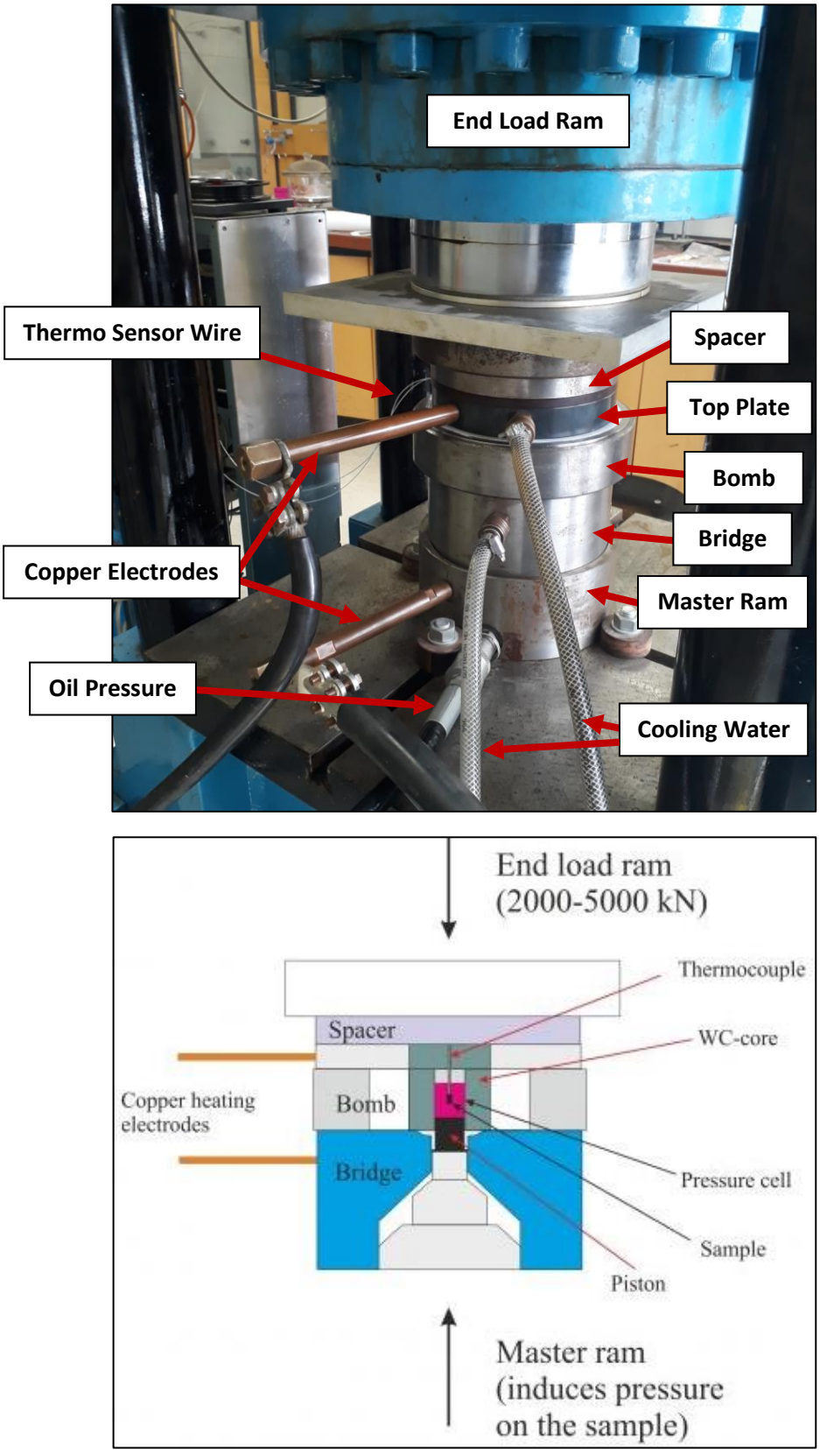


Figure 15: End-load piston cylinder press of the GZG (top) and schematic structure (bottom). The end-load gives the materials the necessary strength to withstand the pressure generated, while the master ram from below generates the actual pressure on the sample.
(Scheme by Dr Enikö Bali, http://enikobali.hupont.hu)



Figure 16: Components of a piston cylinder press. spacer (top left), insulation plate (top right), top plate (middle left), bomb (middle right), bridge (bottom left) and master ram (bottom right).

A well-defined and controlled temperature regime is the core of any experimental study. For this purpose, a temperature sensor is inserted into the assembly that enables measurements as close as possible to the sample, consisting of a platinum and a platinum-rhodium wire with a diameter of 0.2 mm. Both wires are brought into a ceramic tube made of Al_2O_3 and are welded together at the end of the guide (Figure 17).

The wires are insulated from each other except for the welding bead and are led out of the bomb. A temperature-dependent voltage between the wires can be translated into a temperature via a corresponding measuring device, which in return adjusts the electrical output available at the furnace to actively control the temperature at the sample. A pressure dependence for this technique is not reported.

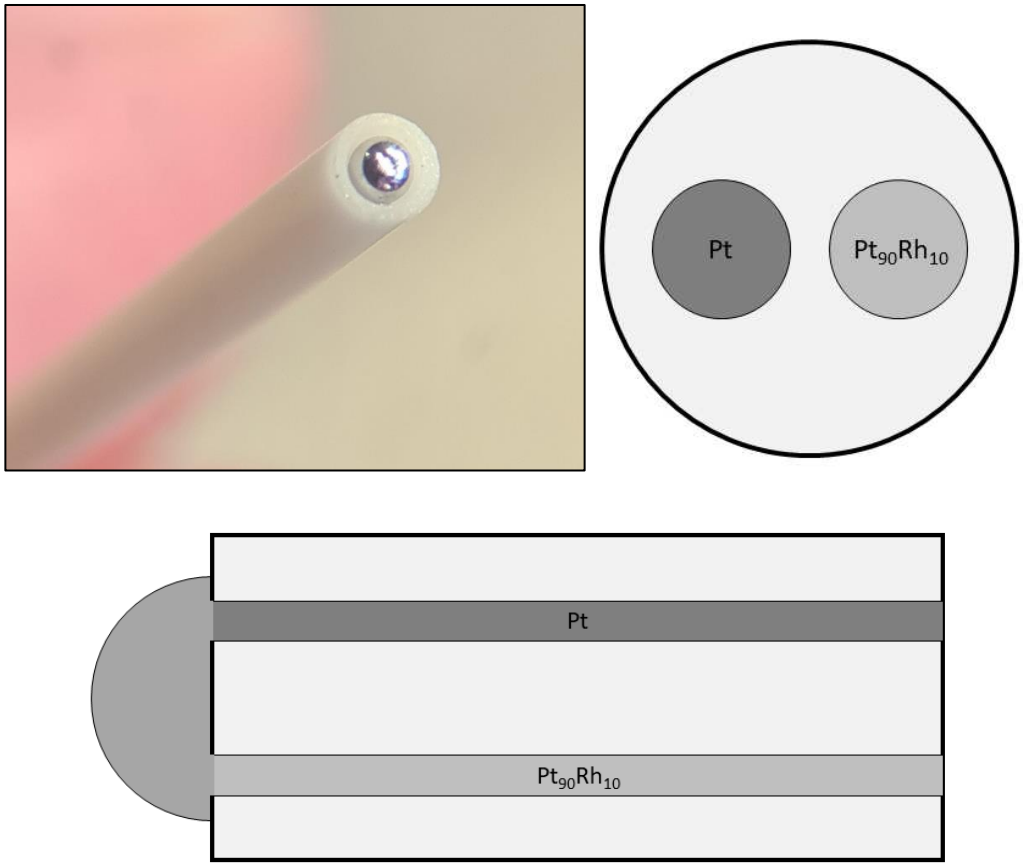


Figure 17: S-type thermosensor consisting of welded platinum and platinum-rhodium wires in an Al_2O_3 guide (top left), in schematic cross-section (top right) and longitudinal section (bottom).

The error given by various manufacturers for this type of sensor is ±1.5°C. In reality, the temperature error in a piston-cylinder-press experiment is significantly higher as shown by simulations and experiments in Schilling & Wunder (2004), who reported large temperature gradients within a piston-cylinder-press (Figure 18). The positioning of the sensor relative

to the specimen therefore yields much more potential for temperature deviations than the sole error of the measurement.

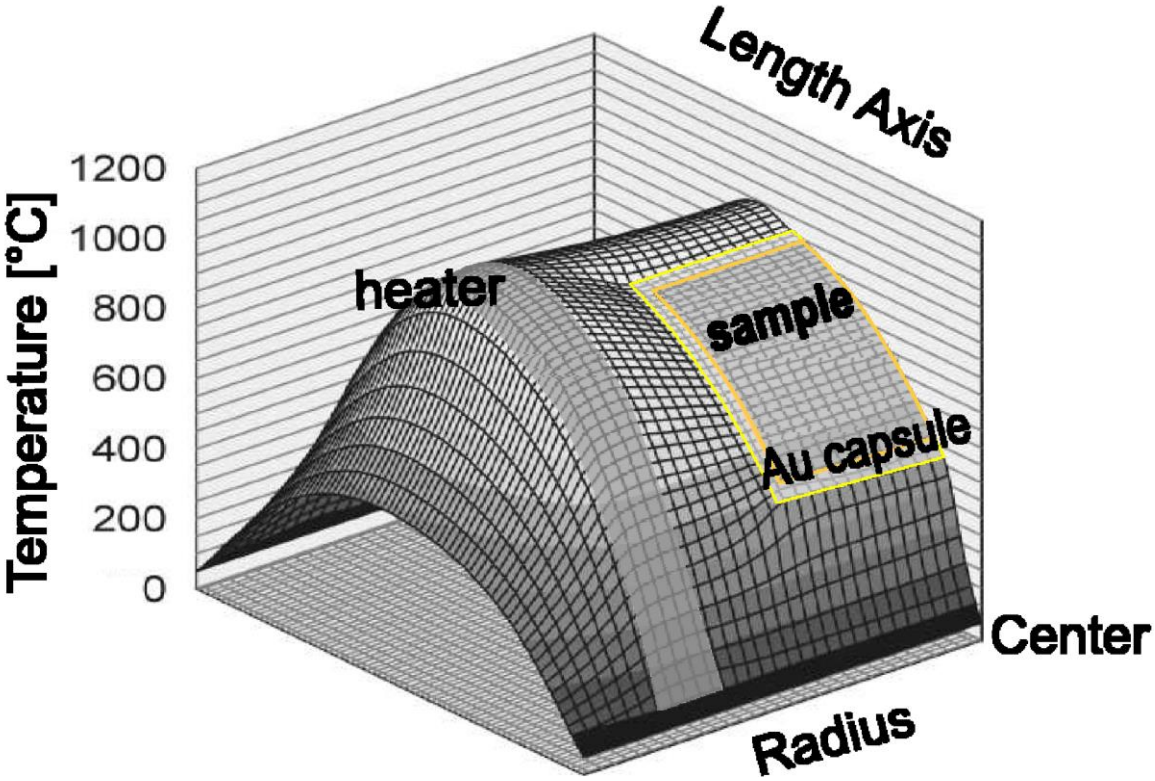


Figure 18: Temperature distribution in a simulation by Schilling and Wunder (2004).

2.1.2 Composition of the water-inhibiting assembly

For this study, a new assembly design was developed that basically follows a design used by Prof. Dr. Roland Stalder (University of Innsbruck). The special requirement for this assembly includes two main features:

1.) A high temperature resistance (up to 1600°C)

2.) The ability to maintain a stable environment regarding the hydrogen partial pressure so that the previously set water content of the sample material remains constant throughout the experiment.

Boron nitride (BN) is a very suitable material for this purpose, as it has been used previously in piston cylinder experiments (Johannes, 1973; Truckenbrodt et al., 1997; Kägi et al., 2005; Sission et al., 2005), is also chemically inert up to high temperatures, and has a high temperature resistance with a melting point of 2967°C. In its hexagonal variant (h-BN), BN is also referred to as "white graphite" because it has similar lubricating properties to graphite even at high temperatures. The cubic variant (CBN) is the second hardest material we know

of and is therefore used for machining hardened steels to name just one application. According to information from the industry (Figure 19), BN loses hardness linearly with increasing temperature and not sudden, like diamond does, which is a well desired characteristic for machining tools. Whether this also applies to hexagonal BN, which we use for our assembly, and thus provides an explanation for the observed "Pseudo-friction" (Chapter 2.2.5, Page 50) is not evident.

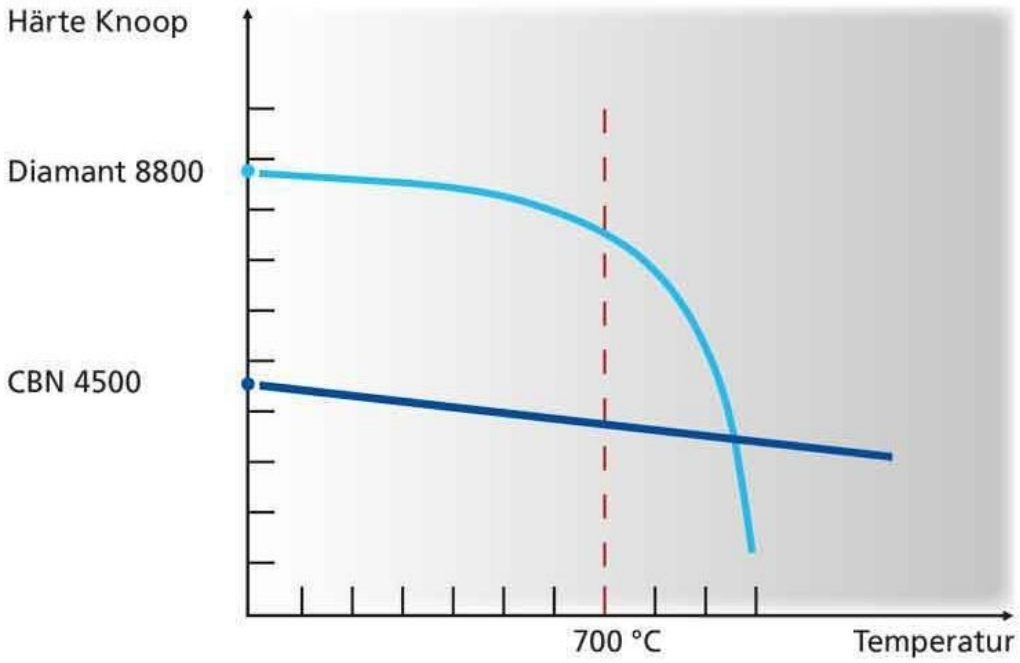


Figure 19: Thermal behaviour of diamond and CBN regarding to hardness and temperature. https://www.schell-tools.com/fileadmin/wiki/graphics/diamant-pkd-cbn-haerte-knoop.jpg

In addition, BN inhibits the diffusion of hydrogen, as it has been proven experimentally (Johannes, 1973; Truckenbrodt et al., 1997). An intake of the intrinsic hydrogen partial pressure of the assembly can therefore be brought to a halt as long as the whole sample is surrounded by BN.

As a result of these requirements, the following structure for our assembly has been chosen (Figure 20): The sample itself is inside a graphite capsule closed with a lid which is later sealed by the prevailing pressure. This capsule is inserted into a bore in a BN cylinder (6), which is closed off at the top by a second cylinder made of BN (7). A hole in this second cylinder contains the thermocouple to allow for temperature readings near the sample. The BN tubes are surrounded by the furnace (5), which makes electrical contact with the piston via two graphite discs (8 & 9). A copper disc is also inserted between the piston and the graphite to create the best possible connection. The furnace (5) is surrounded by a tube

made of Pyrex (4). This serves as a water trap and is itself surrounded by another tube of BN (3). The top is closed by a cylinder of steel (1), which in turn is surrounded by fired pyrophyllite (2). Unfired pyrophyllite contains a lot of water, which must be excluded for our purpose. Therefore, the fired material CERAMIT[10] produced by *Ceramic Substrates and Components (UK) is* used here.

To reduce friction between assembly and WC-core, the outer jacket is coated with *Molykote* and rolled in MoS powder. This also helps to press the assembly out of the core after the experiment is finished.

The design shown here had to be fundamentally changed later on, because major problems with pressure transmission and stability of the thermosensor have arisen. More about this problem can be found in chapter 2.3 (Page 55).

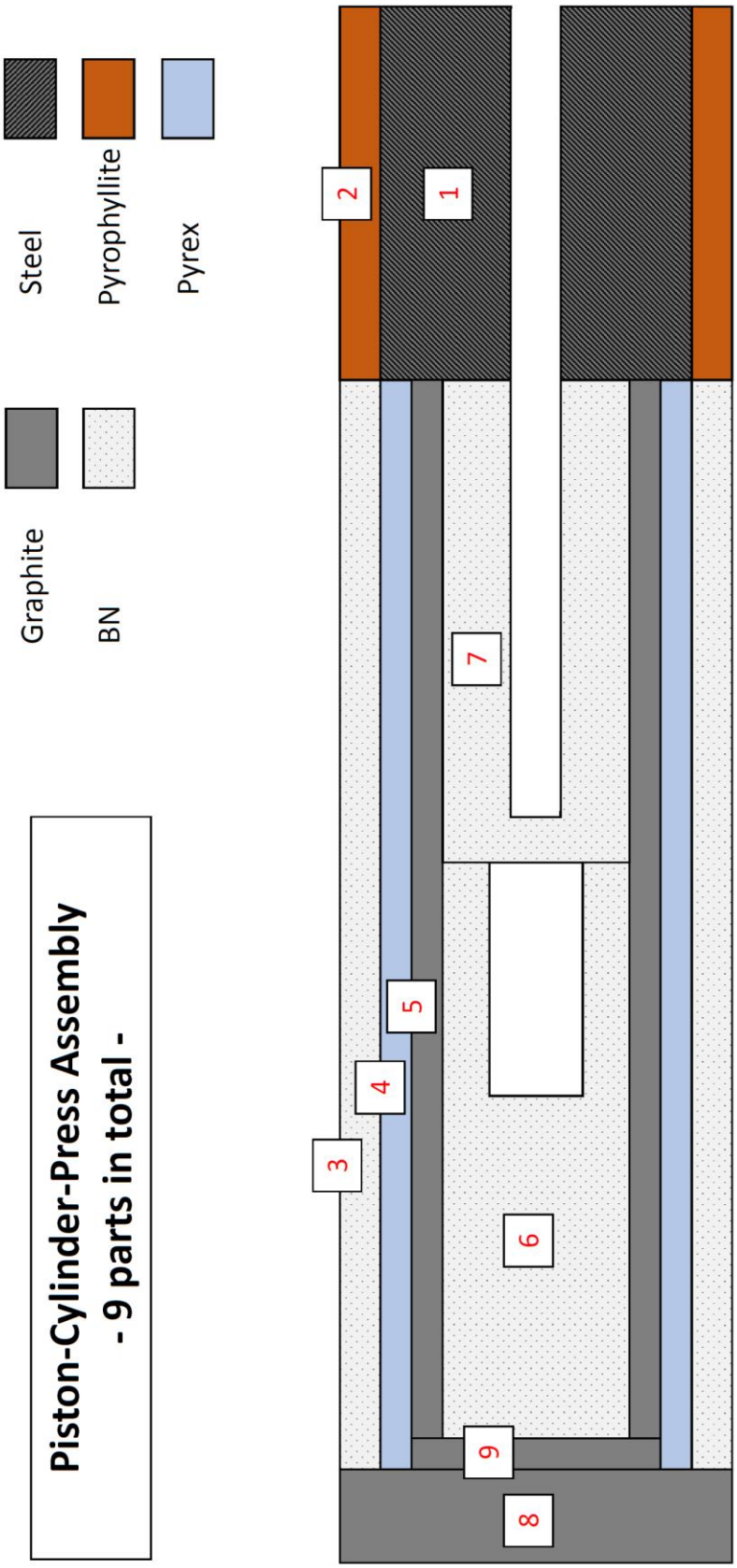


Figure 20: Design of a water-inhibiting assembly made of BN (initial design).

2.1.3 The Internally Heated Pressure Vessel (IHPV)

Every pressure generating method has its designated range of operation. For the piston-cylinder-presses, the lower pressure range is limited at 0.5 GPa, as the materials are hardly compressed enough for a stable setup at these conditions leading to a lack of pressure transfer and functional problems in the heating system. An IHPV was therefore used for the low-pressure LMO experiments at 0.2 and 0.3 GPa.

The IHPV consists of an autoclave (Figure 21) whose pressure chamber is filled with high-purity argon. The pressure of the gas cylinder can be increased to a maximum of 7000 bar via a compressor and hydraulic pressure amplifiers. The sample capsule usually is made of precious metal (typically Pt, Au or AuPd alloys) and hangs on a platinum wire in a ceramic tube. This is fitted with thermocouples at three different points for temperature monitoring. A resistance furnace with two separate heating coils is put around the tube, through which the gas and thus the sample can be heated to the target temperature. Temperature control of the main and secondary windings takes place via temperature sensor TC1 and TC2 (Figure 22). The sample is located exactly between these two. Therefore, the temperature difference between them corresponds exactly to the gradient across the sample and was 10 to 15 °C in the experiments carried out.

To quench the sample conditions, a thin platinum wire attached to electrodes is electrically melted through. This causes the sample to drop into the lower, much colder area of the upright ceramic tube (Figure 22), where it cools rapidly.

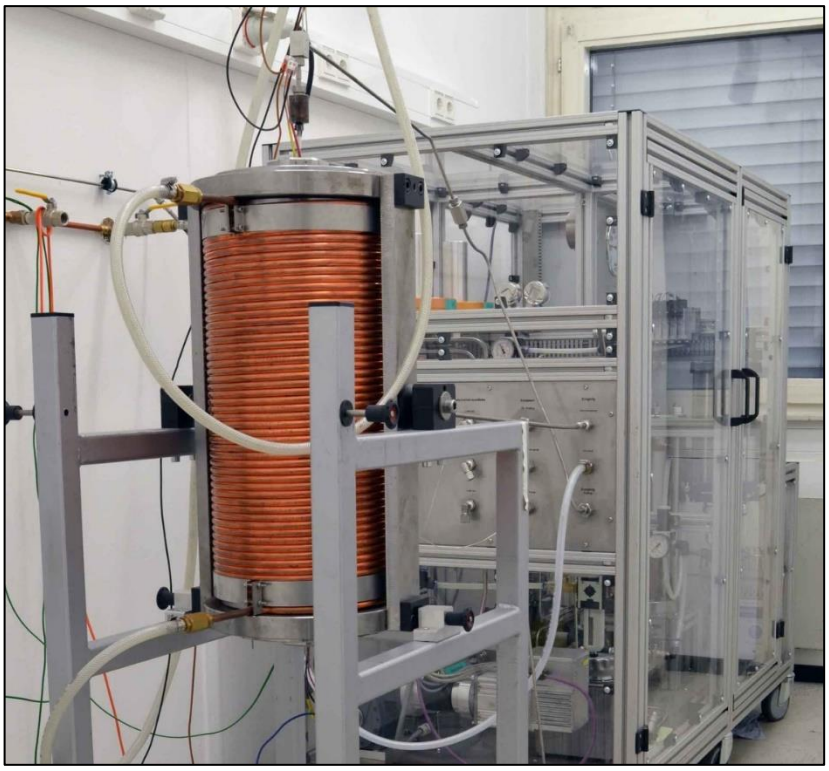


Figure 21: Internally Heated Pressure Vessel (IHPV) of the GZG. In front is the autoclave with cooling water connections, behind it is the plexiglass cabinet with the pressure amplifiers and pressure lines.

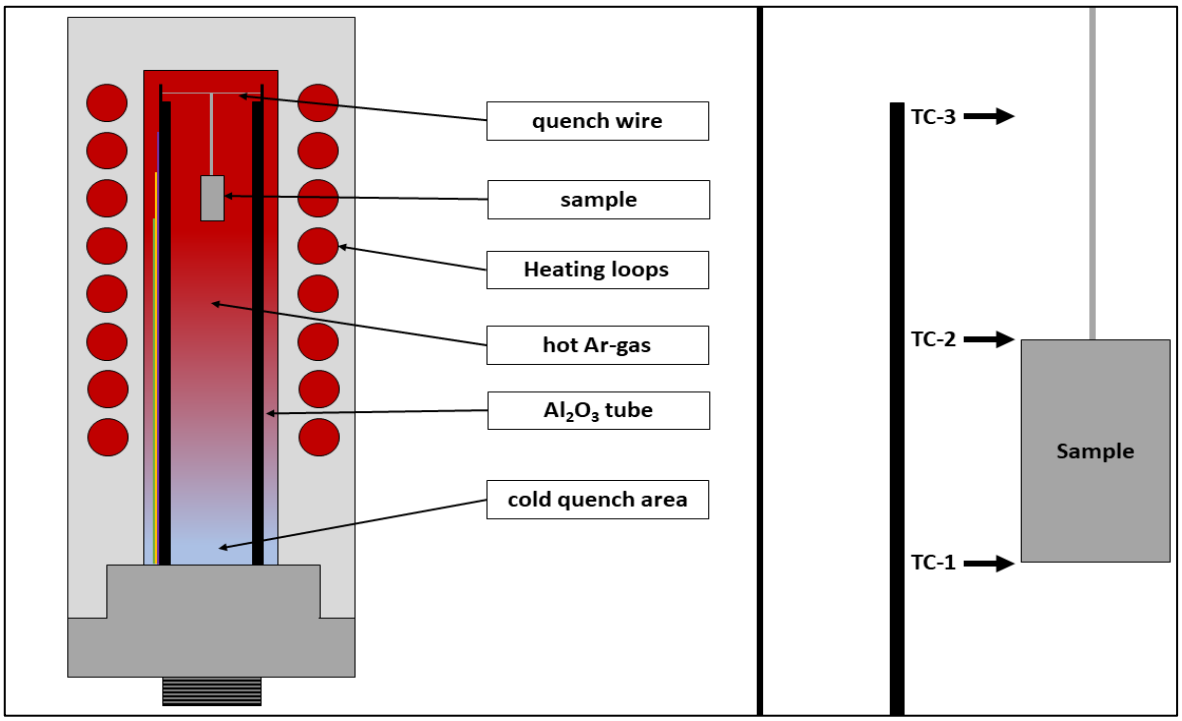


Figure 22: Schematic of the furnace system of the IHPV (left) and position of thermocouples 1, 2 and 3 relative to the sample (right).

2.2 Carrying out the calibration experiments

2.2.1 Why does the assembly need to be calibrated?

Pressure is a key variable for the targeted experiments, as it defines how deep in the LMO our experiments take place. However, the real pressure in the sample capsule cannot be measured directly. Instead, the oil pressure is measured, which presses the piston onto the assembly with an area ratio of 100:1. Theoretically, 100 bar oil pressure should correspond to 10,000 bar on the assembly and thus on the sample. In practice, the sample experiences more like 9,000 bar of pressure in sense of this example.

The observed loss of pressure is due to friction between assembly, piston and the tungsten-carbide core of the bomb. The quantity of this loss depends on the assembly material and the bomb used. Therefore, it cannot be determined across laboratories, but must be investigated individually for each given design and bomb. Since pressure monitoring inside the assembly is technically impossible, phase transitions or melting points known from the literature are used to estimate the loss.

One such often used phase transition is that of α-quartz, which transforms into coesite at a temperature of 1000°C and a pressure of 2.8-3.0 GPa (Figure 23). The phase transition occurs because the crystal lattice thermodynamically adapts to the prevailing environmental conditions. High-pressure phases always have a smaller volume than their low-pressure variations. These are in turn only stable at high pressure and transform back into their low-pressure when brought back to room pressure. At room temperature, the kinetic of this process is so slow, that it practically stands still. Therefore, the experiments are cooled down rapidly by interrupting the power supply and thus the state of the sample is frozen at the target conditions allowing investigations of high-pressure phases.

For the experimental investigation, powdered α-quartz is welded into a precious metal capsule, which is then isothermally exposed to a given pressure during the experiment. If the low-pressure phase (α-quartz) is found in the run product, the pressure for the next experiment is increased. Ideally, the high-pressure phase (coesite) is obtained at a certain point. By comparison of literature values for the phase transition from α-quartz to coesite,, we know exactly how much of the nominal set pressure is transmitted to our sample. The difference is lost by friction and is usually given as a percentage of the nominal pressure.

The aim of the calibration experiments is thus to conduct one experiment just below the phase transition - the capsule still contains α-quartz - and one just above - the capsule now

contains coesite to narrow down the amount of friction lost for our design as much as possible.

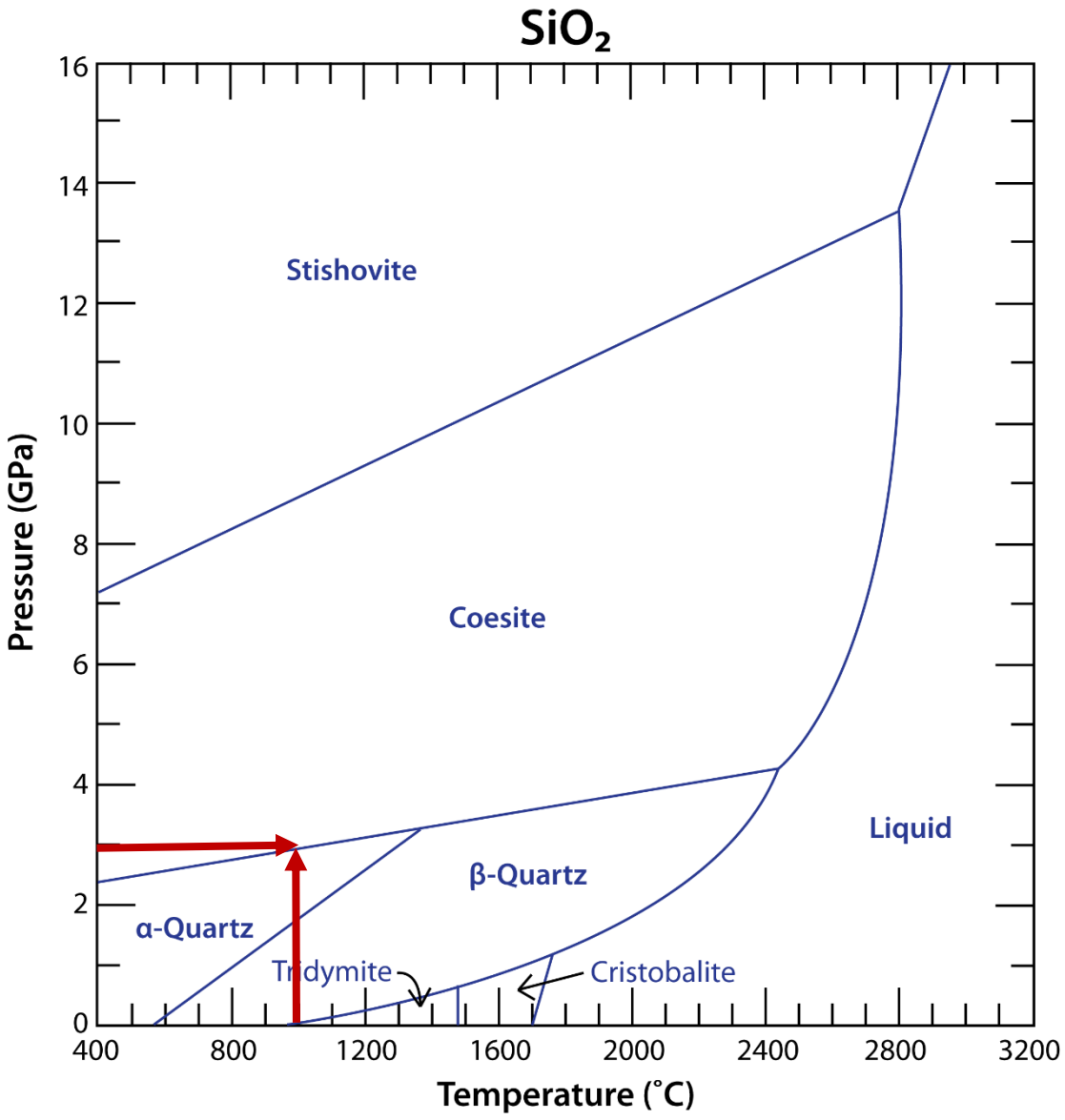


Figure 23: Phase diagram of quartz as a function of ambient pressure and temperature.

Source: https://www.geo.arizona.eduxtalgeos306silica_phase_diagram_large

2.2.2 Calibration by the conversion of α-quartz to coestite

The phase transition from α-quartz at 3 GPa and 1000°C to its high-pressure variant coesite is often used to calibrate piston-cylinder assemblies. The advantage of this transition is its relative insensitivity to temperature changes, i.e. the pressure changes little with increasing temperature. In addition, many experimental studies are conducted in the temperature range around 800 to 1200°C, so the calibration temperature is close to the later experiments.

Experiments with this phase transition at our facility were unsuccessful since the pressure conditions of the phase transition simultaneously represent the load-bearing limit of our piston-cylinder-press. This led to a material failure of the piston before the high-pressure phase could be seen in any run product and caused damage to the press as well (Figure 24). We therefore have chosen to use a phase transitions at lower pressure.



Figure 24: Material failure of the piston due to the high loads during the experiments. Left: intact piston. Right: condition after blow-out

2.2.3 Calibration by the decomposition of albite to jadeite and quartz

As an alternative to the phase transformation of quartz to coesite, the decomposition reaction of albite to jadeite and quartz at 1.6 GPa (Figure 25) is a well-suited alternative to spare the machine. However, the temperature of the transition, 600°C, is significantly lower than the planned experiments of the lunar magma ocean (1000 °C – 1600 °C).

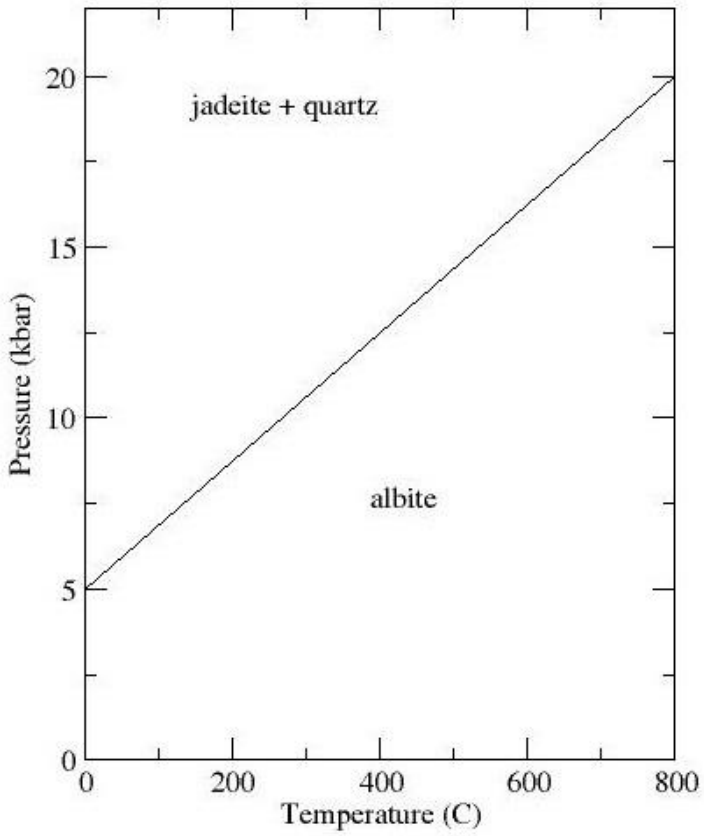


Figure 25: Decomposition of albite into jadeite and quartz as a function of pressure and temperature. Source: https://upload.wikimedia.orgwikipediacommons66aJadeite-stab

A molar ratio of 1:1:1 quartz, jadeite and albite was used for the runs. While the quartz is synthetic, jadeite and albite originate from natural minerals available in the GZG collection. The latter were therefore checked for possible impurities by means of micro-X-ray-fluorescence analysis (µ-XRF).

The powder mixture along with 10 wt% additional water was put in graphite capsules as they would also be used for the later series of LMO experiments. Water serves as a transport medium in solution-precipitation-reactions and thus accelerates the transformation of the minerals, which would be quite slow at 600°C. Run durations were kept at 24h.

2.2.4 Phase determination by means of powder diffraction

For a successful calibration experiment, there should be either only albite or only jadeite and quartz left. Depending on the result, the pressure is above or below the phase transition.

A simple method to investigate the run-products of an experiment is X-ray diffraction using the Debye-Scherrer method. Here, the ground sample is irradiated with directional, monochromatic X-rays in a wavelength range corresponding to the distance between the atoms in a crystal. The X-rays are therefore always diffracted when the Bragg condition (1)

$$n \cdot \lambda = 2 \cdot d \cdot \sin(\theta) \quad (1)$$

is fulfilled. λ is the wavelength of the X-ray radiation used, θ its angle of incidence and d the interplanar spacing in the crystal. The angle θ, for which the Bragg condition is fulfilled, thus depends on the interplanar spacing of the crystal structure. Conversely, the crystal structure can therefore be determined from the intensity maxima for the specular angles θ.

Such a diffractogram is shown in Figure 26. To determine the structure from the intensity maxima as a function of angle θ, an automatic comparison with literature databases such as the Inorganic Crystal Structure Database (ICSD, FIZ Karlsruhe) can be carried out to identify substances with comparable reflective positions. Since in our case all the substances possibly contained are already known, it is sufficient to use diffractograms for quartz (green), albite (red) and jadeite (blue) for comparison as shown in Figure 26. In the depicted example, all three phases in the diffractogram (black) are still present after the experimental run.

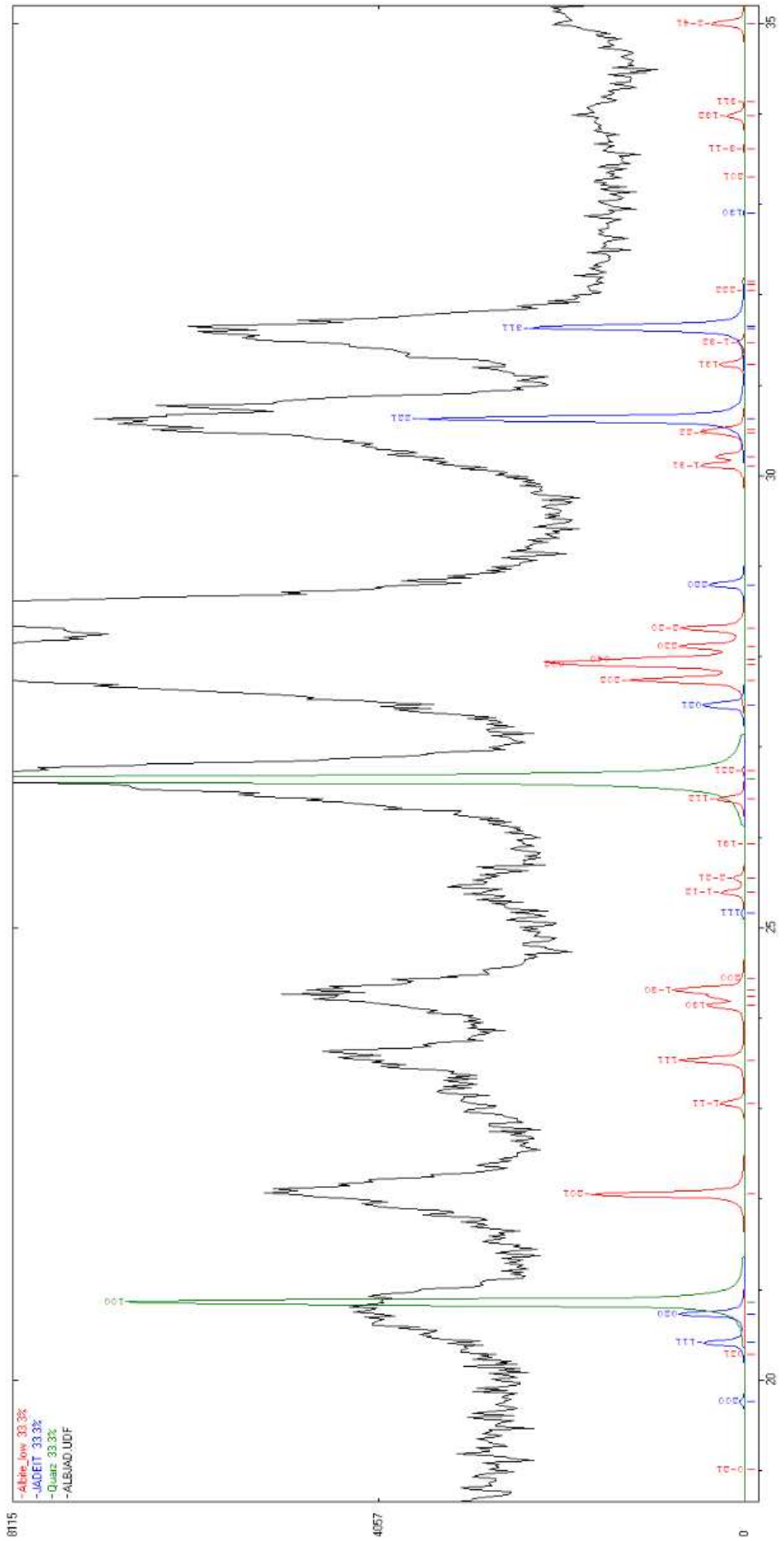


Figure 26: X-ray diffractogram of one of the calibration experiments (black) together with theoretically calculated spectra for quartz (green), jadeite (blue) and albite (red).

2.2.5 Crystallisation problems and pseudo-friction of BN assemblies

The run products of our albite-quartz-jadeite calibration neither show a decay reaction of the albite nor a new formation from jadeite and quartz. This observation could be explained as coincidentally being exactly on the phase transition of both phase assemblages. However, this can be ruled out by running experiments at significantly higher pressure yielded all the same result. This leads to the conclusion that no reaction has taken place, possibly due to a loss of water from the graphite capsule or the formation of C-H compounds, which might change the transport properties of the fluid.

To avoid the need for ion transport by fluids, an albite glass was used instead of the previously used molar powder mixture (Table 4, Experiment 4). Glass has the advantage, that either albite or jadeite and quartz should crystallise directly under the set conditions without solution and precipitation of already existing minerals necessary. Thus, a major ion transport does not have to take place. Since no crystallisation occurred either, the graphite capsule was replaced by a precious metal capsule made of platinum which ultimately led to success, as the low-pressure phase, albite, crystallised (Table 4, Experiment 5).

The pressure was increased in the following experiments, but the decomposition reaction to jadeite and quartz was first observed at 2.75 GPa (Table 4, Experiment 17). Compared with the literature conditions for the phase transition of 1.6 GPa, this corresponds to a pressure loss of about 60%. Typical values for pressure loss due to friction are between 5 to 20%. This high discrepancy between nominal and actual pressure at the sample is unusual and probably does not originate from friction loss between the components.

To investigate the influence of temperature on the experiment, further runs of the decomposition reaction of albite were carried out at 700, 800 and 1000°C (Table 4, Experiments 20 to 25). It can be seen that the difference between nominal and actual pressure at the sample decreases with increasing temperature and approaches more and more realistic values for the pressure loss due to friction (Figure 27).

Table 4: Overview of the calibration experiments. Experiments that had to be terminated during the heating process are recognisable as jumps in the consecutive number. Grey bars show blow outs resulting in a core change.

#	Name	P [kbar]	T [°C]	Assembly	Capsule	TC	Sample	Result
1	KalEx QJA 1	21,9	600	BN CSC	C	S/Al2O3	QJA 1:1:1	-
2	KalEx QJA 2	21,9	600	BN CSC	C	S/Al2O3	QJA 1:1:1	-
3	KalEx QJA 3	16,7	600	BN CSC	C	S/Al2O3	QJA 1:1:1	-
4	KalEx QJA 4	19,5	600	BN CSC	C	S/Al2O3	Alb Glas	-
5	KalEx QJA 5	19,5	600	BN CSC	Pt	S/Al2O3	Alb Glas	-
6	KalEx QJA 6	21,5	600	BN CSC	Pt	S/Al2O3	Alb Glas	-
10	KalEx QJA 10	18	600	BN CSC	Pt	S/Al2O3	Alb Glas	Albite
11	KalEx QJA 11	20	600	BN CSC	Pt	S/Al2O3	Alb Glas	Albite
12	KalEx QJA 12	25	600	BN CSC	Pt	S/Al2O3	Alb Glas	Albite
13	KalEx QJA 13	20	600	BN CSC	Pt	S/Al2O3	Alb Glas	Albite
14	KalEx QJA 14	20	600	Talc/Pyrex	Pt	S/Al2O3	Alb Glas	Albite
15	KalEx QJA 15	30	600	Talc/Pyrex	Pt	S/Al2O3	Alb Glas	Glas
16	KalEx QJA 16	30	600	Talc/Pyrex	Pt	S/Al2O3	Alb Glas	Jd + Qz
17	KalEx QJA 17	27,5	600	Talc/Pyrex	Pt	S/Al2O3	Alb Glas	Jd + Qz
18	KalEx QJA 18	24	600	Talc/Pyrex	Pt	S/Al2O3	Alb Glas	Glas
19	KalEx QJA 19	24	600	Talc/Pyrex	Pt	S/Al2O3	Alb Glas	Albite
20	KalEx QJA 20	24	1000	Talc/Pyrex	Pt	S/Al2O3	Alb Glas	Glas
21	KalEx QJA 21	24	1000	Talc/Pyrex	Pt	S/Al2O3	Alb Glas	Albite
22	KalEx QJA 22	27,5	1000	Talc/Pyrex	Pt	S/Al2O3	Alb Glas	Albite
23	KalEx QJA 23	30	1000	Talc/Pyrex	Pt	S/Al2O3	Alb Glas	Albite
24	KalEx QJA 24	30	700	Talc/Pyrex	Pt	S/Al2O3	QJA 1:1:1	Jd + Qz
25	KalEx QJA 25	30	800	Talc/Pyrex	Pt	S/Al2O3	QJA 1:1:1	Jd + Qz
26	KalEx QJA 26	27,5	600	Talc/Pyrex	Pt	S/Al2O3	QJA 1:1:1	Jd + Qz
27	KalEx QJA 27	24	600	Talc/Pyrex	Pt	S/Al2O3	QJA 1:1:1	Albite
28	KalExCa-Tsch 1	14,9	1300	Talc/Pyrex	Pt	S/Al2O3	Ca-Tsch Glas	-
29	KalExCa-Tsch 2	15	1300	BN CSC	Pt	S/Al2O3	Ca-Tsch Glas	-
30	KalExCa-Tsch 3	15	1300	BN CSC	Pt	S/Al2O3	Ca-Tsch Glas	-
31	KalExCa-Tsch 4	15	1300	BN CSC	Pt	S/Al2O3	Ca-Tsch Glas	-
32	KalExCa-Tsch 5	15	1250	BN CSC	Pt	S/Al2O3	Ca-Tsch Glas	-
33	KalExCa-Tsch 6	15	1300	BN CSC	Pt	S/MgO	Ca-Tsch Glas	-
34	KalExCa-Tsch 7	15	1300	BN+Al2O3	Pt	S/Al2O3	Ca-Tsch Glas	-
35	KalExCa-Tsch 8	15	1300	Talc/Pyrex	Pt	S/Al2O3	Ca-Tsch Glas	-
36	KalExCa-Tsch 9	15	1300	Talc/Pyrex	Pt	S/Al2O3	Ca-Tsch Glas	-
37	Ca-Tsch Kal 1	15	1300	BN+Al2O3	Pt	S/Al2O3	Ca-Tsch Glas	-
38	Ca-Tsch Kal 2	15	1300	BN+Al2O3	Pt	S/Al2O3	Ca-Tsch Glas	-
39	Ca-Tsch Salz 1	15	1300	NaCl+Bn+Al2O3	Pt	S/Al2O3	Ca-Tsch Glas	-
40	Ca-Tsch Salz 2	15	1300	NaCl+Bn+Al2O3	Pt	S/Al2O3	Ca-Tsch Glas	-
45	Ca-Tsch 2E	14	1300	NaCl+Bn+Al2O3	Pt	S/Al2O3	Ca-Tsch Glas	-
46	BNKalCa-Tsch 1A	15	1300	NaCl+Bn+Al2O3	Pt	S/Al2O3	Ca-Tsch Glas	-
47	BNKalCa-Tsch 1B	15	1300	NaCl+Bn+Al2O3	Pt	S/Al2O3	Ca-Tsch Glas	-
48	BNKalCa-Tsch 1C	15	1300	NaCl+Bn+Al2O3	Pt	S/Al2O3	Ca-Tsch Glas	-
49	BNKalCa-Tsch 1D	15	1300	NaCl+Bn+Al2O3	Pt	S/Al2O3	Ca-Tsch Glas	-
50	BNKalCa-Tsch 1E	15	1300	NaCl+Bn+Al2O3	Pt	S/Al2O3	Ca-Tsch Glas	-
51	BNKalCa-Tsch 1F	15	1300	NaCl+Bn+Al2O3	Pt	S/Al2O3	Ca-Tsch Glas	-
52	BNKalCa-Tsch 1G	15	1300	NaCl+Bn+Al2O3	Pt	S/Al2O3	Ca-Tsch Glas	-
53	NaClPyA KalCa-Ts	15	1300	NaCl+Al2O3	Pt	S/Al2O3	Ca-Tsch Glas	-
54	NaClPyA KalCa-Ts	15	1300	NaCl+Bn+Al2O3	Pt	S/Al2O3	Ca-Tsch Glas	-
55	NaClABN Kal 1	14	1300	NaCl+Bn+Al2O3	Pt	B/Al2O3	Ca-Tsch Glas	-

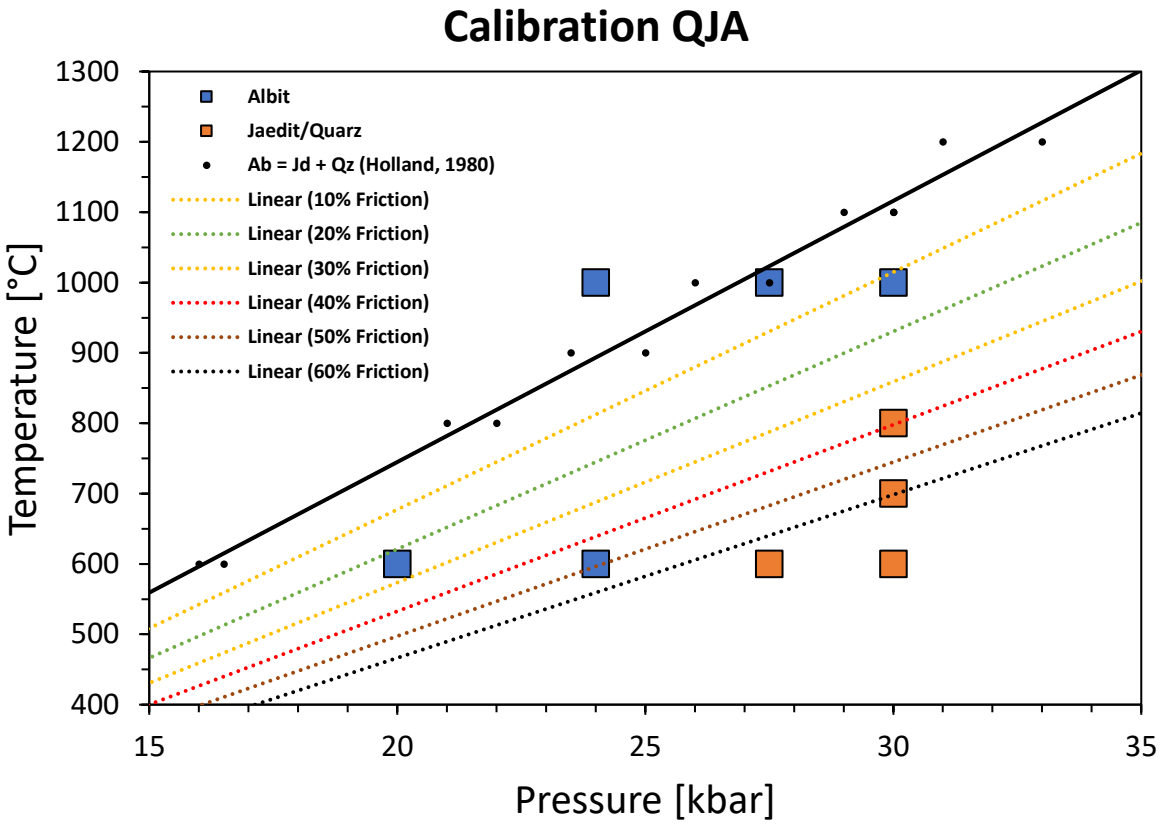


Figure 27: Results of calibration using Ab = Jd + Qz between 600 and 1000°C (blue rectangles = Albite, orange rectangles = jadeite + quartz in the run products). The dotted lines represent (from top to bottom) 10, 20, 30, 40, 50 and 60% friction compared to the data from Holland, 1980 (black line). The black data points show the locations of the calibration experiments reported in Holland, 1980.

This observation suggests that the materials used, especially BN, are not suitable for hydrostatically transmitting the pressure to the sample at low temperature. Rather, it is diverted upward past the capsule by the BN pretending a higher friction for the assembly ("pseudo-friction"). Johannes (1973) reported similar results for low temperature calibrations of BN assemblies, which supports this theory. Based on this, we suggest the use of BN assemblies exclusively for temperatures well above 1000°C.

2.2.6 Reaction of anorthite, gehlenite and corundum to Kushiroite

Following our own suggestion, we only use the BN assembly at temperatures above 1000°C. Since the albite decomposition reaction at 1000°C exceeds the pressure limits of our press, we changed the used system another time to the mineral reaction of anorthite, gehlenite and corundum forming kushiroite (a pyroxene):

Anorthit	+	Gehlenit	+	Korund	=	Kushiroite
$CaAl_2Si_2O_8$		$Ca_2Al_2SiO_7$		Al_2O_3		$CaAlAlSiO_6$

The transition occurs at 1.3 GPa and 1300°C (Hijikata & Yagi, 1967) which should be much better suited for our assembly (Figure 28).

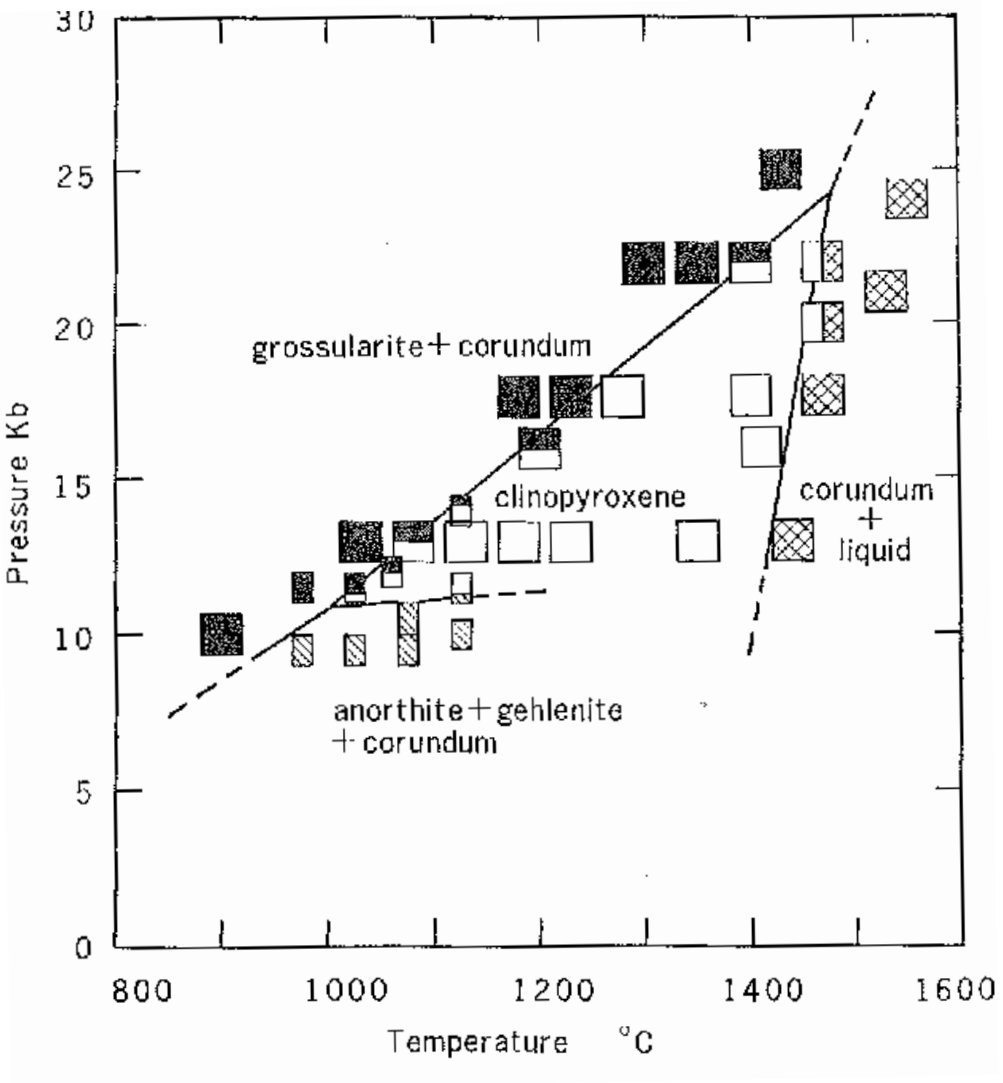


Figure 28: Phase diagram of Kushiroite as a function of temperature and pressure (Hijikata & Yagi, 1967)

The calibration experiments using this mineral reaction represent the largest proportion of the experiments carried out during this study, with 27 experiments (Table 4, Experiments 28 to 55) and almost one year of time required. As can be seen from Table 4, the composition of the assembly used was changed very frequently during this period. The biggest challenge here was the stability of the temperature sensor, which became unstable with an extreme failure rate between 700 and 1000°C. More details on this problem and the adjustments to the assembly can be found in the following chapter 2.3 of this thesis.

After fixing the sensor related problems, the assembly could be calibrated successfully. For this purpose, an experiment was conducted at 1.5 GPa (the sample contains Kushiroite) and 1.4 GPa (the sample contains anorthite, gehlenite and corundum) as confirmed by Raman spectroscopy. The actual transition is reported at 1300°C and 1.3 GPa (Hijikata & Yagi, 1967), resulting in a pressure loss to friction of 10.24% (Table 5). This is in good agreement with previously values determined in this laboratory for the use of salt-based assemblies, which were now used as a consequence of the results reported in chapter 2.3.

Table 5: Calculation of the average pressure loss due to friction as well as the associated conversion factors (1.116 as well as 0.898)

	P [GPa]	$P/P_{reaction}$	$P_{reaction}/P$	friction loss [%]
P_{high} (experiment)	1,5	1,154	0,867	max. 13,33
P_{low} (experiment)	1,4	1,077	0,929	min. 7,14
$P_{reaction}$ (literature)	1,3			
		average	**average**	**average loss**
	Factor	1,116	0,898	**10,24%**

2.3 Development of a stable assembly

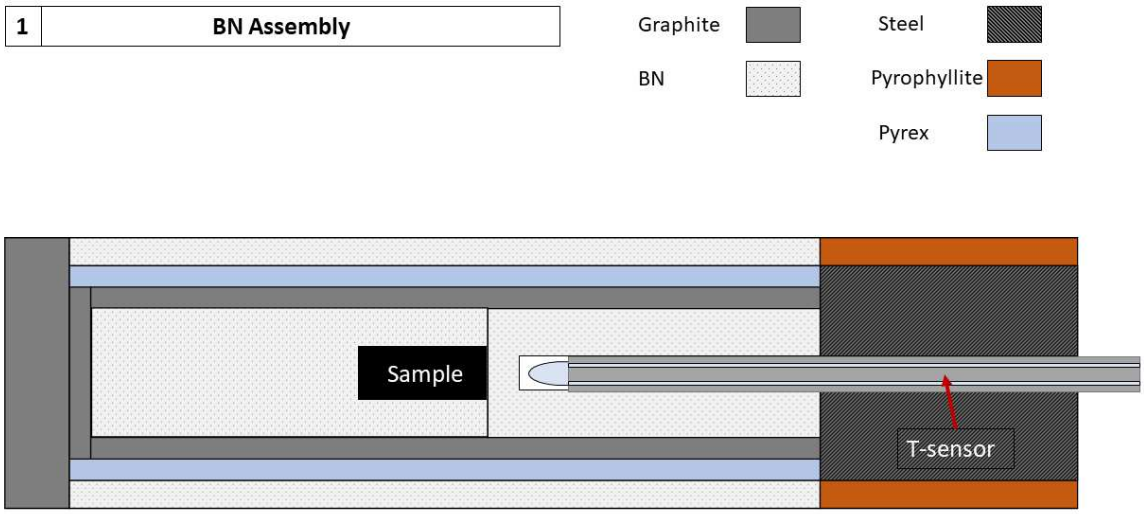


Figure 29: Original assembly design for the LMO experiments with high BN content.

Assembly #1 (Figure 29), which was originally developed for this study, turned out to be faulty during calibration where we observed a very frequent failure of the thermosensor. As a first measure, the guide of the thermosensor was exchanged for Al_2O_3 and an Al_2O_3 disc was inserted as a separation between the capsule and the sample (Figure 30).

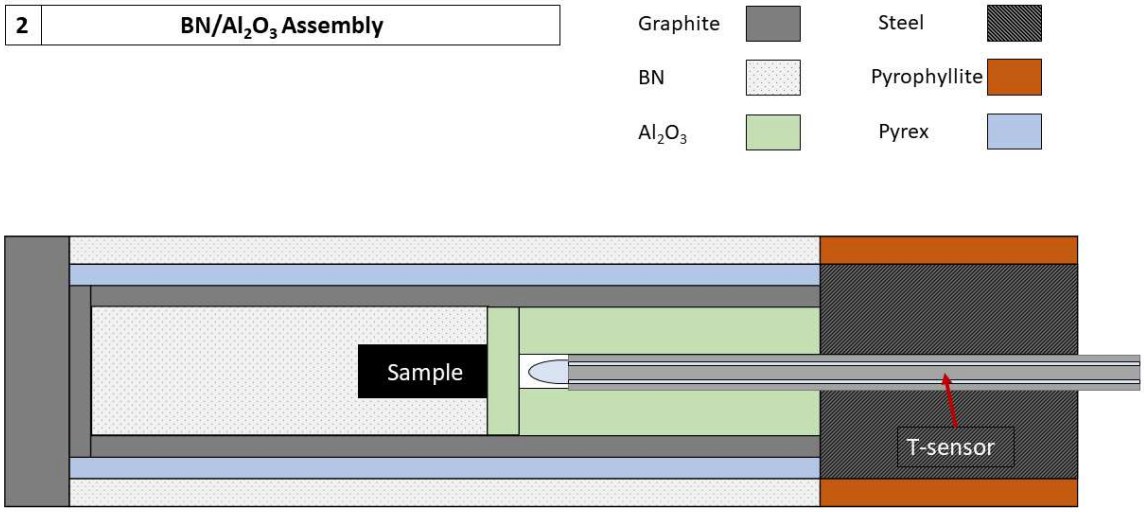


Figure 30: BN assembly with Al_2O_3 guide for the thermosensor.

This configuration only led to a barely noticeable improvement regarding the failure rate. Some experiments were nevertheless successful. However, the data from these experiments show a very high pressure loss due to friction, which is far outside usual values (up to 60% pressure loss, as reported in the previous chapter 2.2.5, Page 50).

We have considered two options as the cause of this:

[A] BN has less friction with the tungsten carbide core at higher temperature

[B] BN only transmits the pressure hydrostatically to the sample above a certain temperature

To check this, we used the previously standard talc-pyrex assembly of the GZG for some experiments. Only the sample chamber was replaced by BN (Design 3, Figure 31) since this part is not relevant for the friction between tungsten carbide core and assembly. The aim was to show, whether the BN assembly (Design 1, Figure 29) has a fundamental problem in the friction between the bomb and the assembly.

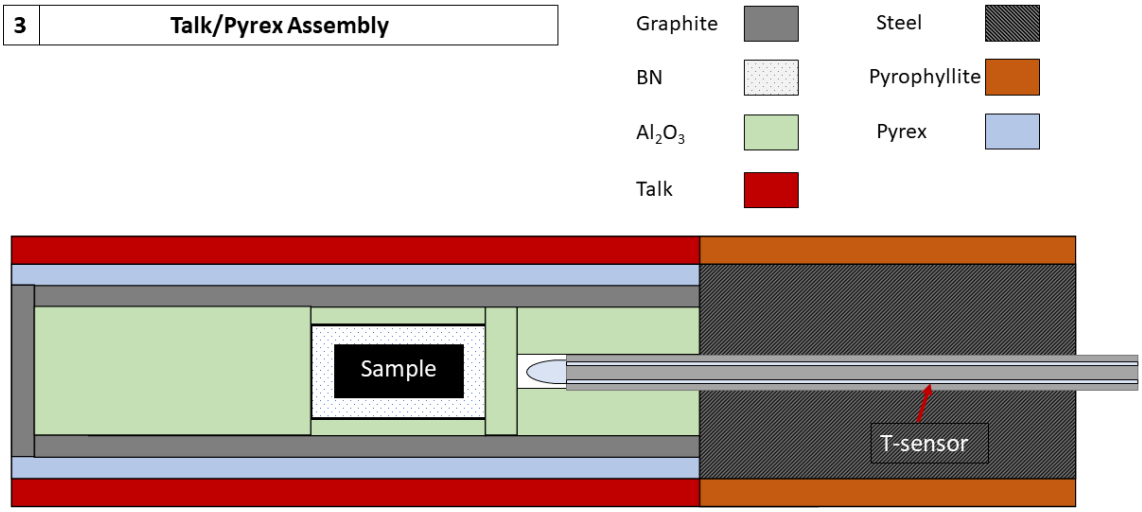


Figure 31 Talk-Pyrex Assembly of the GZG with BN sample chamber.

In this configuration, however, the pressure loss was just as high as in design 2 (Figure 30). Of the two initially suspected variants, [A] can therefore be excluded. To test variant B, calibration experiments at higher temperatures were necessary.

The calibration of the assembly was therefore continued with the reaction gehlenite + anorthite + corundum = kushiroite at 1300°C and 1.3 GPa to test the assumption. In both assembly designs, 1 (Figure 29) and 2 (Figure 30), which was rehabilitated by excluding assumption [A], the thermosensors failed in all cases between 700°C and 1000°C.

To investigate the causes of the failures, the assemblies were embedded in epoxy resin after the experiments and prepared as a cross-section. For design 1, BN was found to be completely unsuitable as a guide for thermal sensors (Figure 32).

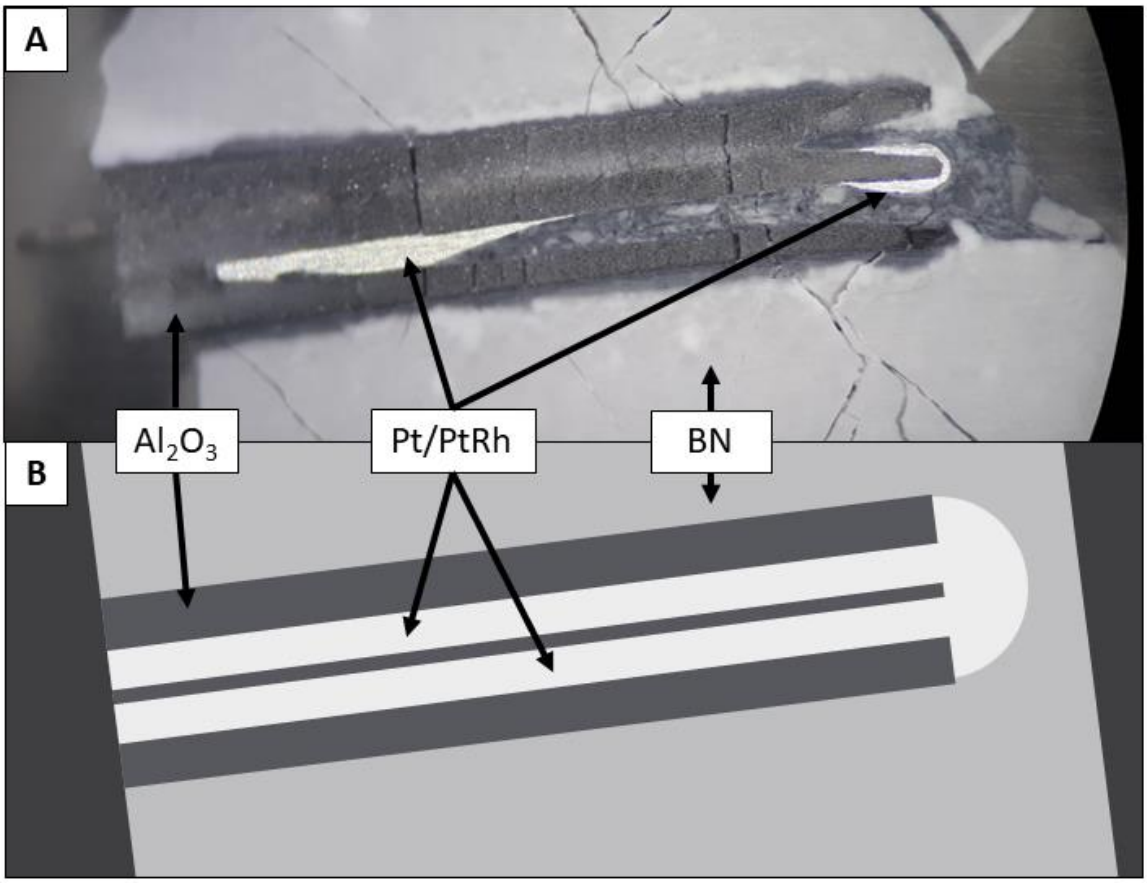


Figure 32: Microscopic image after an experiment with design 1 (A) and schematic representation of an intact thermosensor (B) with BN guide in the same position.

It can be clearly seen that a grey-black marbled mass penetrates the Al_2O_3 sleeve of the thermocouple and thereby displaces the platinum or platinum-rhodium wire. This breaks the electrical contact between the two wires and the thermosensor fails.

The elemental distribution map generated at the scanning electron microscope (SEM) shows that the dark coloured material is BN (Figure 33). Calcium serves here as a proxy for boron and nitrogen, as these are too light to be measured with the EDX system of the SEM. Calcium is present to a small extent in the BN guides, but not in the platinum / platinum-rhodium wire and its Al_2O_3 sleeve. BN was not considered as a guide for thermal sensors in any further experiments due to these results.

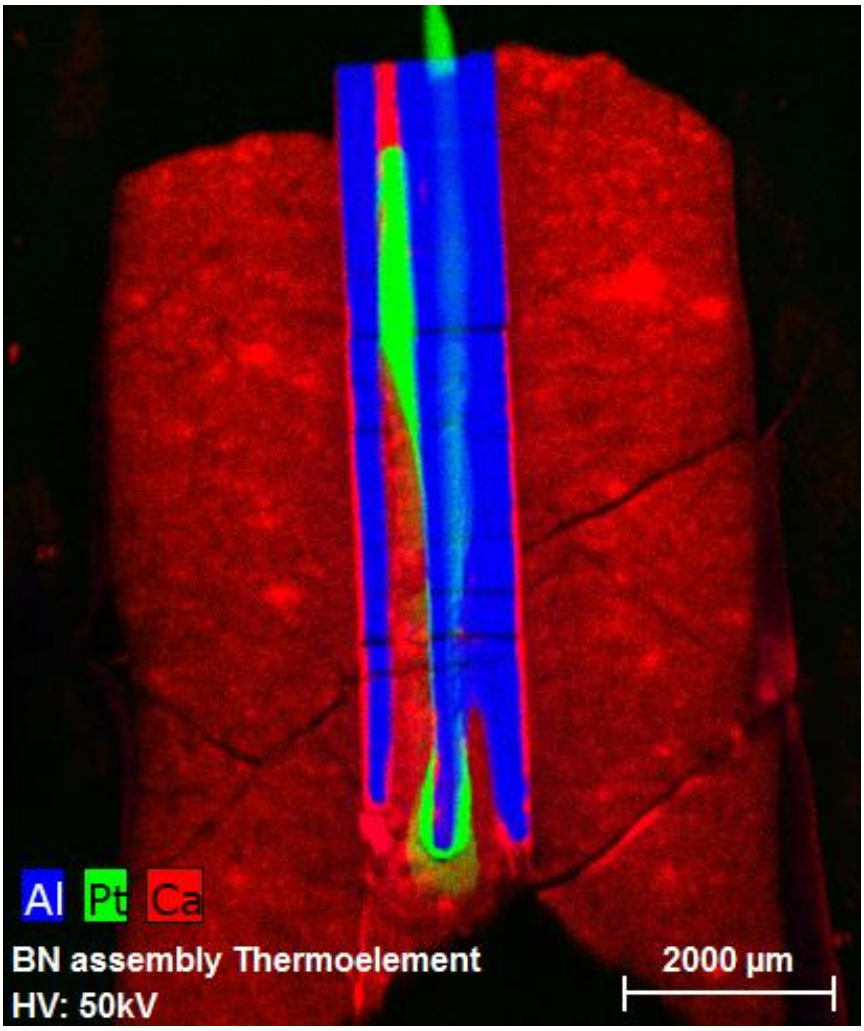


Figure 33: Element distribution map of a thermosensor (EDX).

For the alternative guide of Al_2O_3, failure rates were equally high even though no such effect could be observed by electron imaging. One theory is that the BN of the assembly jacket (see page 41, Figure 20, component 3) becomes too soft at higher temperatures and allows the Al_2O_3 guide to move sideways. Therefore, a new assembly version was used based on the original design by Prof. Dr. Stalder but using pressed NaCl as the assembly jacket (Design 4, Figure 34). In contrast to talc, NaCl is nominally water-free and therefore meets our requirements for the later LMO experiments to work as dry as possible.

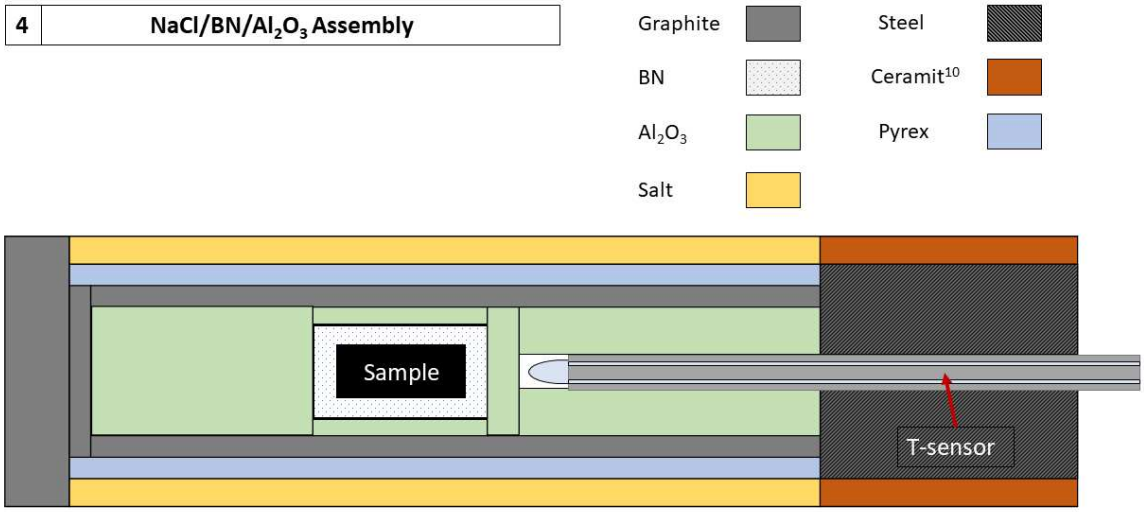


Figure 34: Assembly design 4 with NaCl as mantle material.

The assumption of movement in the assembly as cause for the failures is further supported by images of the furnace in contact with the thermocouple guide, which show strong shearing (Figure 35). This is also critical for the temperature distribution and performance of the furnace and not only a problem for the stability of the thermosensor, which breaks easily by internal movement of the material resulting in a loss of contact between the thin metal wires. However, salt is a standard material for such experiments, so this seems unusual.

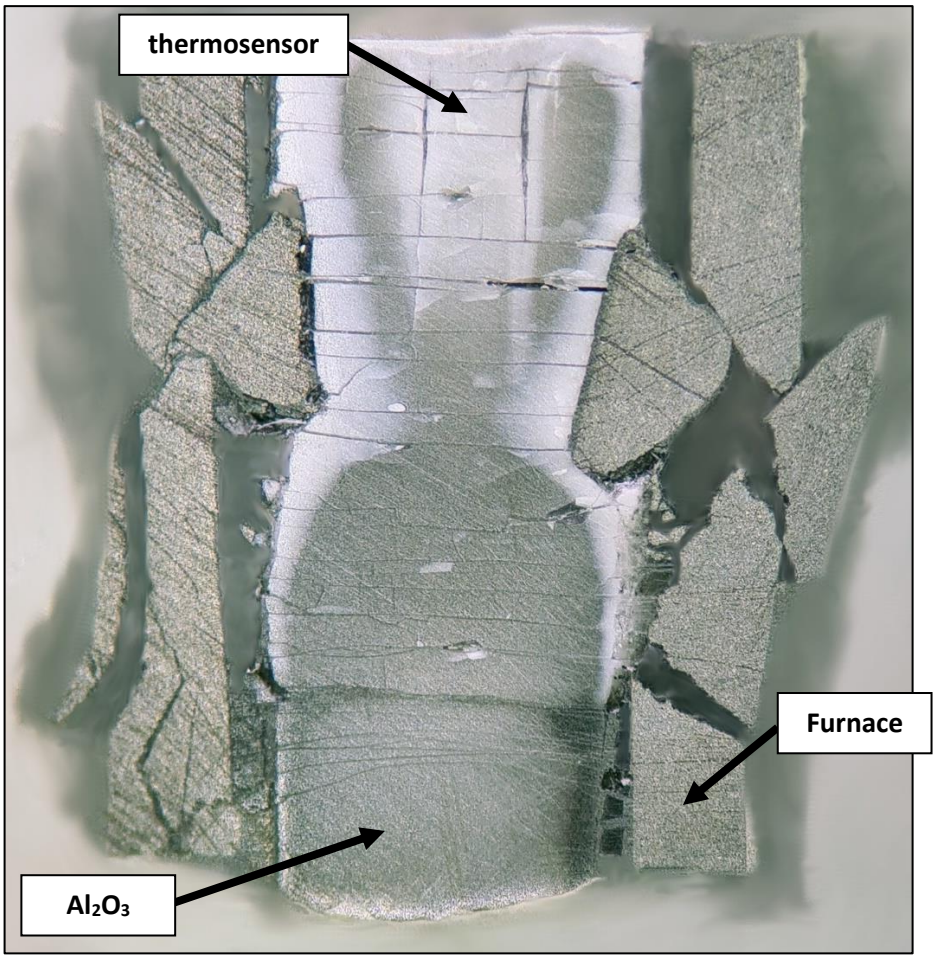


Figure 35: Furnace material (C) around the thermocouple bearing (Al_2O_3) corresponding to parts 5 and 7, Figure 20, page 41. The furnace has been subject to strong shearing due to material movement during the experiment. The first parts of the thermosensor are barely visible at the top of the cross section.

In an ideal assembly, from the sensor's point of view, there is no movement. However, this would not work because hydrostatic pressure can only be transmitted to the sample if the materials fill the available space completely. This is impossible with very rigid materials which do not completely transfer the pressure to the sample. Therefore, materials that have a certain porosity are often used in piston cylinder experiments. The porosity is closed by the pressure in the experiment by breaking the connection between the individual grains so that they can occupy the available cavity at full extend. Through pressure and temperature during the experiment, the material recrystallises back into a single solid.

However, the pressure transmission is only required at the sample since the temperature measurement by the thermosensor does not depend on pressure. If a material with too much porosity is used here, the movement of the material may cause the sensor to break. In the area above the thermosensor, material with less porosity is therefore used.

To minimise movement, a completely rigid material such as steel would be ideal. However, this would result in the thermosensor no longer having a hold in the assembly - it would be pushed out of the measuring range. Since the power of the oven is directly controlled by the measured value of the thermosensor, a spatial distance to the sample greatly increases the temperature inaccuracy. In some experiments, this effect caused the platinum capsule of the experiment (melting point 1772°C) to melt at indicated 1300°C - the sensor was located in a much colder area of the assembly and not at the hotspot. For these reasons, the direct environment of the thermosensor is divided into two parts: steel is used in the upper part to minimize movement and a porous ceramic in the lower part to hold the sensor in place.

Attempts to extend the steel area at the expense of the ceramic part did not improve the durability of the thermosensor (Design 5, Figure 36).

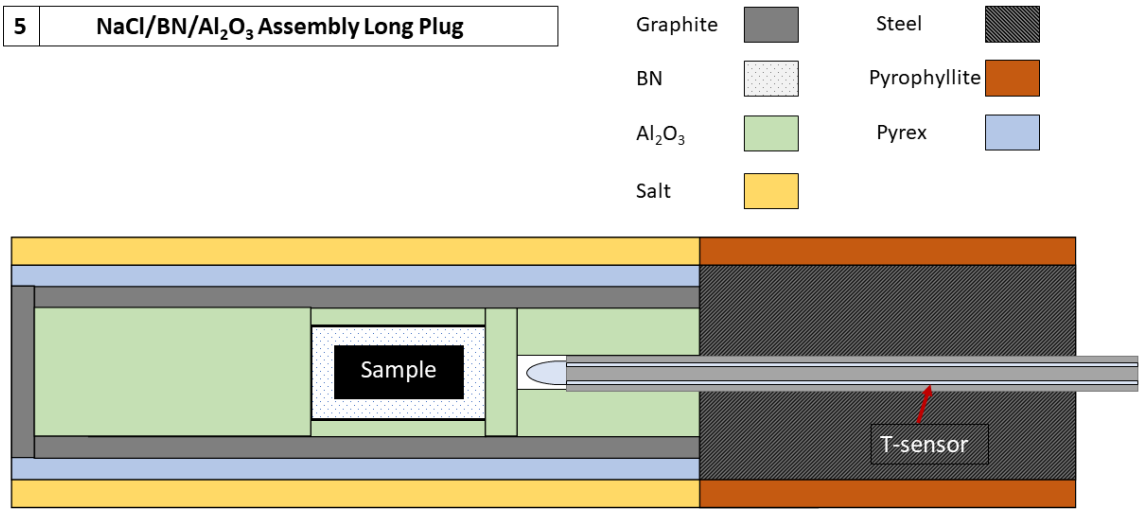


Figure 36: Assembly 5 with extended steel guide on the thermosensor.

As a consequence, we investigated the used ceramic by combining dimensions, weight and the density of Al_2O_3 to calculate an approximate porosity of 42%. After consulting other high-pressure laboratories from the University of Edinburgh and ETHZ, it became obvious, that this amount of porosity is quite high. Magnesium oxide (MgO) tubes, which have much less porosity, were used in the following to manufacture the guiding used for the thermosensors. In parallel, the steel guide was shortened (Design 6, Figure 37). MgO has a significantly

lower porosity than the previously used Al_2O_3. This restricts the movement around the thermosensor.

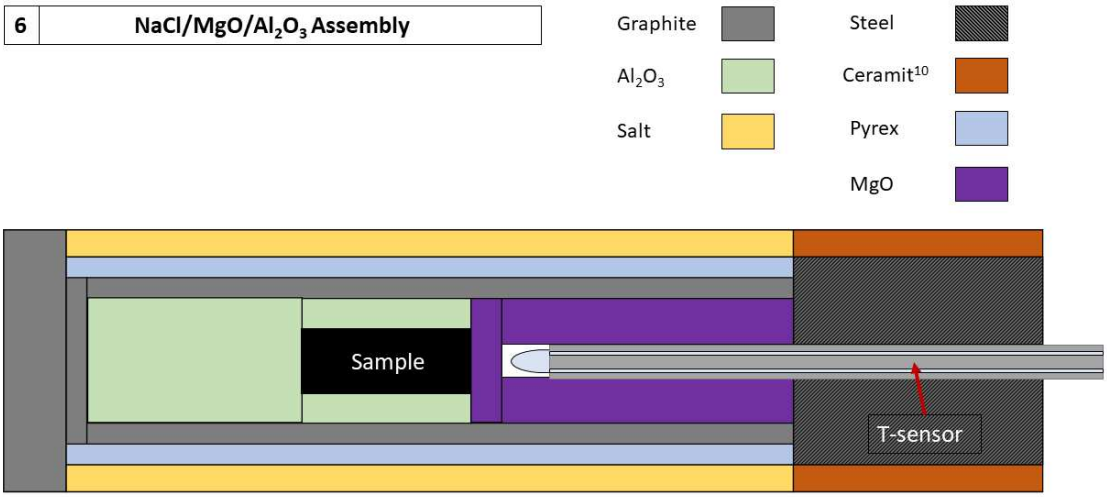


Figure 37: Assembly 6 with MgO as a guide for the thermosensor.

As an additional measure, we have replaced the previous S-type thermocouples (Pt-$Pt_{90}Rh_{10}$) with B-type thermocouples ($Pt_{70}Rh_{30}$-$Pt_{94}Rh_6$). At the same time, we created a recess in the wire guide of the thermocouples with a fine drill so that the welding bead, where both wires are welded together, is countersunk in it (Figure 38). We then filled the recess with a two-component thermocement (Figure 39). This protects the entire wire even better from movement and possible shearing. As a result of these changes, no thermosensor has broken ever after.

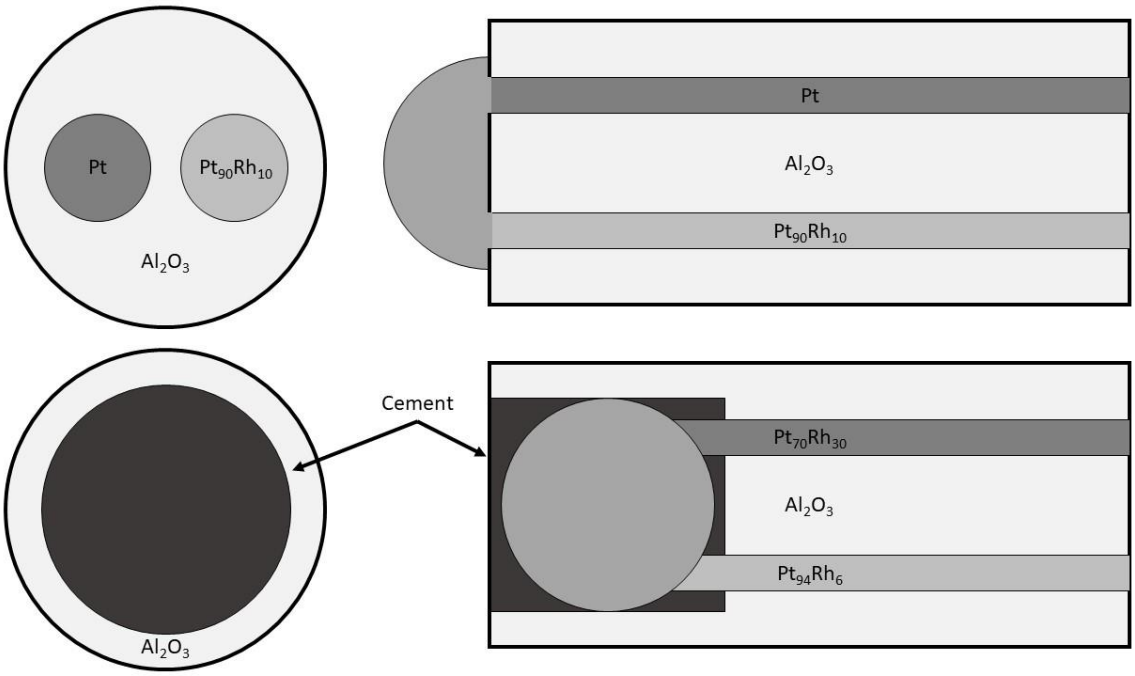


Figure 38: Schematic representation of the thermocouples in top view (left) and cross-section (right) in their previous form (top) and after the adjustments (bottom).



Figure 39: Thermocouple with recessed weld bead (left) and after cementing (right).

Conclusion:

The assembly design 6 used is thus divided into three areas from soft to hard. In the lower area, Al_2O_3 with approx. 40% porosity transmits the pressure to the sample. Above this is the thermosensor guide made of MgO in the lower area and steel in the upper area, which gives the sensor stability and at the same time holds it in the assembly. Both areas are surrounded by Pyrex, which serves as a water trap, and a jacket of pressed NaCl. The furnace system is made of graphite and ends at the bottom in a graphite disc for optimal current transmission.

2.4 Experimental crystallisation of the LMO

The aim of this study is the experimental investigation of the development of the lunar magma ocean, considering the factors chemistry, pressure, temperature, f(O_2) and water content. The influence of the conditions on the crystallisation of the LMO, how they are generated and which assumptions underlie the chosen conditions will be described. Subsequently, the preparation and execution of the experiments will be shown.

2.4.1 Pressure

Pressure is physically defined by the effect of force on a surface. This force action leads to deformations depending on the strength and material properties of the substances involved. The crystal lattices of minerals also react to pressure, e.g. through volume change, lattice alignment or recrystallisation. In addition, minerals always have only a certain stability window. If the conditions leave this window, the minerals adapt to the new environment. This happens either through reactions between different minerals or a change in the crystal lattice of individual minerals.

In geology, these adaptations of minerals have great significance. For example, the drainage reactions of subducted, oceanic continental plates lead to the melting of the overlying rock by the released water, as this lowers the temperature required for melt formation below that of the surroundings. The resulting melt leads to volcanism at the surface. The dehydration of minerals in response to higher ambient pressure is therefore the cause of volcanism in the Earth's subduction zones.

In the case of the lunar magma ocean, the starting point is already a melt. This means that mineral genesis forms directly from the liquid state and depends on which minerals are in their stability window in the current temperature and pressure range.

The pressure therefore has a direct influence on the crystallising phases. The pressure distribution within the lunar magma ocean is therefore an important parameter for this work. The pressure inside the Moon does not increase with depth linearly. The basis for the relationship of pressure to depth in the Moon is the lunar model by Garcia et al. (2011, 2012), which is still considered as a standard work today (Figure 40).

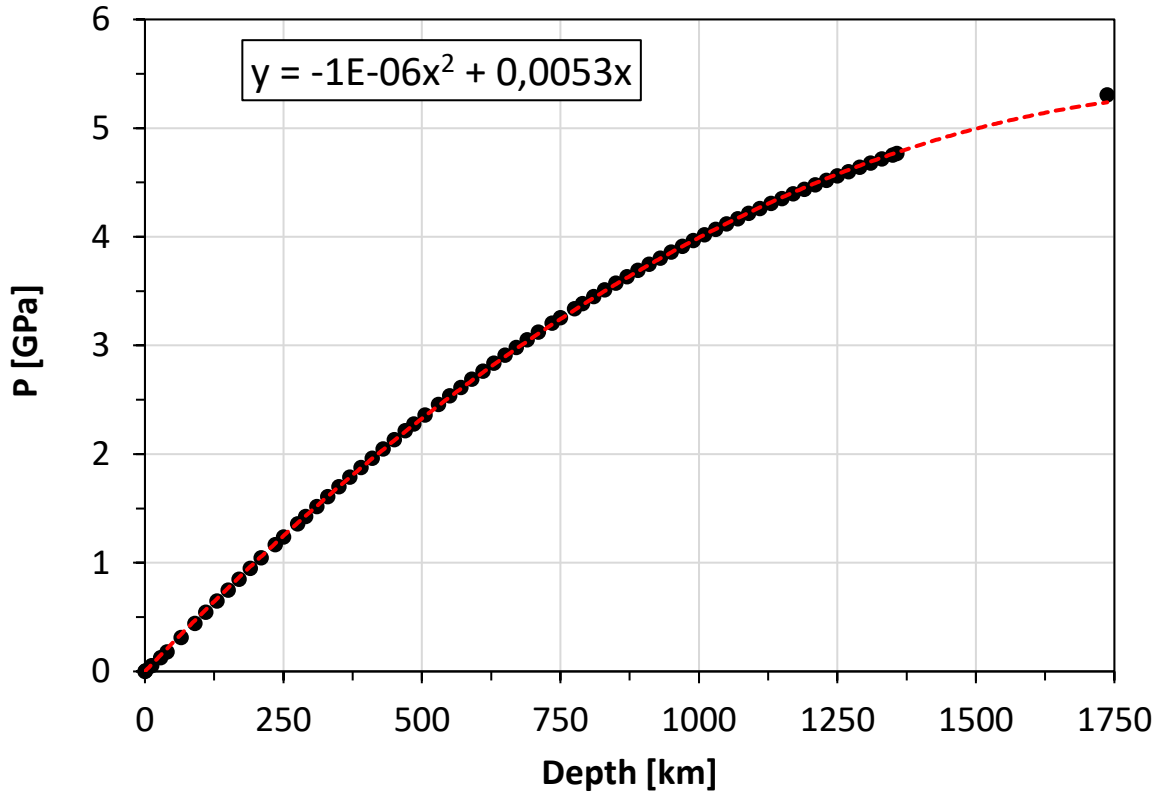


Figure 40: Pressure as a function of depth in the Moon according to Garcia et al. (2011). The black circles correspond to the model data of Garcia et al. (2011), the red dashed line to our regression.

This model incorporates both seismic data from the experiments of the Apollo missions and geodetic observations. Figure 40 shows the values for depth and corresponding pressure determined by Garcia et al. (2011). By regressing the literature data using the software *Sigma Plot,* the pressure P at depth d can be calculated in a good approximation by the following relation (2):

$$P(d) = (-1) \cdot 10^{-6} \cdot d^2 + 0.0053 \cdot d \qquad (2)$$

Compared to the Earth, the pressure inside the Moon is about one sixth of what we would encounter on Earth at the same depth due to the lower mass. In the lunar core (1737 km depth) there is therefore 'only' a pressure of about 5.3 GPa (Garcia et al., 2012). On Earth, the pressure increases by 0.1 GPa about every 3 km, so that this pressure is already reached in the interior of the Earth at a depth of about 160 km. This includes the Earth's crust (0 to 35-70 km) and a small part of the upper mantle which reaches 660 km deep.

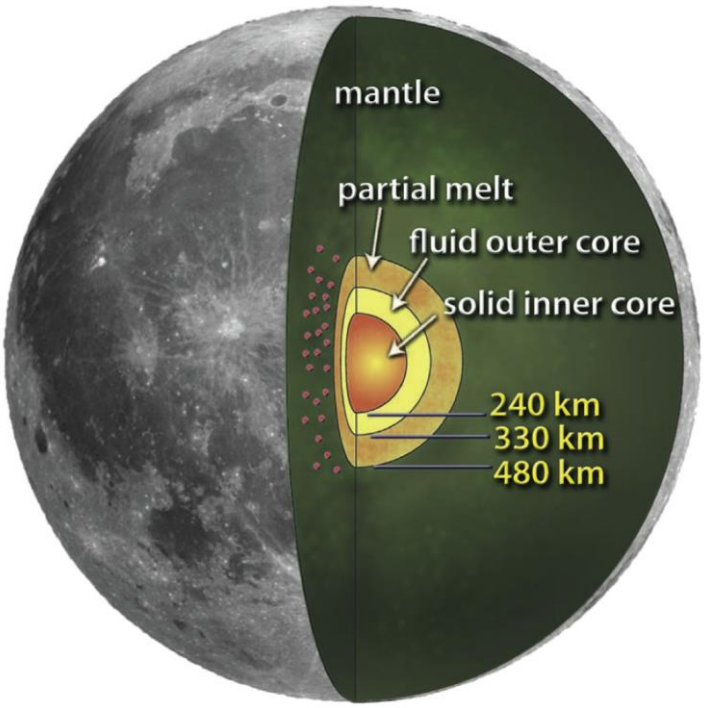


Figure 41: Internal structure of the Moon according to Weber et al., 2011

The pressure in the lunar magma ocean increases from the surface to the bottom at 1400km depth (presumed core-mantle boundary, Figure 41; Weber et al., 2011). If turbulent convection in the ocean provides a homogeneous temperature distribution and chemistry, crystal formation should begin at the point of greatest pressure. Assuming complete fractionation of the minerals, the pressure decreases as the degree of crystallisation of the Moon increases. The crystallisation front shifts further and further towards the surface. The model for the present-day pressure distribution according to Garcia et al. (2011 & 2012) is used as the basis for the pressure conditions in the LMO.

2.4.2 Temperature

Temperature is an important state variable for geological processes, as it provides the energy for numerous processes. If this is missing, many reactions cannot take place. Diamond, for example, only forms at high pressure. At the surface, it is metastable and reacts back to graphite. This happens so slowly at room temperature that the process practically stands still - the necessary activation energy for the retrograde reaction is missing. If the material is heated to ~800°C, the reaction takes place immediately and the diamond will turn back into graphite. Furthermore, the temperature determines whether and to what extent material melts or crystallises.

The geothermal gradient, i.e. the increase in temperature with the depth of the Moon, is not a component in the standard model of Garcia et al. (2011). The only available data come from heat flux experiments at 1.5 and 3 metres depth from Apollo 15 (site: Hadley Rille, 2.1 $\mu W/cm^2$) and Apollo 17 (site: Taurus Littrow, 1.4 $\mu W/cm^2$) (Keihm & Langseth, 1977). Considering the distribution of radioactive elements at the sites, the average heat flux is 1.8 $\mu W/cm^2$ (Langenseth et al., 1976). The Earth's heat flux is significantly higher, averaging 8.7 $\mu W/cm^2$ (Pollack et al., 1993). The temperatures inside the Moon calculated from this, among other factors, vary from model to model by several hundred Kelvin (Jones & Hood, 1988; Mueller et al., 1988; Khan et al., 2006). But even if we had precise knowledge of the current temperature distribution in the Moon, this only represents the current temperature equilibrium that has set in after the initial cooling of the LMO was completed. For our experiments, however, we must look at the cooling process itself.

Since the Moon is thought to have originated from a 4000 to 6000K hot debris disk (Nakajima & Stevenson, 2018), we assume a homogeneous temperature well above the liquidus as starting condition. As the LMO cools down, the crystallisation starts at the very bottom and will move as a crystallisation front towards the surface, as new crystals always form where the pressure is highest in the remaining magma (Figure 42). The temperature, in contrast to the static pressure inside the Moon, is therefore a variable that changes over time. The correlation between pressure and temperature for our experiments therefore always represents only one specific moment of crystallisation when the crystallisation front crosses the selected pressure range. If the temperature is chosen higher, there will be few or no crystals and if chosen lower, most of the sample will be solid.

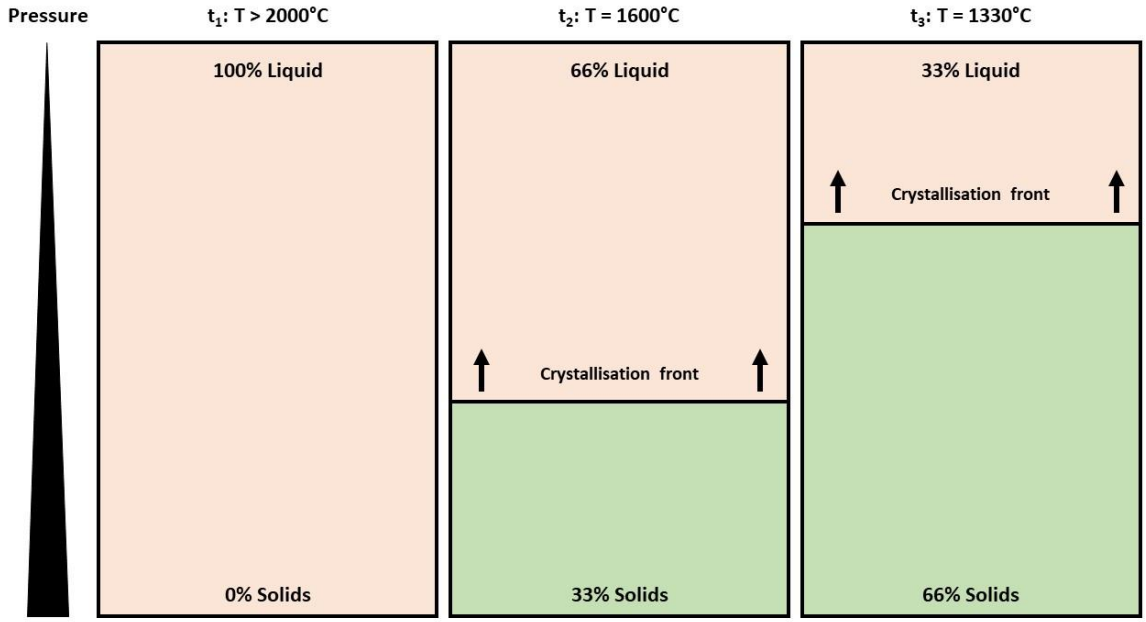


Figure 42: Schematic representation of LMO cooling at three arbitrary times (t_1, t_2 & t_3). The pressure is highest at the bottom of the LMO and decreases towards the surface without changing over time while the crystallisation front rises towards the surface during cooling.

Therefore, to be able to determine the starting conditions for the experiments, the most detailed work to date on the crystallisation of LMO was used as a guide. Rapp and Draper (2018) chose their temperature conditions precisely to achieve a melt fraction of 75% in their respective experiments. A regression of these authors' data using the software SigmaPlot yields the relationship between temperature and pressure shown in (3).

$$T(P) = (a + b * P - c * P^2)^2 \quad (3)$$

with

a = 31.70549585
b = 4.726306909
c = 0.514760460

where T describes the temperature at pressure P. Figure 43 shows the relationship graphically. This correlation should now represent the conditions, where experimental runs yield approximately 75% of melt fraction. This is only true for the used compositions since a chemical variation will lead to different liquidus temperatures for the system.

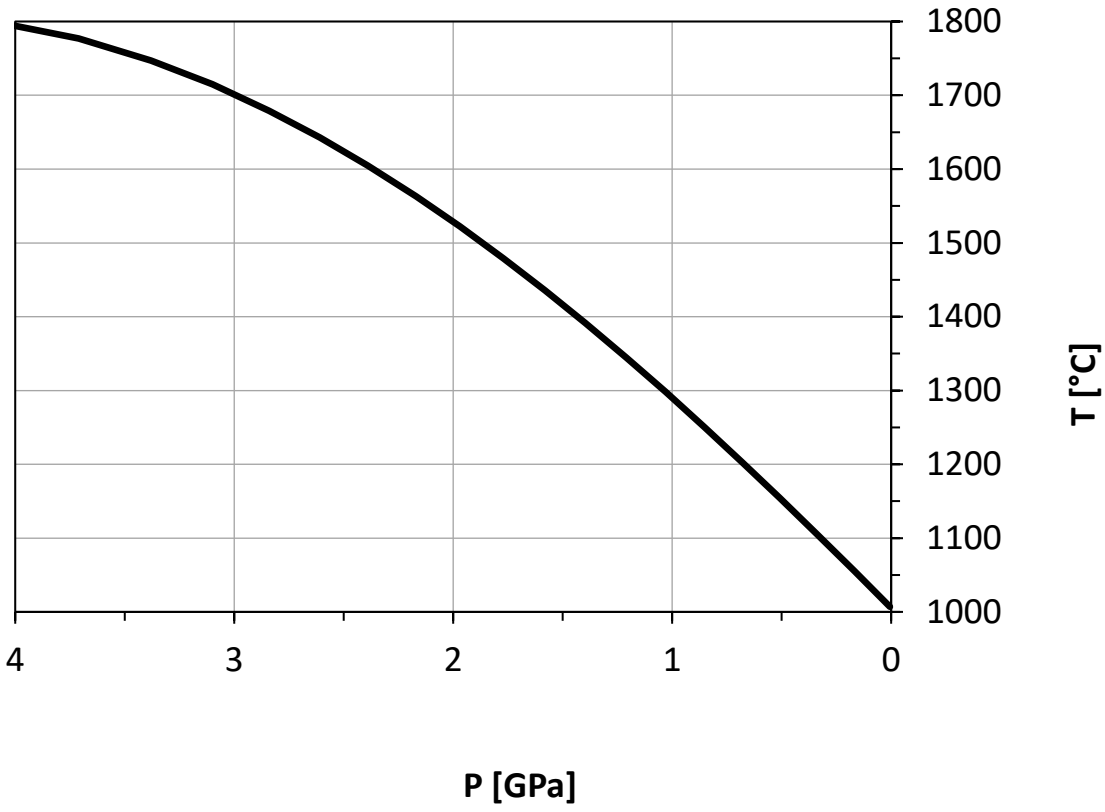


Figure 43: Relationship between pressure (P) and temperature (T) in the LMO determined from the data of Rapp & Draper (2018).

2.4.3 Crystallisation progress (PCS)

Percent Solid (PCS) is often used in context of the LMO crystallisation. This is a measure of the percentage of the magma ocean that has crystallised. Due to the spherical shape of the Moon, the relationship between PCS, depth and pressure in the Moon is not linear. It is also directly related to the initially assumed depth of the LMO, as the volumes of the crystallising deep sections increase towards the surface. For example, assuming a 1400km deep LMO, the shell of the lowest 100 km corresponds to 0.9 vol% while the outermost 100 km contributes 16.4 vol%. The crystallisation progress at depth D can be calculated from the ratio between the already crystallised volume of the LMO at depth D ($VLMO_{(D)}$) and the total volume of the LMO with maximum depth D_0 ($VLMO_{(D0)}$). The equation for this is (4)

$$PCS(D) = 100 \times \frac{\boldsymbol{VLMO_{(D)}}}{\boldsymbol{VLMO_{(D_0)}}} \tag{4}$$

with

$$\boldsymbol{VLMO_{(D)}} = V_{(r)} - Vcore \tag{5}$$

$$= \frac{4}{3}\,\pi\,(r_M - D)^3 - \frac{4}{3}\pi(r_M - D_0)^3$$

$$= \frac{4}{3}\pi\,[(r_M - D)^3 - (r_M - D_0)^3]$$

and

$$\boldsymbol{VLMO_{(D0)}} = \frac{4}{3}\pi \times {D_0}^3 \tag{6}$$

V_r describes the volume of the sum of LMO and core and V_{core} the volume of the core (or primitive mantle, if applicable) at lunar radius r_M. For this work, the lunar radius r_M is assumed to be 1737.4 km and the maximum depth of the LMO (D_0) 1400 km. This results in a core area (r_M - D_0) of 337.4 km. In a simplified representation with these values, the equation is therefore (7)

$$PCS(D) = 100 \times \frac{\frac{4}{3}\pi\,(1737.4\ km - D)^3 - 1.60888071 \times 10^8\ km^3}{2.1806987543 \times 10^{10}\ km^3} \tag{7}$$

with D as the current depth of crystallisation. This formula describes, how much of our model LMO has been crystalised at a particular depth D. Table 6 summarises the relationship between pressure, temperature, depth (previous chapters) and PCS in tabular form.

Table 6: Relationship between depth, pressure, temperature and degree of crystallisation of LMO.

Depth km [km]	P [GPa]	T [°C]	PCS [%]
0	0,00	1005	100,0
5	0,03	1014	99,1
10	0,06	1023	98,3
15	0,09	1031	97,4
20	0,12	1040	96,6
25	0,14	1048	95,7
30	0,17	1057	94,9
35	0,20	1065	94,0
40	0,23	1073	93,2
45	0,26	1082	92,4
50	0,28	1090	91,6
75	0,42	1130	87,5
100	0,56	1168	83,6
125	0,69	1205	79,8
150	0,82	1241	76,1
175	0,94	1275	72,5
200	1,07	1307	69,1
225	1,19	1338	65,7
250	1,30	1368	62,5
275	1,42	1397	59,3
300	1,53	1424	56,3
325	1,64	1450	53,4
350	1,75	1475	50,6
375	1,86	1498	47,8
400	1,96	1520	45,2
425	2,06	1542	42,7
450	2,16	1562	40,2
475	2,26	1581	37,9
500	2,36	1599	35,7
600	2,72	1661	27,5
700	3,06	1710	20,7
800	3,38	1747	15,1
900	3,67	1774	10,5
1000	3,95	1793	7,0
1100	4,21	1805	4,2
1200	4,45	1810	2,2
1300	4,68	1810	0,9
1400	4,90	1807	0,0

2.4.4 Oxygen fugacity

The oxygen fugacity is a measure of how reducing or oxidising a mixture of substances is under certain conditions and can be seen as the amount of oxygen available for reaction in a sample (Albarède, 2011). In reality, the numerical value is so small that this can be thought of less as an amount of actual free roaming oxygen atoms and more as the reaction potential of the sample. Nevertheless, the oxygen fugacity has significant influence on all multivalent elements in magmatic systems and thus, on the crystallising phases. Iron, for example, is under very reducing conditions more abundant in its metallic form (Fe^0), divalent (Fe^{2+}) under intermediate conditions and trivalent (Fe^{3+}) under oxidising conditions. This influences, for example, whether haematite ($Fe^{3+}{}_2O_3$) or magnetite ($Fe^{2+}Fe^{3+}{}_2O_4$) crystallises from a melt or whether iron precipitates in its metallic form from it (Frost, 1991).

To create corresponding oxidation conditions in the laboratory experiment certain chemical reactions are used. These buffer the conditions until one of the substances involved is completely used up. An overview of example substance reactions and the generated conditions can be found in Figure 44.

Direct measurements on Apollo era volcanic samples suggest conditions from one log-unit above (IW+1) to two log-units below (IW-2) the iron-wüstite-buffer (Papike et al., 1998, Longhi, 1992; Shearer et al., 2006), thus near or at saturation of metallic iron (Potts et al., 2021). It can therefore be assumed that the mantle of the Moon, from which the measured melts originated, is similarly reduced and therefore more reducing than the Earth's mantle (Rutherford & Papale, 2009; Sato, 1976).

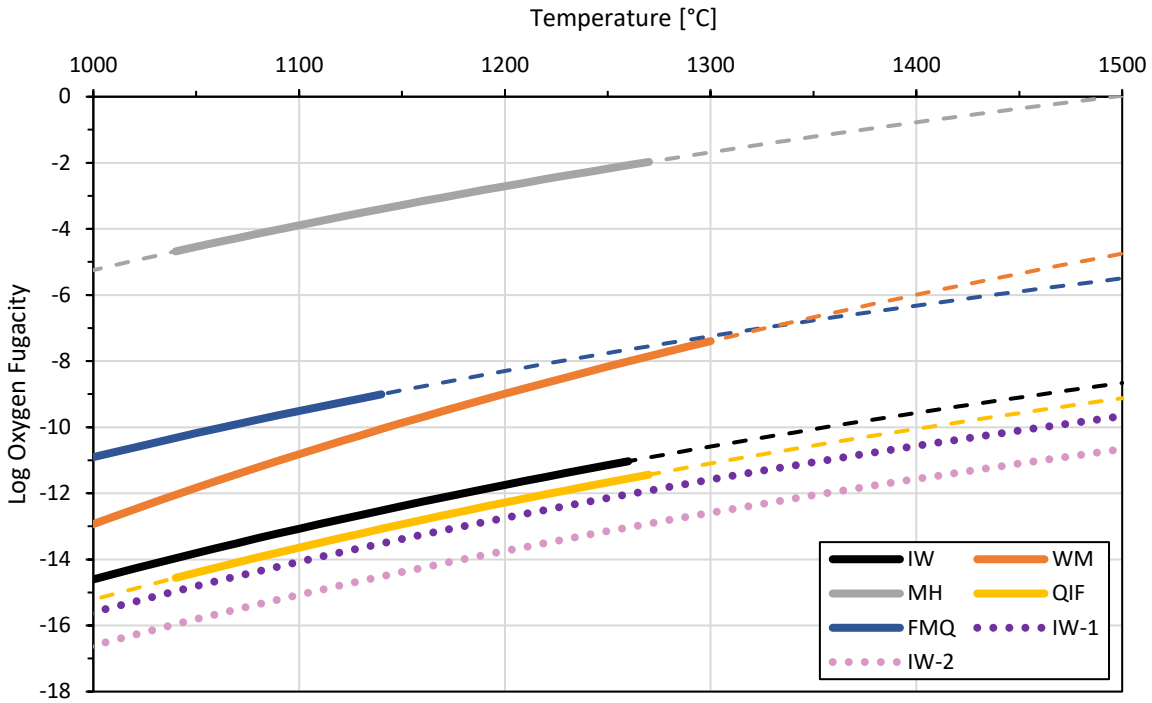


Figure 44: Oxygen fugacity of buffer reactions as a function of temperature. The data from Myrs & Euster (1983) (solid lines) was extrapolated to the entire temperature range of our runs (dashed lines). The oxygen fugacity while using Cr + Cr_2O_3 buffers and Fe-capsules was reported as roughly between IW-1 to IW-2 (Potts et al., 2021) (dotted lines).

MH	*: 4 Fe_3O_4 + O_2*	*= 6 Fe_2O_3*
NiNiO	*: 2 Ni + O_2*	*= 2 NiO*
FMQ	*: 3 Fe_2SiO_4 + O_2*	*= 2 Fe_3O_4 + 3 SiO_2*
WM	*: 3 $Fe_{1-x}O$ + O_2*	*= Fe_3O_4*
IW	*: 2 Fe + O_2*	*= 2 FeO*
QIF	*: 2 Fe+SiO_2 + O_2*	*= Fe_2SiO_4*

To adapt the redox conditions of the experiments to the conditions in the LMO, an appropriate environment must be created in the sample capsule. Rapp and Draper (2018) have used graphite capsules for this purpose. This creates reducing conditions in the experiment, as free oxygen is bound by the graphite as CO. According to Thompson & Kushiro, 1972 and Myers & Eugester, 1983, this produces conditions in the stability field of wüstite. Somewhat more specific information can be found in Holloway et al. (1992), who give conditions ranging from IW+1 to IW+2 for the use of graphite capsules. Furthermore, the authors claim, that the presence of graphite is not yet a buffer for f(O_2). Rather, the graphite increases the CO_2 content in the sample material and thus acts as a oxygen sink. In addition, carbonates are formed (Holloway et al., 1992). Both are undesirable and can influence the outcome of the experiments, as sample LPUM-300-1 of this thesis

demonstrates (Chapter 3.1, Page 104). For this study, a lower oxygen fugacity is aimed for which is closer to the estimates based on the Apollo samples. The reaction (8)

$$2\ Cr + 3\ O_2 \Leftrightarrow 2\ Cr_2O_3 \quad (8)$$

generates estimated conditions from IW-1 to IW-2 (Potts et al., 2021; Holzheid & O'Neill, 1995), which is very close to the lunar mantle conditions (Papike et al., 1998, Longhi, 1992; Shearer et al., 2006). If one of the components is consumed, the reaction comes to an halt and the experiment is no longer buffered.

For this study, a mixture of 90 mol% Cr and 10 mol% Cr_2O_3 was prepared, as the conditions in the piston-cylinder-press are much more oxidising than IW without a buffer. Therefore, only Cr is expected to be consumed. The mixture was sealed in capsules of pure platinum to prevent a chemical reaction with the sample material. The capsule with the buffer is placed in the capsule with the actual sample and has direct contact with it. The sample itself is contained in a capsule of pure iron (99.9%) (Figure 45), which aids the buffer by the iron-wüstite reaction (9).

$$2\ Fe + O_2 = 2\ FeO \quad (9)$$

The oxygen fugacity is thus already lowered to approximately IW+0.

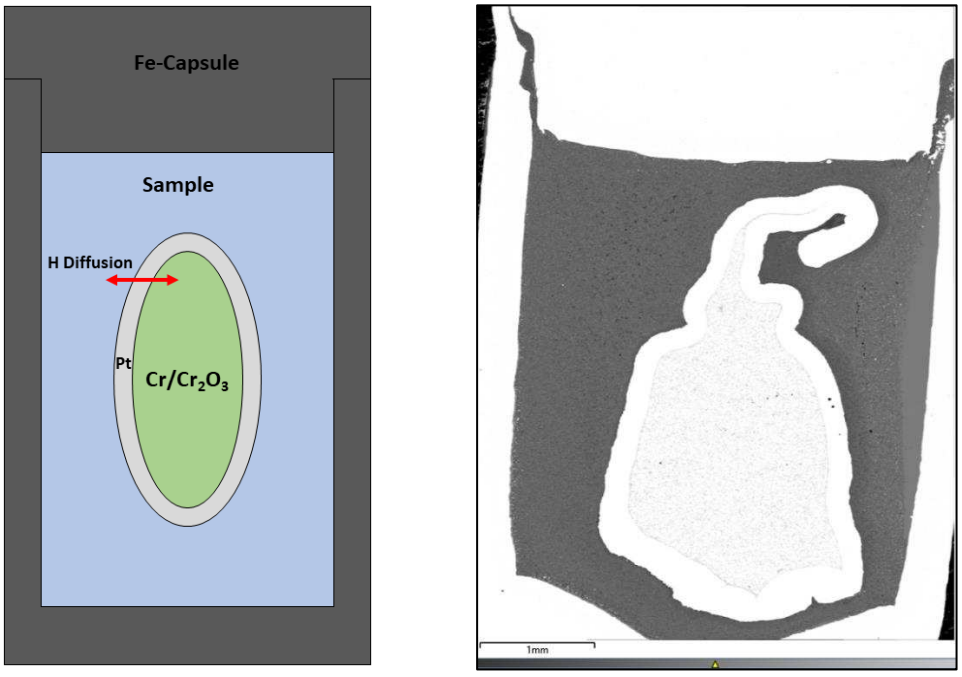


Figure 45: Capsule design with Cr-Cr_2O_3 buffer to generate reducing f(O_2) conditions (left) and SEM image of a successful experiment with the design used (right).

In such designs, the transfer of the $f(O_2)$ conditions from the buffer into the sample capsule occurs via the exchange of hydrogen, which can diffuse easily through the platinum wall while oxygen is too large to do so by its own. The hydrogen reacts with free oxygen in the sample and thus carries the information from the buffer into the sample capsule.

Electron optical images of the sample runs depict an alloy of chromium and platinum that has formed on the inner wall of the buffer capsule, as already described in Potts et al. (2021). This does not affect the diffusion of hydrogen and thus the exchange of conditions (Stokes et al., 2019).

2.4.5 Chemical composition

The chemical composition of a crystallisation experiment is of crucial importance. The presence or absence of certain elements as well as their concentration decisively determines which crystals are formed. For example, potassium-free melts will never form orthoclase ($KAlSi_3O_8$), whereas the calcium and sodium content influences the proportion of anorthite ($CaAl_2Si_2O_8$) or albite ($NaAlSi_3O_8$) components in a feldspar. At the same time, the composition has a direct influence on physical melt properties such as density and melting point as well as viscosity.

The choice of chemical composition for the experiments in this study is inspired by the study of Rapp and Draper (2018) and thus, the Lunar Primitive Upper Mantle (LPUM, Longhi, 2006, Table 7). The compositions we chose are shown comparatively in Table 7.

The sample materials are always prepared according to the same principle: the chemicals dried at 500°C (1000°C for MgO) are mixed in a mortar and decarbonated at 1000°C for >12h. The mixture is melted at 1600°C for 30 min in an iron-saturated platinum crucible and then quenched in a water bath. The resulting glass is pulverised, ground into powder and melted again at 1600°C for 30 min. This process is repeated a second time to homogenize the resulting glass. Subsequently, the compositions are tested using the µ-XRF as well as the EDX detector of our scanning electron microscope.

Table 7: Compositions of the experiments of Rapp and Draper (2018) (top) compared to the compositions used for our study (bottom). All compositions are based on the LPUM (Longhi, 2006, top-left)

Name	LPUM	L-PC1	L-PC3	L-PC5	L-PC8	L-PC10	L-PC14	L-PC16	L-PC20	L2-GM21	L-GM24	L-GM25
P (Gpa)		4	3	2,5	2	1,6	1,2	0,8	0,5	0,0001	0,0001	0,0001
T (°C)		1800	1700	1600	1550	1450	1325	1250	1150	1050	1025	1000
SiO_2	**45,70**	45,70	47,22	47,96	48,86	51,53	50,47	47,45	47,91	46,14	45,83	44,49
TiO_2	**0,15**	0,15	0,20	0,22	0,25	0,33	0,41	0,51	1,36	2,51	3,73	4,04
Al_2O_3	**4,13**	4,13	5,45	6,11	6,95	8,85	10,73	12,59	15,89	11,20	8,73	7,77
FeO	**8,11**	8,11	8,94	9,35	9,75	9,24	9,75	11,75	15,53	22,74	25,93	28,14
MnO	**0,12**	0,12	0,13	0,14	0,14	0,14	0,11	0,02	0,27	0,36	0,42	0,55
MgO	**38,23**	38,23	33,45	31,09	28,25	22,64	19,43	16,23	6,15	4,29	2,59	1,77
CaO	**2,94**	2,94	3,86	4,32	4,90	6,25	8,02	10,06	11,01	10,03	10,01	10,03
Na_2O	**0,10**	0,10	0,13	0,15	0,17	0,22	0,29	0,37	1,28	1,64	1,10	0,92
K_2O	**0,01**	0,01	0,01	0,01	0,02	0,02	0,03	0,05	0,08	0,06	0,06	0,07
P_2O_5	**0,01**	0,01	0,01	0,01	0,02	0,02	0,03	0,03	0,48	1,01	1,57	2,20
Cr_2O_3	**0,50**	0,50	0,59	0,63	0,69	0,76	0,73	0,93	0,04	0,02	0,01	0,01
Total	**100,00**	**100,00**	**100,00**	**100,00**	**100,00**	**100,00**	**100,00**	**100,00**	**100,00**	**100,00**	**100,00**	**100,00**

Name	LPUM-300	LPUM-285	LPUM-210	LPUM-150	LPUM-100	LPUM-075	LPUM-050	LPUM-030	LPUM-020
P (Gpa)	3,00	2,85	2,10	1,50	1,00	0,75	0,50	0,30	0,20
T (°C)	1700	1680	1550	1440	1290	1230	1150	1050	1025
SiO_2	47,22	47,45	48,68	51,27	48,96	47,53	47,91	46,14	45,83
TiO_2	0,20	0,21	0,24	0,35	0,46	0,65	1,36	2,51	3,73
Al_2O_3	5,45	5,65	6,78	9,32	11,66	13,13	15,89	11,20	8,73
FeO	8,94	9,06	9,67	9,37	10,75	12,37	15,53	22,74	25,93
MnO	0,13	0,13	0,14	0,13	0,07	0,06	0,27	0,36	0,42
MgO	33,45	32,74	28,82	21,84	17,83	14,58	6,15	4,29	2,59
CaO	3,86	4,00	4,78	6,69	9,04	10,22	11,01	10,03	10,01
Na_2O	0,13	0,14	0,17	0,24	0,33	0,52	1,28	1,64	1,10
K_2O	0,01	0,01	0,02	0,02	0,04	0,05	0,08	0,06	0,06
P_2O_5	0,01	0,01	0,02	0,02	0,03	0,10	0,48	1,01	1,57
Cr_2O_3	0,59	0,60	0,68	0,75	0,83	0,78	0,04	0,02	0,01
Total	**100**	**100**	**100**	**100**	**100**	**100**	**100**	**100**	**100**

Figure 46 shows the chemical development of the compositions. In general, the magnesium content decreases, while iron and calcium accumulate. This also applies to the aluminium at the beginning. Later, crust formation sets in and aluminium is removed from the system through plagioclase crystallisation. The magnesium number ($Mg\# = Mg/(Mg+Fe)$) is steadily decreasing.

This parameter can be used to estimate the differentiation of rocks. While granite is around ~0.35, ultramafic rocks such as dunite have a magnesium number of ~0.95. The compositions used here range from ~0.84 to ~0.09.

Minor elements such as chromium, titanium, manganese, sodium, potassium and phosphorus are hardly present at the beginning, but accumulate more and more towards the end of the series.

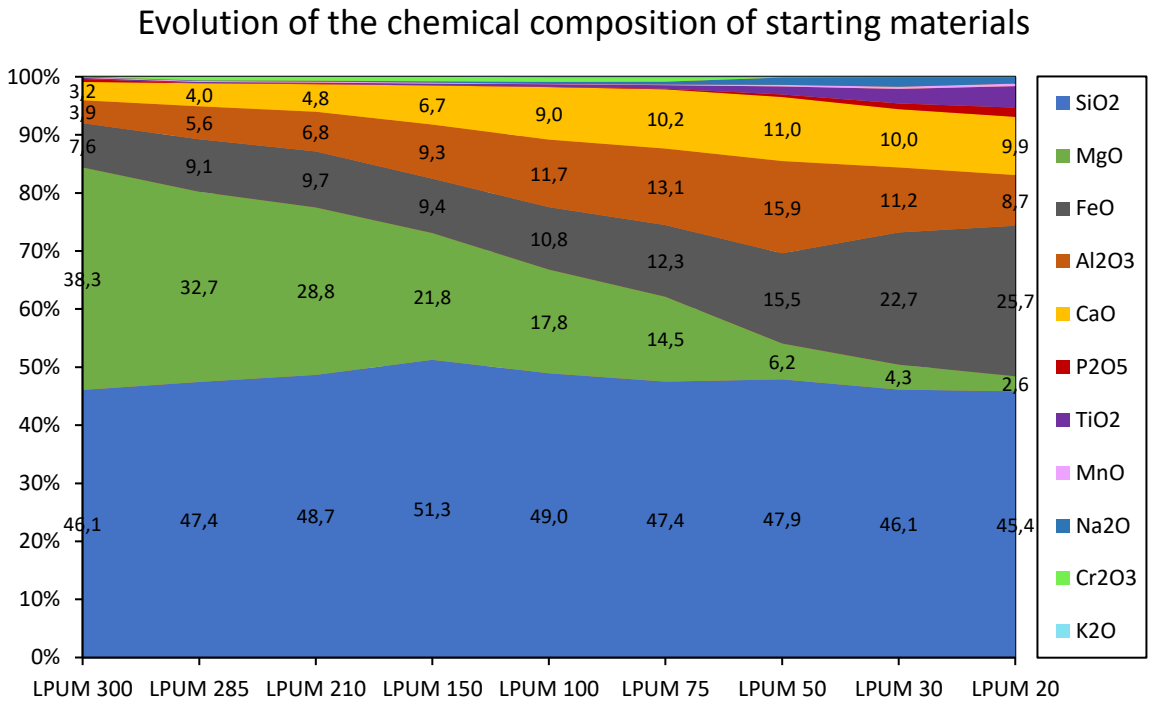


Figure 46: Composition of the starting materials for the indexed experiments.

2.4.6 Characterisation of the starting melts

Sometimes, rocks cannot be practicably classified by their mineral content and a chemical classification is used. For magmatic rocks, the alkalis of the composition (Na_2O, K_2O) are plotted against the silicate content (SiO_2) (TAS plot, Figure 47).

The compositions used as starting material in this work can be consistently described as basaltic in the sense of this method. As the crystallisation of the LMO progresses, the SiO_2 content is expected to increase until it decreases again from experiment LPUM 150 onwards. The reason for this is the crystallisation of pyroxenes and later plagioclase compared to the previously olivine-dominated compositions reported in Rapp and Draper (2018). The alkali content is consistently low and never exceeds 2%. A clear increase can only be observed from experiment LPUM 075 onwards.

Another tool to show the evolution of magmatic rocks is the AFM plot (A = Na_2O+K_2O, F = $FeO+Fe_2O_3$, M = MgO) (Figure 48). Here, the three components A, F and M are normalised, which are important parameters of magmatic rocks. Other chemical components of the composition such as SiO_2 or Al_2O_3 are therefore not considered.

From this, the development of the LMO is clearly outlined: The melt, which is dominated by magnesium at the beginning, is enriched with iron with each additional percent of crystallisation. Towards the end of the crystallisation of the LMO, this should lead to the formation of metal oxides. Meanwhile, alkalis hardly play a role in the chemical composition but increase slightly to the end of the series.

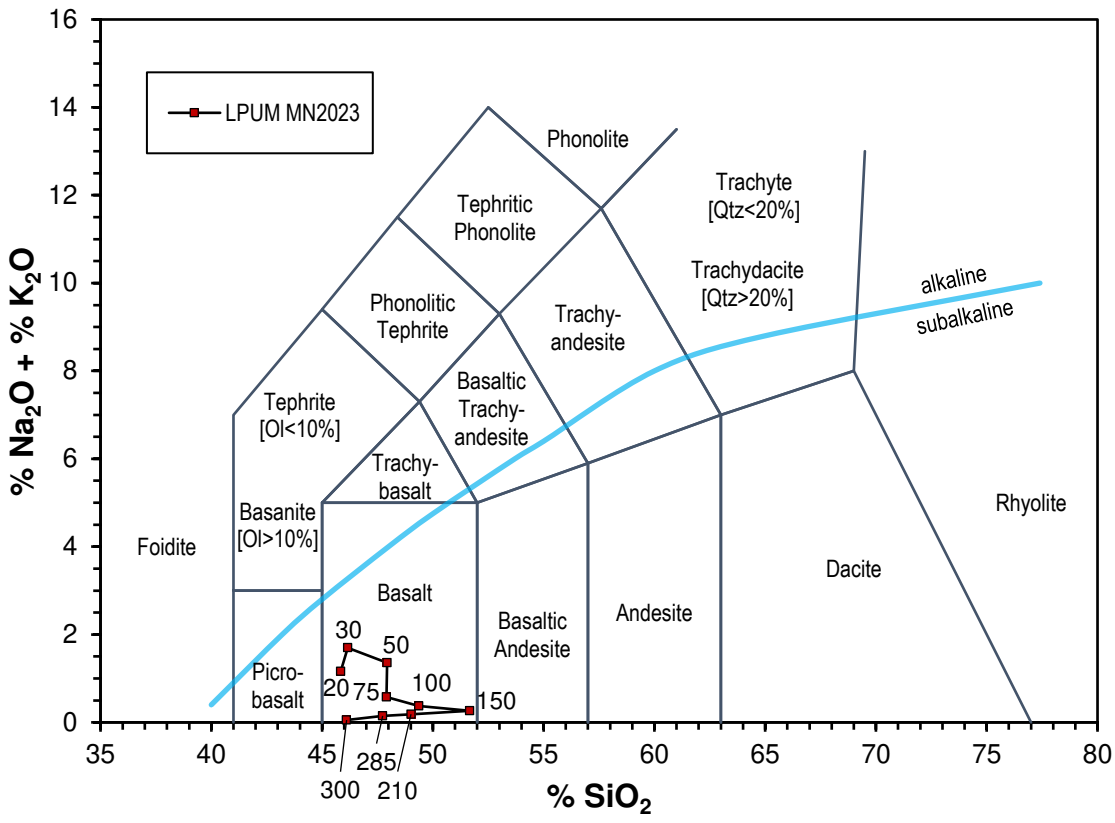


Figure 47: Initial compositions of the experiments in the TAS diagram. The compositions can be described as basaltic throughout.

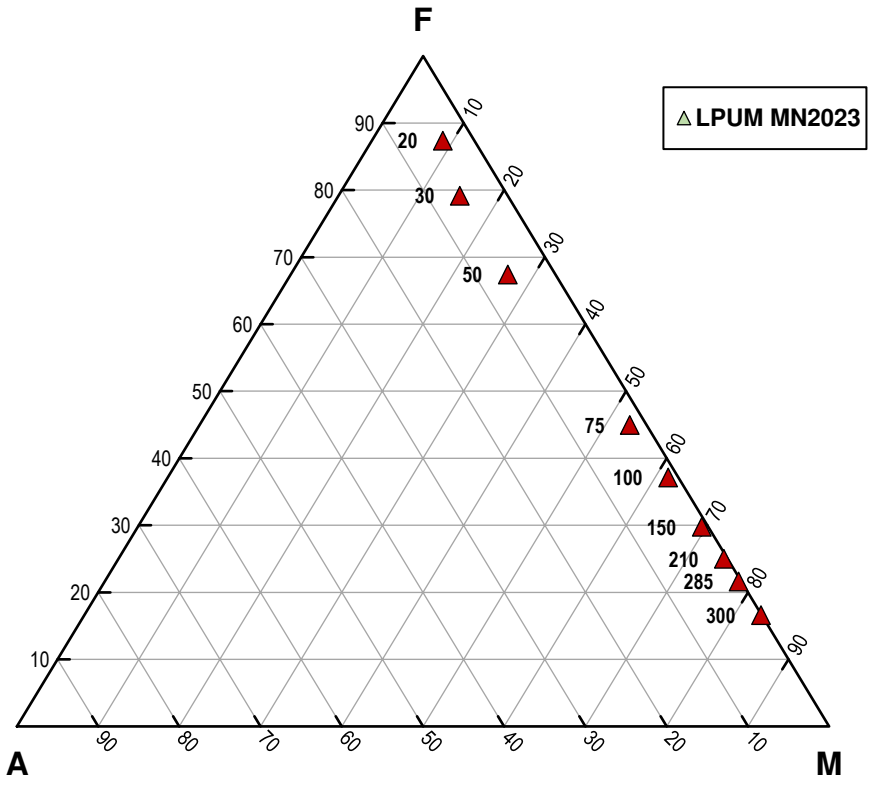


Figure 48: Initial compositions of the experiments in the AFM plot

2.4.7 Water

Of all quantities considered, water is the most difficult to adjust. Reducing conditions shift the H_2/H_2O ratio in favour of H_2. Hydrogen, however, escapes the capsule very easily because its small size allows it to diffuse through most materials virtually unimpeded. Therefore, the transport pathway out of and into the capsule must be inhibited. Truckenbrodt et al. (1997) reported, that a jacket of BN around the sample inhibits the diffusion of hydrogen out of and into the sample capsule and can thus keep the water content stable for up to 3 days. BN was therefore considered as a main component of our self-designed piston-cylinder-press assembly.

The first experiments planned for our experimental series have to be very dry to replicate the initial conditions in the LMO of 50 to 100 ppm. Therefore, starting material devoid of water must be generated, which is not trivial, considered even nominally dry produced glass has a water content of a few hundred ppm. The reason for this is an equilibrium with air humidity during the melting process, which cannot be prevented in normal melting furnaces. To nevertheless produce sample material for the first, very dry experiments, a melting furnace developed by Dr. Andreas Kronz (GZG) was tested in which the material can be heated to high temperature while surrounded by an argon atmosphere.

2.4.8 Melting tests in a graphite furnace under Argon atmosphere

The graphite furnace of the Geochemistry Department at the GZG is a graphite tube held in a gas stream of argon. The sample hangs as a moist powder in the loop of a molybdenum wire inside of this tubing. If a current is now applied to the tube, temperatures of up to 3000°C can be generated (Figure 49). The sample equilibrates with the intrinsic water content of the high-purity argon, which is considerably lower than in air. The sample can be released via an electromagnet so that it drops out of the vertical graphite tube into a water tank where it is quenched to glass (Figure 50 & Figure 51).

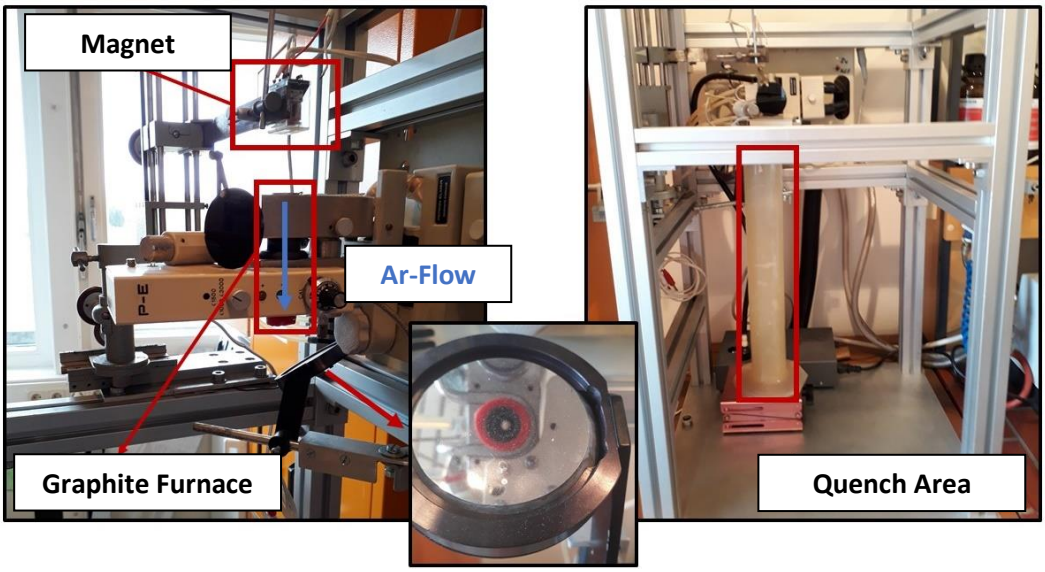


Figure 49: Structure of the Geochemistry Graphite Furnace (GZG)

As a disadvantage of this method, only very small sample volumes of one to two cubic millimetres can be produced at a time. Furthermore, volatile elements such as sodium degas easily due to the high temperatures. At the same time, molybdenum and tungsten diffuse from the wire loop into the sample and contaminate it (Table 8). As an alternative, iridium wire could be used, but this is incredibly expensive.

Table 8: Molybdenum and tungsten contamination of the samples due to the melting process in the graphite furnace. (Measurement: micro-XRF, Bruker Tornado M4, GZG)

Spektrum	Mo	W	MgO	Al2O3	SiO2	CaO	TiO2	Cr2O3	MnO	Fe2O3
LPUM_2000C_Glas 015.spx	0.33	0.04	40.32	3.76	43.76	3.10	0.17	0.46	0.13	7.93
LPUM_2000C_Glas 014.spx	0.33	0.04	40.30	3.81	43.68	3.10	0.17	0.47	0.13	7.97
LPUM_2000C_Glas 013.spx	0.35	0.03	40.41	3.81	43.83	3.11	0.17	0.45	0.13	7.71
LPUM_2000C_Glas 012.spx	0.27	0.04	40.27	3.82	43.85	3.15	0.17	0.46	0.13	7.85
LPUM_2000C_Glas 011.spx	0.31	0.04	40.44	3.78	43.76	3.09	0.17	0.45	0.13	7.83
LPUM_2000C_Glas 010.spx	0.23	0.04	40.51	3.80	43.67	3.13	0.17	0.46	0.13	7.86
LPUM_2000C_Glas 009.spx	0.33	0.04	40.51	3.81	43.66	3.10	0.17	0.45	0.13	7.82
LPUM_2000C_Glas 008.spx	0.31	0.04	40.57	3.81	43.59	3.11	0.17	0.45	0.13	7.82
LPUM_2000C_Glas 007.spx	0.29	0.04	40.71	3.88	43.58	3.15	0.17	0.45	0.12	7.61
LPUM_2000C_Glas 006.spx	0.24	0.04	40.61	3.80	43.68	3.14	0.18	0.45	0.13	7.75
LPUM_2000C_Glas 005.spx	0.26	0.04	40.67	3.94	43.53	3.14	0.17	0.45	0.13	7.69
LPUM_2000C_Glas 004.spx	0.26	0.04	40.51	3.89	43.56	3.19	0.18	0.45	0.13	7.79



Figure 50: Graphite furnace of the geochemistry department at the GZG. Left: Sample hanging on a Mo wire in a graphite tube at ~2300°C under argon atmosphere. Middle: The wire is unclipped and the sample falls out of the argon stream into a water column. Right: The sample cools down in a few 100ms and solidifies into glass.

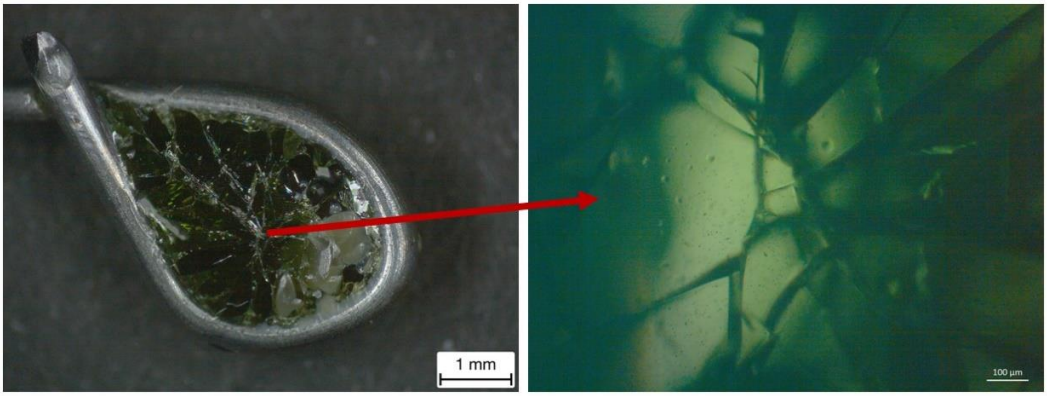


Figure 51: Mo-loop with sample after the experiment: The majority of the sample has solidified into a glass, in which, however, the first microcrystallites can be found as well as some larger forsterites in the lower area of the loop.

For comparison, a sample with a well-known water content from the departmental stock was exposed to this process. By IR spectroscopy before and after the experiment, it was found that the water content was reduced from approximately 300 ppm (standard melting furnace in air) to 47ppm (melting under argon atmosphere) (Figure 52).

The method has proven viable for producing dry samples, but at the same time changes the chemistry of the volatile elements with simultaneous contamination with molybdenum and tungsten. This method was therefore not used to prepare starting materials. Instead, nominal dry glasses were used.

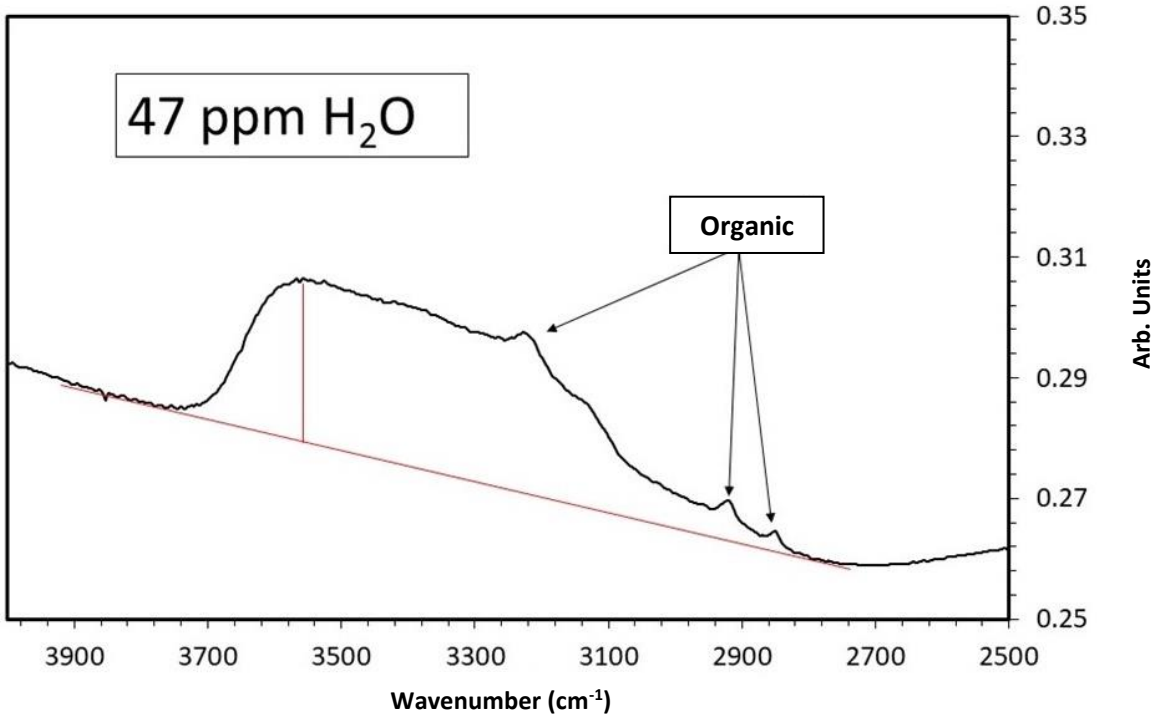


Figure 52: IR spectrum of the OH band of a sample with known water content. The water content no longer corresponds to the previously measured 300 ppm but has dropped to ~47ppm.

2.5 Carrying out the experiments

The following chapter will describe how the experiments are carried out. This study follows the experimental series of Rapp and Draper (2018) which agrees well with the model of Garcia et al. (2011) in its P-T conditions (Figure 53, Table 9).

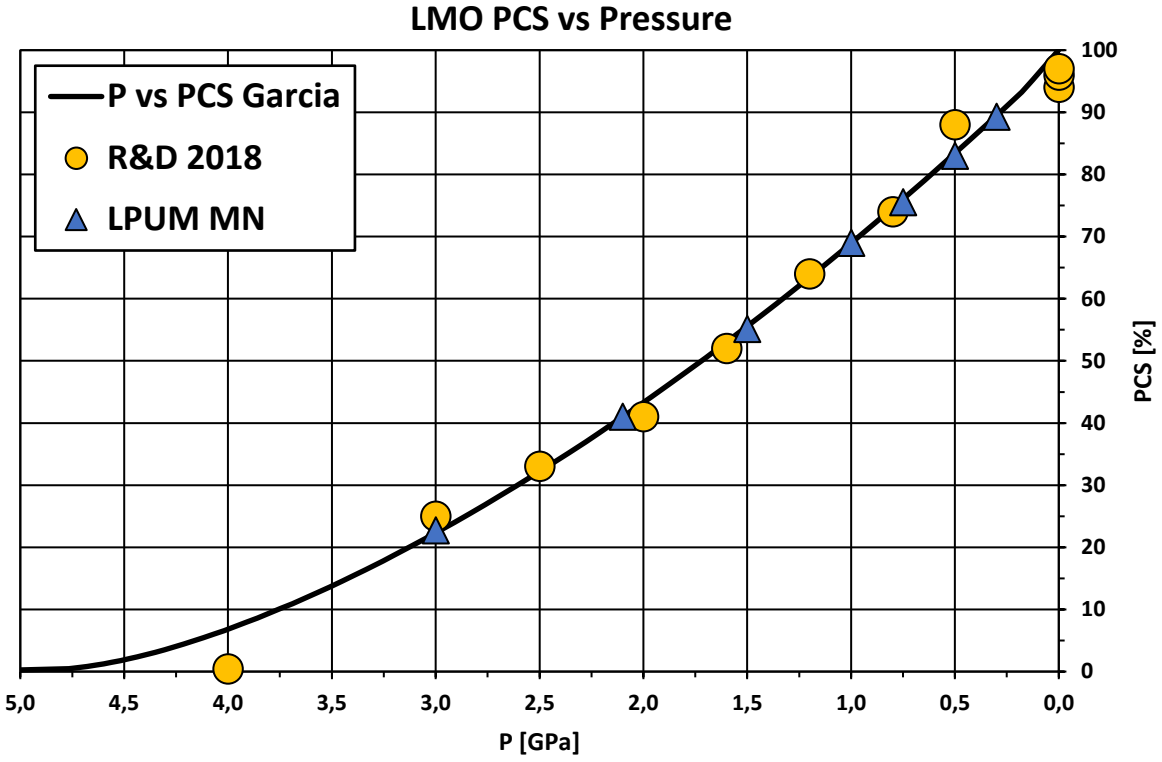


Figure 53: Relationship between PCS and pressure for the lunar model of Garcia et al. (2011), Rapp and Draper (2018) and this study.

Table 9: Experimental conditions of the experiments by Rapp and Draper (2018)

P (Gpa)	4	3	2.5	2	1.6	1.2	0.8	0.5	0.0001	0.0001	0.0001
T (°C)	1800	1700	1600	1550	1450	1325	1250	1150	1050	1025	1000
t (h)	0,5	1	3	6	6	12	24	24	46	88	87
PCS (result)	25	33	41	52	64	74	88	94	96	97	99.5

The only deviation are the experiments at pressure <0.5 GPa and pressure >3 GPa. Since our piston-cylinder-press is limited to 3 GPa, our first experiment, our series starts from there and continues with P- T conditions based on the model of Garcia et al. (2011). We do not share the assessment of Rapp and Draper (2018) that the pressure below 0.5 GPa is no longer important and can be set to 1 bar. The final melt of LMO crystallisation occurs below the 30-60 km thick lunar crust formed by upwelling plagioclase during crystallisation.

Thus, the crystallisation front never reaches the surface but ends at pressure conditions of 0.2 to 0.3 GPa. Therefore, for this study, all experiments below 0.5 GPa were performed under pressure in an internally heated pressure vessel (IHPV) at 0.2 to 0.3 GPa rather than ambient pressure.

The duration of the experiments at high temperature was kept relatively short, as equilibrium is quickly reached. As the series progressed, the time of the experiments was increased to 24h.Some experiments had severe problems and had to be terminated early, resulting in lower run durations. An overview of the conditions can be found in Table 10.

Table 10: Overview of the successful LPUM experiments. For all experiments, a B-type thermocouple in Al_2O_3 conduction was used.

Name	Sample	Capsule	Buffer	T [°C]	P [Gpa]	t [h]	Method	Remarks
LPUM 300-1	LPUM 1	Pt	C	1600	3,00	1,5	PCP	-
LPUM 285-2	LPUM 285	Fe	Cr/Cr2O3 in Pt	1550	2,10	2,0	PCP	-
LPUM 210-2	LPUM 210	Fe	Cr/Cr2O3 in Fe	1550	2,10	6,0	PCP	-
LPUM 210-3	LPUM 210	Mo	Mo (Capsule)	1650	2,10	1,0	PCP	loss of contact
LPUM 210-4	LPUM 210	Mo	Mo (Capsule)	1625	2,10	1,0	PCP	loss of contact
LPUM 150-1	LPUM 150	Fe	Cr/Cr2O3 in Pt	1440	1,50	24,0	PCP	buffer leaked
LPUM 150-3	LPUM 150	Fe	Cr/Cr2O3 in Pt	1440	1,50	16,0	PCP	2 µl H2O in buffer
LPUM 100-1	LPUM 100	Fe	Cr/Cr2O3 in Pt	1290	1,00	2,0	PCP	-
LPUM 075-1	LPUM 075	Fe	Cr/Cr2O3 in Pt	1230	0,75	3,5	PCP	-
LPUM 050-1	LPUM 050	Fe	Cr/Cr2O3 in Pt	1150	0,50	24,0	PCP	-
LPUM 030-1	LPUM 1bA	Pt	Cr/Cr2O3 in Pt	1050	0,30	24,0	IHPV	-
LPUM 030-2	LPUM 1bA	Pt	Cr/Cr2O3 in Pt	1050	0,30	24,0	IHPV	Pt Fe-saturated
LPUM 020-1	LPUM 1bB	Pt	Cr/Cr2O3 in Pt	1025	0,20	2,0	IHPV	2 µl H2O in buffer

For each experimental run, the prepared assembly was coated with MoS paste and rolled in MoS powder. After insertion into the bomb, a copper plate was placed underneath the assembly to insure optimal electrical contact. The bomb was mounted in the piston-cylinder-press where 72-80t of end load was applied to the stack. Cooling water, electricity and thermocouple were then connected. After initial pressurisation of 0.3 GPa, an automated heating ramp at 40°C/min was initialized while pressure was manually adjusted linearly with temperature until the target values were reached.

The initial pressure loss due to deformation of the assembly was manually readjusted within the first hour and later automatically maintained at +/- 200 bar by a screw press. The displayed temperature showed a maximum deviation of +/-2°C, whereas the real error has been significantly greater due to the spatial distance between sample and sensor.

At the end of the intended duration or in case of serious problems (e.g. severe water leakage, power deviation of the furnace), the experiments were quenched by switching off

the power supply at an estimated 150°C/s. To avoid cracking of the samples, depressurisation was accomplished by the screw press at slow rates. The assemblies were then pressed out of the bomb and the sample capsules could be recovered.

2.5.1 Sample preparation

To prepare the samples for analysis, they were sawn into halves using a wire saw (0.3 mm wire, 20 µm diamond trim; Figure 54). This method minimises material loss through sawing compared to classical saw blades and puts less stress on the occasionally fragile samples.

The capsule halves obtained were embedded in epoxy resin tablets and, after hardening, prepared with fine abrasive paper for subsequent polishing using a 1 µm diamond paste. The polished samples were degassed in a vacuum drying oven at 80°C for at least 24 h and then carbon coated. The samples were stored in an airtight cabinet with desiccant until analysis.



Figure 54: Specimen capsule attached to specimen holder with Crystal Bond (top left), sawing process with diamond-coated wire (top right) and split specimen capsules before polishing (bottom left) and in the SEM (bottom right).

2.6 Analytical Methods

2.6.1 Scanning electron microscope JEOL JSM-IT500



Figure 55: JSM-IT500 InTouchScope™ SEM of the GoeLem Laboratory of the GZG

The main analysis of the LMO samples was carried out with a scanning electron microscope (SEM) of the type JSM-IT500 InTouchScope™ from JEOL (Figure 55). In electron microscopy, an electron beam is generated via an electron source (here: tungsten filament). This is focused on the sample via various electron-optical lenses and apertures (Figure 56). When the electrons hit the sample, they interact with the material. Among other interactions, secondary electrons and backscattered electrons are produced. The former provide information about the surface morphology, while the amount of the latter depends on the atomic masses and thus, densities. This is particularly useful for our samples, as it makes different mineral compositions visible despite the smoothly polished sample surface. By scanning the sample with the electron beam, an image is finally generated from the point information. In addition, characteristic X-ray radiation is produced during the interaction between sample and electron beam. Its energy is directly dependent on the respective elements, which is why an EDX detector (here: Oxford Instruments) enables a chemical analysis of the specimen in the micrometre range. Element distribution maps can also be created. The JSM-IT500 InTouchScope™ uses has an accelerating voltage of 0.3-30 kV with an energy resolution of 127 eV (Mn Kα).

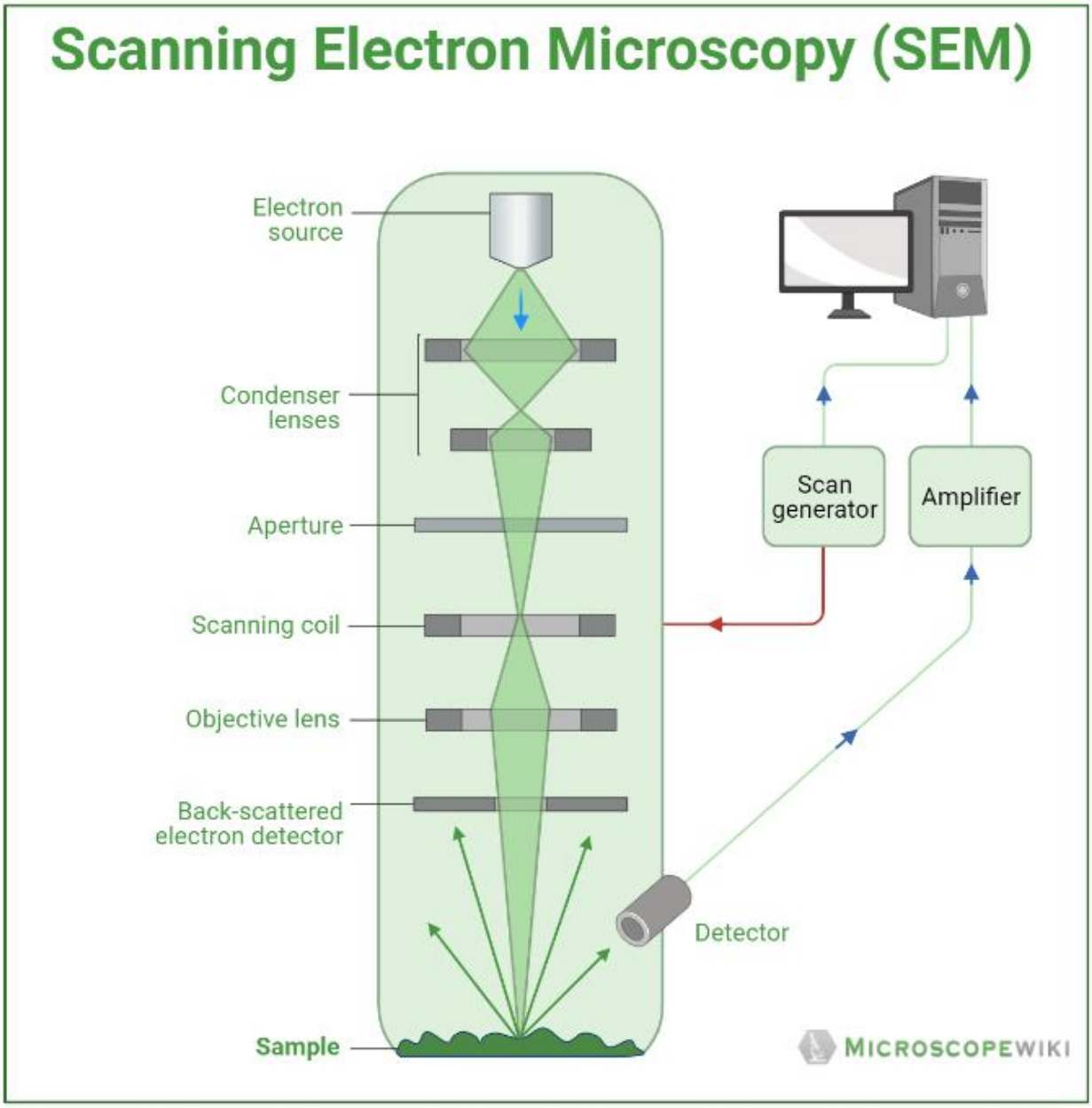


Figure 56: Schematic representation of the internal structure of an SEM (credit; https://microscopewiki.com/scanning-electron-microscope/)

2.6.2 µ-XRF Bruker "M4" Tornado

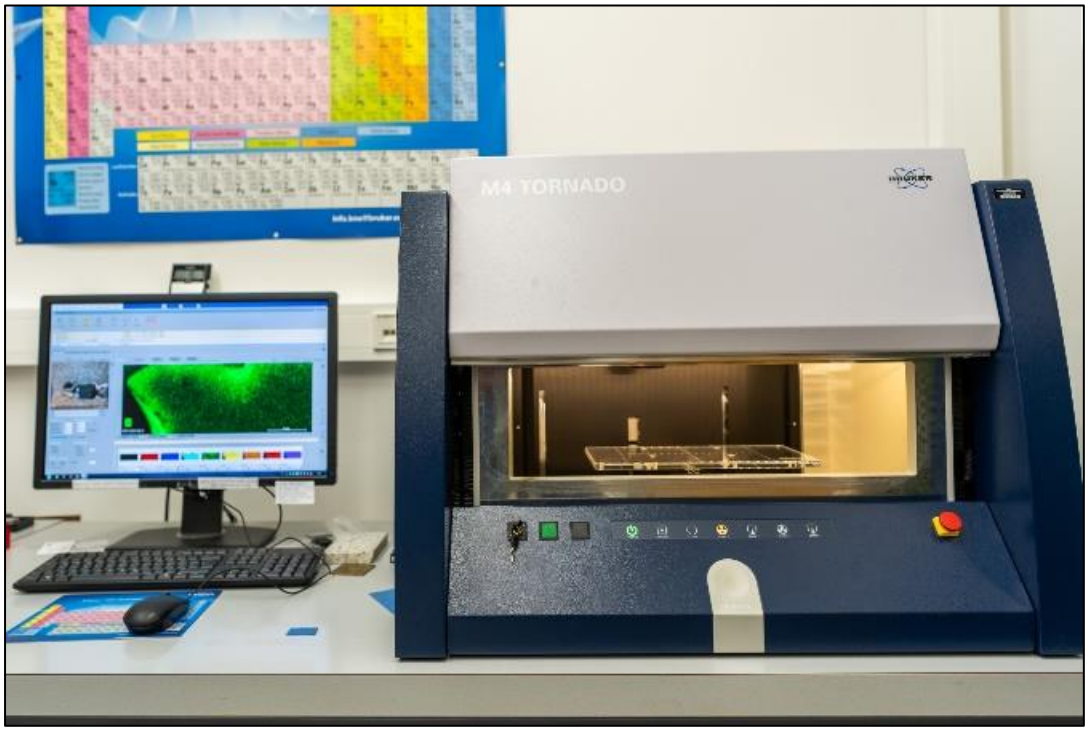


Figure 57: Micro X-ray fluorescence spectrometry (Micro-XRF) Bruker M4 TORNADO of Mineralogy Göttingen (image: Max Schanofski)

The composition of the starting glasses was determined by micro X-ray fluorescence analysis (µ-XRF) on a Bruker M4 "TORNADO" (Figure 57). For this method, an X-ray beam is focused in a 20 mbar vacuum chamber through capillary optics onto a 20 µm measuring spot (Figure 58).

The characteristic fluorescent radiation produced by the interaction between radiation and the atomic shell of the respective elements is recorded as a spectrum via a silicon drift detector. In an iterative process, the software then calculates the most probable composition that produced this spectrum and outputs it as a result.

A major advantage of the method is the low time and preparation effort as well as the small measuring spot compared to other fluorescence methods. The method also dispenses with reference standards, which reduces the effort at the cost of a further reduced accuracy. The device used here was calibrated especially for silicate glass compositions using a microprobe via internal house standards. The deviations were entered into the µ-XRF software using correction factors. For reasons of comparability, the composition of the initial glasses for the LMO experiments was also cross-checked with the EDX detector of the SEM.

The Bruker M4 "Tornado" used here has an X-ray tube with a rhodium target. The accelerating voltage is 50 kV with a beam current of 200 µA (chemical analysis) or 400 µA (mapping).

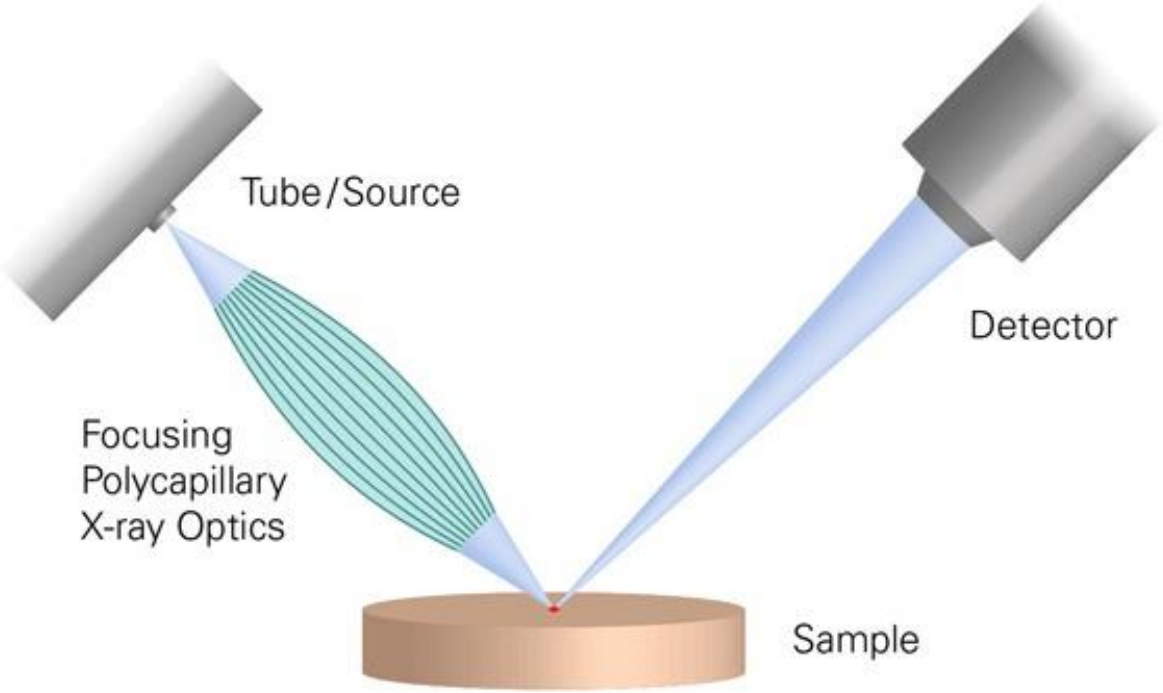


Figure 58: Schematic representation of the X-ray optics of a Bruker M4 "Tornado". (https://www.thetatech.com.tw/attachments/editor/M4/M4_polycapillary_caption.jpg)

2.6.3 IR-spectrometer Hyperion 3000 with ATR unit Bruker Vertex 70



Figure 59: Infrared spectrometer Bruker "Hyperion 3000" (right) with ATR unit "Vertex 70" (left)

All determinations of water content in this work were carried out with an infrared spectrometer of the type "Hyperion 3000" (Figure 59) in transmission. Infrared spectroscopy utilises the fact that molecular bonds tend to oscillate when exposed to light in the infrared range. The energy (and thus wavelength) absorbed for these oscillations is characteristic for the respective bond. The spectrum (I) recorded at the detector can be compared with a reference spectrum without sample (I_0), whereby the absorption spectrum I/I_0 can be calculated.

To determine the water content of a sample, the height of the absorption band is combined with the sample thickness and the absorption coefficient using Lambert-Beer's law (10).

$$E_\lambda = Log_{10}\left(\frac{I}{I_0}\right) = \varepsilon_\lambda * c * d \qquad (10)$$

E_λ describes the extinction, I the intensity of the radiation after passing through the sample, I_0 the initial intensity of the radiation, ε_λ the absorption coefficient, c the substance concentration and d the thickness of the sample.

ATR unit "Bruker Vertex 70":

With the help of the ATR unit "Vertex 70", the mineral composition of powder samples can be analysed, among other applications. ATR stands for Attenuated Total Reflection. The method makes use of totally reflected light forming an evanescent wave. In the Bruker Vertex 70, this is achieved by pressing a diamond onto the powder sample. The evanescent wave formed by total reflection in the diamond penetrates about one wavelength deep, i.e. a few µm, into the sample material and can interact with the matter (Figure 60). As before, the interaction with molecular bonds leads to absorption spectra. The sum of the molecular bonds in a mineral leads to a characteristic fingerprint that can be compared with reference spectra via database matching.

The ATR method was used in this work alongside radiography to identify the mineral content in the calibration samples.

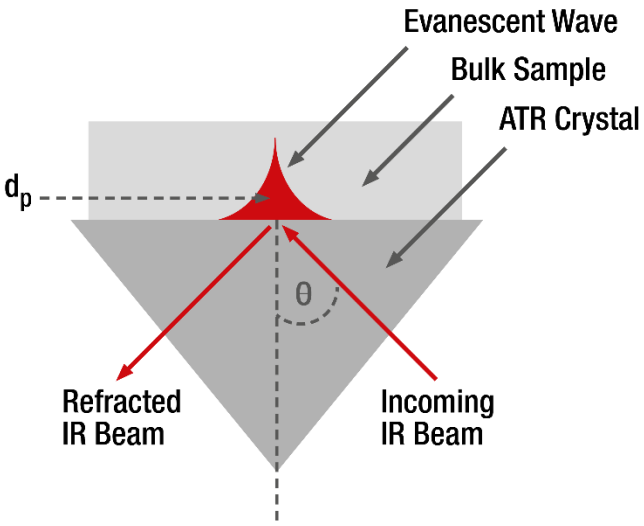


Figure 60: Schematic representation of the evanescent wave by total internal reflection in the ATR crystal (https://wiki.anton-paar.com/ch-de/abgeschwaechte-totalreflexion-atr/)

2.6.4 Raman spectrometer Horiba Jabin-Yvon HR800UV

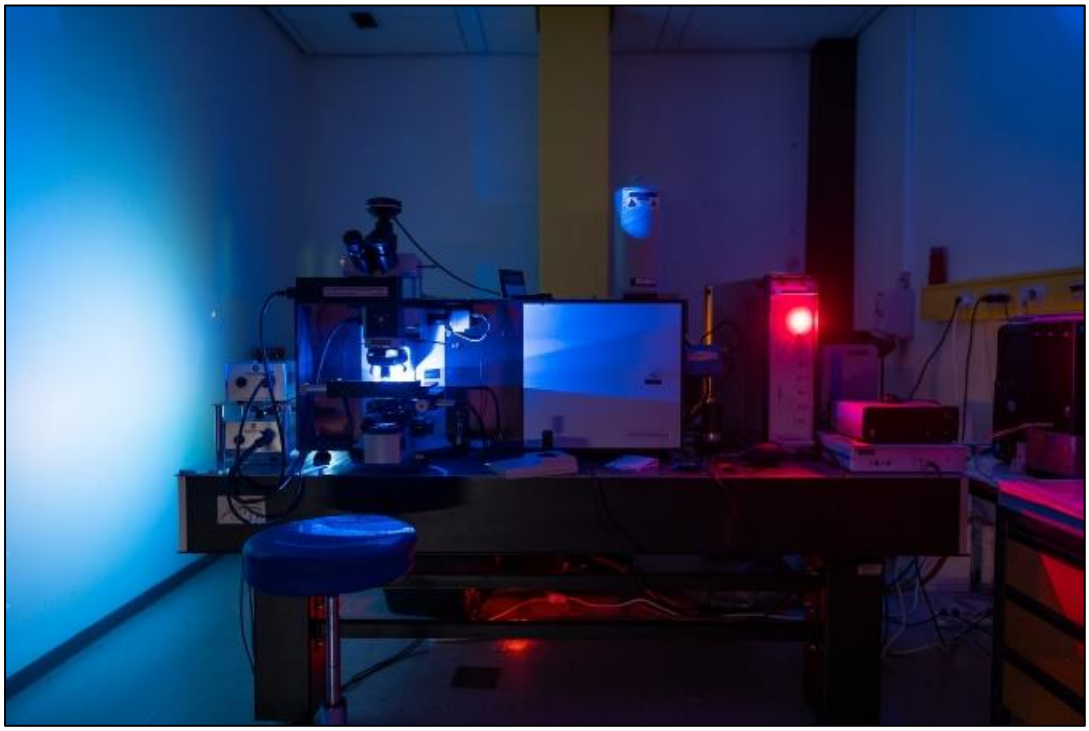


Figure 61: Raman spectroscopy: Horiba Jobin-Yvon Labram HR800UV

A Raman spectrometer utilises the fact that monochromatic light (usually from a laser) is scattered not only elastically (Rayleigh) but also inelastically (Raman). Since Raman scattering is very unlikely, its intensity is a thousand times lower than elastic scattering. In this type of interaction, either the energy of the photon is transferred to the vibrational energy of the molecule (Stokes-Raman scattering) or, conversely, vibrational energy is transferred from the molecule to the photon (anti-Stokes-Raman scattering). As a prerequisite for this effect, the molecules must be polarisable and are referred to as Raman scatterers. Raman spectroscopy is thus complementary to infrared spectroscopy in the nature of the molecular compounds that can be investigated.

The frequency differences of the Raman-scattered photons to the frequency of the monochromatic excitation can be recorded with a suitable detector. The position of the peaks present is mineral-characteristic and can be used via database matching to determine crystals, but also other substances. In the case of crystals, the intensity of the peaks depends on the orientation of the crystal lattice relative to the excitation and is therefore of secondary importance if the orientation is unknown. Besides the identification of substances, the width of the peaks in the spectrogram indicates the

degree of order in the crystal lattice. Very sharp bands testify to well-crystallised minerals, while glasses or disordered crystals appear as broad, smeared bands.

A major advantage of this method is the high spatial resolution (a few µm) when the exciting laser is focussed via a microscope, the low preparation effort and the possibility of obtaining non-destructive material determinations, which is particularly important for art objects.

In this work, the Raman spectrometer was mainly used to screen and identify the mineral content of the LMO samples before chemical analysis on the SEM. A blue laser with a wavelength of 488 nm was used as the monochromatic light source for this purpose.

2.6.5 Melt fraction determination with MATLAB

Electron optical images of our samples show that the minerals obtained are small and of large number. Without computer support, only a rough estimation of the modal ratios of the different phases as well as the melt would be possible. However, the exact proportions of melt and solids determine the degree of crystallisation of the LMO (PCS) and the relative proportions of the minerals to each other determine the composition of the crystallising layer and are therefore of importance.

In order to determine these proportions, a segmentation of the images according to grey levels is necessary. This was done using a self-written script in MATLAB (see Appendix 6.2, Page 248).

For this purpose, the electron-optical image was processed in contrast and brightness in such a way that the components could be distinguished from each other as well as possible. The capsule walls, if present, are always pure white due to their high relative density. Since these would otherwise not be distinguishable from iron spheres in the sample, they were coloured with grey value 0 (black). In the example shown below, the few olivines near the edge of the capsule (Figure 62) were also marked with grey value 20 to better distinguish them from other, dark minerals in the sample.

The programme itself segments according to a predefined principle: All grey values <1 are disregarded as capsule or holes in the sample (Figure 63). Likewise, all grey values >255 (white) represent the fraction of iron beads and/or spinels, as these can only be chemically distinguished from each other.

To separate the other minerals from each other, the script outputs a histogram of the image, which can be used to manually set limits for the following segmentation. The number of boundaries needed is determined by the number of different phases (minerals + melt). This is an iterative process that is repeated until the result is satisfactory. The script outputs the segmented image portions as images and counts the pixels contained in the respective boundaries. The phase proportions can then be calculated by equation 11

$$F_{Phase\ n} = \frac{P_{Phase\ n}}{\sum_{k=1}^{n} P_{Phase\ n}} * 100 \qquad (11)$$

where $F_{Phase\ n}$ corresponds to the phase fraction of the n-th phase in the total mixture and $P_{Phase\ n}$ corresponds to the pixel fraction of the nth phase, while n is determined by the number of phases.

In the example shown, it becomes clear that this procedure is not flawless. This becomes particularly obvious with Figure 66 and Figure 67. For these minerals, the grey values overlap to such an extent that they cannot be clearly segmented from each other. This results in errors in the calculation of the phase fractions, which are, however, still considered to be lower than by merely estimating the values.

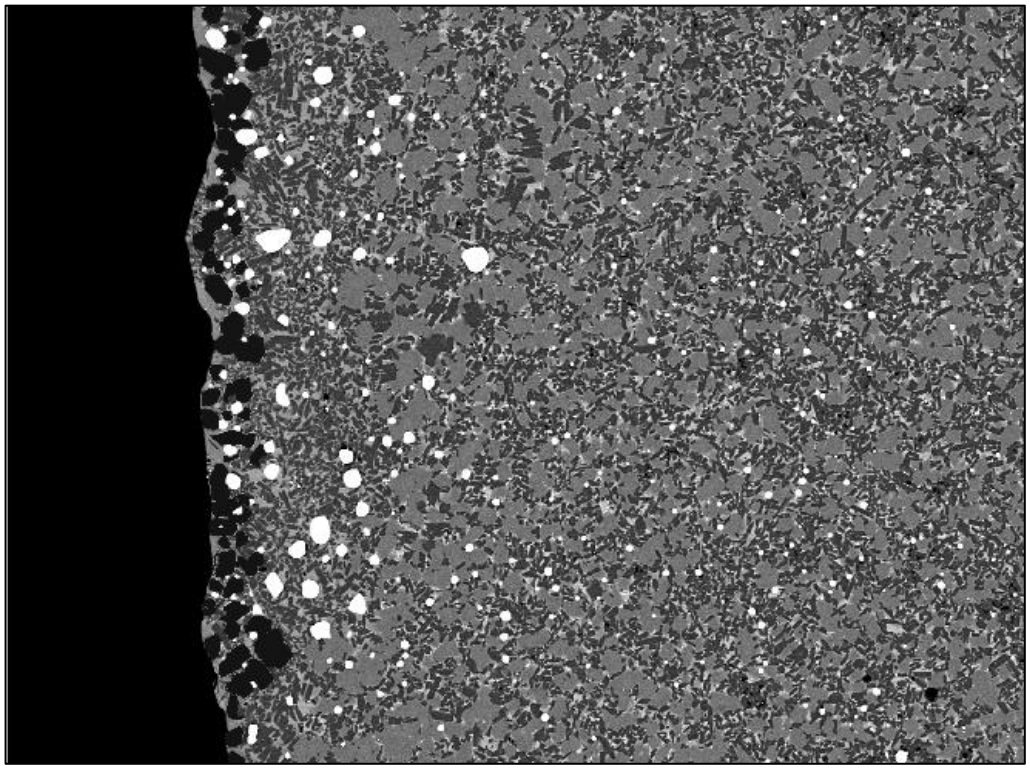


Figure 62: Original image of sample LPUM 050-1, already prepared for segmentation.

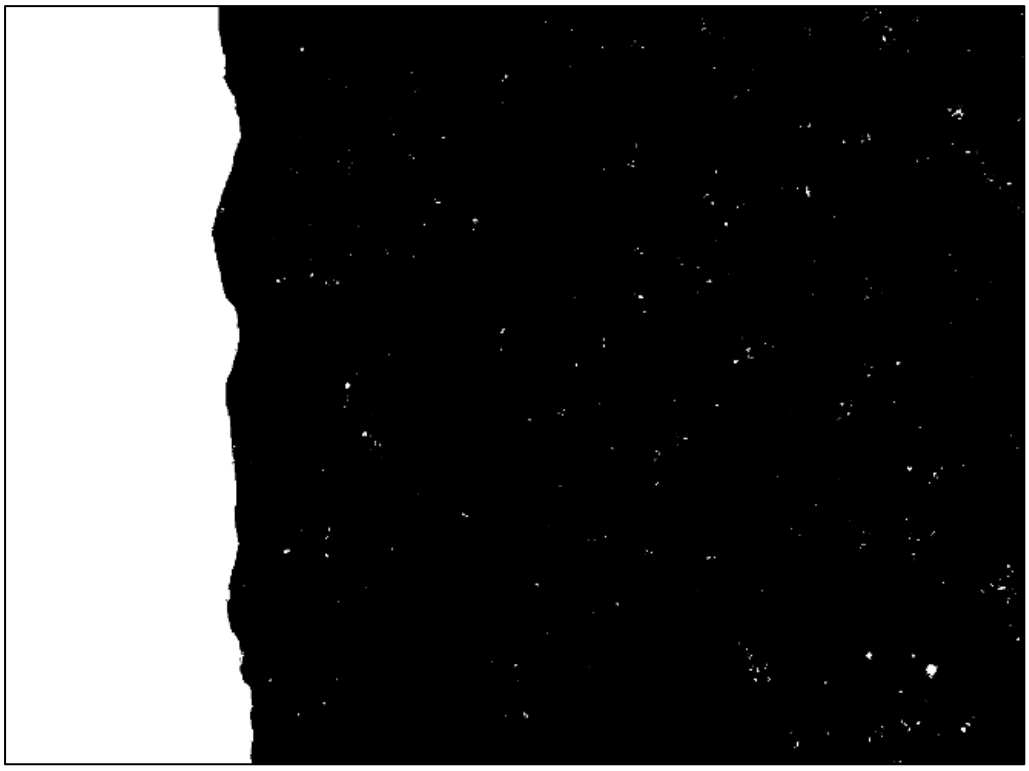


Figure 63: Capsule and holes of sample LPUM 050-1 (grey values 0 - 1)

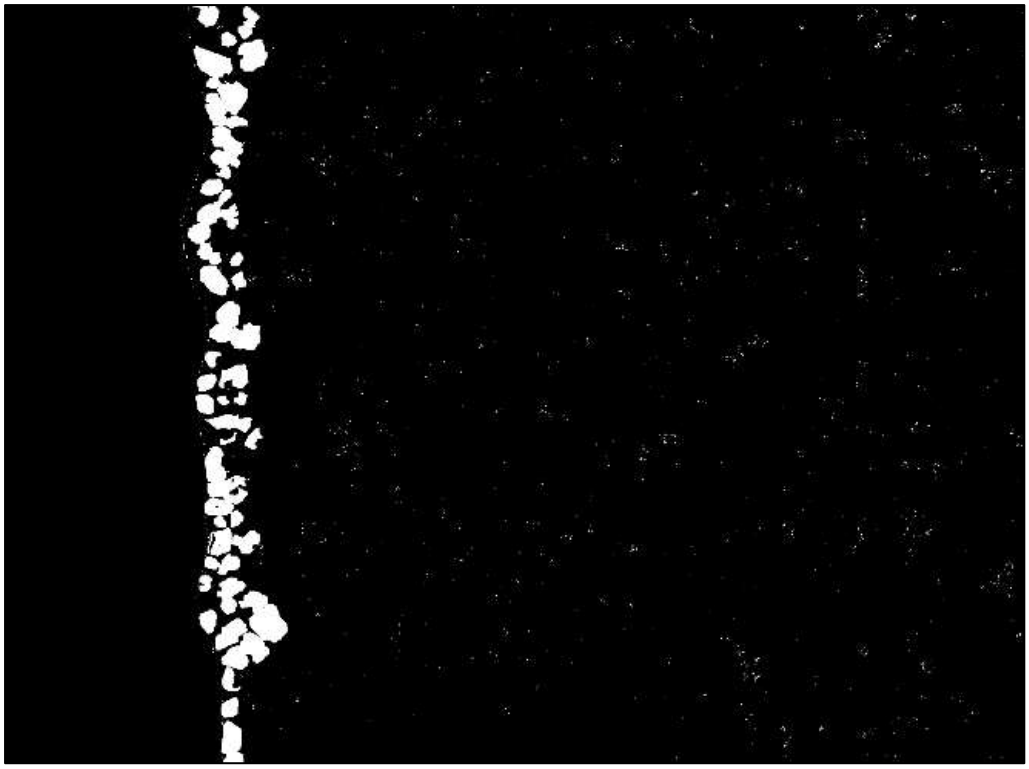


Figure 64: Olivine of sample LPUM 050-1 (grey values 2 - 21)

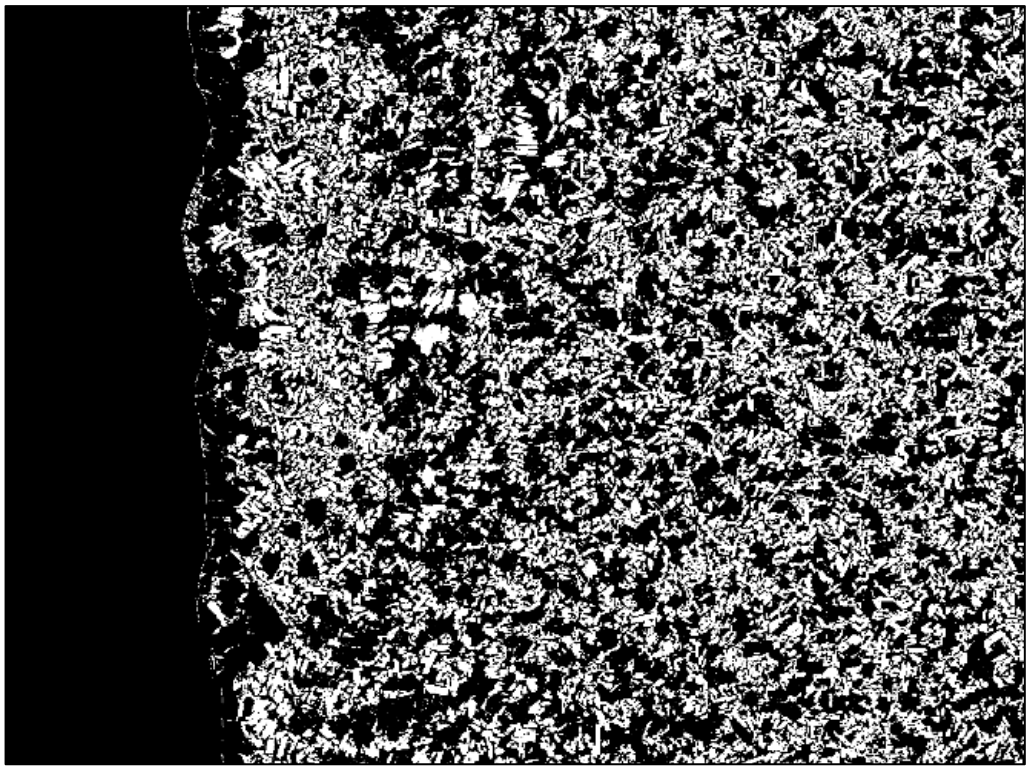


Figure 65: Plagioclase of sample LPUM 050-1 (grey values 22 - 90)

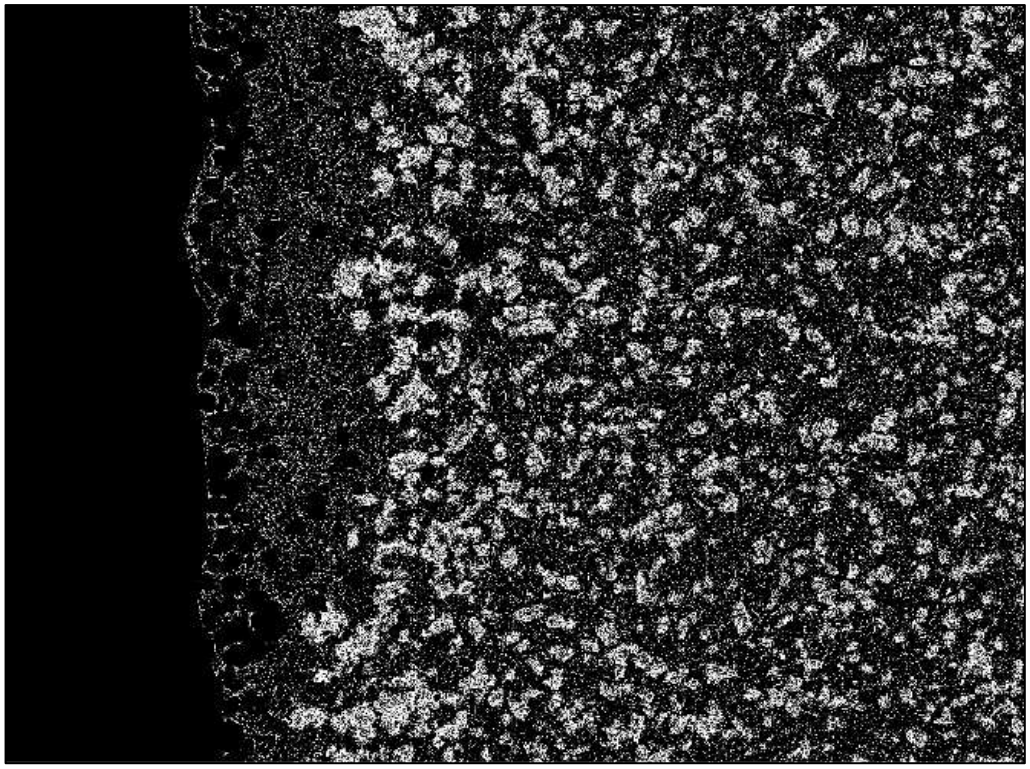


Figure 66: Orthopyroxene of sample LPUM 050-1 (grey values 91- 120)

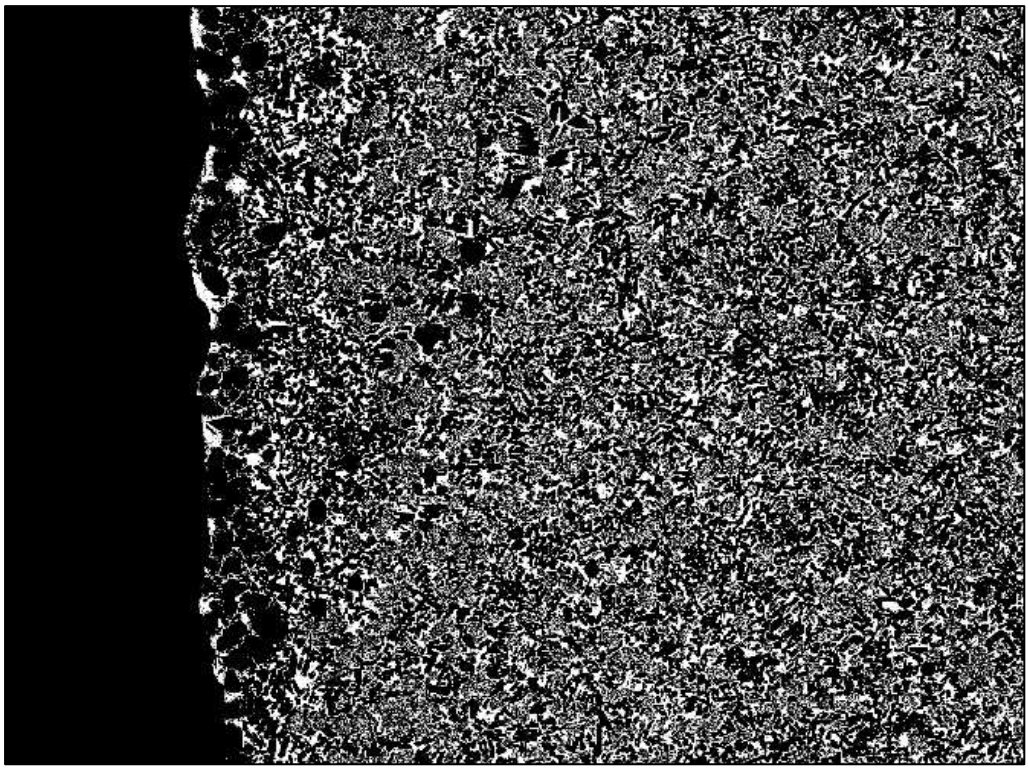


Figure 67: Melt of sample LPUM 050-1 (grey values 121- 254)

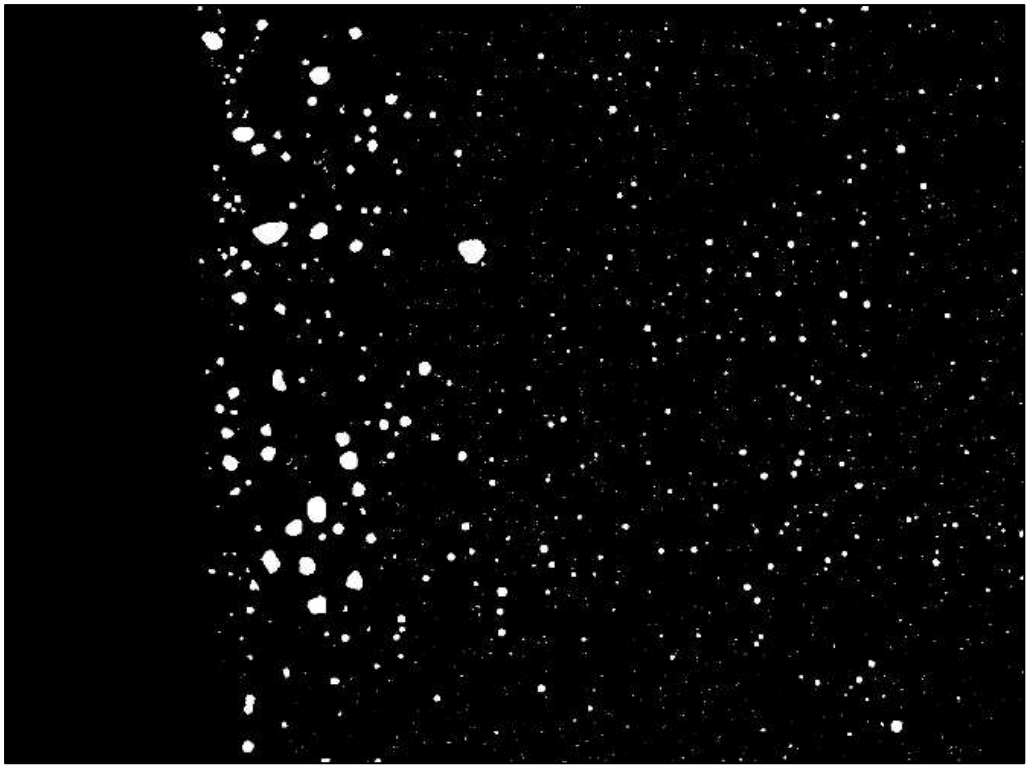


Figure 68: Fe spheres of sample LPUM 050-1 (grey values 255-256)

3 Results

The results of the experiments are described below. For each sample there is an overview with relevant data and a short sample description followed by an overview image of the whole sample and two detail images. This is followed by an overview of the mineral compositions and the greyscale images used to determine the mineral proportions using MATLAB. The analyses on which these data are based on can be found in the Appendix and in the digital supplements.

3.1 LPUM 300-1 // 680 km depth

Method:	PCP	**Pressure**	3.00 GPa	**Temperature**	1600°C
Duration	1.5h	**f(O_2) Buffer:**	C	**Capsule:**	Pt

Oxide	**SiO_2**	**TiO_2**	**Al_2O_3**	**FeO**	**MnO**	**MgO**	**CaO**	**Na_2O**	**K_2O**	**P_2O_5**	**Cr_2O_3**
wt%	46,10	0,17	3,93	7,62	0,13	38,30	3,18	0,05	0,003	0,50	0,02

Melt fraction: 15,3%	**Crystals:** Olivine (57,8%), OPX (42,1%)

LPUM 300-1 has been conducted at 3 GPa and 1600°C and therefore the experiment with the highest P-T conditions of all runs. It is also the only experiment with carbon as f(O_2) buffer instead of the Cr-Cr_2O_3 mixture used later (Figure 71). The high temperature necessitates not using iron as the capsule material, as this would melt, even when an increase of the melting point by pressure is considered. Thus, Platinum was used.

The sample is almost completely crystallised. The melt (15.3%) is only visible as a fine, bright mesh between the minerals (84.7%) (Figure 69 & Figure 74). The minerals are 20 to 150 µm in size. The smooth, somewhat lighter mineral is orthopyroxenes (57.8%), the somewhat darker, rough mineral is olivine (42.1%) (Figure 70 & Figure 75).

The chemical composition of the minerals is very homogeneous. The orthopyroxenes are enstatite with a mean composition of $En_{95.8}Fe_{3.3}Wo_{1.0}$ (Figure 73). The olivine can be characterised as forsterite with a mean composition of $Fo_{96.8}Fa_{3.2}$ (Figure 72). The composition of the melt could not be determined unambiguously, as the fine distribution led to many mixed analyses with the adjacent mineral phases.

In the Raman spectrum of the sample, carbonate signatures can be found frequently, which presumably developed as a reaction between sample material and the carbon buffer. These carbonates could not be clearly identified.



Figure 69: Overview image of sample LPUM 300-1 with outer platinum capsule (white) and carbon as buffer material (black in contact with the sample).

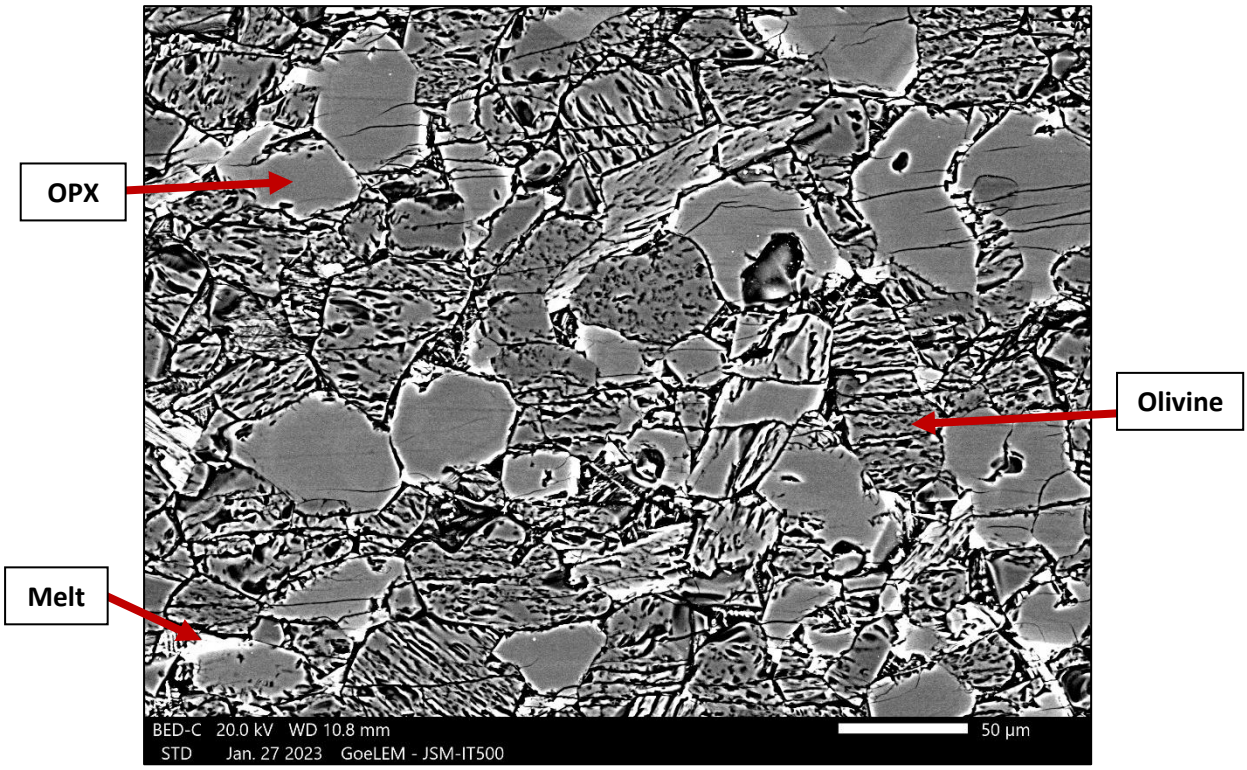


Figure 70: Close-up of sample LPUM 300-1 with pyroxene (grey, smooth), olivine (grey with fractures) and melt (white).

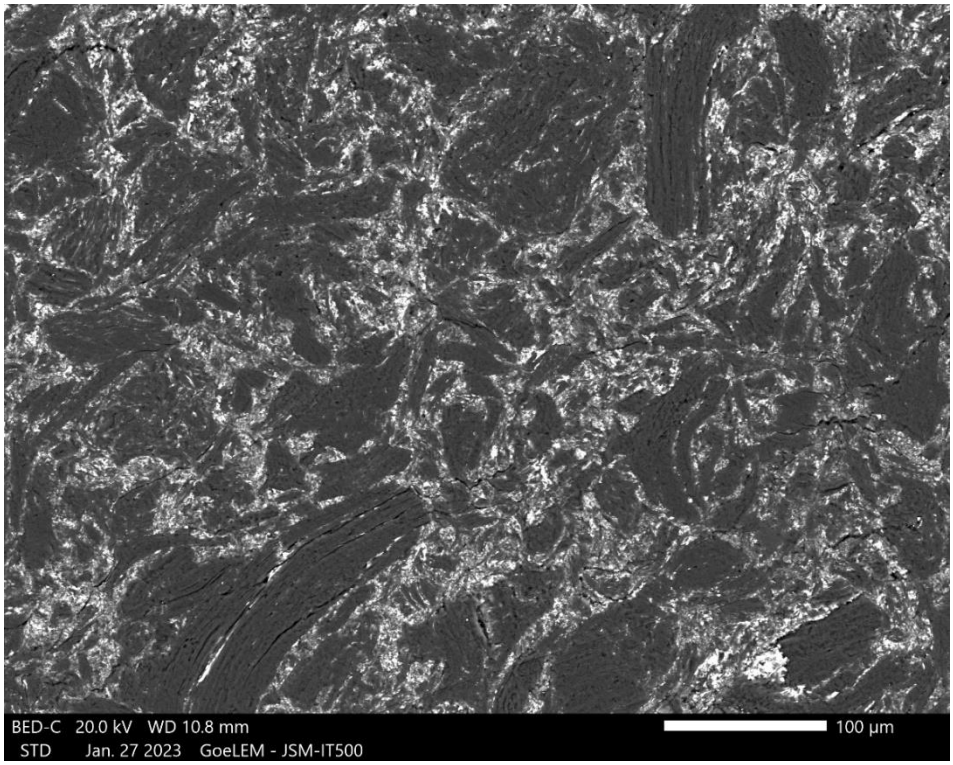


Figure 71: Close-up of the carbon buffer of sample LPUM 300-1. The carbon is black, in between there is lighter siliceous material from sample

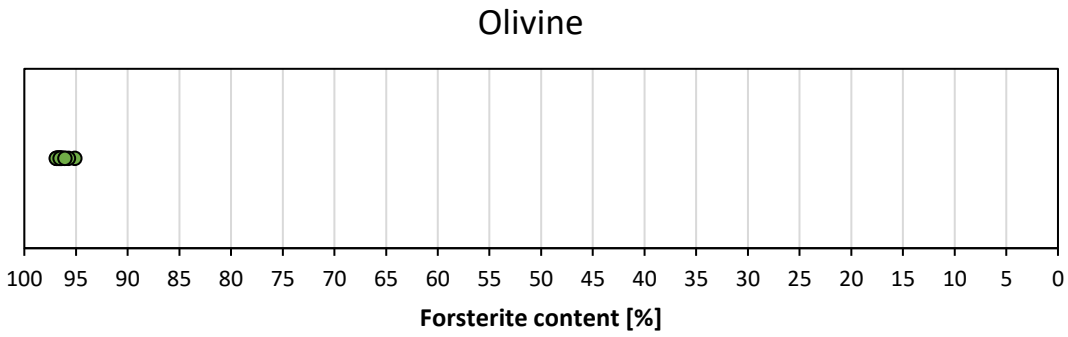


Figure 72: Forsterite content of olivine in sample LPUM 300-1

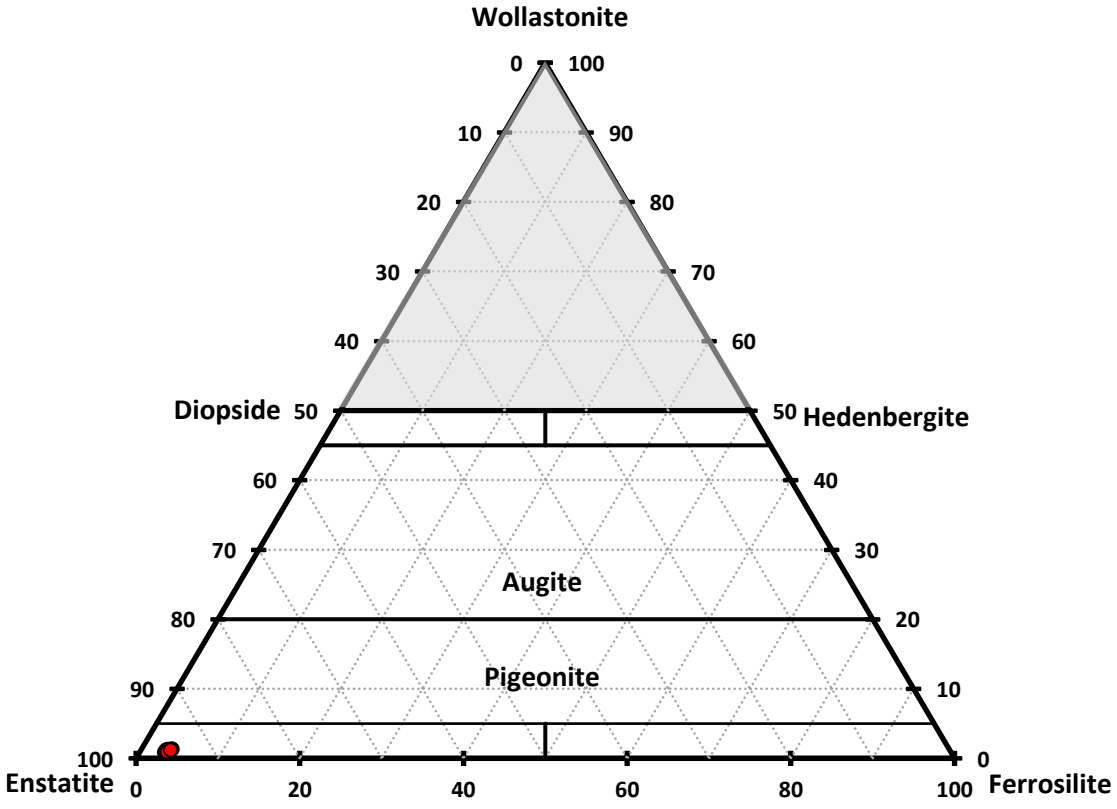


Figure 73: Composition of orthopyroxenes in the sample LPUM-300-1.

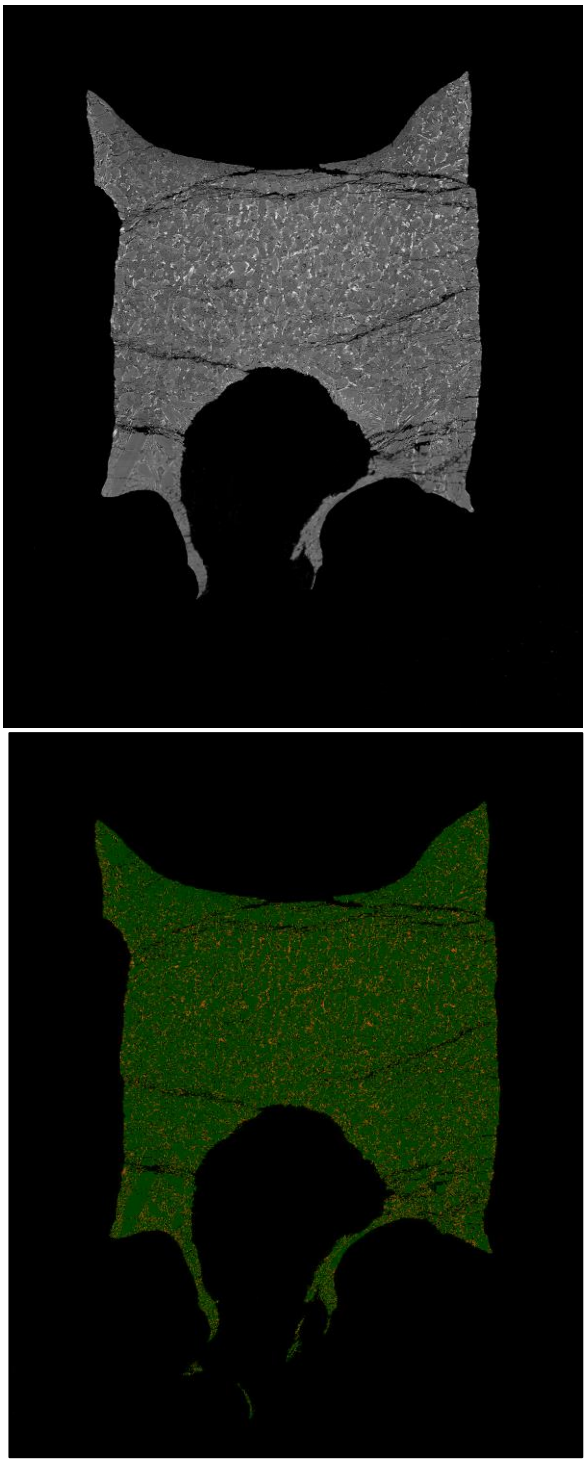


Figure 74: Separation by grey values of sample 300-1 using MATLAB. Original image (top) and constructed image from the separation (bottom).

Orange: Melt
Green: Minerals
Black: Holes & Capsule

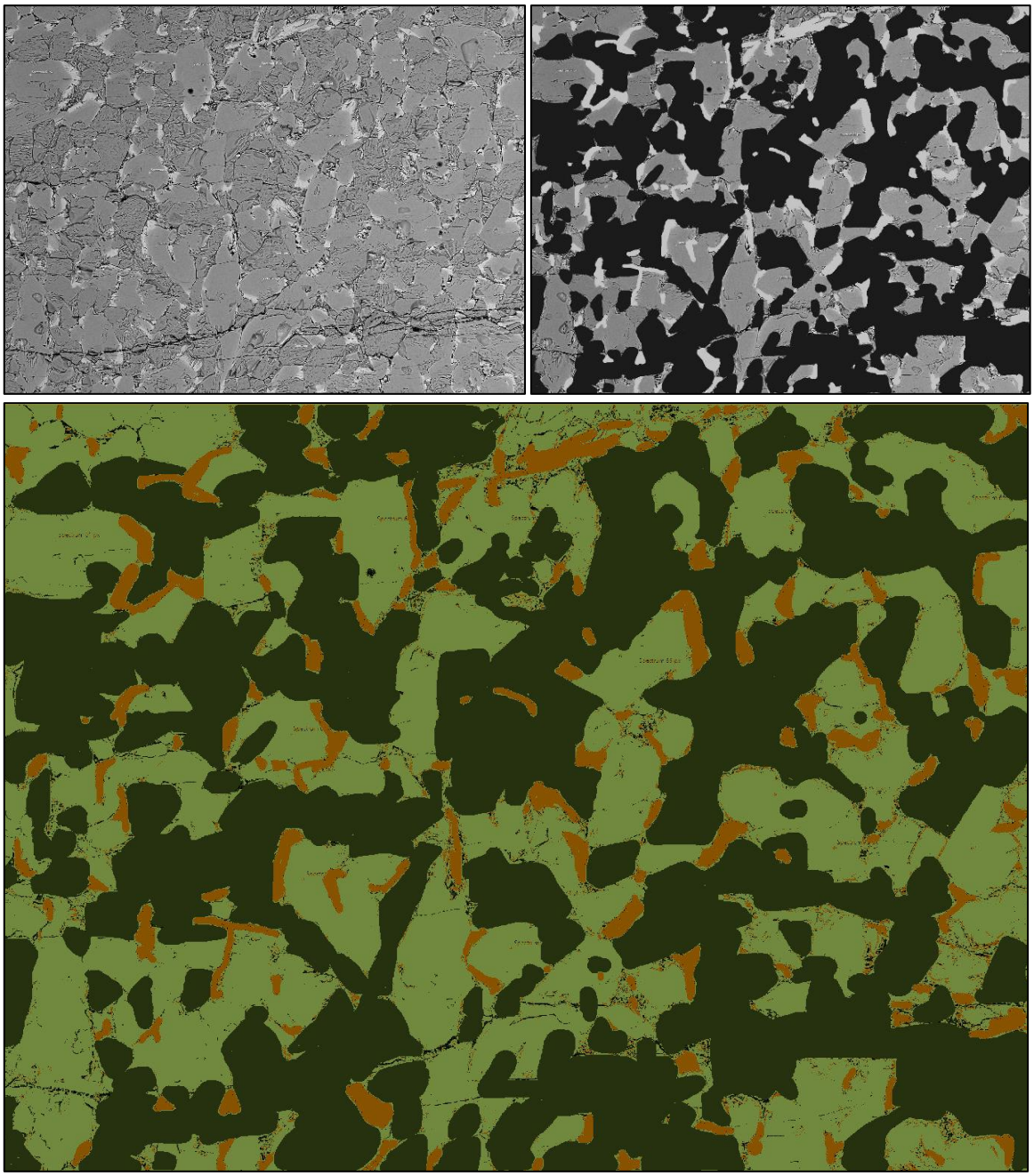


Figure 75: Separation by grey values of sample 300-1 using MATLAB. Original image (top) and constructed image from the separation (bottom)

Orange: Melt
Dark Green: Olivine
Light Green: OPX
Black: Capsule/Holes

3.2 LPUM 285-2 // 435 km depth

Method:	PCP	**Pressure**	2.10 GPa	**Temperature**	1550°C
Duration	2.0h	**f(O_2) Buffer:**	Cr-Cr_2O_3	**Capsule:**	Fe + Pt

Oxide	**SiO_2**	**TiO_2**	**Al_2O_3**	**FeO**	**MnO**	**MgO**	**CaO**	**Na_2O**	**K_2O**	**P_2O_5**	**Cr_2O_3**
wt%	47,45	0,21	5,65	9,06	0,13	32,74	4,00	0,14	0,01	0,01	0,60

Melt fraction: 24,7%	**Crystals:** OPX (76,5%), Olivine (22,5%), Fe-nuggets (0,99%)

LPUM 285-2 (Figure 76) was originally intended for 2.85 GPa and 1680°C. However, we lowered the conditions to 2.10 GPa and 1550°C since 1550°C turned out to be the maximum experimental temperature for iron capsules (melting point: 1538 °C at 1 bar). At any higher temperature, the capsule was molten.

The sample consists of 76.3% minerals and 24.7% melt (Figure 81). The minerals are difficult to segment from each other due to the similar grey values in the images (Figure 77 & Figure 78). The estimate of 76.5% enstatite, 22.5% forsterite and 0.99% Fe-nuggets is therefore subject to uncertainty.

The crystals have a size of <1 - 50µm without any noticeable preference for a size class. There is also no difference in size distribution between olivine and orthopyroxene. The melt seems to be evenly distributed.

It is striking that the olivine and the Fe spheres are more common near the iron capsule, while the orthopyroxene becomes more frequent towards the platinum capsule. Among the crystals, idiomorphic crystal faces are found as well as round, presumably dissolved crystals. The inner wall of the iron capsule also shows signs of dissolution.

Chemically, the randomly measured minerals are homogeneous in their composition (Figure 79 & Figure 80). It can therefore be assumed that equilibrium has been reached. The orthopyroxene has the mean composition of $En_{91.9}Fs_{5.8}Wo_{2.3}$, the olivine of $Fo_{95.4}Fa_{4.6}$.

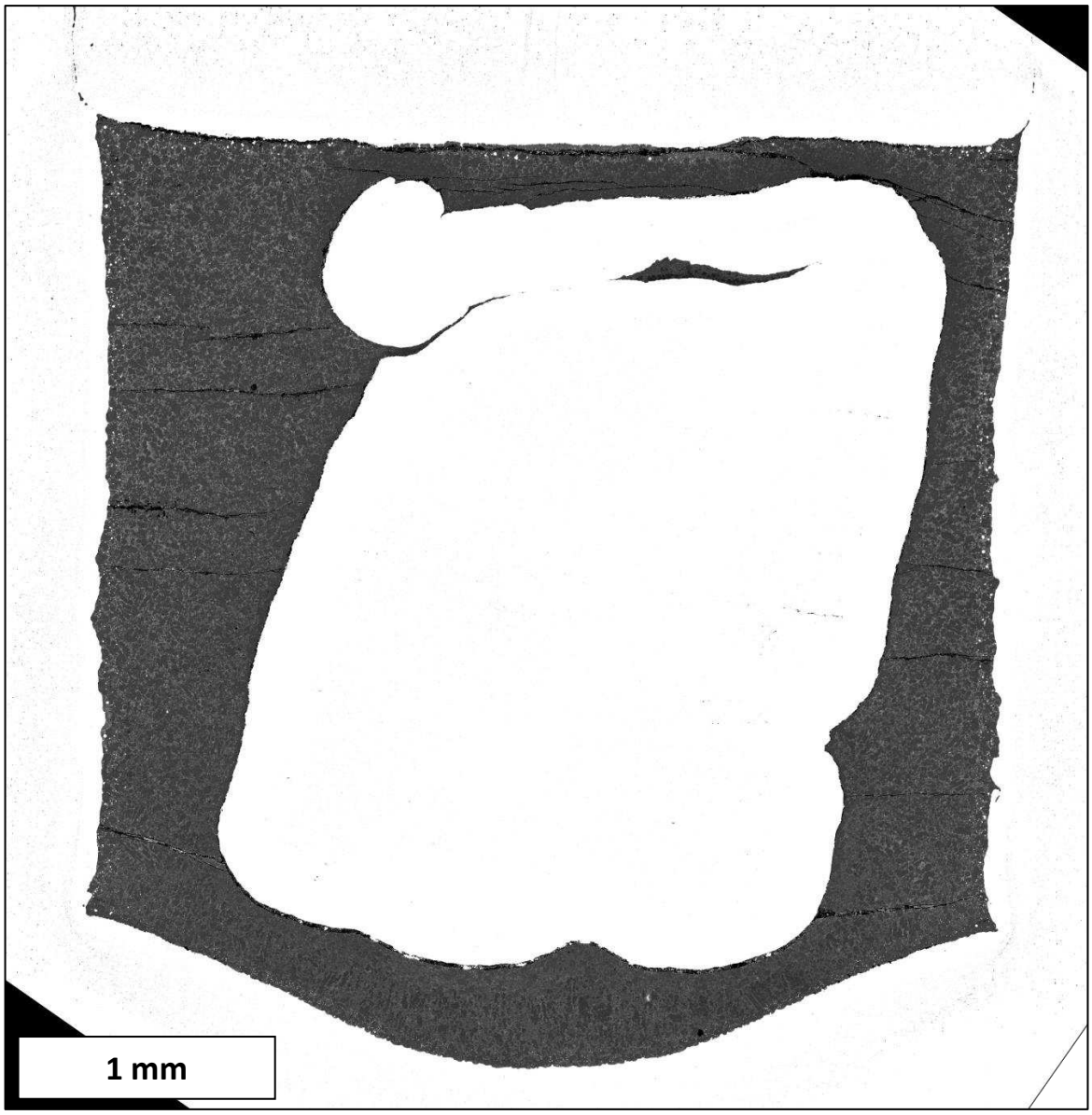


Figure 76: General view of sample LPUM 285-2 (grey) with outer iron and inner platinum capsule (white).

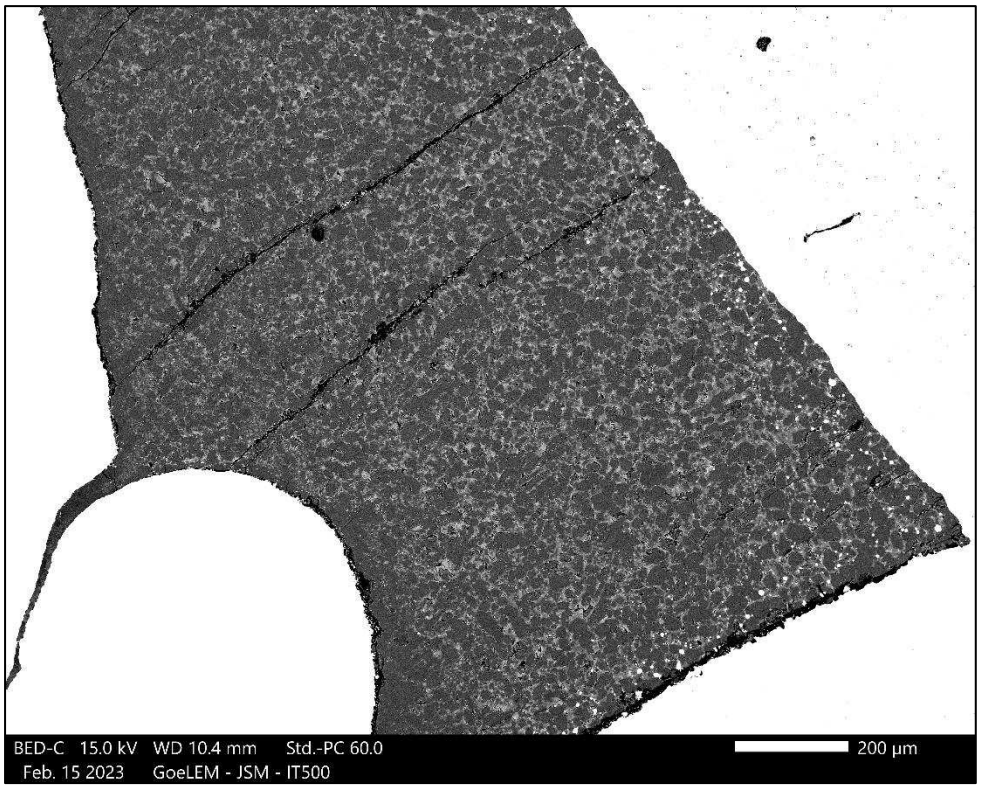


Figure 77: Close-up of sample LPUM 285-2 with pyroxene (dark grey), olivine (grey) and melt (light).

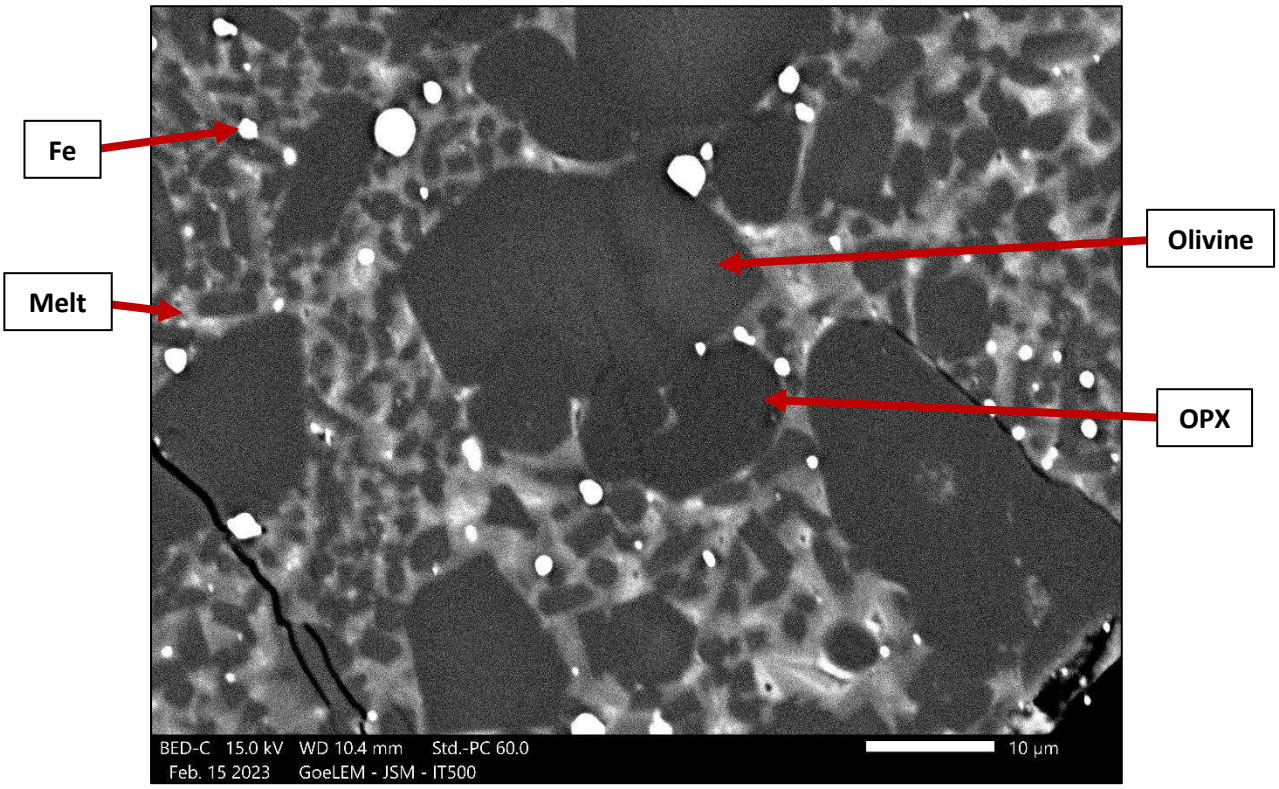


Figure 78: Close-up of sample LPUM 285-2 with pyroxene (dark grey), olivine (grey) melt (light grey) and Fe-nuggets (white).

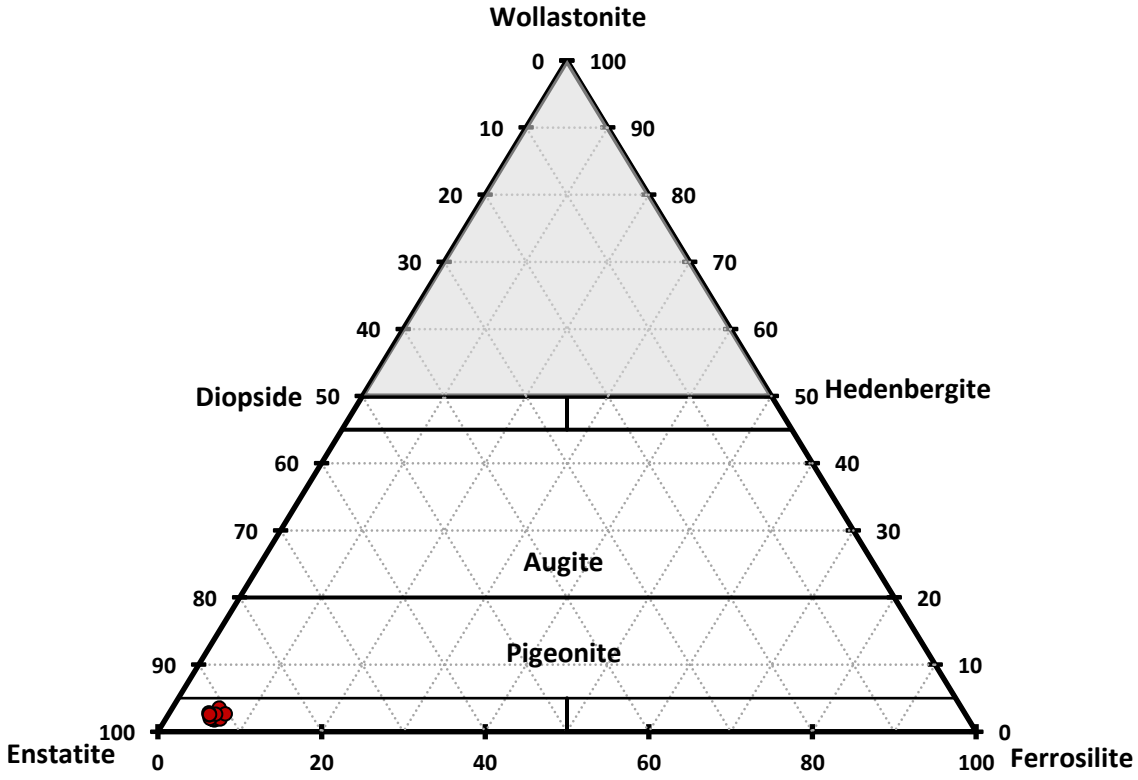


Figure 79: Composition of orthopyroxenes in the sample LPUM-285-2

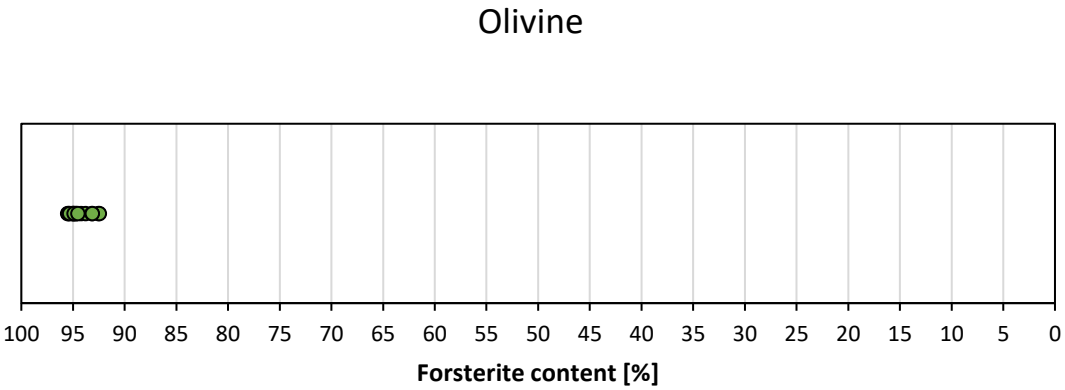


Figure 80: Forsterite content of olivine in sample LPUM 285-2

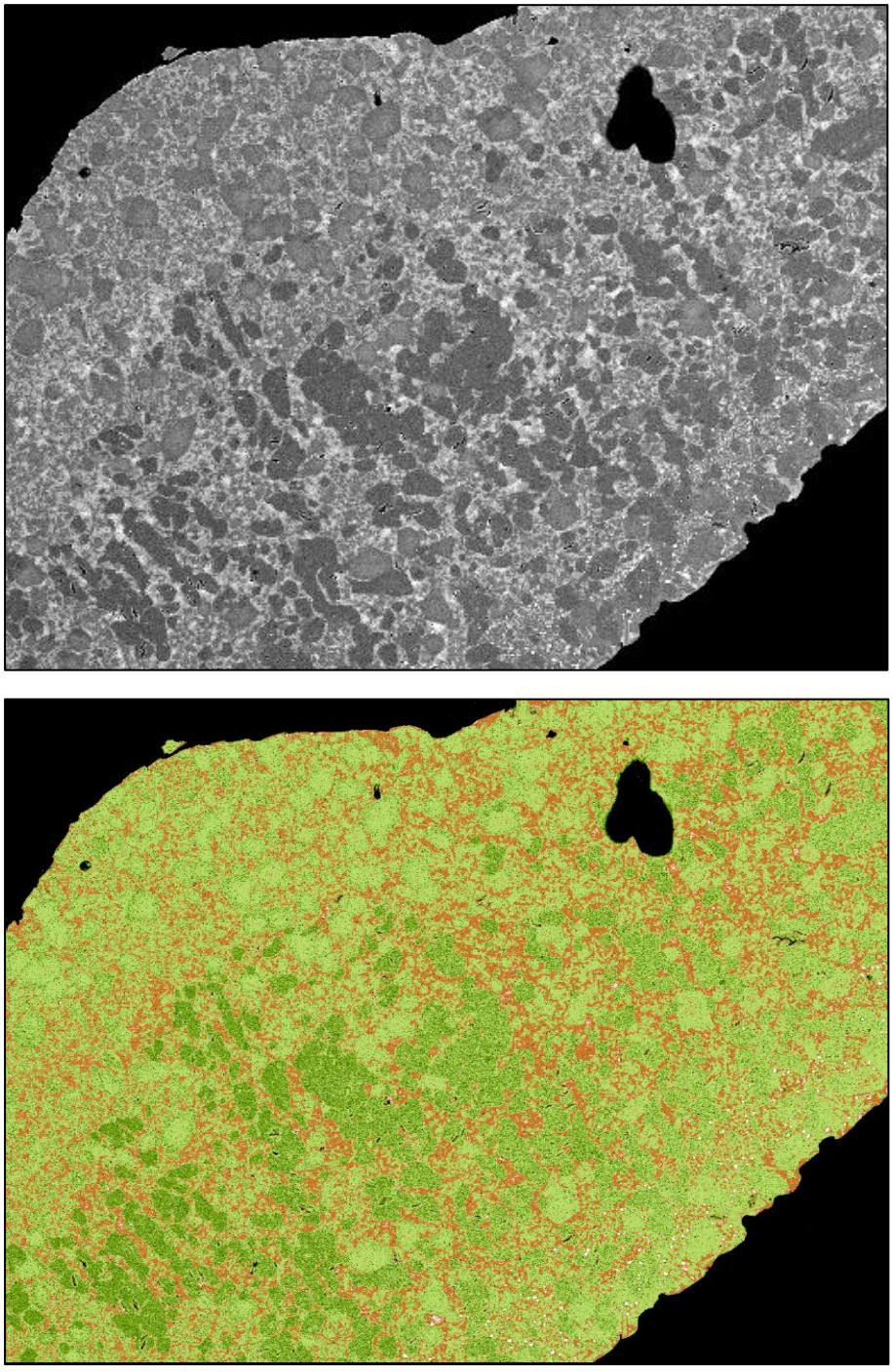


Figure 81: Separation by grey values of sample 285-2 using MATLAB. Original image (top) and constructed image from the separation (bottom)

Orange: Melt
Dark Green: Olivine
Light Green: OPX
White: Fe-Nuggets
Black: Capsule/Holes

3.3 LPUM 210-2 // 435 km depth

Method:	PCP	**Pressure**	2.10 GPa	**Temperature**	1550°C
Duration	6.0h	**f(O_2) Buffer:**	Cr-Cr_2O_3	**Capsule:**	Fe + Fe

Oxide	**SiO_2**	**TiO_2**	**Al_2O_3**	**FeO**	**MnO**	**MgO**	**CaO**	**Na_2O**	**K_2O**	**P_2O_5**	**Cr_2O_3**
wt%	48,68	0,24	6,78	9,67	0,14	28,82	4,78	0,17	0,02	0,02	0,68

Melt fraction:	13,5%	**Crystals:**	OPX (56,1%), Olivine (22,4%), CPX (7,3%), Fe-Nuggets (1,8%)

LPUM 210-2 is identical to LPUM 285-2 in its P-T range, but with the composition intended for these conditions. In addition, iron was used as the capsule material for the buffer instead of platinum for this experiment. Since iron is very soft near the melting temperature, the inner buffer capsule deformed now is in contact with the walls of the sample capsule. It is impossible to say if a connection between upper and lower sample part is maintained, hence, there is no visible difference between the upper and lower half of the sample (Figure 82).

The sample is highly crystallised (86.5%). The solids consist of 56.1% OPX, 22.4% olivine, 7.3% CPX and 1.8% Fe-nuggets (Figure 83, Figure 84 & Figure 87). The sampled minerals show a homogeneous composition (Figure 85 & Figure 86).

Area measurements indicate that the sample is chemically zoned (Figure 88). In the border area to the buffer capsule, calcium is more abundant than magnesium. This could be due to a chemical separation of the melt, which pools close to the buffer. Changes of the melt chemistry by the large degree of crystallisation could explain the occurrence of CPX at this early stage of the series.

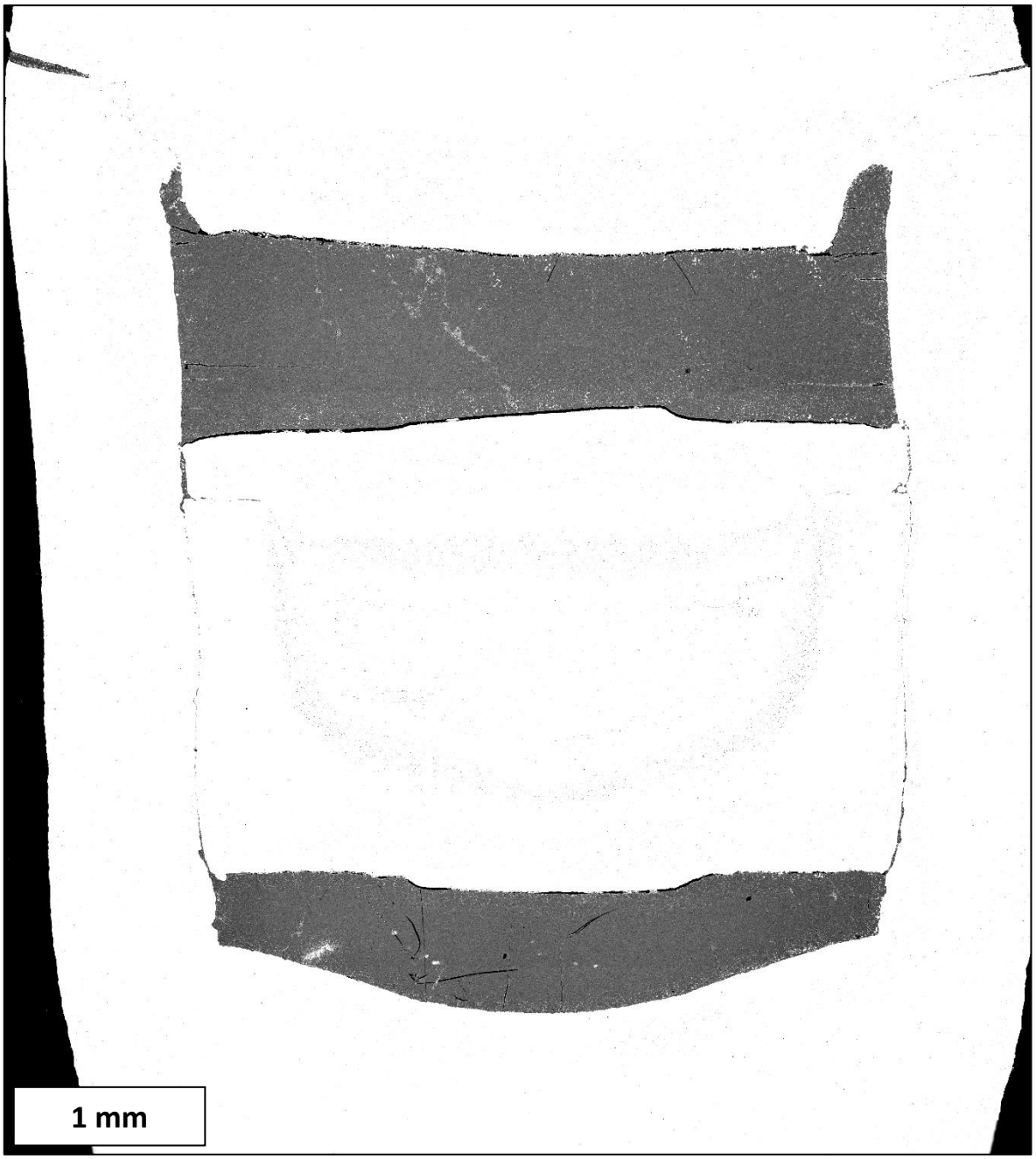


Figure 82: General view of sample LPUM 210-2 with outer and inner iron capsule (white). The buffer material is visible as a grey shadow in the inner iron capsule.

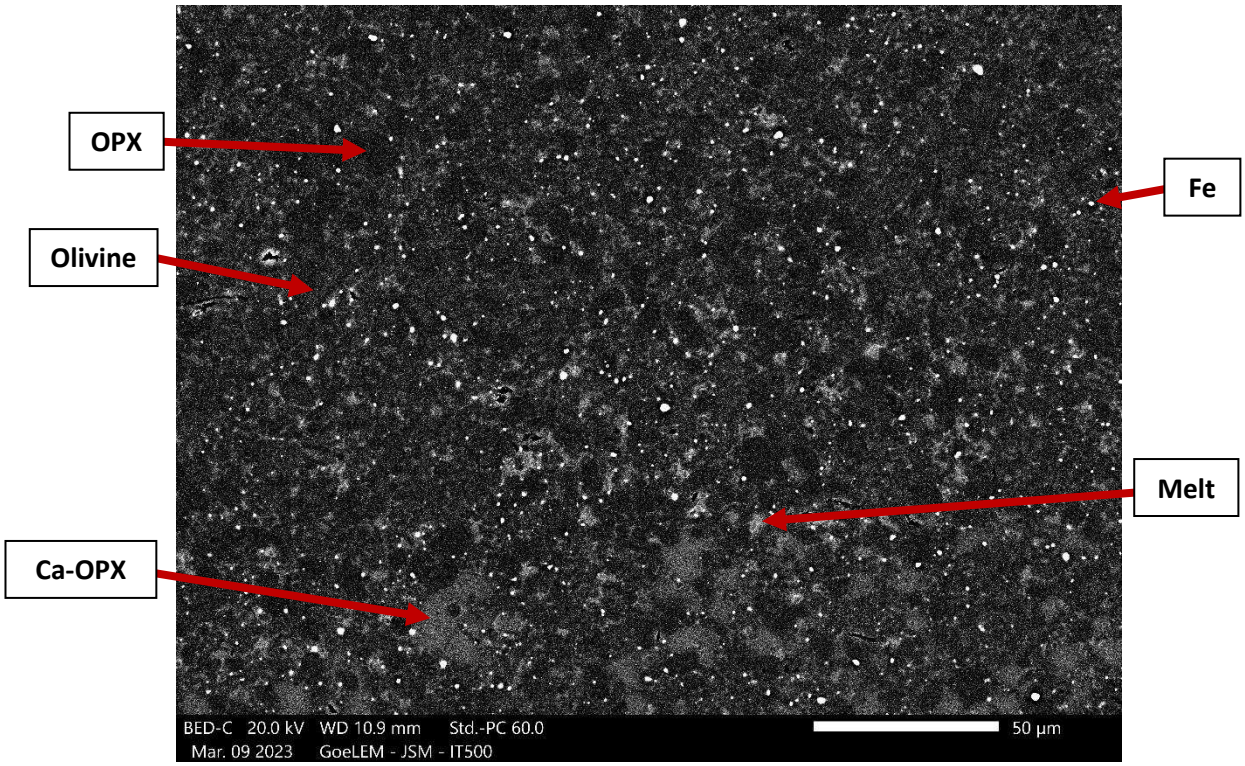


Figure 83: Close-up of sample LPUM 210-2 showing pyroxene (grey), olivine (light grey) and Fe spheres (white).

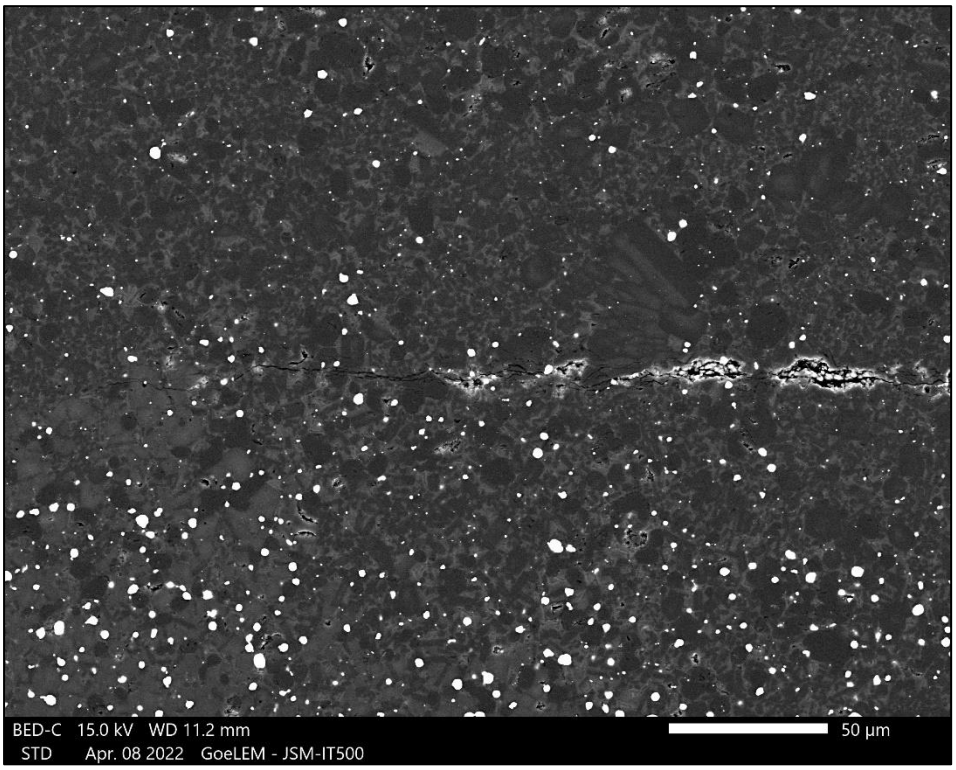


Figure 84: Close-up of sample LPUM 210-2 showing pyroxene (grey), olivine (light grey) and Fe spheres (white).

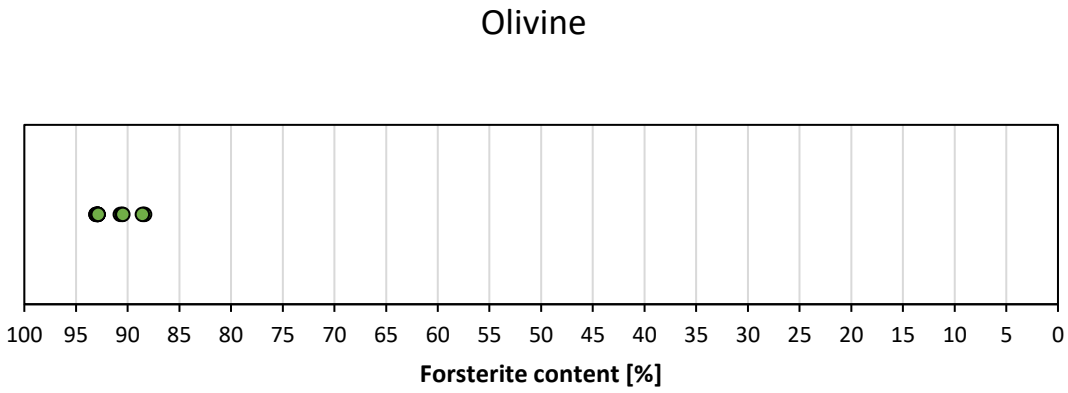


Figure 85: Forsterite content of olivine in sample LPUM 210-2

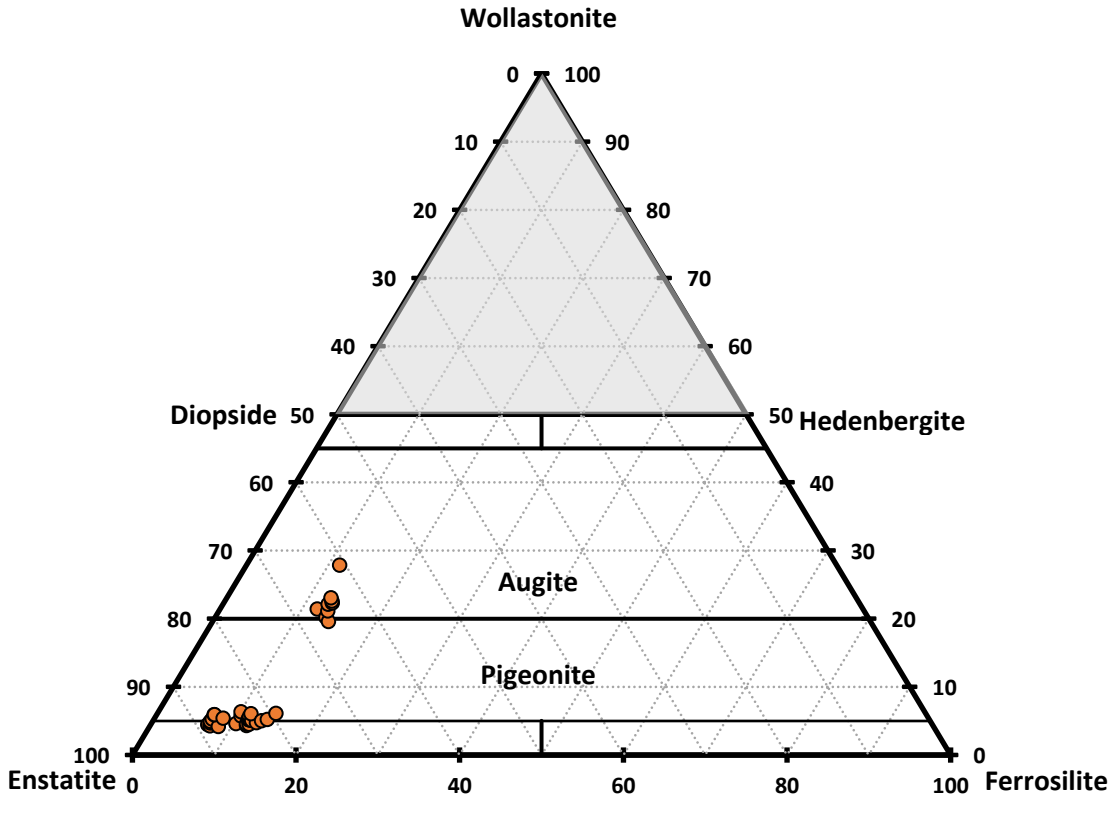


Figure 86: Mineral composition of the Pyroxenes in sample LPUM 210-2

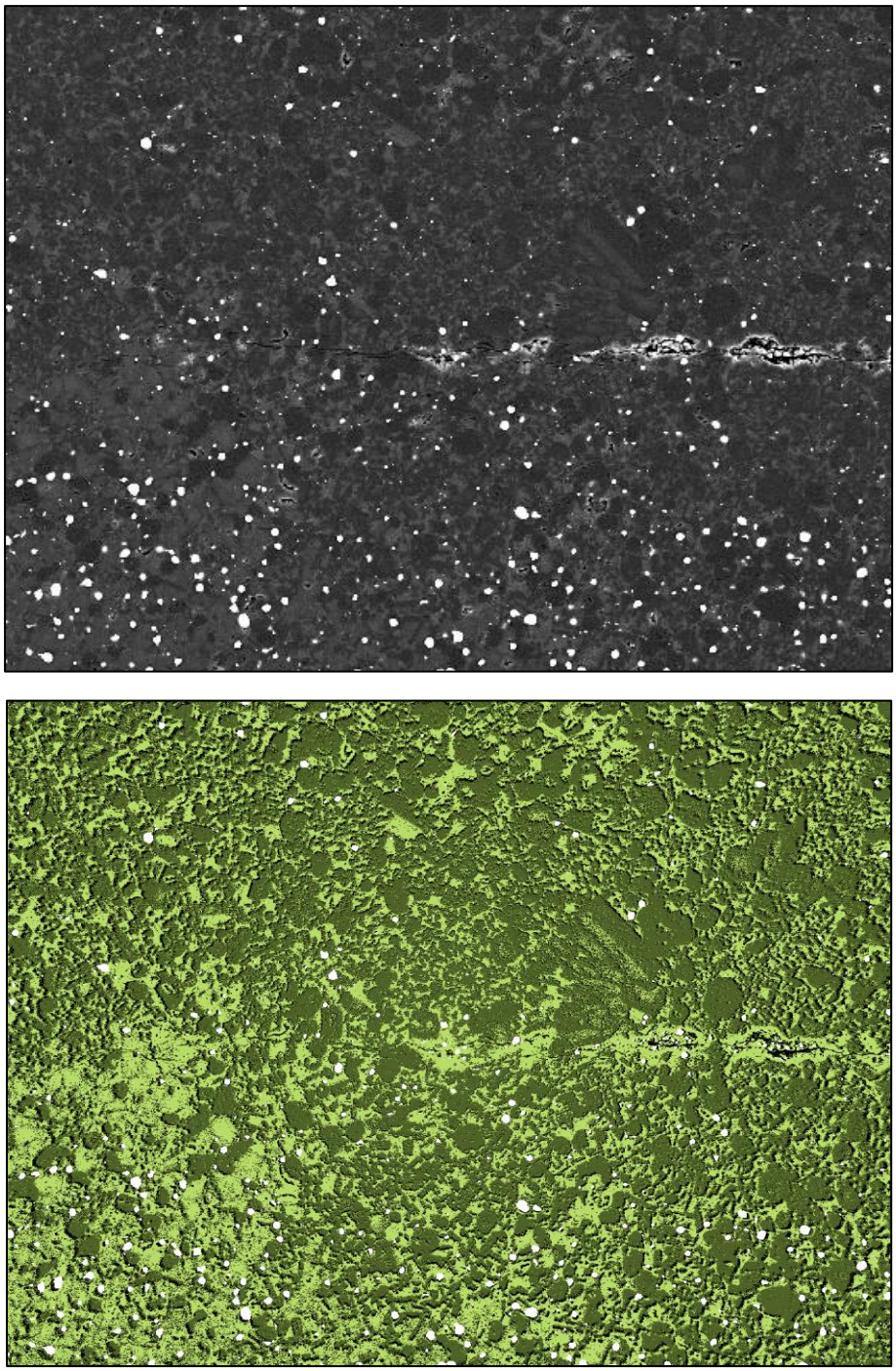


Figure 87: Separation by grey values of sample 210-2 using MATLAB. Original image (top) and constructed image from the separation (bottom).

Dark Green: Olivine
Light Green: OPX
White: Fe-Nuggets
Black: Capsule/Holes

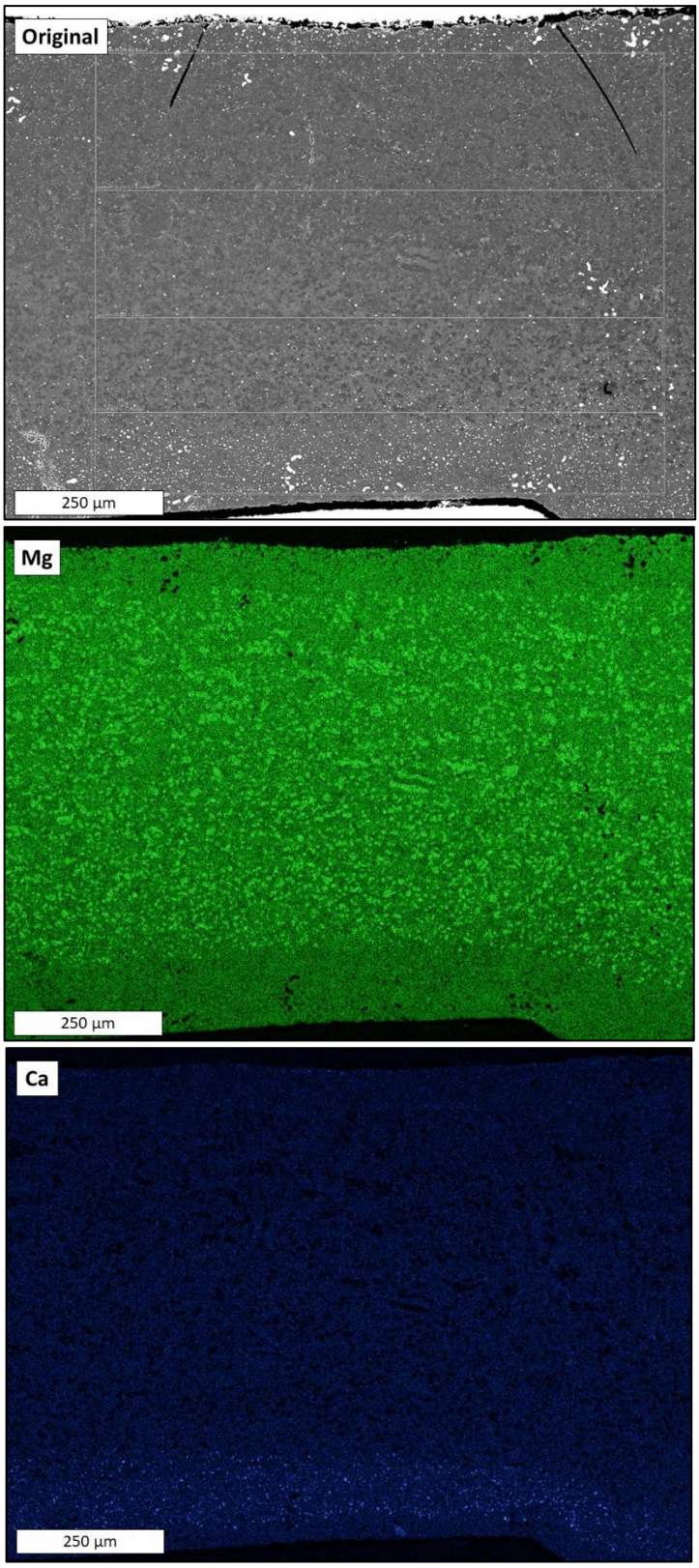


Figure 88: Area measurement of sample LPUM 210-2 in the BSE image (top) and as distribution of magnesium (middle, green) and calcium (bottom, blue).

3.4 LPUM 150-1 // 294 km depth

Method:	PCP	**Pressure**	1,50 GPa	**Temperature**	1440°C
Duration	24h	**f(O_2) Buffer:**	Cr-Cr_2O_3	**Capsule:**	Fe + Pt

Oxide	**SiO_2**	**TiO_2**	**Al_2O_3**	**FeO**	**MnO**	**MgO**	**CaO**	**Na_2O**	**K_2O**	**P_2O_5**	**Cr_2O_3**
wt%	51,27	0,35	9,32	9,37	0,13	21,84	6,69	0,24	0,02	0,02	0,75

Melt fraction: 55,7%	**Crystals:** OPX (96,25%), Fe-Nuggets (3,75%)

LPUM 150-1 is a partially failed experiment. The overview image (Figure 90) clearly shows that a large part of the Cr-Cr_2O_3 buffer is missing. The platinum capsule that contained it has formed an alloy with the iron capsule, as the elemental distribution map shows (Figure 89, left). The chromium of the buffer has dissolved in the melt of the sample, which has coloured the glass in a deep blue (Figure 89, right).

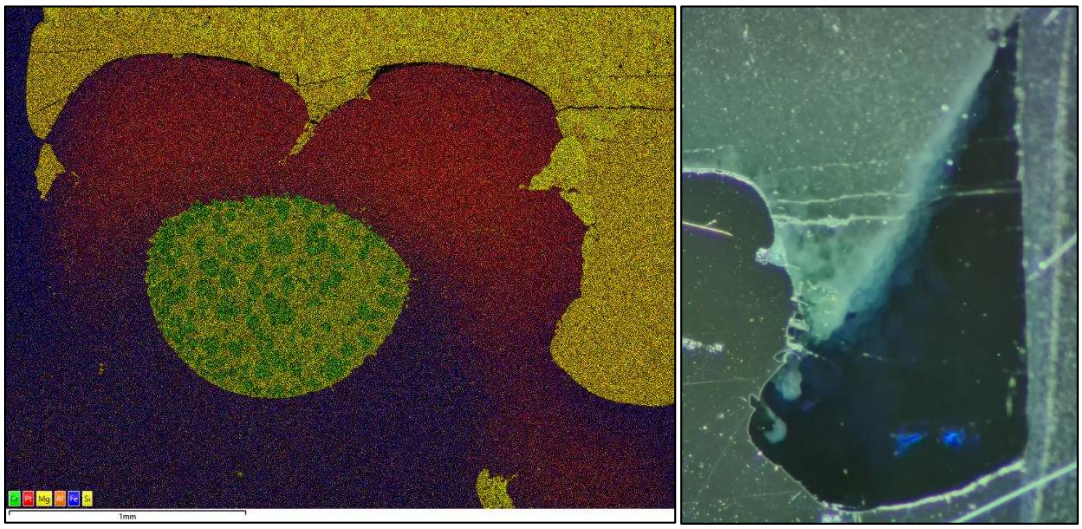


Figure 89: Elemental distribution map of Cr (green), Pt (red), Mg (yellow), Al (orange), Fe (blue) and silicon (yellow) (left) and photograph (right) of sample LPUM 150-1.

It is striking that the mineral portion of the sample (42.66%) is concentrated in the middle, upper area of the capsule, while the melt (55.68%) pools at the lower edges (Figure 90 & Figure 93). In the lower area of the mineral portion, the melt is clearly in contact with itself, while this is questionable for the upper area near the former capsule lid.

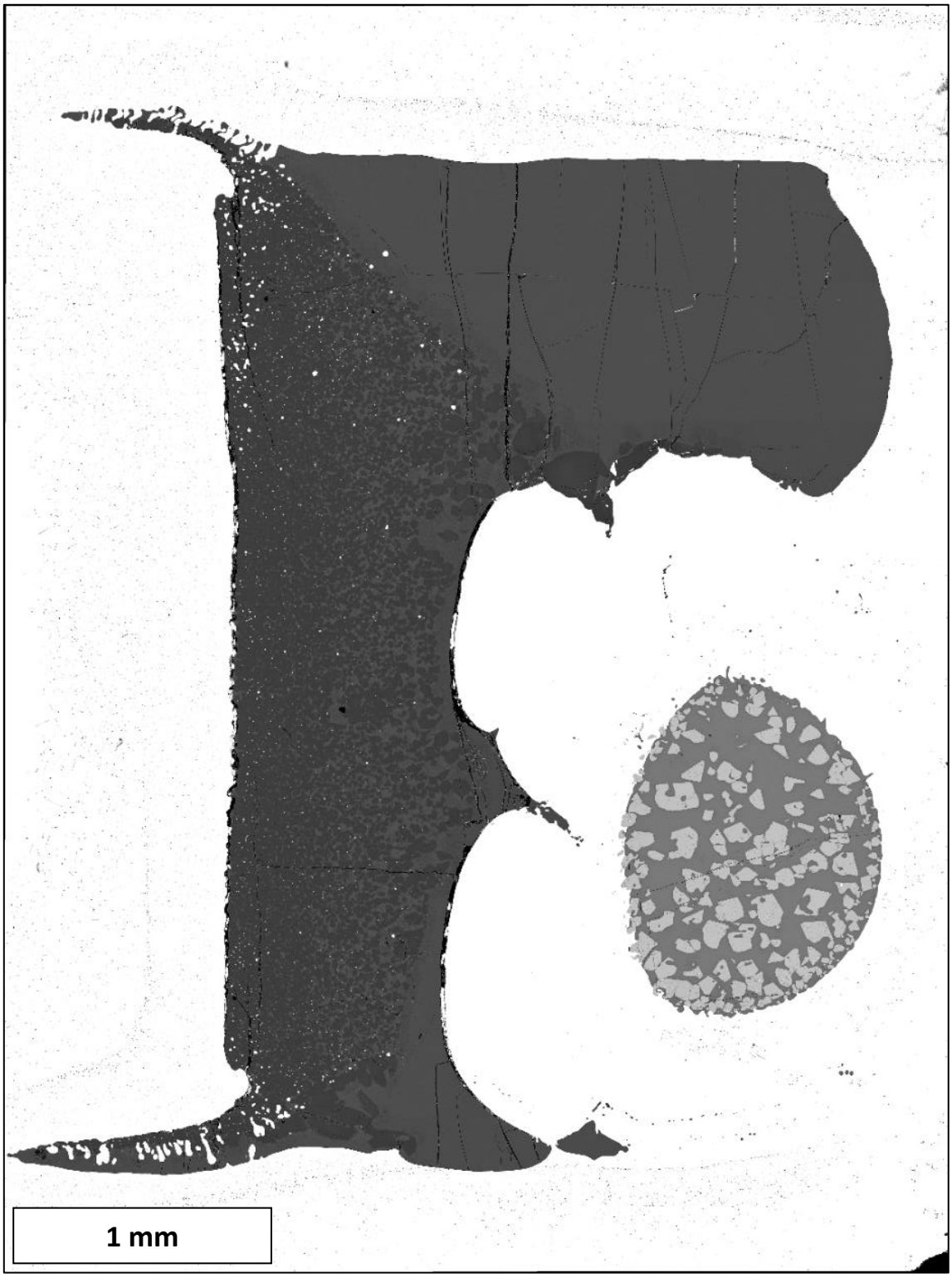


Figure 90: General view (rotated 90° to the left) of sample LPUM 150-1. The buffer capsule in the lower left quarter of the image has fused with the surrounding iron capsule. In its remains there is a dark, chromium-containing silicate melt with lighter magnesiochromite.

The crystals have a size of 10 to 50 µm, are predominantly of idiomorphic shape and show bright growth rims. Quench crystallisation is visible in the lower image area of Figure 91. The Fe-nuggets are sub-micrometre to 10 µm in size, whereby larger diameters are reached in the areas of mineral accumulation and only very small nuggets are visible in glass dominated parts (Figure 91).

Instead of the buffer, a silicate melt with 25% chromium content is found in the fused remains of the platinum capsule, containing magnesiochromite with the approximate mineral composition $Fe_{0.25}Mg_{0.57}Al_{0.21}Cr_{1.88}O_4$ (Figure 90).

Chemically, the orthopyroxene is enstatite with the average composition $En_{94.8}Fs_{2.7}Wo_{2.5}$. A random analysis of the enstatites in the sample does not show much variation in composition, so it can be assumed that equilibrium has been reached (Figure 92).

Due to a possible influence by the leaked buffer, the experiment was repeated as LPUM 150-3.

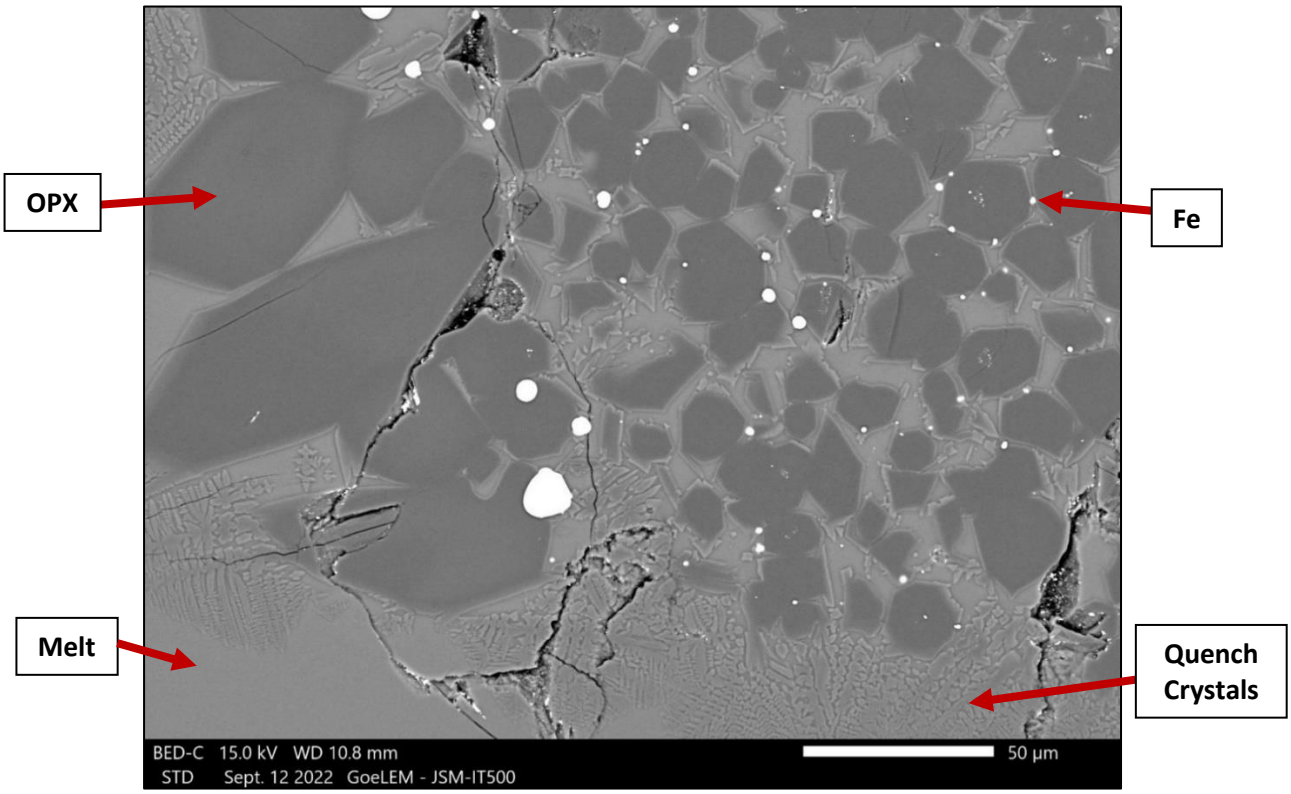


Figure 91: Close-up of sample LPUM 150-1 with dark orthopyroxene in a lighter melt with white iron nuggets. Quench crystallisation can be seen, especially in the lower part of the image.

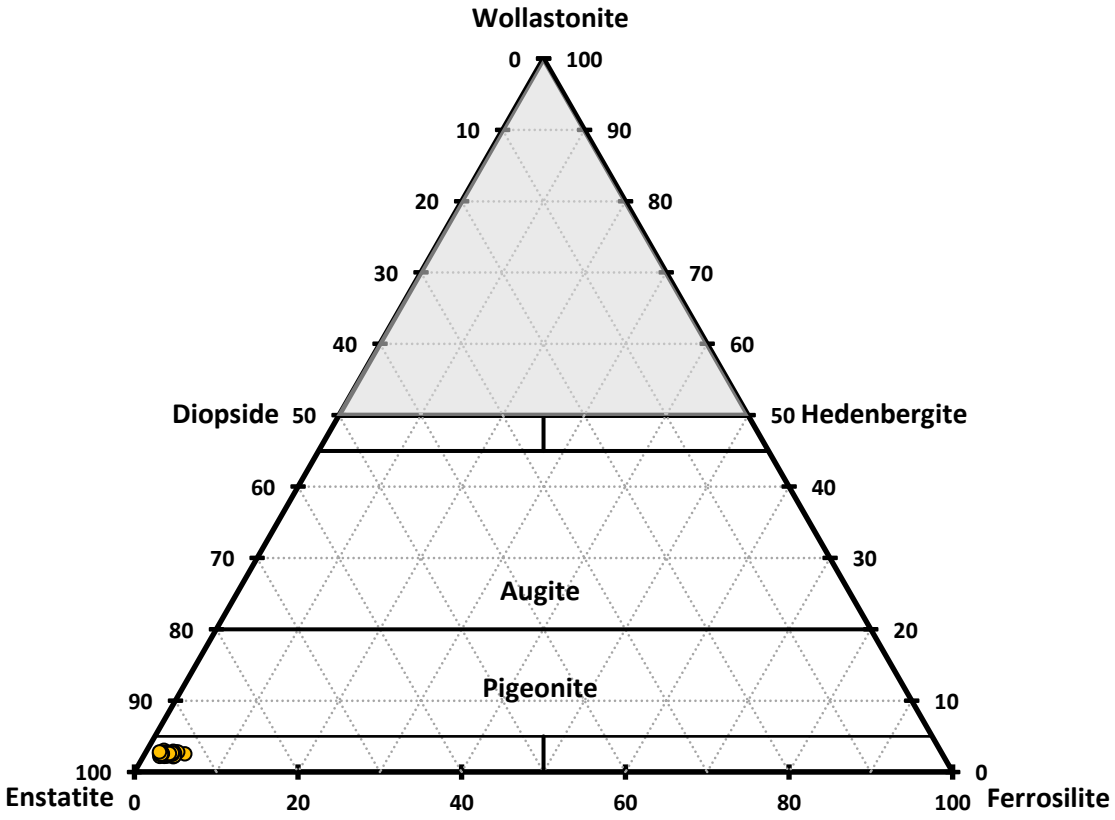


Figure 92: Mineral composition of the orthopyroxenes in sample LPUM 150-1

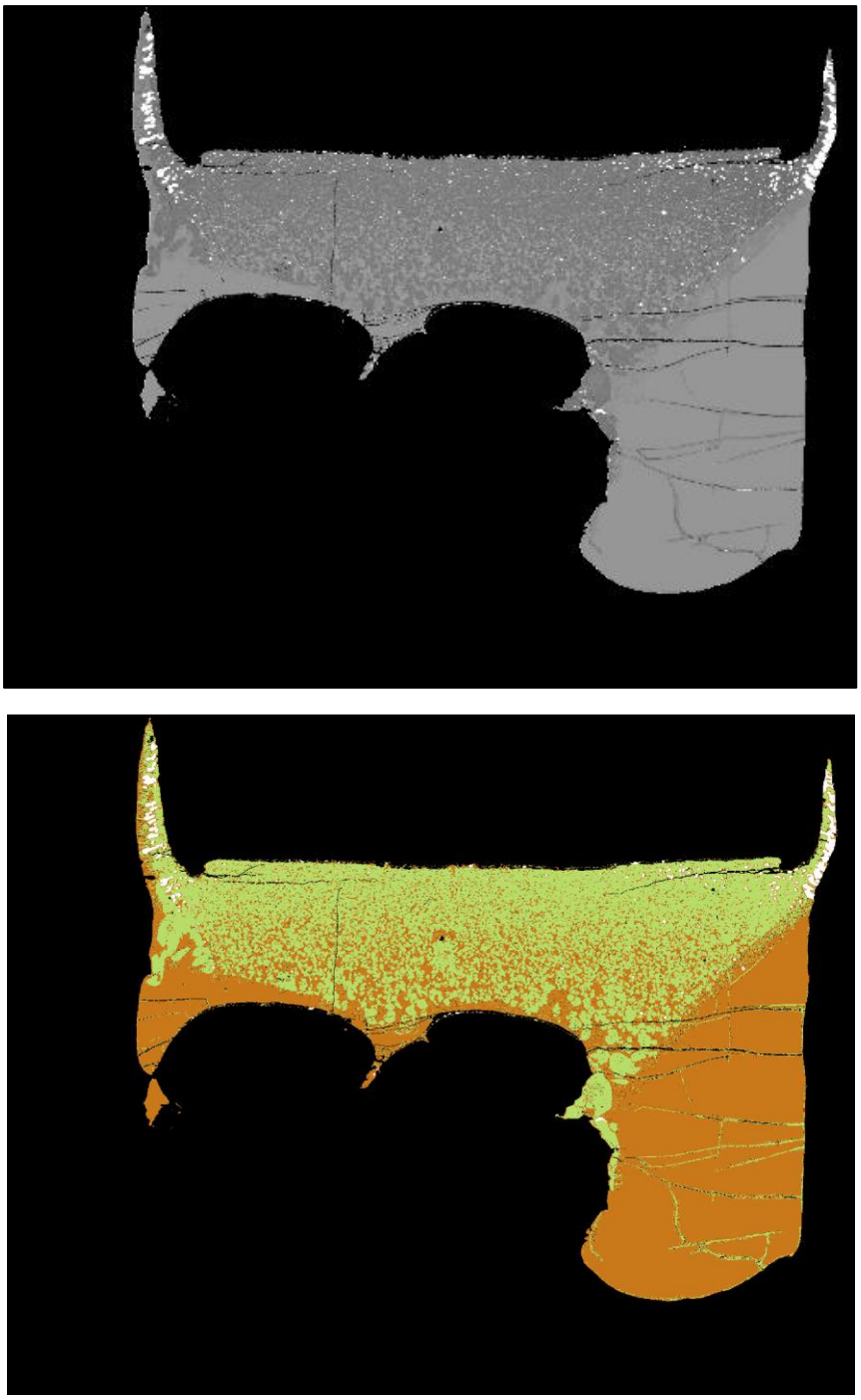


Figure 93: Separation by grey values of sample 210-2 using MATLAB. Original image (top) and constructed image of the separation (bottom).

***Orange**:* *Melt*
***Light Green**:* *OPX*
***White**:* *Fe-Nuggets*
Black: Capsule/Holes

3.5 LPUM 150-3 // 294 km depth

Method:	PCP	**Pressure**	1,50 GPa	**Temperature**	1440°C
Duration	6h	**f(O_2) Buffer:**	Cr-Cr_2O_3	**Capsule:**	Fe + Pt

Oxide	**SiO_2**	**TiO_2**	**Al_2O_3**	**FeO**	**MnO**	**MgO**	**CaO**	**Na_2O**	**K_2O**	**P_2O_5**	**Cr_2O_3**
wt%	51,27	0,35	9,32	9,37	0,13	21,84	6,69	0,24	0,02	0,02	0,75

Melt fraction: 40,5%	**Crystals:** OPX (99%), Fe-nuggets (1%)

LPUM 150-3 (Figure 94) is a repeat of LPUM 150-1, since the leaking of buffer material contaminated the latter. Thus, the experimental conditions and the starting material of both experiments are identical, only the duration of the experiment was reduced from 24h to 6h to prevent the buffer capsule from disintegrating again. Furthermore, an amount of 2 µl of water was added to the buffer to investigate a change in the buffer behaviour compared to other experiments.

No significant differences in the mineral content compared to LPUM 150-1 could be found. The sample contains 99% orthopyroxene and 1% Fe-nuggets (Figure 95, Figure 96 & Figure 98). However, the orthopyroxene has a higher proportion of ferrosilite (

Figure 97). Due to the direct contact of sample and buffer in LPUM 150-1, the calculated oxygen fugacity is estimated to be 4.2 log-units below the IW buffer while the f(O_2) in LPUM 150-3 is calculated to be 2.4 log-units below the IW buffer reaction (see chapter 3.13, page 171, for calculation). This might be the cause for the lower the proportion of iron-nuggets in LPUM 150-3 (1%) compared to LPUM 150-1 (3.7%), since more iron is available for the mineralisation of the orthopyroxene.

The minerals reach a size of 20 - 30 µm while the iron nuggets do not exceed a few microns (Figure 96). The distribution of the phases is largely homogeneous, with only an minor accumulation of minerals on the capsule wall of the buffer as well as an accumulation of melt on the capsule wall of the iron capsule (Figure 94).

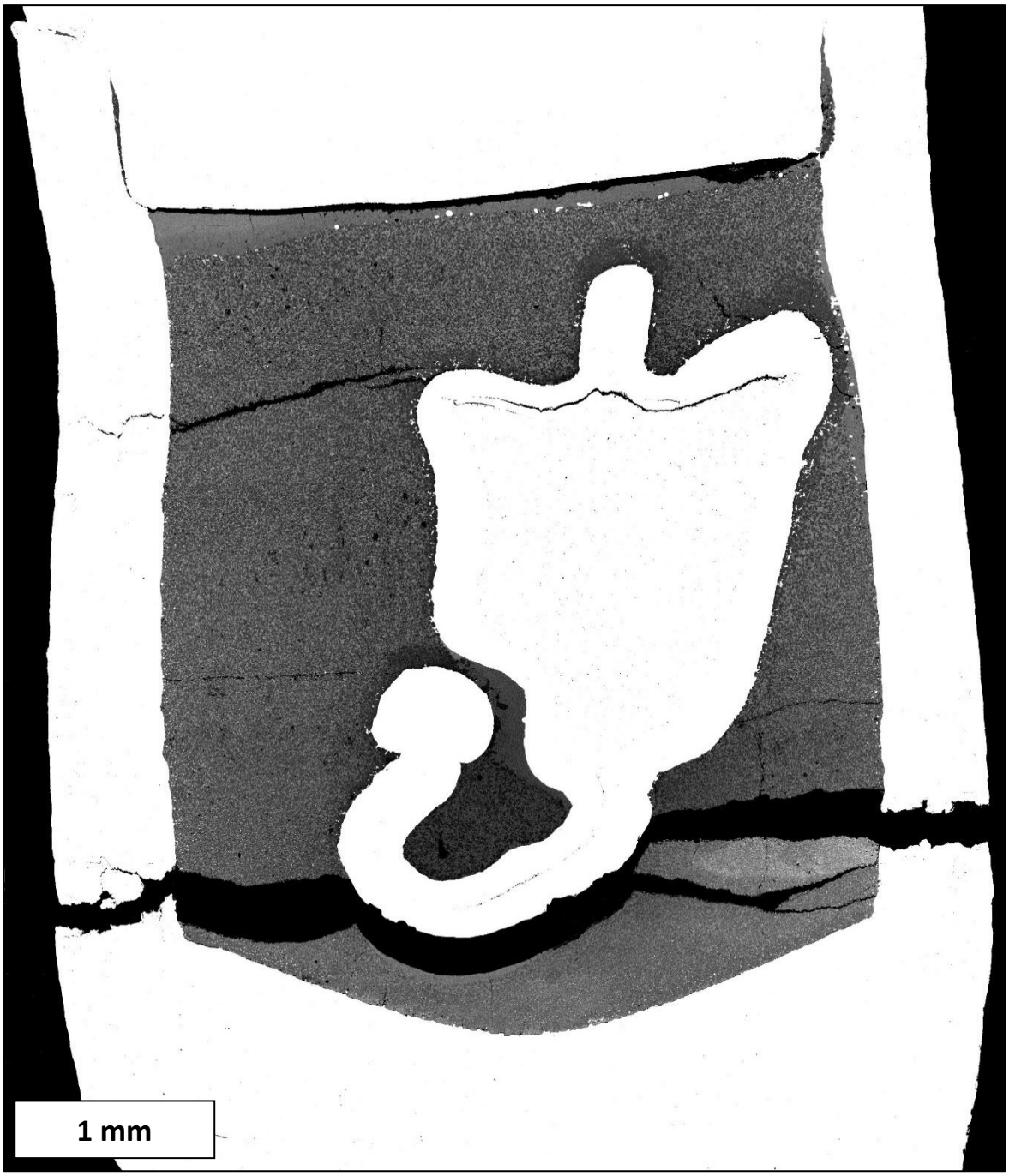


Figure 94: General view of sample LPUM 150-3

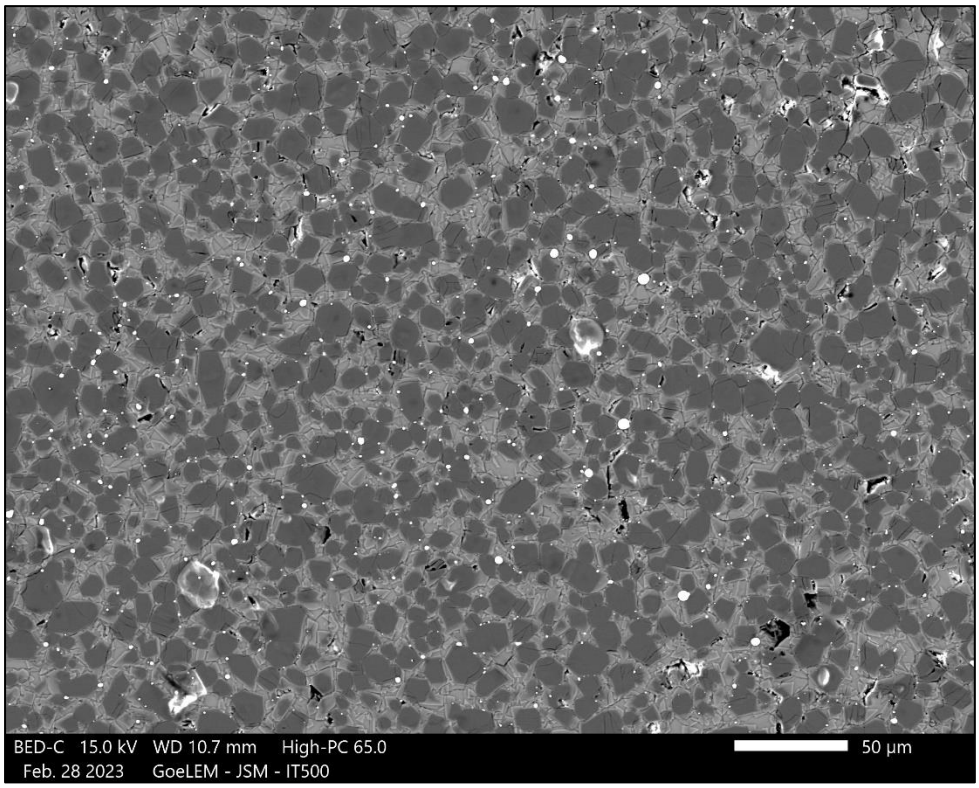


Figure 95: Close-up 1 of sample LPUM 150-3 showing dark orthopyroxene with light quench edges in melt with white Fe-nuggets.

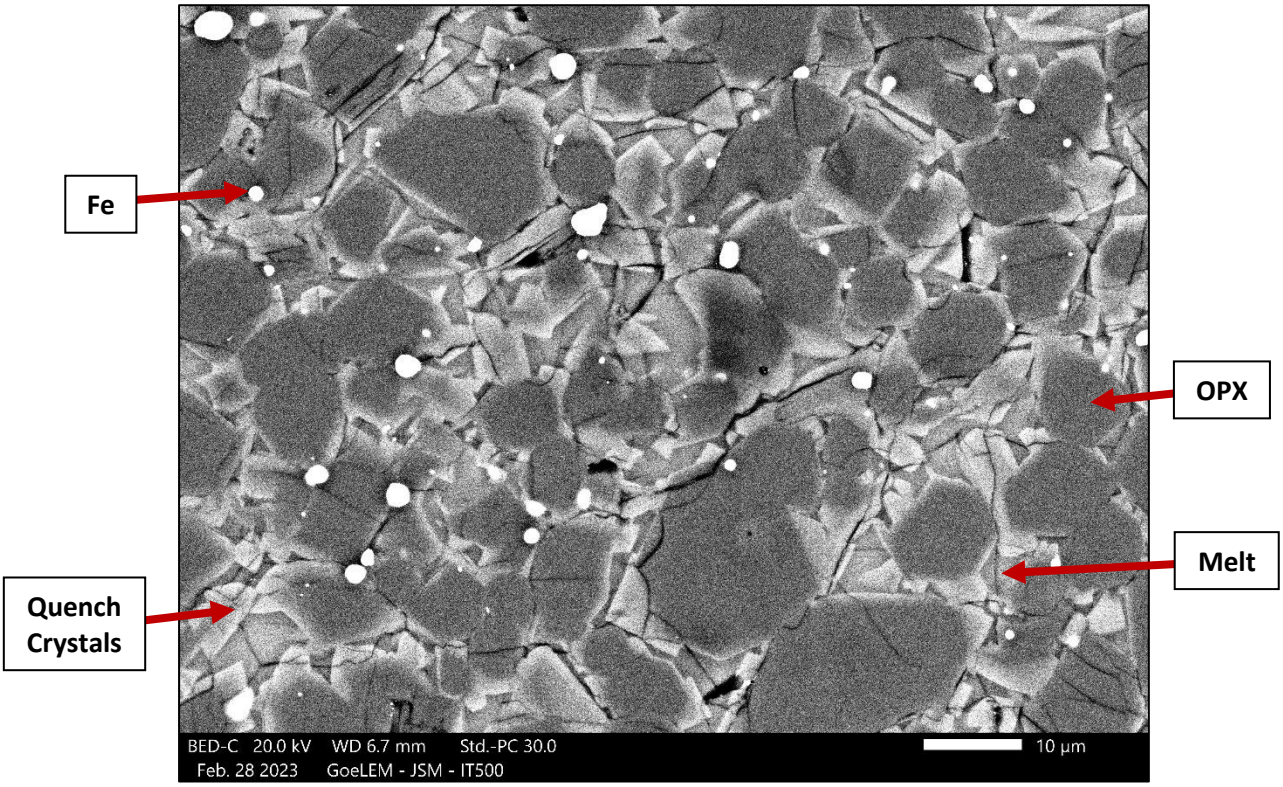


Figure 96: Close-up 2 of sample LPUM 150-3 showing dark orthopyroxene with light quench edges in melt with white Fe-nuggets.

In the immediate vicinity of the platinum capsule, the nuggets consist of a $Pt_{33}Fe_{66}$ alloy.

A striking feature of the sample is an extensive crack that runs through the entire sample capsule, but not through the buffer (Figure 94). This is a post-experimental bursting of the sample capsule due to a high hydrogen partial pressure. This was generated by the reduction of the 2 µl of water in the buffer material (more details in chapter 3.12, page 168). Cracks in the buffer capsule are not visible but could be on the back side hidden in the sample material.

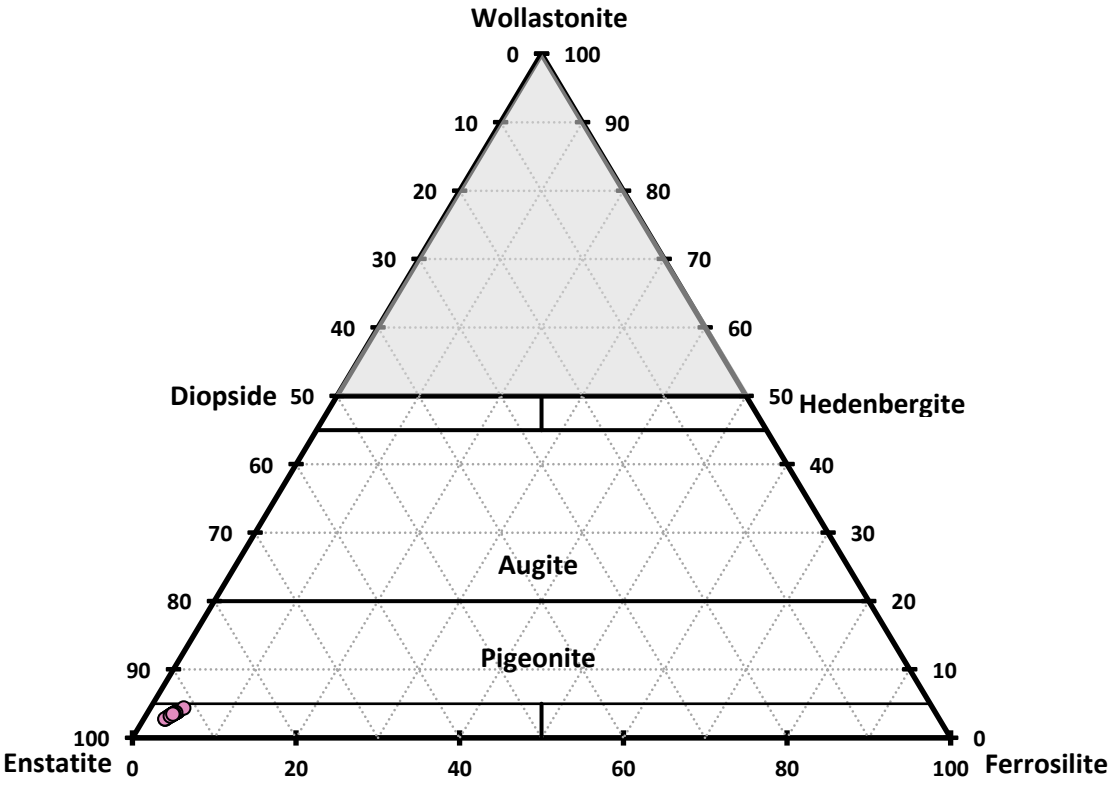


Figure 97: Composition of orthopyroxenes in sample LPUM 150-3

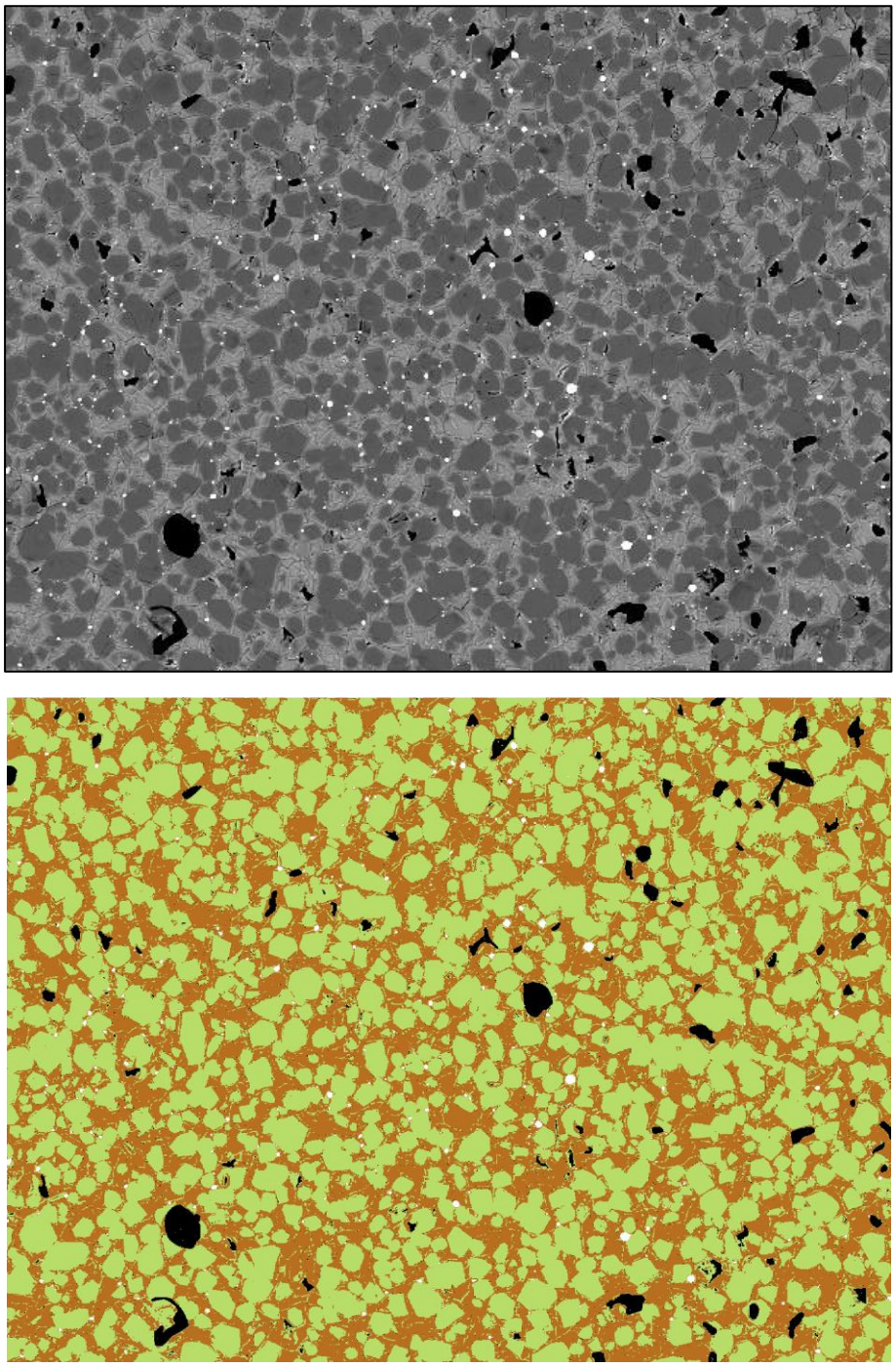


Figure 98: Separation by grey values of sample 150-3 using MATLAB. Original image (top) and constructed image of the separation (bottom).

***Orange**:* *Melt*
***Light Green**:* *OPX*
***White**:* *Fe-Nuggets*
***Black**:* *Holes*

3.6 LPUM 100-1 // 186 km depth

Method:	PCP	**Pressure**	1,00 GPa	**Temperature**	1290°C
Duration	2.0h	**f(O_2) Buffer:**	Cr-Cr_2O_3	**Capsule:**	Fe + Pt

Oxide	**SiO_2**	**TiO_2**	**Al_2O_3**	**FeO**	**MnO**	**MgO**	**CaO**	**Na_2O**	**K_2O**	**P_2O_5**	**Cr_2O_3**
wt%	48,96	0,46	11,66	10,75	0,07	17,83	9,04	0,33	0,04	0,03	0,83

Melt fraction: 93,6%	**Crystals:** OPX (71,9%), Olivine (28,1%), Fe-nuggets (0,02%)

The sample LPUM 100-1 stands out due to its high melt content of 93.6%. The minerals show clear, idiomorphic grain boundaries and are 10 to 200 µm in size. Close to minerals, the Fe-nuggets (0.02 %) are larger with sizes up to 10 µm and very small (<1µm) in the melt (Figure 101).

A separation of the grey values to determine the different mineral proportions using Matlab was not successful due to very similar densities of OPX and olivine in this sample (Figure 104). However, due to the small number of minerals, each of them could be sampled individually using EDX, resulting in a composition of 82 orthopyroxenes (71.9%) and 32 olivines (28.1%) (Figure 100). The percentages determined in this way are, unlike other samples, derived by number and not area fraction.

Chemically, all orthopyroxenes can be classified as enstatite with an average composition of $En_{85.8}Fs_{11.3}Wo_{2.9}$ (Figure 102). Only a few minerals show a more magnesium-rich composition at the expense of the iron content while the calcium content remains unchanged. The olivine of the sample is forsterite with a mean composition of $Fo_{87.2}Fa_{12.8}$ (Figure 103).

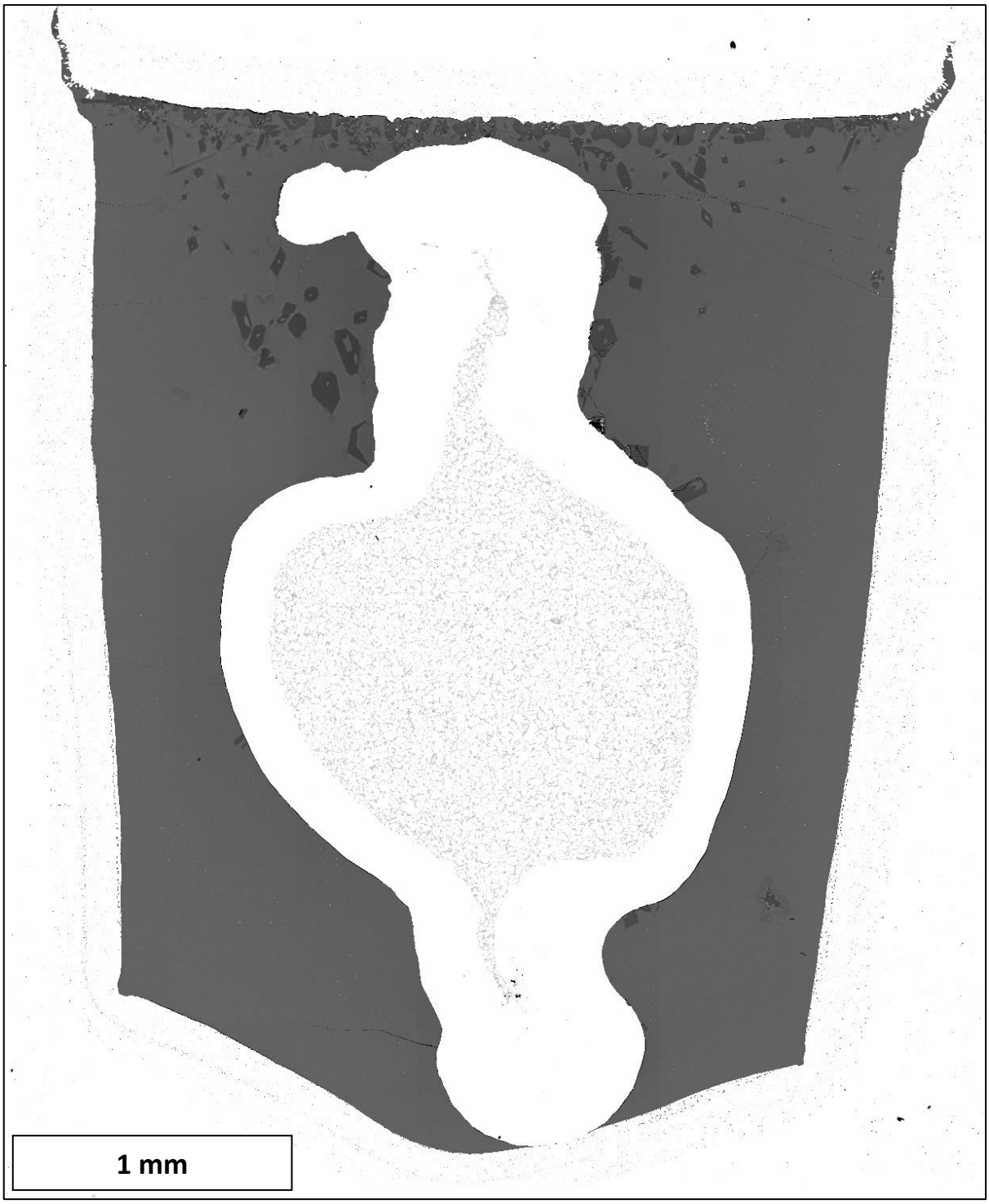


Figure 99: General view of sample LPUM 100-1 with outer iron capsule (white) and inner platinum capsule (white) with buffer material

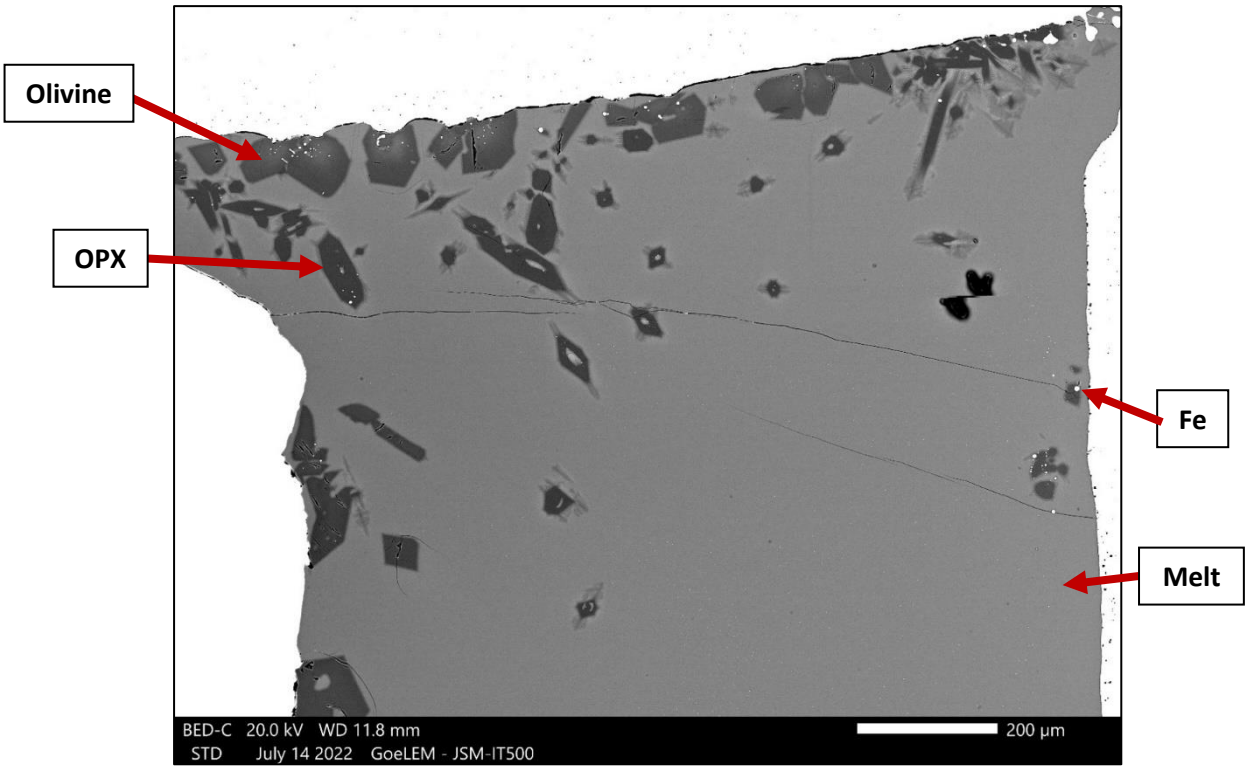


Figure 100: Close-up of sample LPUM 100-1 with pyroxene (grey), olivine (light core) and melt (light grey).

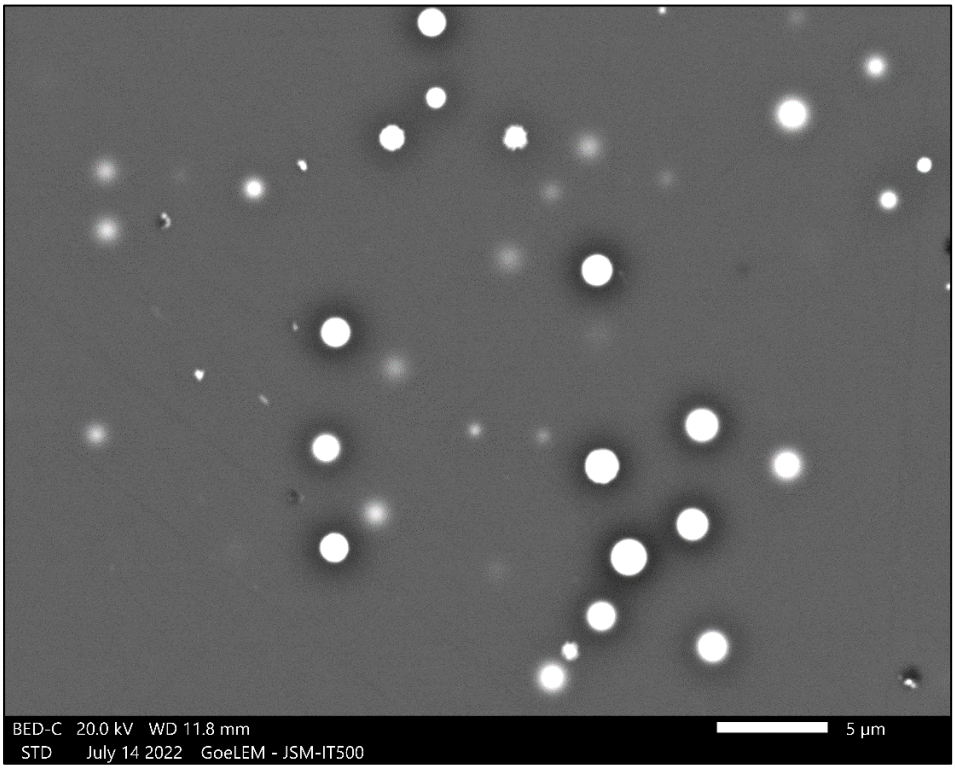


Figure 101: Close-up of sample LPUM 100-1 with Fe-nuggets inside the melt

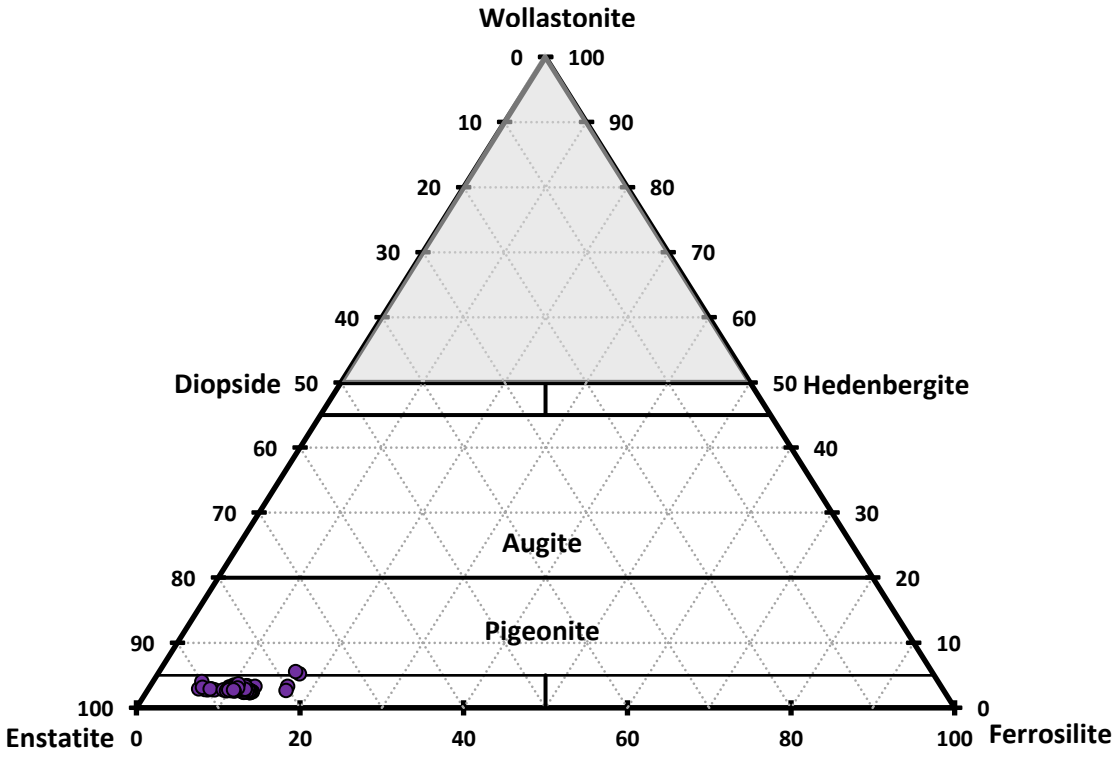


Figure 102: Mineral composition of the orthopyroxenes in sample LPUM 100-1

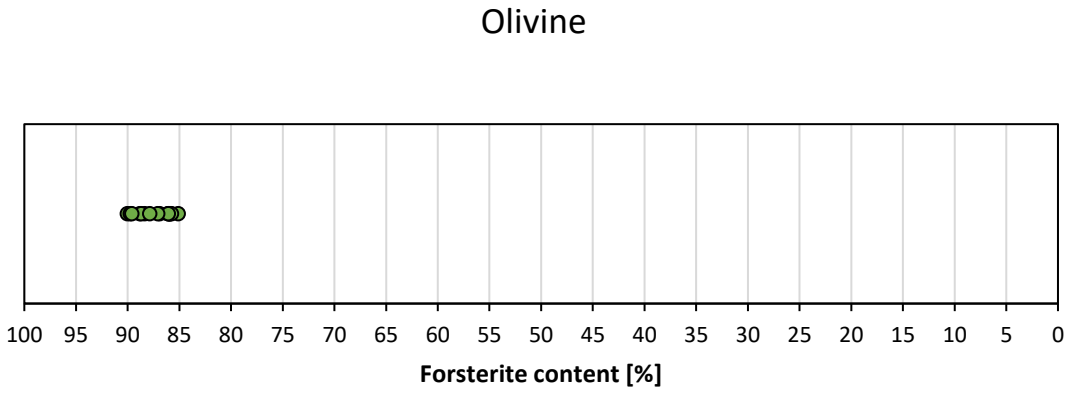


Figure 103: Mineral composition of the Pyroxenes in sample LPUM 100-1



Figure 104: Separation by grey values of sample 100-1 using MATLAB. Original image (top) and constructed image from the separation (bottom).

Orange: Melt
Green: OPX + Olivine
Black: Capsule/Holes
White: Fe-Nuggets (not visible)
Black: Capsule/Holes

3.7 LPUM 075-1 // 137 km depth

Method:	PCP	**Pressure**	0,75 GPa	**Temperature**	1230°C
Duration	3.5h	**f(O_2) Buffer:**	Cr-Cr_2O_3	**Capsule:**	Fe + Pt

Oxide	**SiO_2**	**TiO_2**	**Al_2O_3**	**FeO**	**MnO**	**MgO**	**CaO**	**Na_2O**	**K_2O**	**P_2O_5**	**Cr_2O_3**
wt%	47,36	0,65	13,08	12,33	0,06	14,53	10,18	0,52	0,05	0,10	0,78

Melt fraction:	57,4%	**Crystals:**	CPX (74,9%), Olivine (17,5%), Fe-Nuggets (4,5%), Spinell (3,1%)

Sample LPUM 075-1 (Figure 105) has a melt content of 57.4%. The solids (42.6 %) can be subdivided into 74.8% clinopyroxene, 17.5% olivine, 4.5% Fe-nuggets and 3.1% spinel (Figure 111). The minerals are heterogeneously distributed over the sample (Figure 106). In general, the mineral density increases towards the platinum capsule of the buffer. Olivine is predominantly found directly at the edge of the iron capsule, where also most of the Fe-nuggets and the melt is located. The proportion of spinel increases strongly with proximity to the platinum capsule of the buffer. The proportion of clinopyroxene also increases towards the platinum capsule but extends much closer into the sample than the spinel. The majority of the minerals show bright (i.e. denser) rims, which are probably a result of the quenching process.

The melt distribution indicates that it is no longer interconnected close to the platinum capsule due to the high crystal content. Therefore, a chemical separation within the sample is considered, which influences the crystallisation of the minerals.

The largest minerals reach dimensions of 10 - 50 µm for olivine and 5 - 30 µm for the pyroxenes. Two 100 µm olivines are found isolated in the middle capsule area (Figure 105 & Figure 107). Both mineral groups show both, idiomorphic as well as rounded crystal boundaries, presumably formed by dissolution. With <1 to 3 µm, the spinel and Fe-nuggets are much smaller and can be distinguished by their idiomorphic and xenomorphic shapes, respectively.

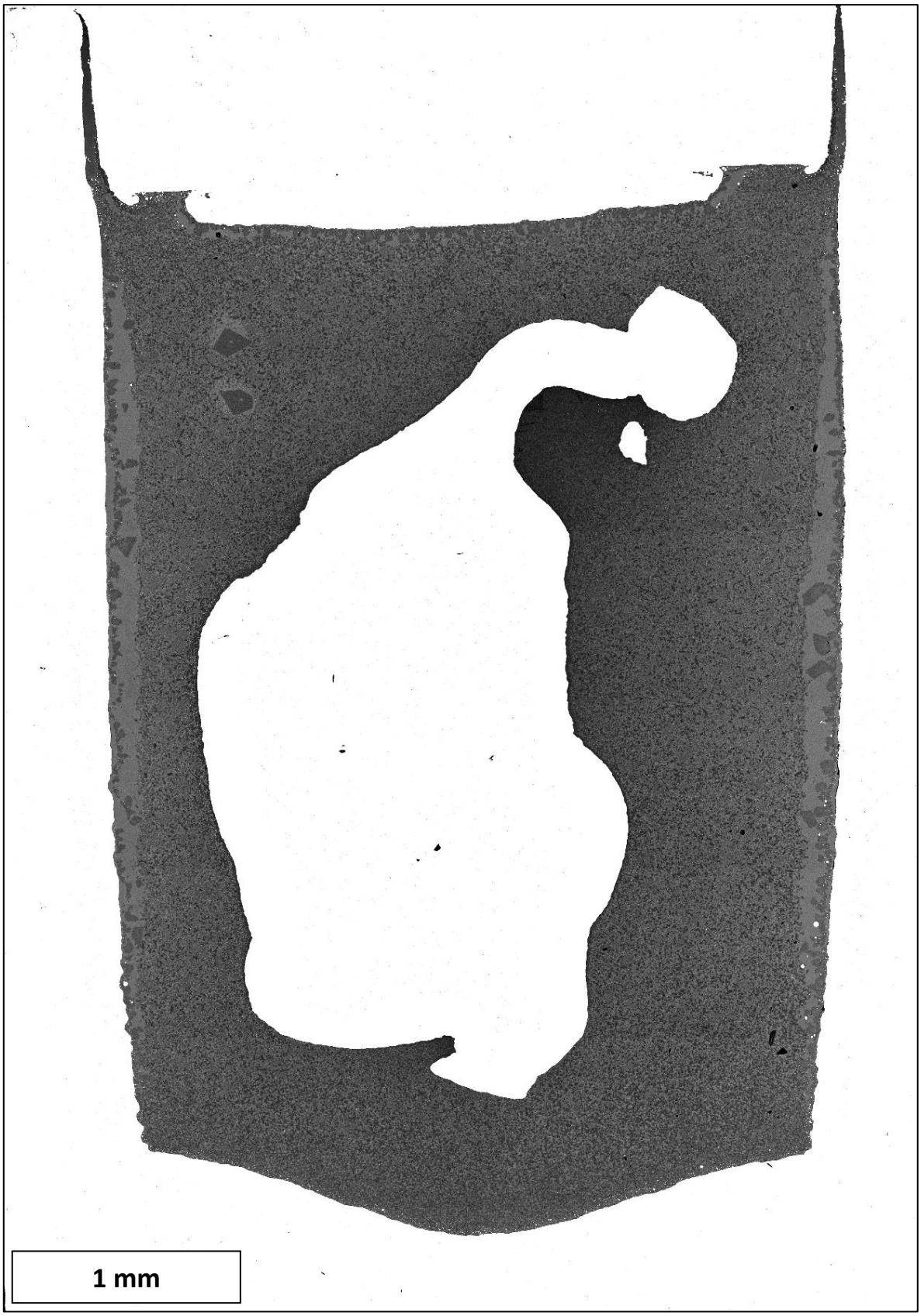


Figure 105: General view of sample LPUM 075-1 with outer iron capsule (white) and inner platinum capsule with buffer material (white).

Chemically, the majority of clinopyroxenes are pigeonites with an average composition of $En_{69.9}Fs_{15.2}Wo_{14.9}$ (Figure 108, Mineral 1-29), but also augite is found (Figure 108, Mineral 30-49). The olivine is homogeneous and can be characterised as forsterite with the composition $Fo_{81.5}Fa_{18.5}$ (Figure 109). The spinel composition is insufficiently measurable due to the small crystal size, resulting in only 6 usable measurements of 29 sampled minerals due to frequent mixed spectra with the silicate melt and/or other minerals. However, the spinel can be identified as picotite, a variety of herzynite, with the mean composition $(Fe_{0.38}Mg_{0.64})(Al_{1.54}Cr_{0.38})_2O_4$ (Figure 110). Due to the small number of successfully sampled minerals, little can be said about the homogeneity.

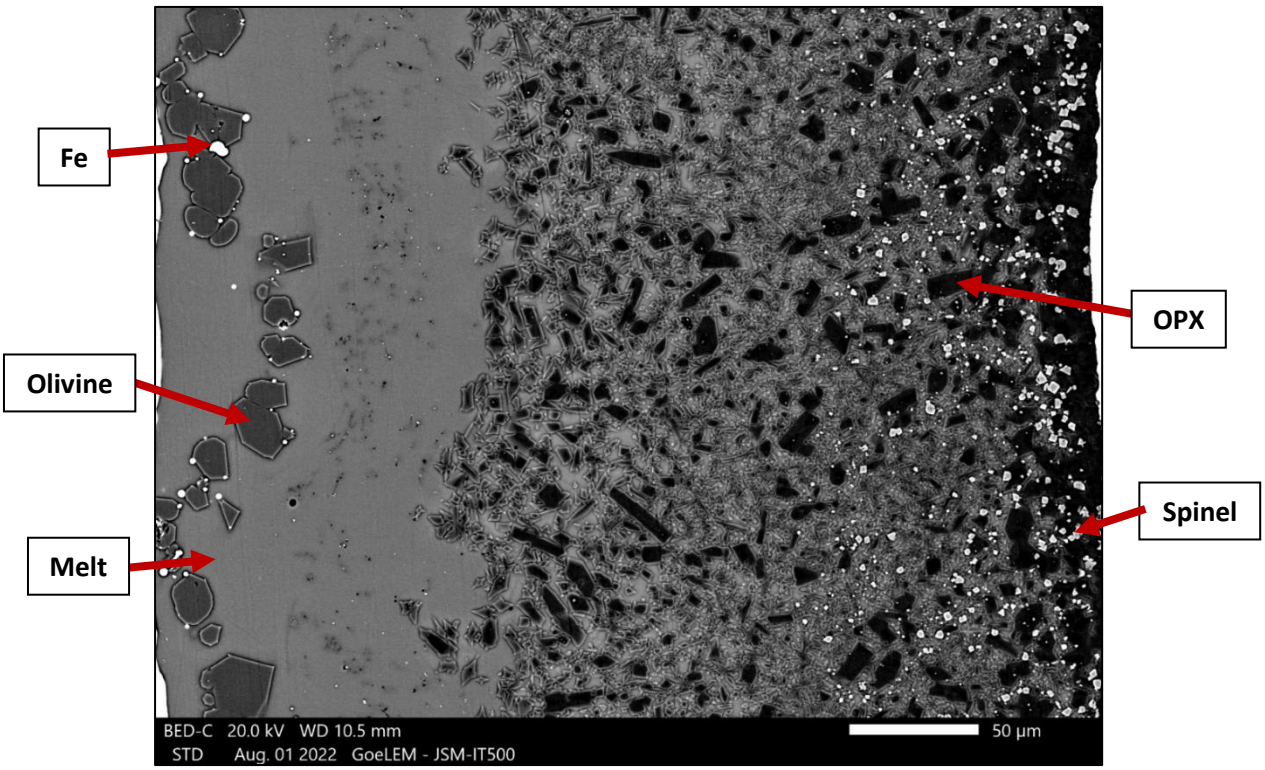


Figure 106: Close-up of sample LPUM 075-1 with visible separation of minerals (black: pyroxene; grey: olivine; white & angular: spinel; white & round: Fe-nuggets) and melt.

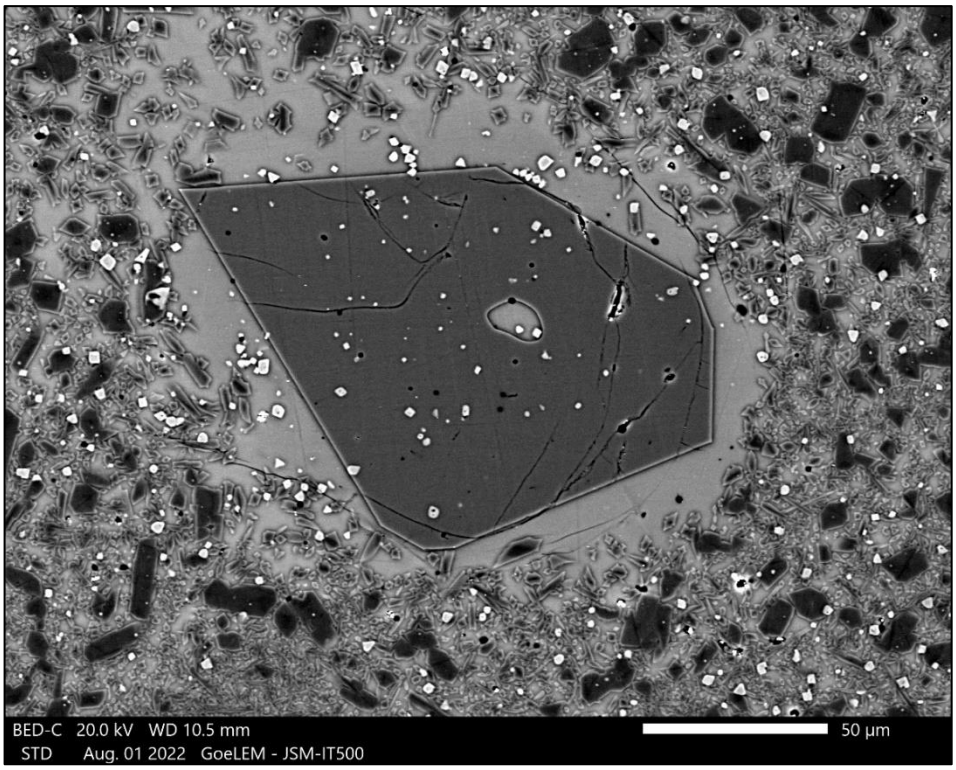


Figure 107: Close-up of sample LPUM 075-1 with one of the centrally located olivines

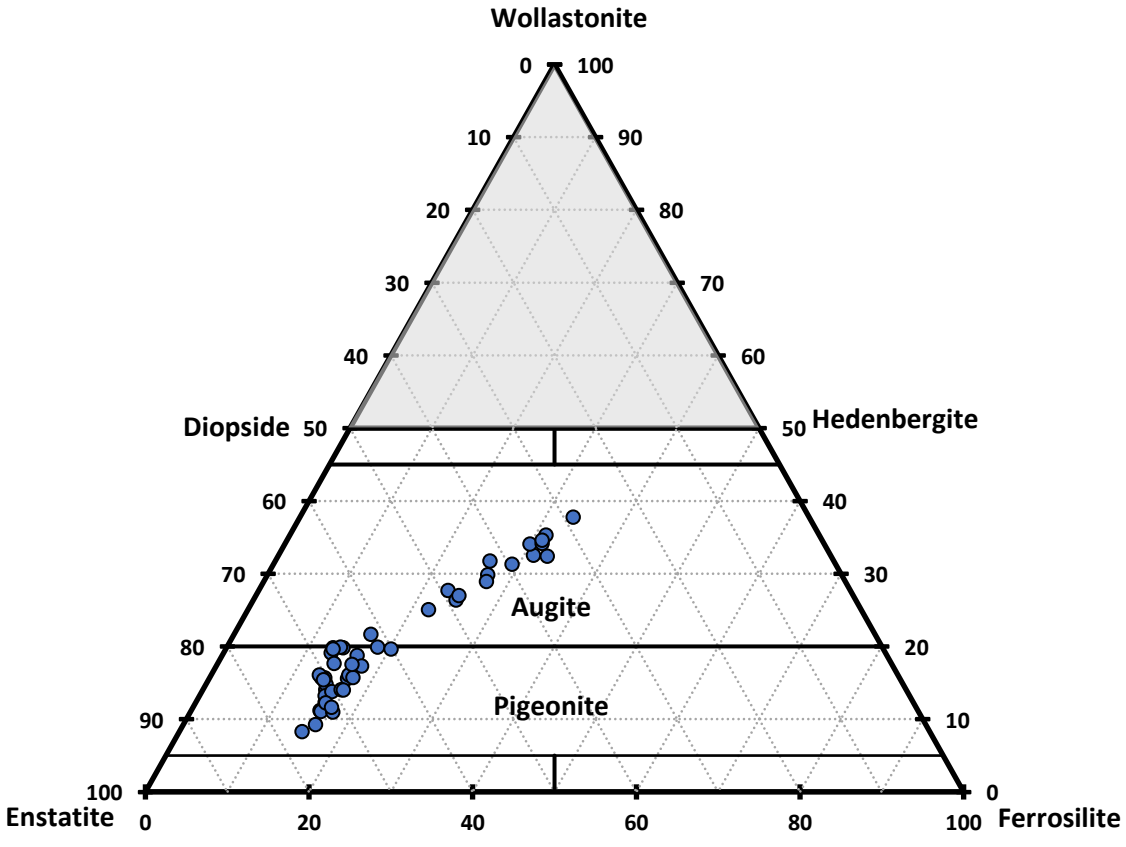


Figure 108: Mineral composition of the pyroxenes in sample LPUM 075-1.

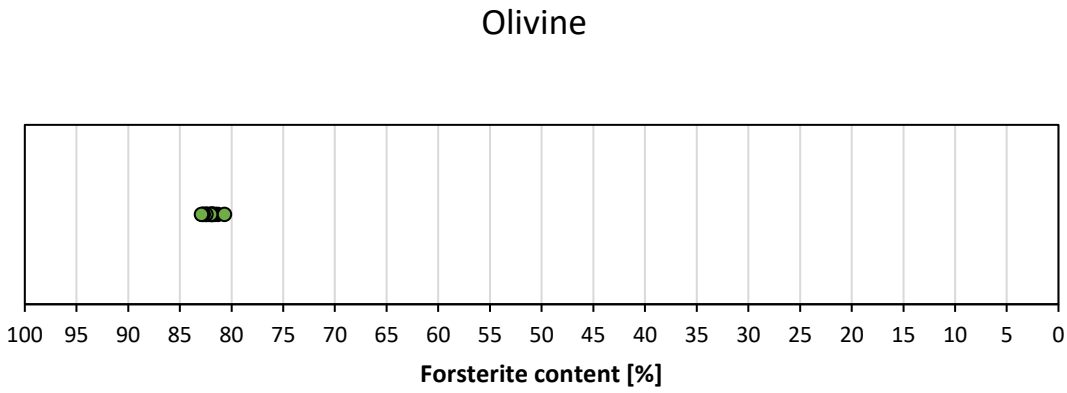


Figure 109: Mineral composition of the Pyroxenes in sample LPUM 075-1

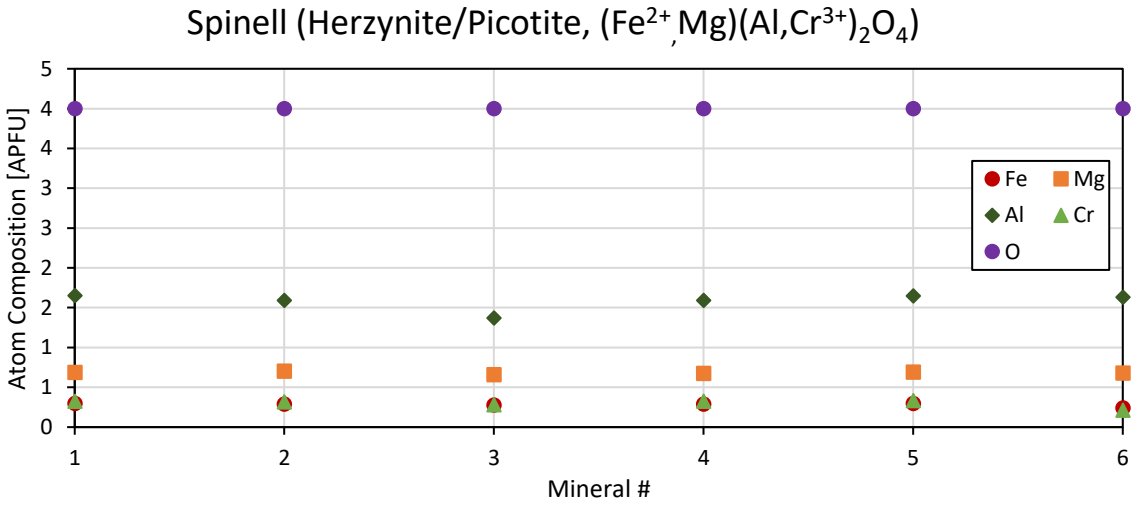


Figure 110: Mineral composition of the spinels in sample LPUM 075-1.

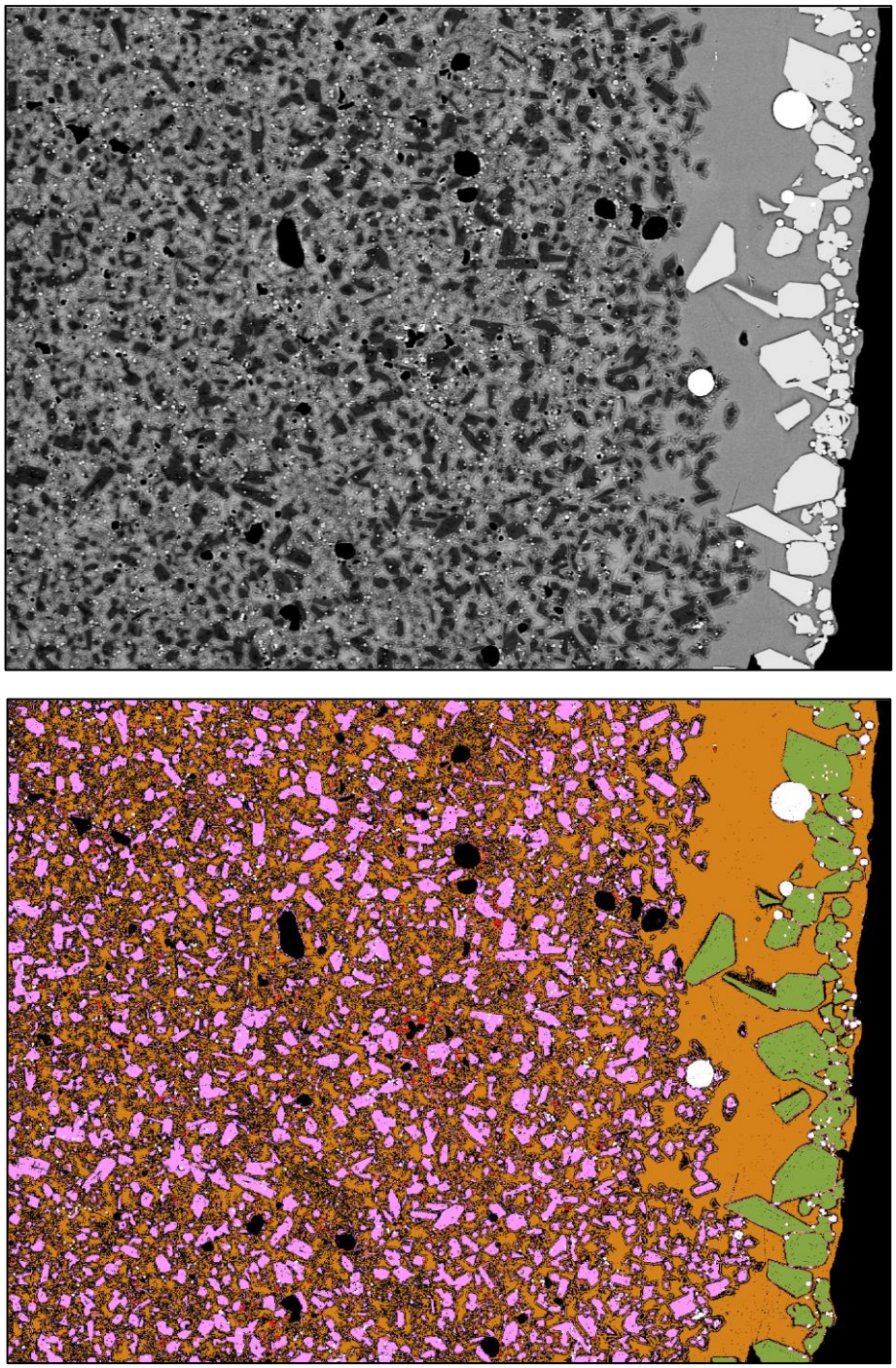


Figure 111: Separation by grey values of sample 075-1 using MATLAB. Original image (top) and constructed image from the separation (bottom)

Orange: Melt
Green: Olivine
Pink: CPX
Red: Spinel
White: Fe-Nuggets
Black: Capsule/Holes

3.8 LPUM 050-1 // 90 km depth

Method:	PCP	**Pressure**	0,50 GPa	**Temperature**	1150°C
Duration	24h	**f(O_2) Buffer:**	Cr-Cr_2O_3	**Capsule:**	Fe + Pt

Oxide	**SiO_2**	**TiO_2**	**Al_2O_3**	**FeO**	**MnO**	**MgO**	**CaO**	**Na_2O**	**K_2O**	**P_2O_5**	**Cr_2O_3**
wt%	47,91	1,36	15,89	15,53	0,27	6,15	11,01	1,28	0,08	0,48	0,04

Melt fraction:	32,3%	**Crystals:**	Plagioclase (59,3%), CPX (31,7%), Olivine (5,2%), Fe (3,9%)

Sample LPUM 050-1 has a melt content of 32.3%. Similar to the previous sample, the melt is also separated (Figure 112). This inhomogeneity is more pronounced in the right capsule half than in the left, where this effect is hardly visible. For the separated area, the melt content increases gradually from the buffer to the iron capsule.

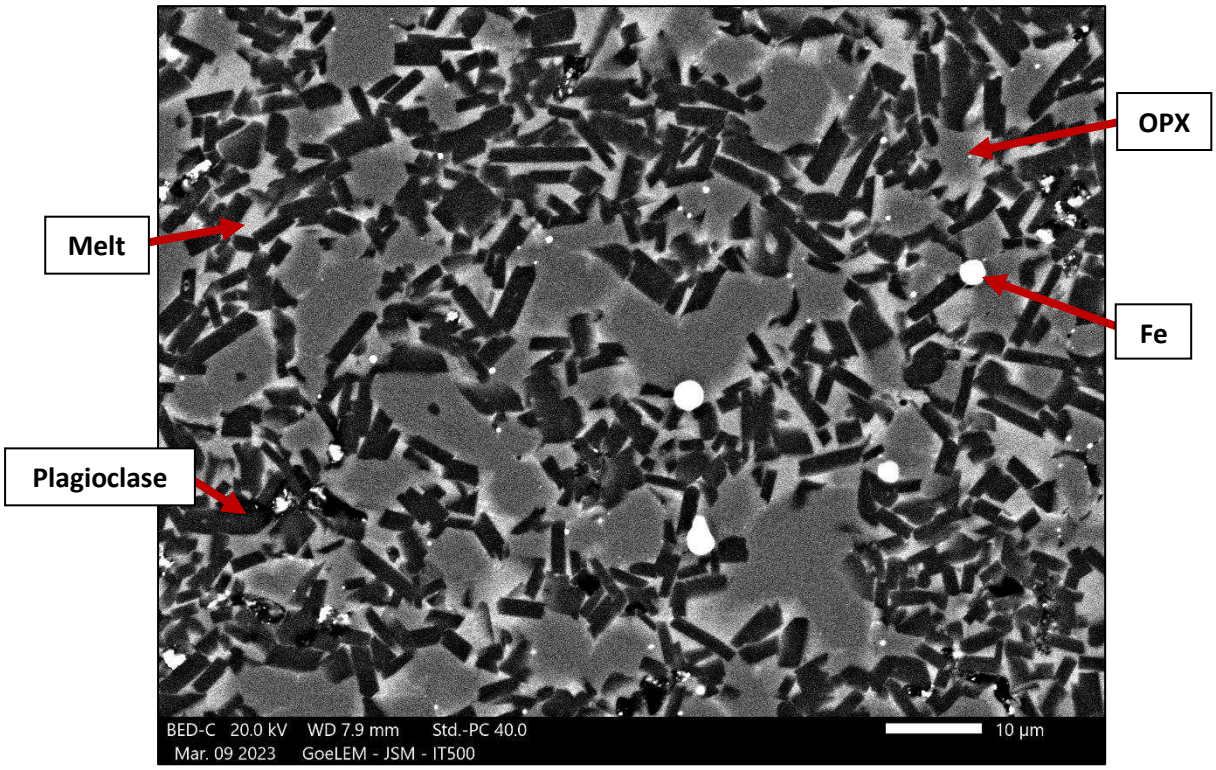
It can be assumed that the melt near the platinum capsule could not maintain contact with the rest of the sample. By means of an area analysis of the EDX detector, the deviation in the chemical composition of the three areas can be depicted (Figure 115).

This separation is also evident in the crystallisation products. Olivine is only found close to the iron capsule (Figure 114). In the middle area of Figure 114, more Fe-nuggets and smaller crystals are found than in the left area, where the crystals are larger.

Despite the high modal content of 59.3 %, the plagioclase is very small in size (<10 µm), but idiomorphic. The pyroxenes (31.7 %) and olivines (5.2 %) reach up to 30 µm and show clear crystal faces. The Fe-nuggets (3.9 %) average at 10 µm in size. Chemically, the plagioclase is $Ab_{21.6}An_{78.3}Or_{0.1}$ (bytownite) (Figure 118), the CPX is $En_{54.3}Fs_{31.4}Wo_{14.3}$ (pigeonite) (Figure 116) and the olivine is $Fo_{55.3}Fa_{46.7}$ (Figure 117).



Figure 112: General view of sample LPUM 050-1 with outer iron capsule (white) and inner platinum capsule with buffer material (white).



*F*igure 113: Detailed image of sample LPUM 050-1 with plagioclase (black), OPX (grey), melt (light) and Fe spheres (white).

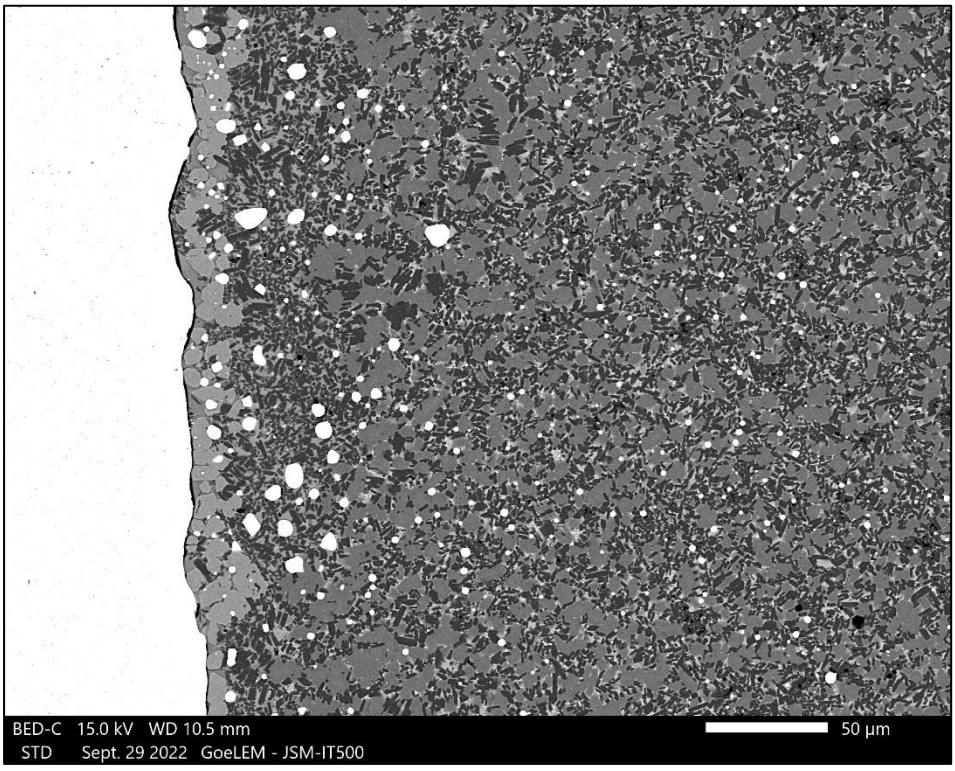
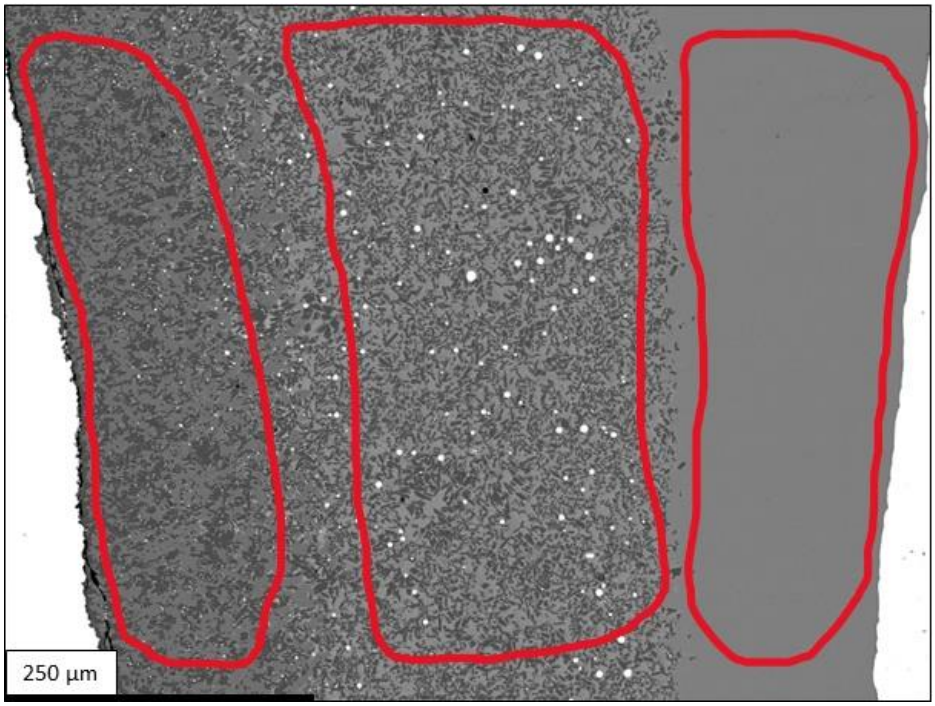
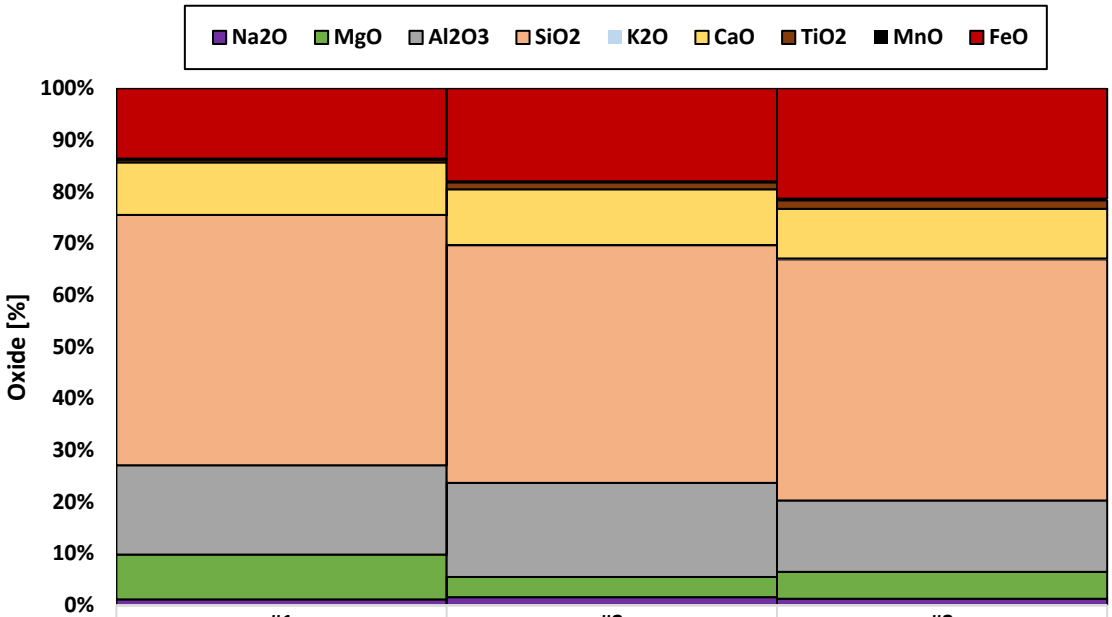


Figure 114: Close-up of sample LPUM 050-1 with olivine (light grey, at the white capsule edge, left), plagioclase (black), OPX (grey), melt (light) and Fe spheres (white).





	#1	#2	#3
FeO	13,62	18,01	21,36
MnO	0,24	0,24	0,34
TiO2	0,5	1,31	1,63
CaO	10,12	10,73	9,62
K2O	0	0,1	0,15
SiO2	48,48	45,97	46,69
Al2O3	17,25	18,18	13,77
MgO	8,65	3,89	5,22
Na2O	1,13	1,56	1,23

Figure 115: SEM image of the area of chemical separation in sample LPUM 050-1, measurement areas of the area measurements as well as their chemical composition

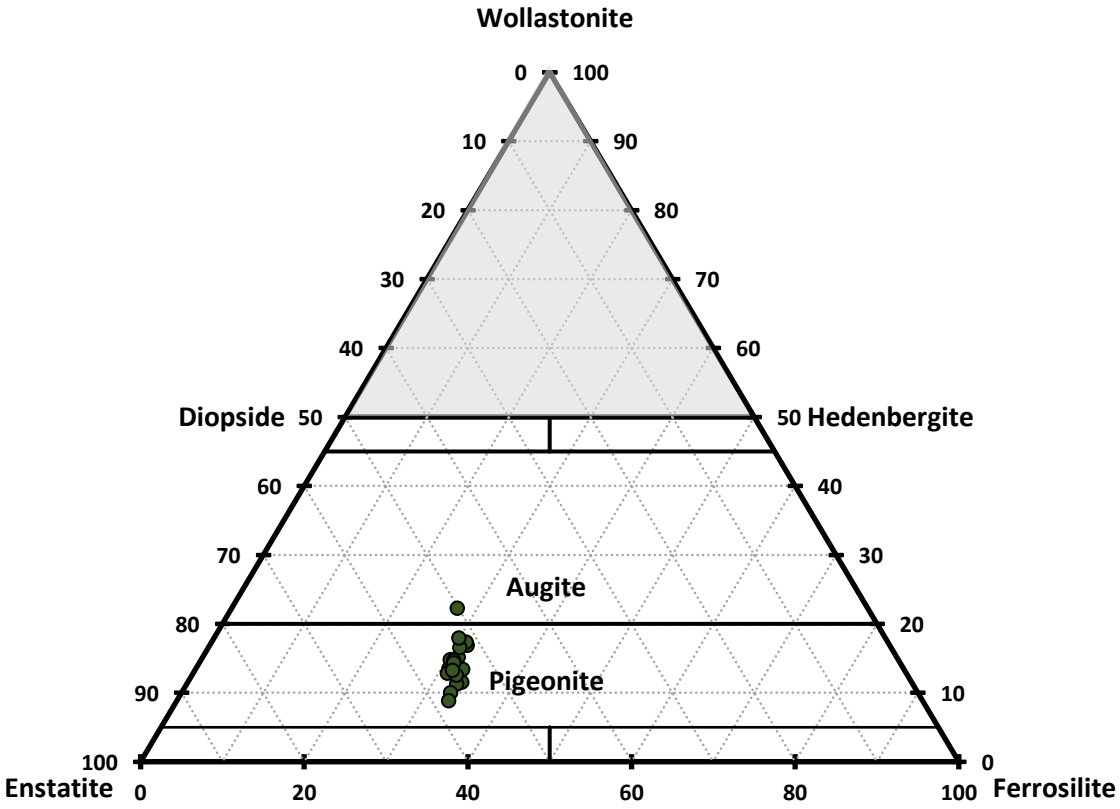


Figure 116: Mineral composition of the clinopyroxenes in sample LPUM 050-1

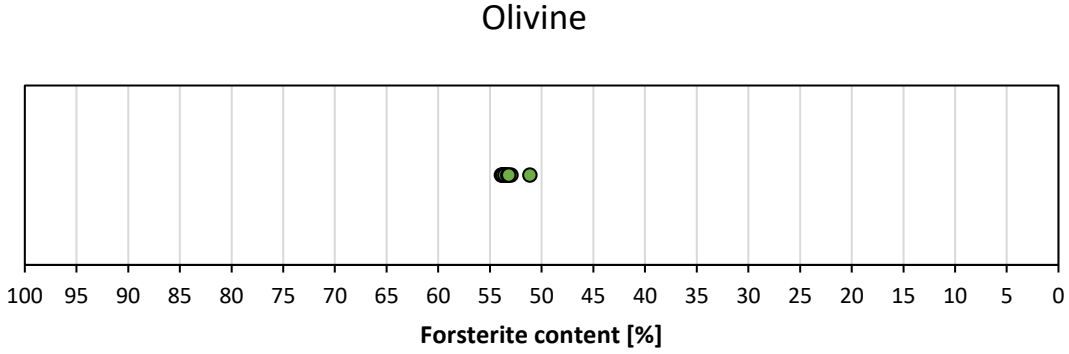


Figure 117: Mineral composition of the Pyroxenes in sample LPUM 050-1

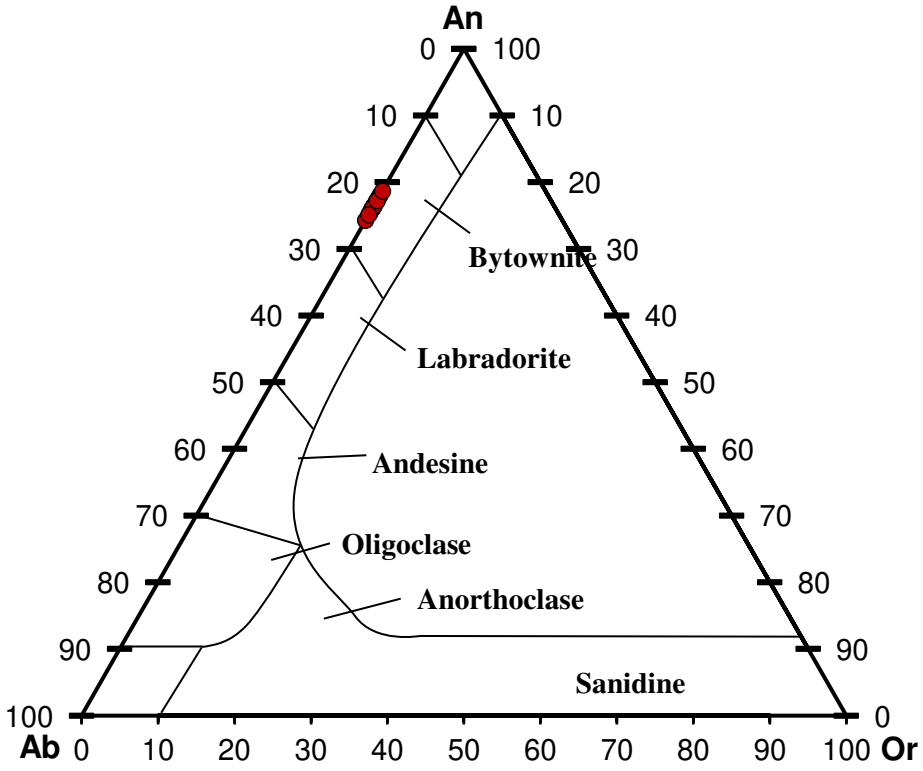


Figure 118: Mineral composition of the plagioclase in sample LPUM 050-1

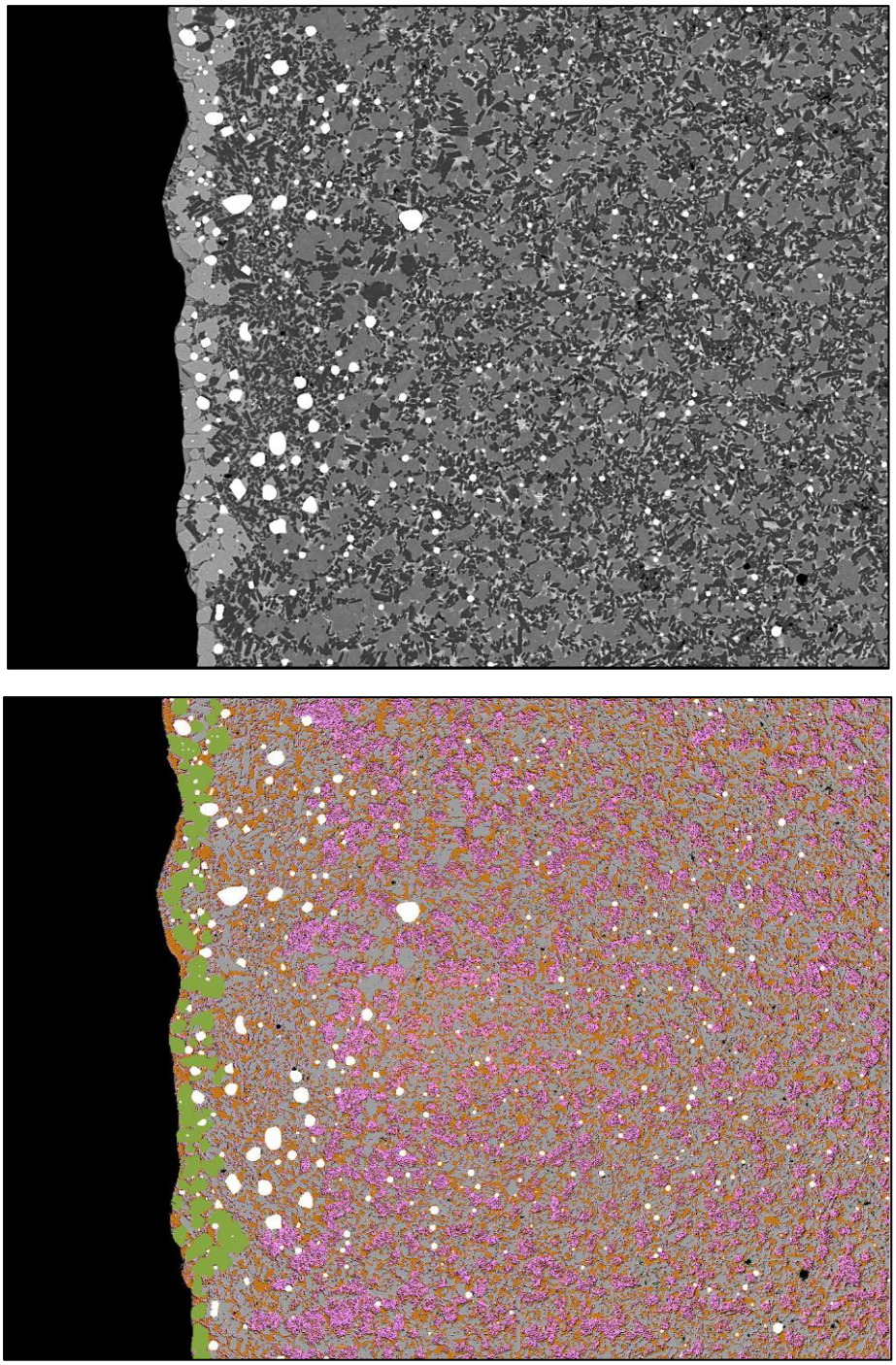


Figure 119: Separation by grey values of sample 050-1 using MATLAB. Original image (top) and constructed image from the separation (bottom).

Orange: Melt
Green: Olivine
Pink: CPX
Grey: Plagioclase
White: Fe-Nuggets
Black: Capsule/Holes

3.9 LPUM 030-1 // 53 km depth

Method:	IHPV	**Pressure**	0,30 GPa	**Temperature**	1050°C
Duration	24h	**f(O_2) Buffer:**	Cr-Cr_2O_3	**Capsule:**	Pt + Pt + Pt

Oxide	**SiO_2**	**TiO_2**	**Al_2O_3**	**FeO**	**MnO**	**MgO**	**CaO**	**Na_2O**	**K_2O**	**P_2O_5**	**Cr_2O_3**
wt%	46,14	2,51	11,20	22,74	0,36	4,29	10,03	1,64	0,06	1,01	0,02

Melt fraction:	41,6%	**Crystals:**	CPX (37,9%), Plagioclase (36,2%), Spinel (16,3%), Quartz (9,3%)

LPUM 030-1 (Figure 120) is the first low-pressure experiment to be carried out in an internally heated pressure vessel (IHPV) rather than in a piston-cylinder-press, as the latter is not designed for conditions below 0.5 GPa.

The sample consists of 41.6% melt and 58.4% solids of which 37.9% is clinopyroxene, 36.2% plagioclase, 16.3% spinel and 9.7% quartz (Figure 121, Figure 122 & Figure 125). The pyroxenes are elongated and form crystals with up to 250 µm in length. The plagioclase is also columnar and reaches a maximum of 100 µm. Quartz and spinel are much smaller with 5-20 µm. The spinel often shows idiomorphic crystals, while the quartz is xenomorphic. Among all crystal, specimens with clear signs of dissolution can be found.

The distribution of the minerals over the sample is homogeneous regardless of location. Therefore, we assume that the sample part which was lost when sawing the triple capsule had an identical composition and, thus, has no influence on the result (Figure 120).

Chemically, the clinopyroxene is augite ($(Ca,Mg,Fe)_2Si_2O_6$), which is very close to the boundary to diopside ($MgCaSi_2O_6$) (Figure 132). The measured minerals are homogeneous in composition and do not show much variation. The plagioclase can be classified as labradorite with a mean composition of $Ab_{35.0}An_{64.0}Or_{1.0}$. The metal oxides are about 60% magnetite ($Fe^{2+}Fe^{3+}{}_2O_4$), 12.8% magnesioferrite ($MgFe^{3+}{}_2O_4$), 12.4% spinel ($MgAl_2O_4$), 10.6% ilmenite ($FeTiO_3$) and 0.9% titanite ($CaTiSiO_3$).



Figure 120: General view of sample LPUM 030-1 with outer and inner platinum capsule (white). The buffer material can be seen as a shadow in the inner platinum capsule.

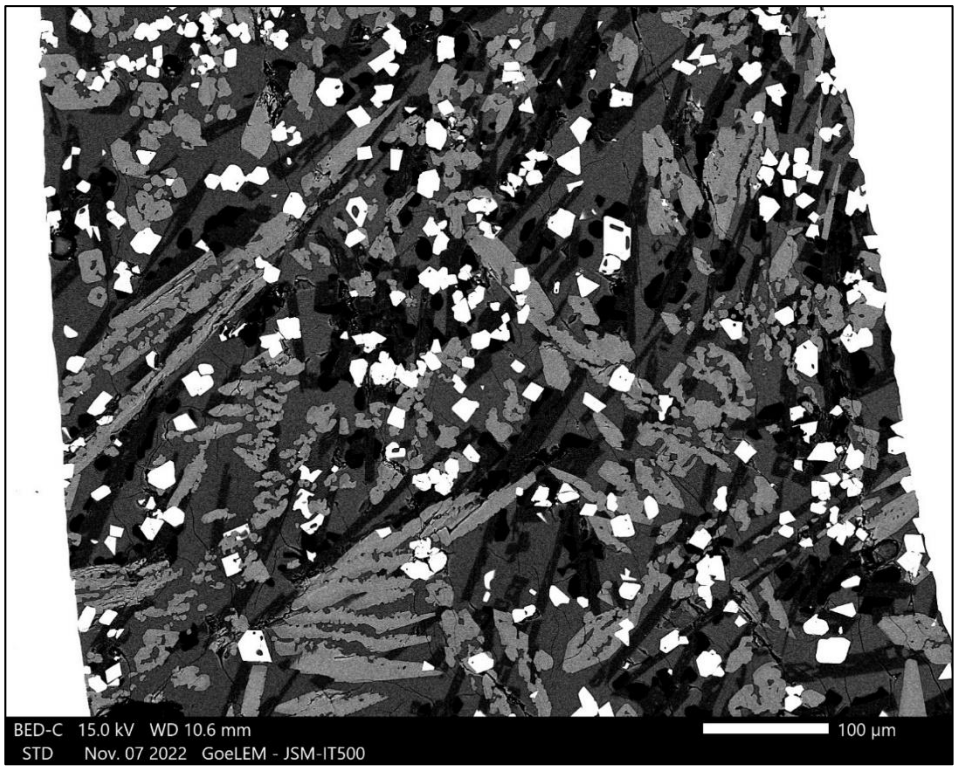


Figure 121: Close-up of sample LPUM 030-1 with quartz (black), plagioclase (almost black), melt (dark grey), clinopyroxene (light grey) and spinel (white).

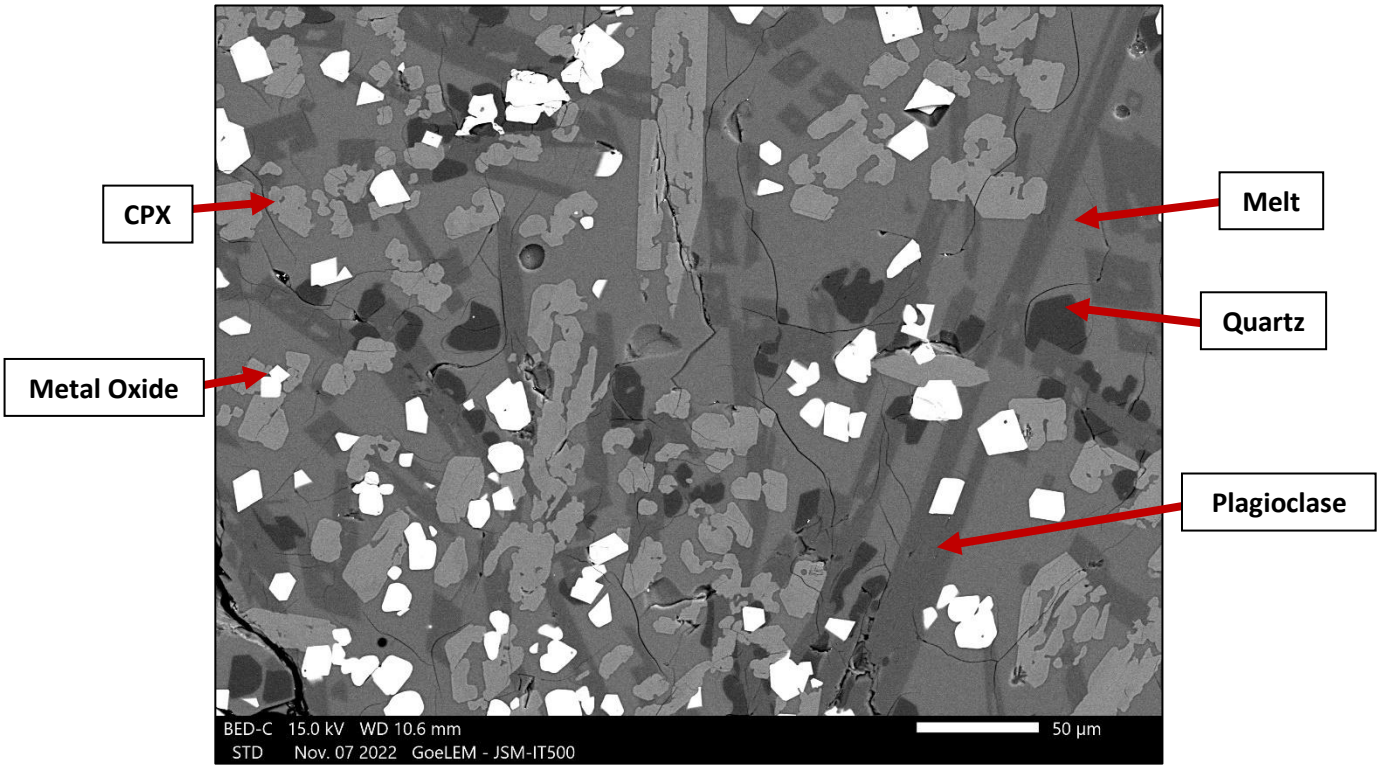


Figure 122: Close-up of sample LPUM 030-1 showing quartz (black), plagioclase (dark grey), fusion (grey), clinopyroxene (light grey) and spinel (white).

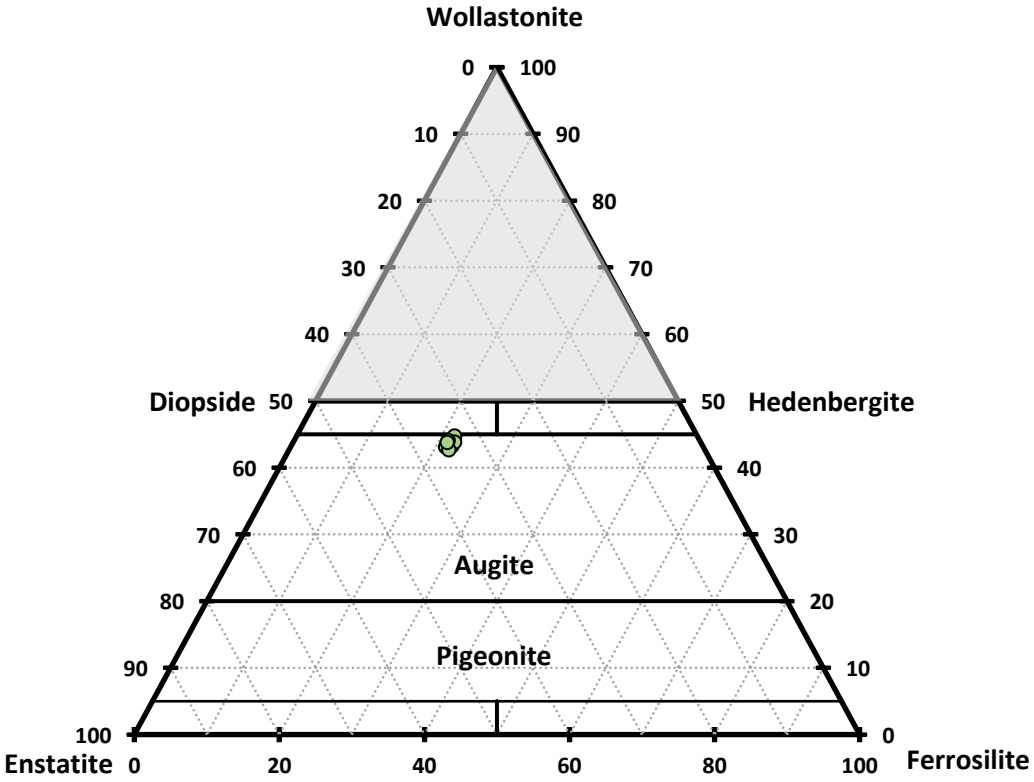


Figure 123: Mineral composition of clinopyroxene in sample LPUM 030-1

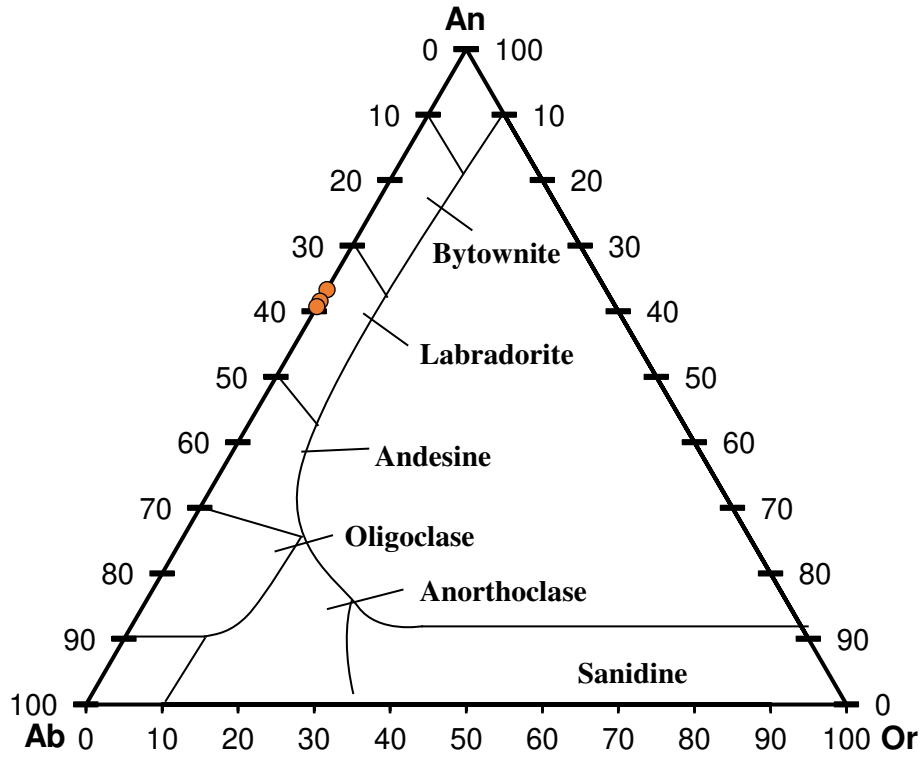


Figure 124: Mineral composition of the plagioclase in sample LPUM 030-1.

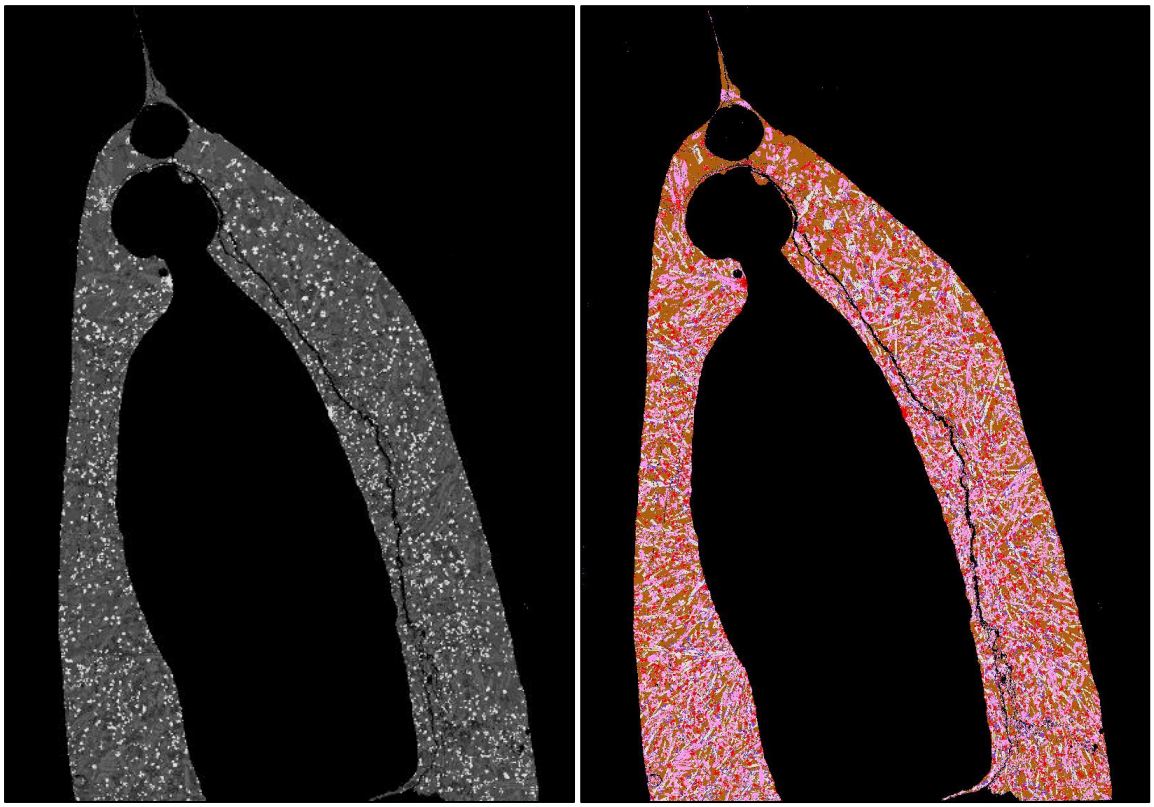


Figure 125: Separation by grey values of sample 030-1 using MATLAB. Original image (left) and constructed image from the separation (right)

Orange: Melt
Pink: CPX
Grey: Plagioclase
Red: Spinel
Purple: Quartz
Black: Capsule/Holes

3.10 LPUM 020-1 // 35 km depth

Method:	IHPV	**Pressure**	0,20 GPa	**Temperature**	1025°C
Duration	2h	**f(O_2) Buffer:**	Cr-Cr_2O_3	**Capsule:**	Pt + Pt

Oxide	**SiO_2**	**TiO_2**	**Al_2O_3**	**FeO**	**MnO**	**MgO**	**CaO**	**Na_2O**	**K_2O**	**P_2O_5**	**Cr_2O_3**
wt%	45,42	3,70	8,65	25,70	0,42	2,57	9,92	1,09	0,06	1,56	0,01

Melt fraction:	27,0%	**Crystals:**	Plag. (29,9%); Magnetite (26,8%); CPX (26,2%); Quarz (12,3%)

Sample LPUM 020-1 (Figure 126) is another IHPV experiment consisting of a platinum double capsule, with the buffer being located in the outer capsule. As in experiment 150-3, 2 µL of water was added to the specimen to investigate the influence on the buffer effect in the IHPV experiment. The capsule shows no cracks and is not inflated. More details on the investigation of the buffer behaviour can be found in chapter 3.12, page 168.

Due to the short crystallisation time of 2h, the crystals in LPUM 020-1 are very small with an average of 1-4 µm (Figure 127 & Figure 128). At the same time, their distribution over the sample is homogeneous, although local clusters have formed. These consist of plagioclase and quartz surrounding a region of clinopyroxene and melt (Figure 127). The contained iron-titanium oxides are evenly distributed across the sample.

The mineralogically largest proportion is formed by plagioclase with an average of $An_{69.0}Ab_{30.9}KSP_{0.1}$ (bytownite / labradorite) (29.9%) (Figure 134). The metal oxides have an insignificantly lower proportion of about 26.8%. Their composition cannot be derived without exact knowledge of the cation speciation. If ilmenite is assumed to be the titanium sink, a mixture of 65.6% magnetite ($Fe^{2+}Fe^{3+}{}_2O_4$), 24.9% ilmenite ($FeTiO_3$), 5.0% spinel ($FeAl_2O_4$) and 4.6% titanite ($CaTiSiO_3$) can be calculated. Another 26.2% of the sample is formed by augite with a mean composition of $En_{25.0}Fs_{34.2}Wo_{40.8}$. Quartz ($SiO_2$) accounts for a proportion of 12.3% of all solids. The composition of the minerals shows more variation than in other samples (Figure 129 & Figure 130). It is possible that a final equilibrium has not yet been reached due to the short runtime. To derive the given mineral proportions, an average of different BSE-images was used since the mineral composition varies from image to image (Figure 131).

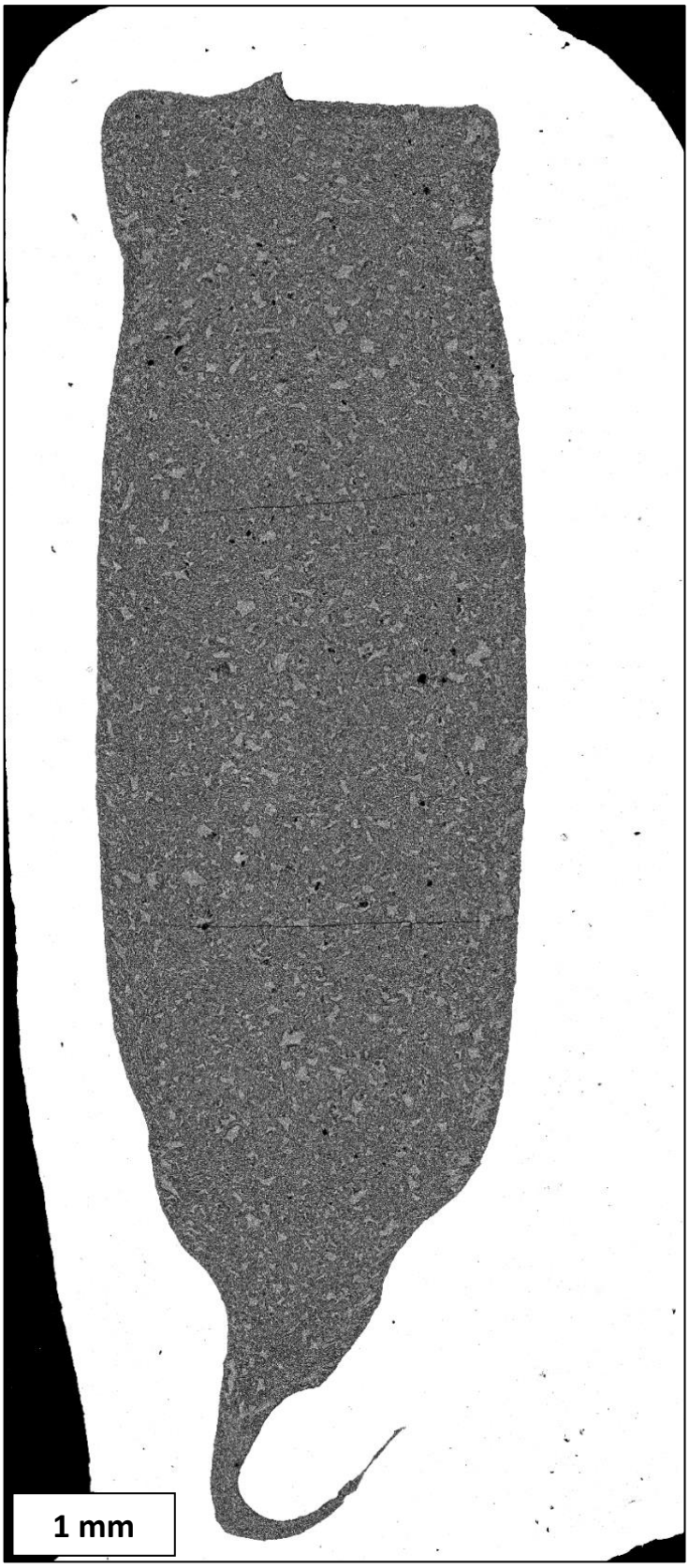


Figure 126: General view of sample LPUM 020-1 with outer and inner platinum capsule (white). The buffer material is contained within the white area around the sample.

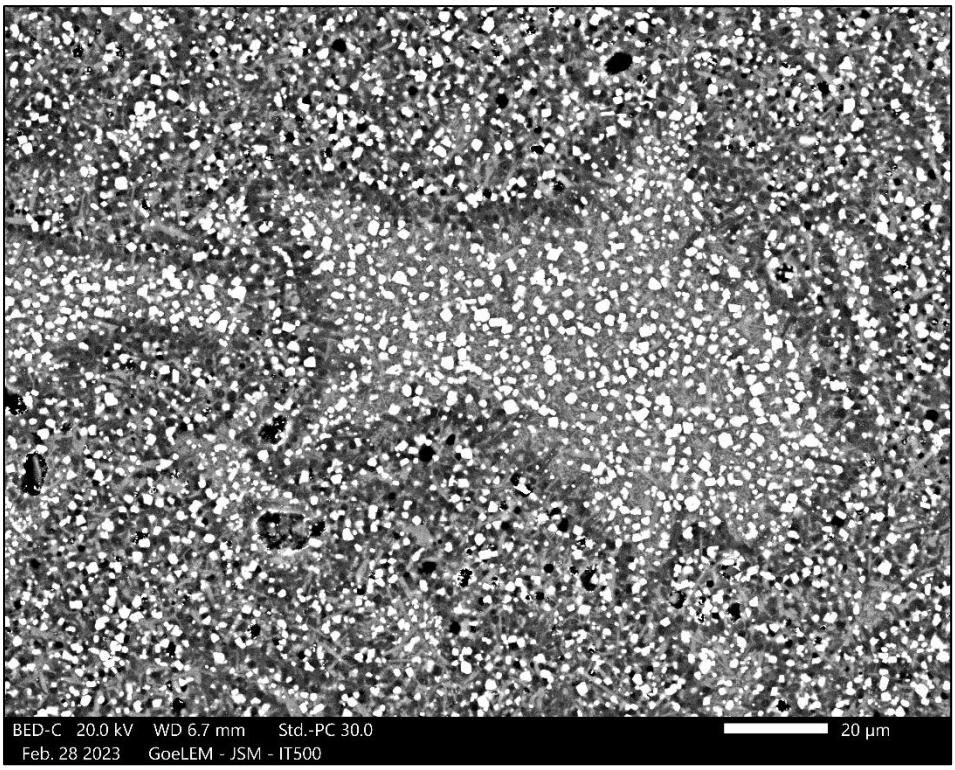


Figure 127: Detail image 1 of sample LPUM 020-1 with magnetite (white), pyroxene (light grey), fusion (grey), plagioclase (dark grey) and quartz (black).

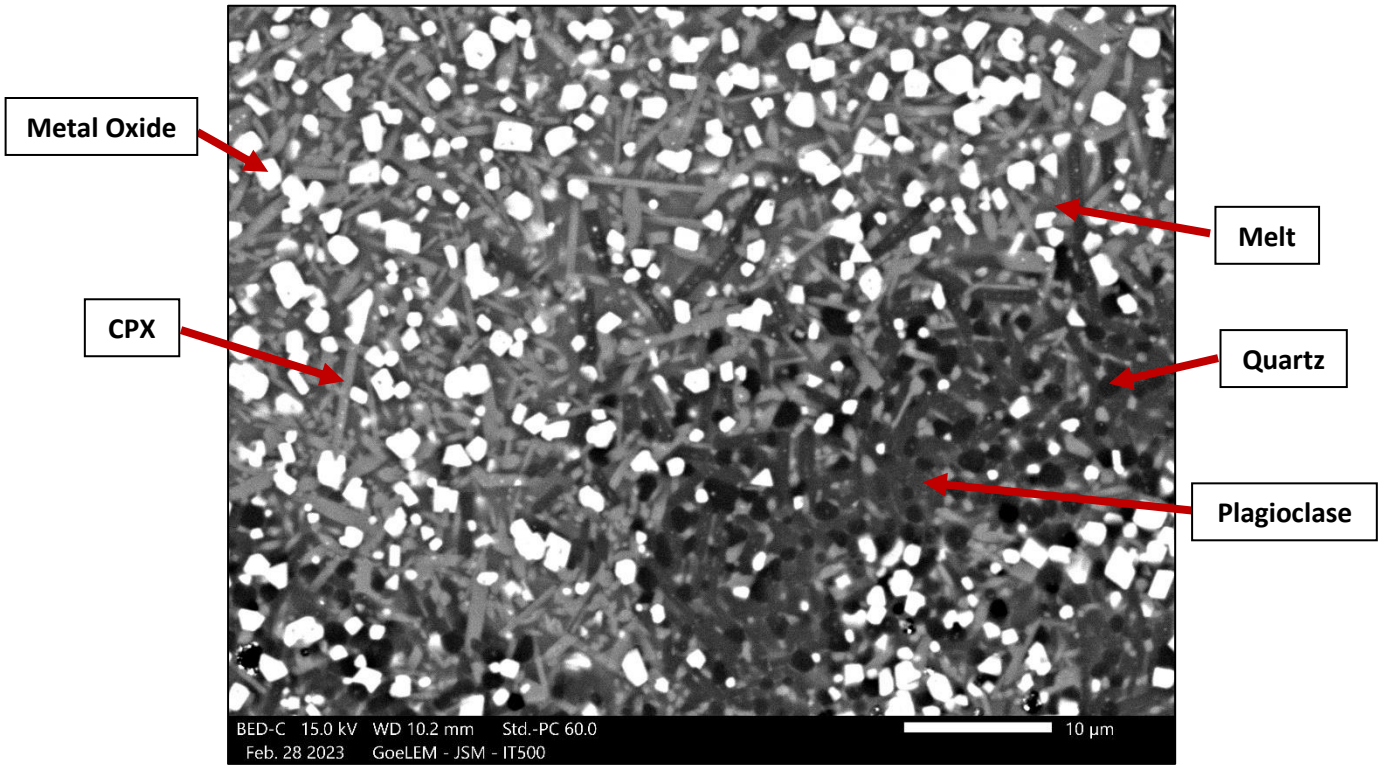


Figure 128: Close-up 1 of sample LPUM 020-1 with magnetite (white), pyroxene (light grey), fusion (grey), plagioclase (dark grey) and quartz (black).

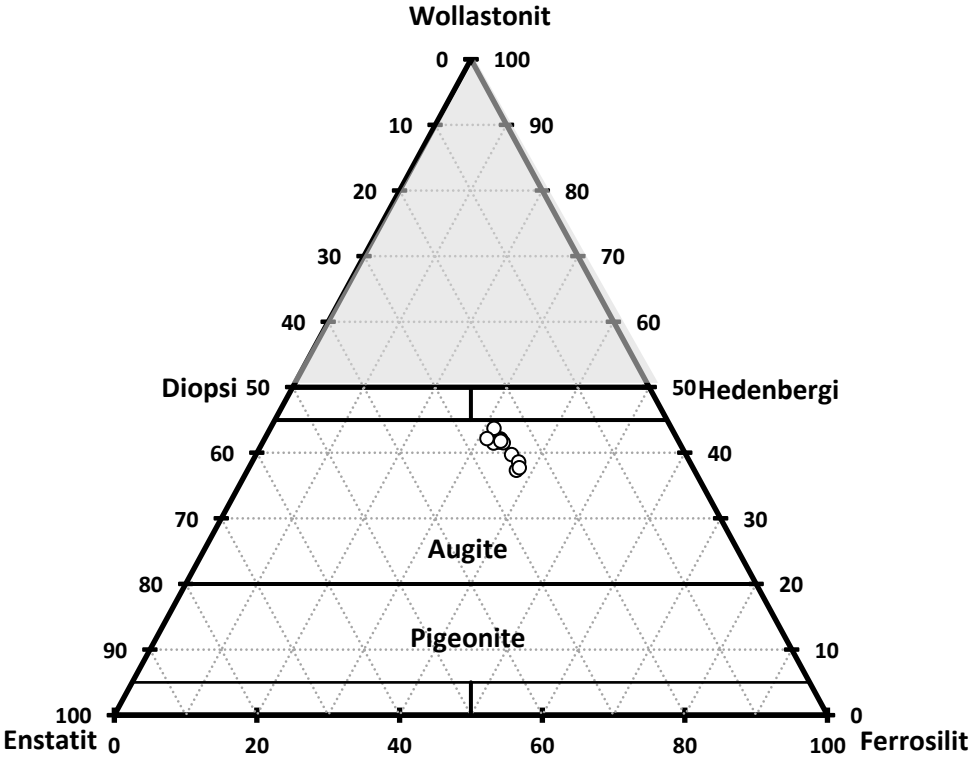


Figure 129: Mineral composition of clinopyroxene in sample LPUM 020-1

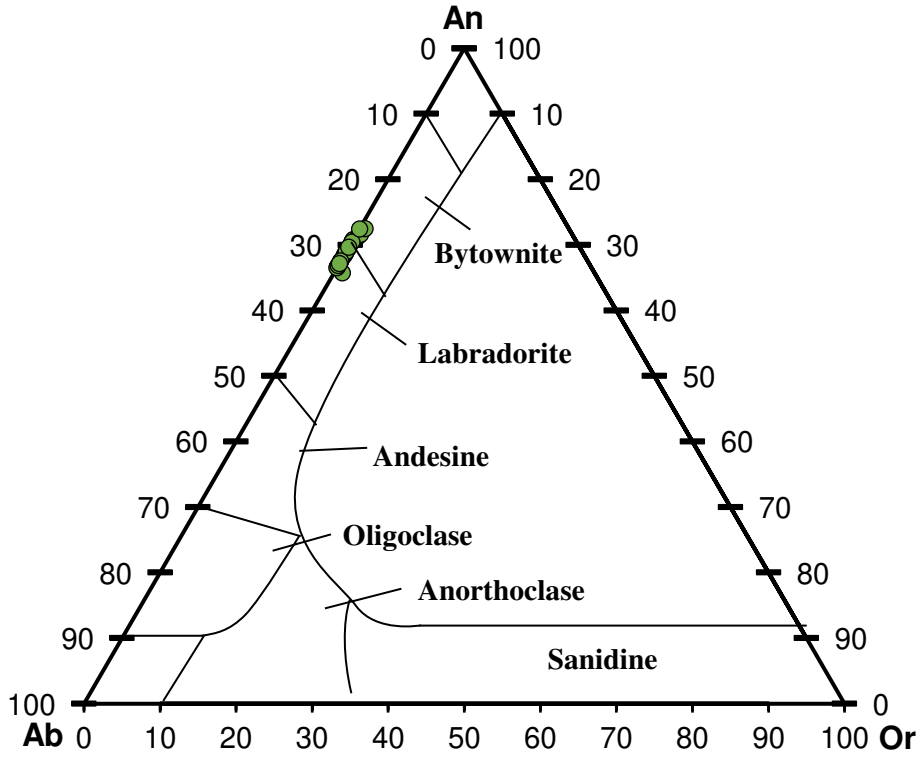


Figure 130: Mineral composition of the plagioclase in sample LPUM 020-1.

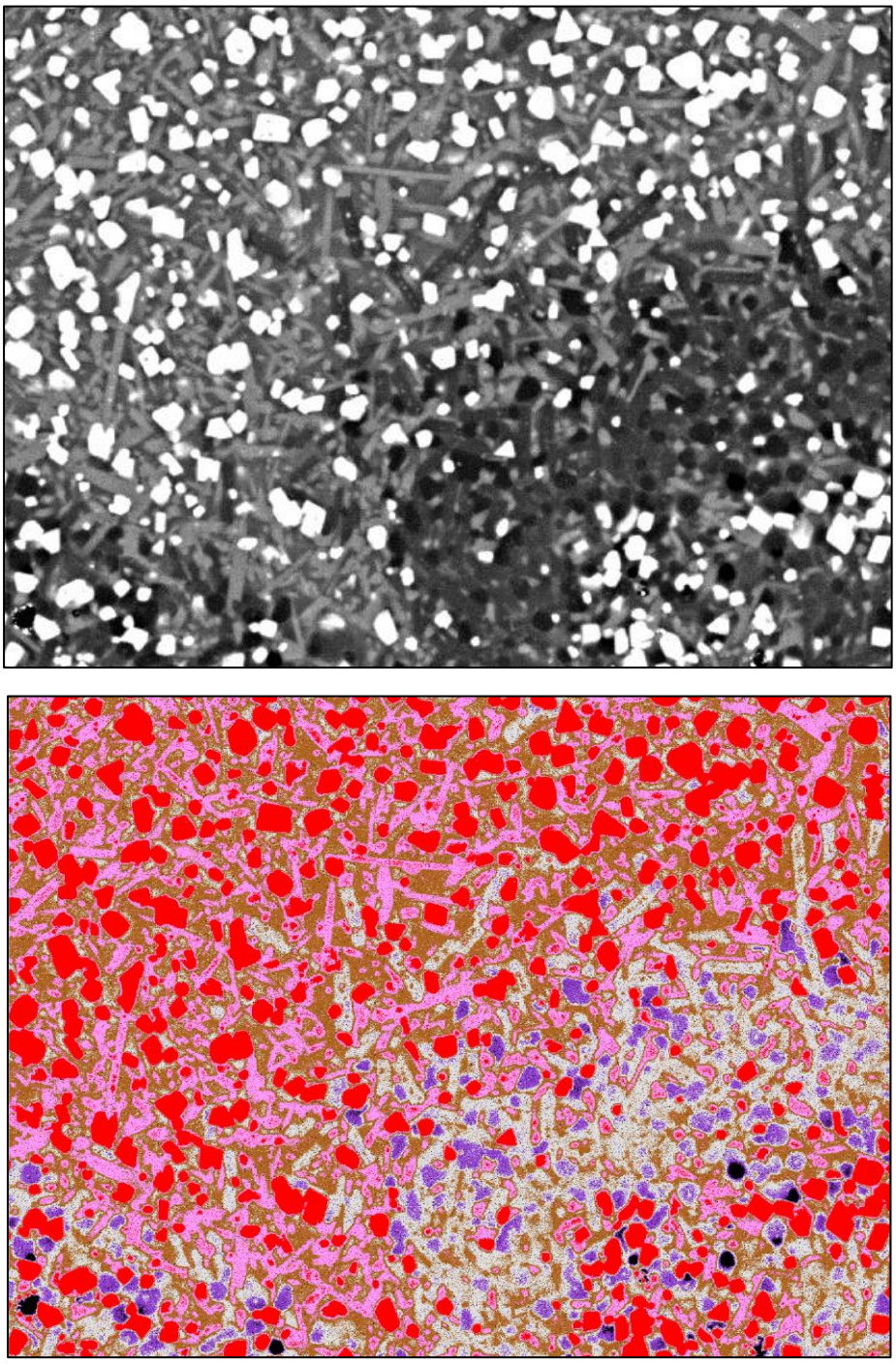


Figure 131: Separation by grey values of sample 020-1 using MATLAB. Original image (top) and constructed image from the separation (bottom).

Orange: Melt
Grey: Plagioclase
Purple: Quartz
Red: Spinel
Black: Capsule/Holes

3.11 Summary of the mineral compositions

If the mineral compositions are plotted in the corresponding ternary plots, the picture shown in Figure 132 emerges for the pyroxenes. Over wide areas (LPUM 300-1 to LPUM 100-1) only enstatite is found, even if it gains iron content to a small extent. In relation to the Moon, this covers a depth of 1400km to 168km. After that, the composition changes much more rapidly. Both calcium and iron content increase steadily, so that in LPUM 075-1 and LPUM 050-1 pigeonites are found (137km - 90km) and finally in LPUM 030-1 and 020-1 augites (53km - 35km).

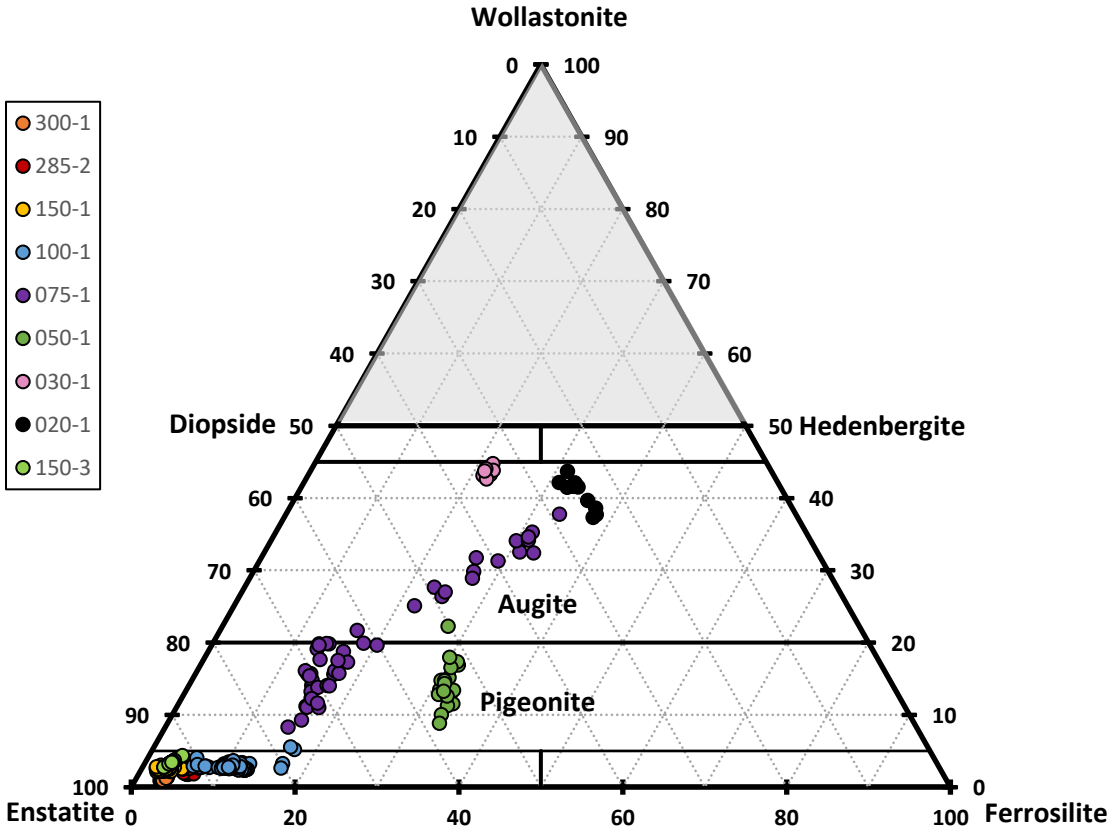


Figure 132: *Classification of the pyroxene in all applicable experiments*

The composition of the olivine is plotted in Figure 133 as forsterite content. 3 out of 9 samples contain no olivine. In the remaining samples, there is a clear trend from magnesium-rich olivine to an iron-rich fayalite component. Here, too, the iron content in the mineral increases significantly faster from experiment LPUM 075-1 onwards, which corresponds well with the trend of the pyroxenes in Figure 132.

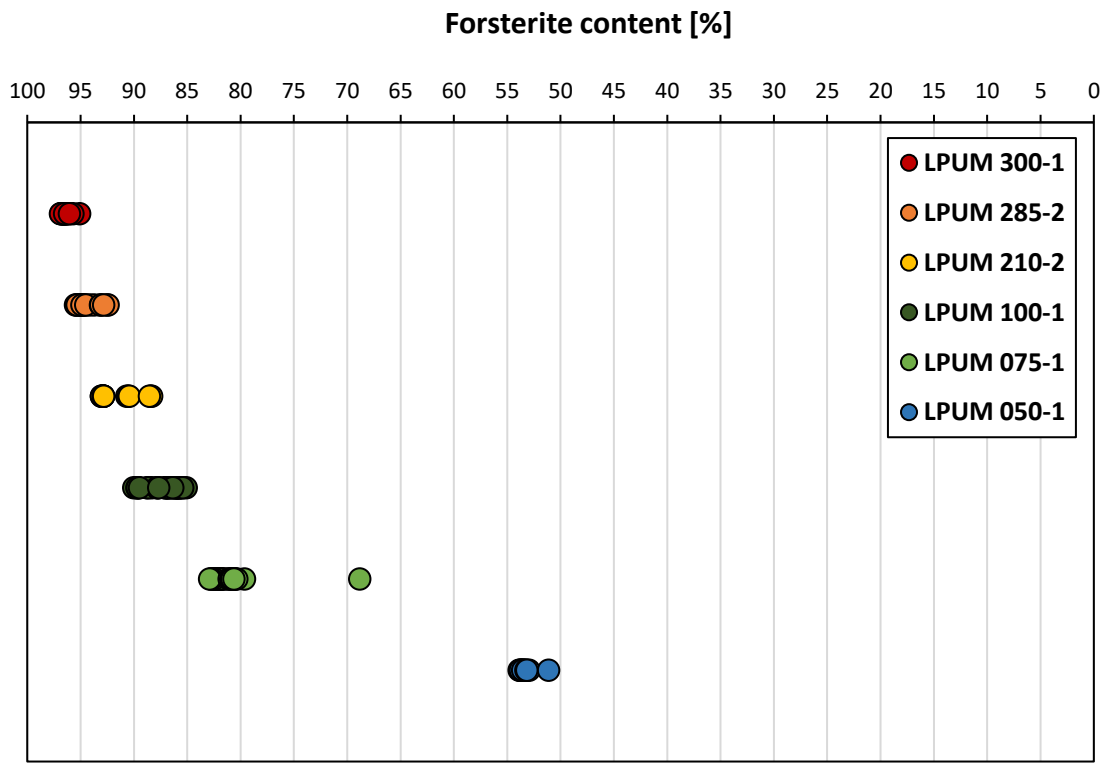


Figure 133: Forsterite content of olivine across all applicable experiments

Plagioclase was found in three experiments (050-1, 030-1 and 020-1). This shows an anorthite content between 60% and 80%. Orthoclase is almost absent, clearly reflecting the very low potassium composition. The plagioclases can thus be classified as labradorites and bytownites (Figure 134). Compared to crustal samples from the Apollo-era, this is much less Anorthite content than found for the Moon but comparable to contents found in Rapp and Draper (2018).

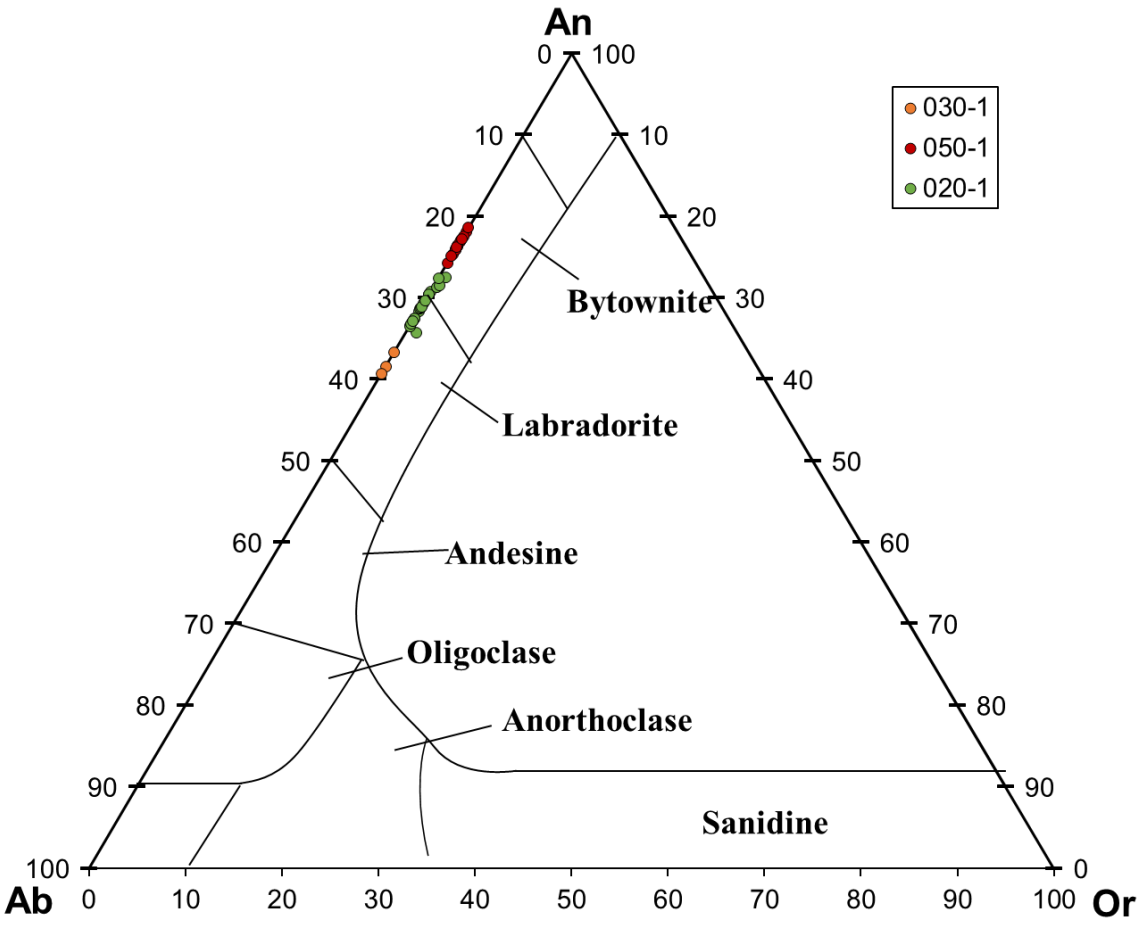


Figure 134: Classification of feldspar for alll applicable experiments

3.12 Buffer development

A buffer is a chemical reaction intended to keep the oxygen available for reaction at a defined level. However, it is not trivial to check if the target conditions have been reached.

One first indicator is whether and in what ratio the product and reactant of the buffer reaction are present. If one of the components is missing, the buffer is used up and is not able to maintain the conditions for the full duration of the experiment. However, even if both components are present, there may be a misinterpretation: The reaction may have been inhibited or stalled by rim formation of the components or an insufficient surface-to-volume ratio and resulting long diffusion pathways.

Even when those parameters are inconspicuous, the conditions must be transferred into the sample material by the following mechanism: The H_2/H_2O ratio in the buffer material increases with decreasing oxygen fugacity. Hydrogen is, thus, produced, which diffuses almost unhindered through the capsule wall of the buffer into the sample, where it generates the redox conditions in the sample material via reaction (12).

$$Fe_2O_3 + H_2 \Leftrightarrow 2FeO + H_2O \quad (12)$$

The buffer reaction continues until the water in the buffer is completely consumed while the produced hydrogen is oxidised to water in the sample. Once an equilibrium has been reached within the sample, the excess H_2 accumulates. H_2 hardly dissolves in the melt and therefore builds up gas pressure reaching thousands of bar and thus can cause capsules to inflate or burst, as sample LPUM 150-3 shows. Since reaction 12 generates water in the sample, the buffer materials were used nominally dry to not unnecessarily increase the water content of our otherwise dry specimens.

As we used Cr-Cr_2O_3 buffers for our runs, the corresponding reaction in our buffers can be written as (13)

$$2\ Cr\ +\ 1{,}5\ O_2\ \Leftrightarrow\ Cr_2O_3 \quad (13)$$

Therefore, the electron-optical image of our buffers should show a shift in the ratio between Cr and Cr_2O_3 in case of a successful reaction. For the generation of reduced conditions, oxygen needs to be bound and thus, the shift should only be in favour of the formation of Cr_2O_3.

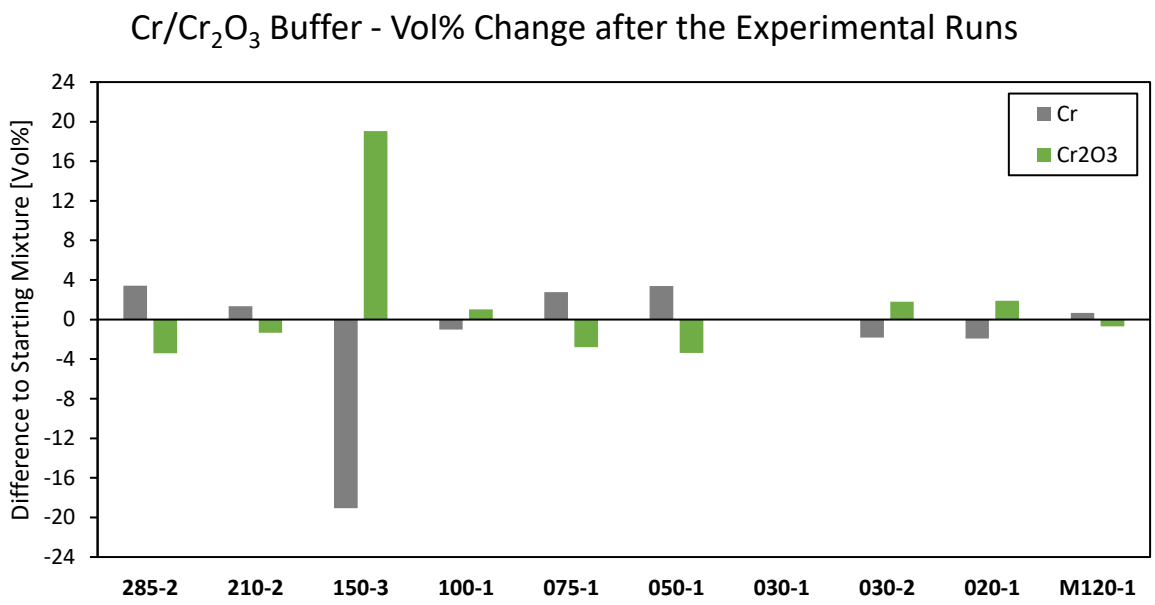


Figure 135: Difference in the ratio of vol% chromium and Cr_2O_3 to the calculated volume of both phases in the starting material. Sample 030-1 matches exactly the starting content and is therefore barely visible.

We used a ratio of 90 mol% Cr and 10 mol% Cr_2O_3 for the starting material of the buffer. Combined with the density of chromium (7.14 g/cm^3) and Cr_2O_3 (5.22 g/cm^3) as well as the molar masses (2 Cr: 103.992 g/mol; Cr_2O_3: 151.99 g/mol), we can derive that the mixture theoretically consisted of 81.8 vol% Cr and 18.2 vol% Cr_2O_3 prior to the experimental runs. Applying the same greyscale separation via Matlab that was already used for the samples (chapter 2.6.5, page 98), we get the Vol% of the buffer material after the runs. Compared to the derived volume ratio in the mixture before the runs, the change in vol% and thus the consumption of buffer material can be determined (Figure 135).

Of all the experiments evaluated, only LPUM 150-3 shows a clear consumption of buffer material. This is also evident in the electron-optical image in direct comparison to other buffers (Figure 136). LPUM 150-3 is the only piston-cylinder-press experiment, where 2 µl of water were added to the buffer mix for testing purposes. Apparently, the water was completely reduced to H_2 by the buffer material consuming it. The excess gas collected in the sample and generated a sufficiently large pressure to burst the capsule after depressurisation at the end of the experiment.

The nominally dry buffers can only form very little H_2 (and, thus, gas pressure) because there is hardly any water to be reduced. It is therefore questionable, if the dry buffers could generate the required redox conditions in our samples.

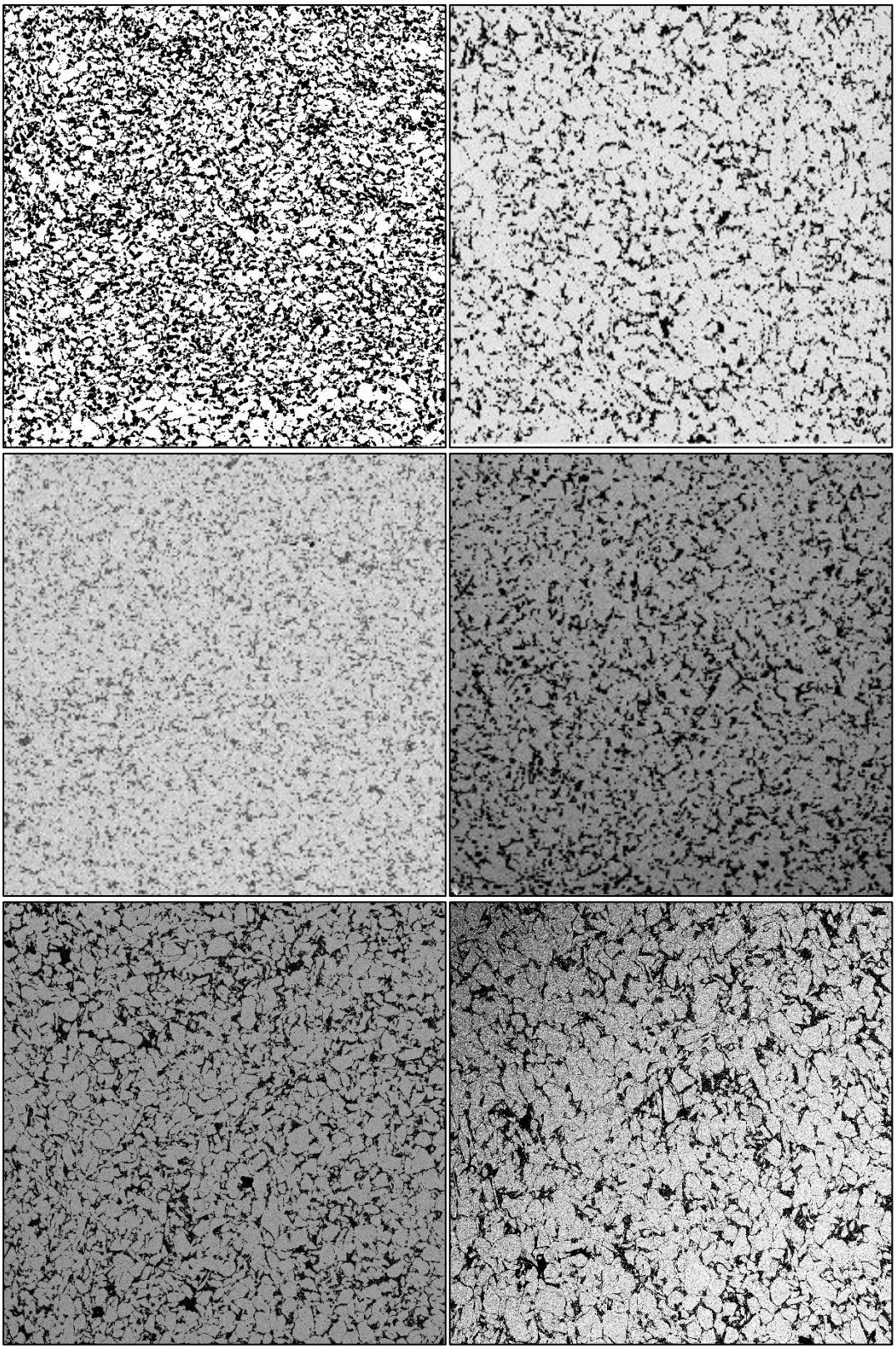


Figure 136: Buffer state in the electron microscope image after the experiments LPUM-150-3, 100-1, 075-1, 050-1, 030-1 and 020-1 respectively.

3.13 Estimating the redox conditions

Redox conditions are usually estimated by means of the Fe^{2+} to Fe^{3+} ratio. However, it is hardly possible to determine the ratio on the micrometre-sized melt fractions in our samples, e.g. by means of wet chemical methods. Instead, in samples containing metallic iron (Fe^0), an estimate of the redox conditions can be derived from the exchange of iron between the melt and metallic iron nuggets (14) (Potts et al., 2021)

$$Fe^0 + \frac{1}{2}O_2 = FeO. \quad (14)$$

The equilibrium constant (K) belonging to equation 14 can be written as

$$\log K = \log\left(\frac{\alpha_{feO}^{melt}}{\alpha_{Fe}^{metal}}\right) - \frac{1}{2}\log\left(fO_2\right). \quad (15)$$

The activity α can be transformed into the molar mass X and the activity constant γ to

$$\log K = \log\left(\frac{X_{FeO}^{melt} \times \gamma_{FeO}^{melt}}{X_{Fe}^{metal} \times \gamma_{Fe}^{metal}}\right) - \frac{1}{2}\log\left(fO_2\right). \quad (16)$$

We intend to give the redox conditions relative to the iron-wüstite buffer. Since the reactants of this buffer are wüstite (FeO) and iron (Fe), the activities for these are 1 and simplify equation 16 as follows

$$\log(K) = \frac{1}{2}\log\left(f_{O_2}^{IW}\right), \quad (17)$$

which, when combined with equation 16, yields

$$\Delta\left(f_{O_2}^{IW}\right) = 2\log\left(\frac{X_{FeO}^{melt} \times \gamma_{FeO}^{melt}}{X_{Fe}^{metal} \times \gamma_{Fe}^{metal}}\right), \quad (18)$$

where $\Delta\left(f_{O_2}^{IW}\right)$ describes the difference in log units from the iron-wüstite buffer. The molar fractions of the melt (X_{FeO}^{melt}) and the iron spheres (X_{FeO}^{metal}) are obtained from the EDX analyses on the samples, where a fraction of 100% iron was assumed for the iron nuggets as in Potts et al. (2021).

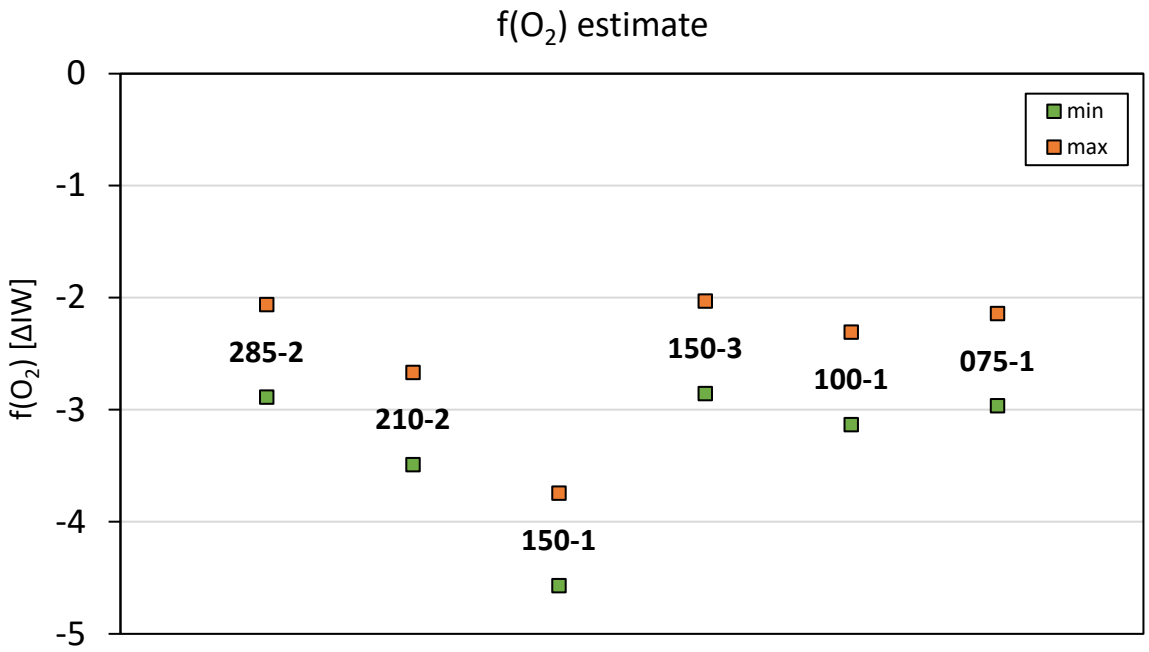


Figure 137: Estimated values of oxygen fugacity for all samples with iron nuggets present relative to the iron-wüstite buffer.

The activity coefficients γ_{melt} are composition dependent. Reference values can be found in O'Neill & Eggins (2002). For this study, the minimum and maximum values for (γ_{melt}) from O'Neill & Eggins (2002), 0.88 and 2.26 respectively, were used as a rough estimate, since none of the reported compositions completely match our compositions.

The resulting estimates of IW-2.1 to IW-4.4 are displayed in Figure 137. The results show that the redox conditions of all samples are below IW-2 while most of the samples are in the range from IW-2 to -3. This also applies to sample LPUM 150- 3, where the buffer is the only one to show a clear conversion of the initial material (Figure 136). This consumption of buffer material is due to the reduction of the added water to H_2. At the same time, there is no difference in the redox conditions compared to samples with nominally dry buffers. This leads to the conclusion that the addition of water is not necessary to provide the desired conditions for the experiments used here since apparently, even the few hundred ppm of water in the nominally dry material are sufficient to ensure communication between sample and buffer material during the experiment.

The twin sample of LPUM 150-3 is sample LPUM 150-1, which is significantly further reduced with an average of IW-4.16, although no water was added. However, in this sample the capsule material of the buffer has formed an alloy with the capsule material of the sample, which has destroyed the integrity of the buffer capsule. This process removed larger amounts of iron from the melt, thereby affecting the estimated value in equation 18

resulting in lower estimated values for the redox conditions. This effect is even more pronounced in sample LPUM-M 120-1 (Chapter 4.3.2, page 194). Due to the formation of platinum-iron alloys, this sample is mathematically at $f(O_2)$ conditions of IW-9, i.e. far outside realistic values for the redox state of our experiments.

Sample LPUM 210-2 also has a lower average than the other samples (IW-3.08). Unlike other experiments, the buffer here is located in an iron capsule instead of a platinum capsule. This may act as its own buffer due to the original iron-wüstite reaction. In this way, the reduction of the sample is supported yielding further reduced conditions than platinum capsules.

Despite these variations, the remaining experiments agree with the estimated redox conditions of the LMO.

4 Discussion

4.1 The lunar interior as shown by the run products

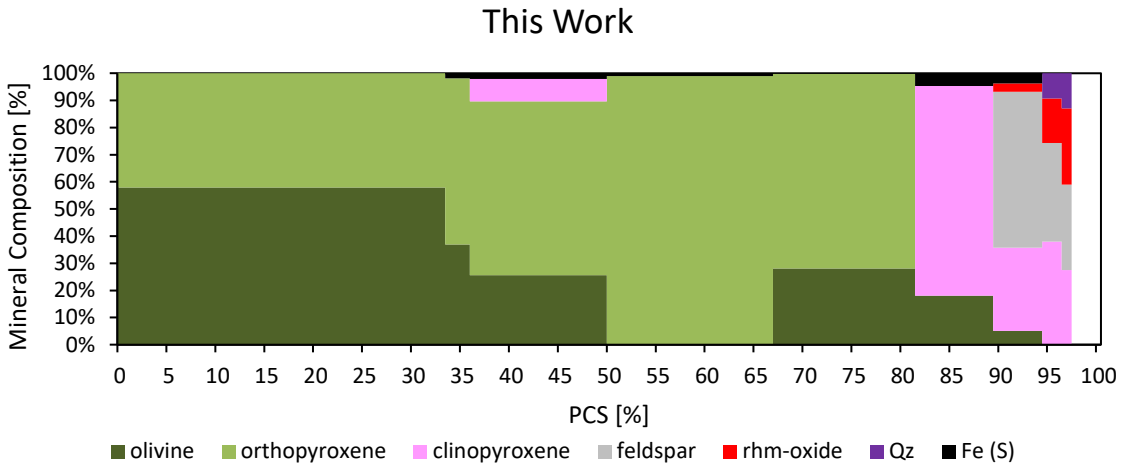


Figure 138: LMO mineral composition as a result of our study vs. the degree of crystallisation (PCS).

From the experimentally obtained data, the mineral sequence for the LMO shown in Figure 138 can be obtained. The sequence begins in the deep LMO with olivine-OPX cumulates, which continue to a depth of 115 km (81 PCS) except for an absence of olivine between 50 and 66 PCS. The OPX is replaced at 81 PCS by CPX, while the olivine fraction successively decreases until it no longer occurs in the sequence at 94 PCS. The formation of anorthosite (and, thus, of the lunar crust) by ascending plagioclase begins at 89 PCS, i.e. at a depth of about 65 km. At the same time, the first metal oxides occur, with a continuously increasing fraction until the end of the sequence. Quartz, which has so far only been observed in two other studies (cf. Figure 5, Page 11), appears from 94 PCS on.

Completely new in our sequence is the occurrence of CPX in the deeper mantle at 35 to 50 PCS, which has not been noted in any other work so far, as well as the precipitation of elemental iron in the form of nuggets from most of our samples. This shows that the lunar core formation is ongoing at our selected redox conditions of IW-2, thus causing the chemical composition of the Moon to lose iron in the early crystallisation stage, which is not available for the crystallisation of the dense metal oxides at the higher crystallisation stages.

Moreover, our sequence is in good agreement with the results of other experimental studies of LMO crystallisation, which show a mineralogically comparable internal structure of the Moon consisting of olivine, OPX, CPX and plagioclase. A direct comparison with the study by Rapp and Draper (2018) reveals differences that occurred despite the comparable chemical composition and conditions (Figure 139). In their study, OPX only appears from 52 PCS on and completely replaces the previously formed olivine. At the same time, crust

formation starts at 74 PCS (155 km depth), almost 100 km earlier than our sequence predicts. The metal oxides are found later and to a lesser extent than in our sequence. In the last crystallisation step, apatite occurs in Rapp and Draper (2018), which has not been observed in any of our experiments.

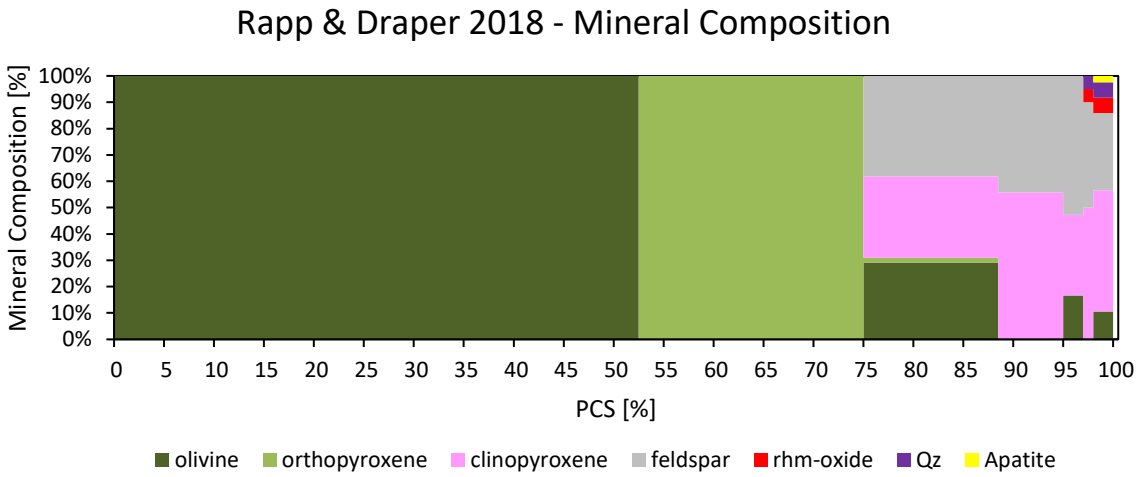


Figure 139: LMO mineral composition as given in Rapp and Draper versus the degree of crystallisation (PCS).

In the following, these differences will be analysed with respect to the conducted experiments seen individually. The experiments in the high P-T range (LPUM 300-1, 285-2, 210-2 and 150-3) show a high degree of crystallisation (Figure 140). Limitations of the Iron capsule (max. 1550°C) and the assembly (unstable above 1400°C) prevent the technically required conditions for high melt fractions in the deep LMO for our setup. The runs of Rapp and Draper (2018) (Figure 141) have no such limitations and, therefore, show increased melt fractions. A high degree of crystallisation results in a stronger change of the melt chemistry and thus, phases present in later crystallisation stages occur at the given P-T-conditions. At the same time, the experimental runs each show only a static P-T-regime. As crystallisation progresses, however, these conditions would have to change to account for the upwards movement of the crystallisation front in the LMO. This leads to incorrect conditions for large sections of the experiments we conducted.

One such example is LPUM 210-2. Due to its high degree of crystallisation (84.7%), this run extends into depths where the pressure should be 0.33 GPa instead of 2.1 GPa. In this way, the stability of the crystallising phases is influenced resulting in a small amount of CPX present, which otherwise first occurs at 81 PCS. The occurrence of CPX in the deeper Moon is therefore an artefact of the high degree of crystallisation.

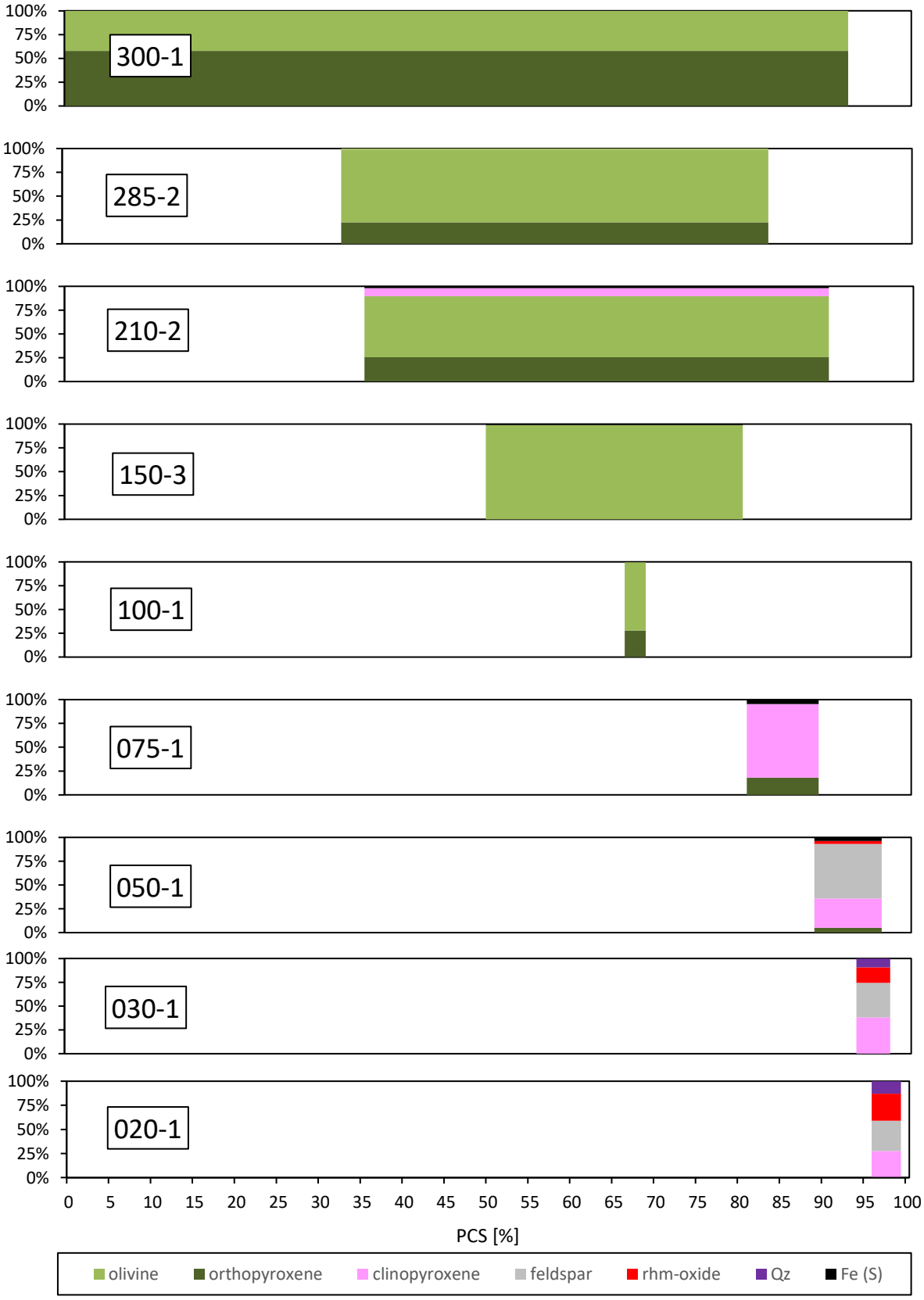


Figure 140: Composition of the LMO in the overall result of the experiments individually for each experiment vs. the degree of crystallisation (PCS).

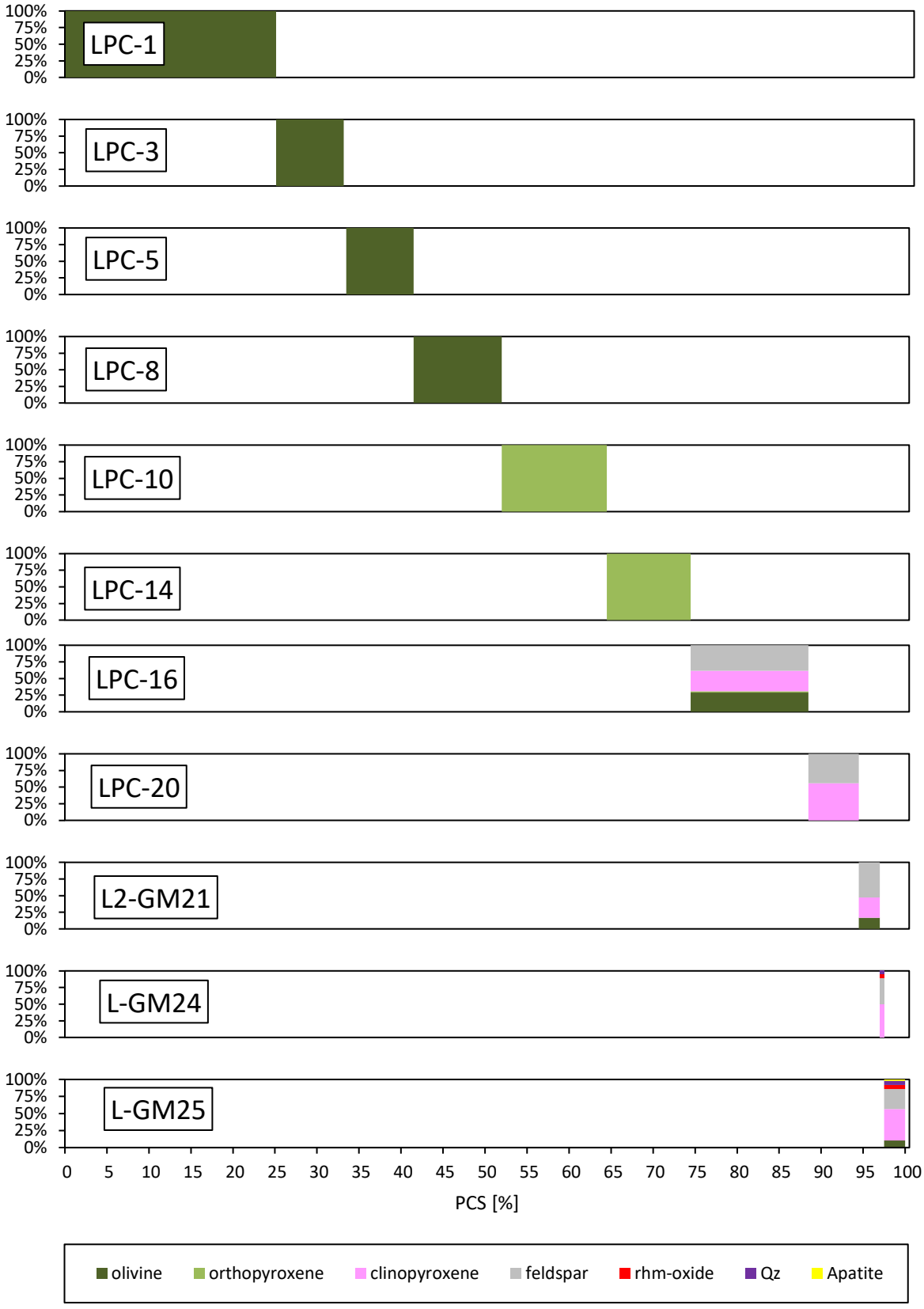


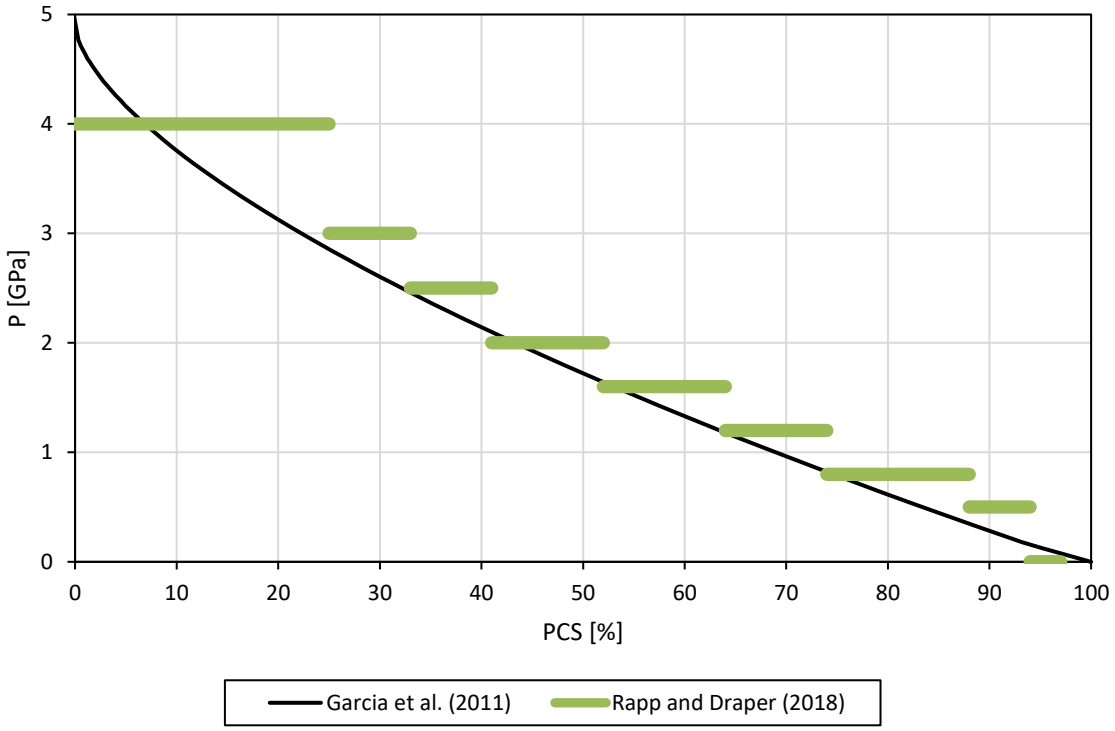
Figure 141: Composition of the LMO of the individual experiments as given in Rapp and Draper (2018).

Comparing the experimental pressure ranges of our series with the model of Garcia et al. (2011), the differences become even clearer (Figure 142). Ideally, all experiments should follow the black crystallisation path. This is largely the case for the runs of Rapp and Draper (2018), with their experiments overestimating the pressure to a minor extent. However, this can hardly be prevented, as infinitely small crystal fractions cannot be generated experimentally.

The large crystal fractions also account for the olivine-OPX-cumulates found for the deep LMO in our experiments, since this prevents the simulated fractionation of the formed minerals. Thus, these are indeed equilibrium experiments in which all phases can react with each other without interruption for broad ranges inside the LMO. This explanation is supported by earlier work on equilibrium crystallisation by Rapp and Draper (cf. Figure 5, page 11, LPUM / Equilibrium + Fractionational / 4GPa) in which almost identical cumulates were observed.

The assumption of complete fractionation for the early LMO with its turbulent convection, which should prevent sinking of formed minerals, is a simplification anyway. Although the effect is undesired, it is therefore more in line with realistic crystallisation conditions in the deep LMO. The experiments in the lower P-T range are not limited by the capsule and assembly materials and show much higher melting fractions allowing for an improved simulation of fractionation (Figure 142).

Since the compositions of our experiments are based on the data from Rapp and Draper (2018) and not on the previous experiment, the effect of low melting fractions of individual experiments has no influence on the remaining experiments.



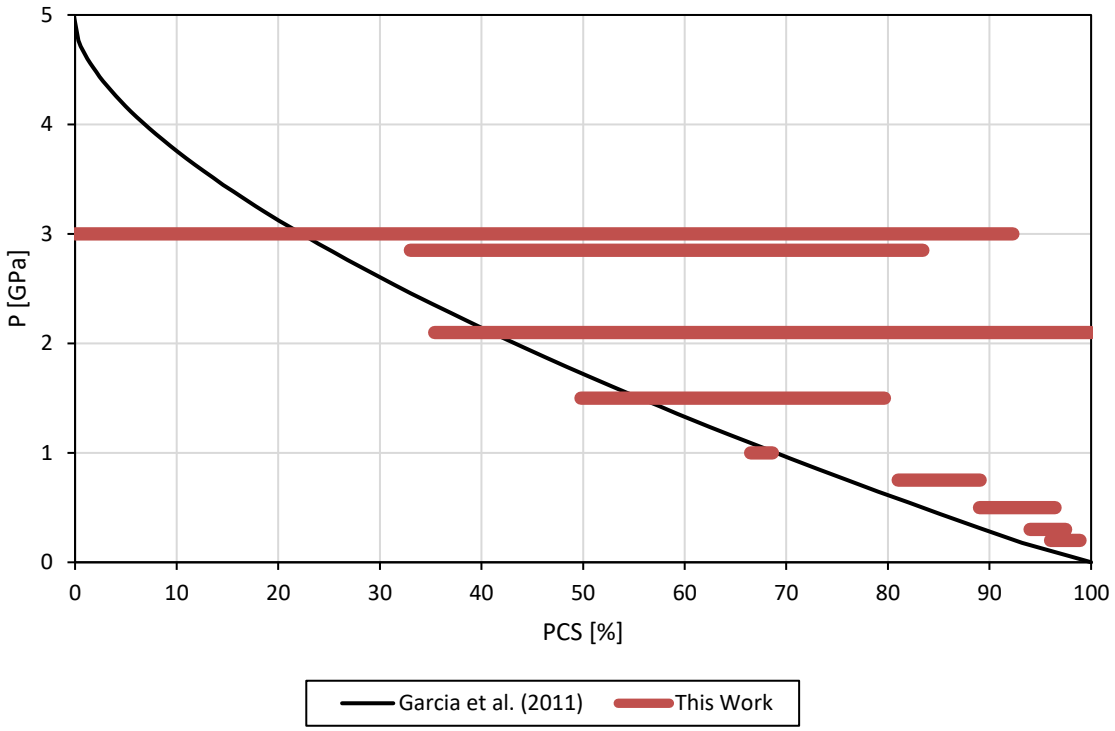


Figure 142: Pressure versus crystallisation progress of the experiments of Rapp and Draper (2018) (top) and this paper (bottom) versus the lunar model of Garcia et al. (2011). Each horizontal bar corresponds to a crystallisation experiment.

The occurrence of Fe-nuggets, which could be detected in almost all samples, has not been observed before in any experimental study concerning LMO solidification. Iron is very soluble in silicate melts in its divalent and trivalent oxide forms (FeO and Fe_2O_3). As the oxygen fugacity decreases, the Fe^{2+}/Fe^{3+}-ratio initially increases. If it continues to drop, elemental iron (Fe^0) appears. This precipitates out of the melt and forms spheres.

The oxygen fugacity in our runs is estimated 2.1 to 4.4 log units below the IW buffer (Figure 137) which is in the very reducing range and, thus, are well compatible with the occurrence of metallic iron.

Since the nuggets have a much higher density (Fe: 7.874 g/cm^3) than the melt, they would have to fractionate in a magma ocean and, thus, would be lost to the system. Since our experiments are based on the data from Rapp & Draper (2018) instead of on our own experiments, the runs can only be analysed separately and, thus, do not allow direct conclusions on the evolution of cumulates in the LMO due to precipitating iron.

Nevertheless, this shows that oxygen fugacity does not only influence the speciation of individual atoms and the crystallisation process, but also the chemical composition of the LMO in its development. For this reason, we have taken a closer look at experiments with and without Fe-nuggets..

4.2 Fe-nuggets - Result of the conditions?

Fe-nuggets occurred in 8 of 11 successful experiments (73%, Table 11). It is striking that the nuggets occur exclusively in those experiments whose capsule material is iron. However, these are also the experiments that were carried out in the piston-cylinder-press. The exception here is LPUM 300-1 but since this experiment does not contain a Cr-Cr_2O_3 buffer, but the less reducing carbon, it is of limited informative value. Therefore, it is worthwhile to investigate if there is a difference in the intrinsic oxygen fugacity of the piston-cylinder-press compared to the internally heated pressure vessel or a pure correlation between capsule material and the occurrence of the nuggets.

Table 11: Characteristics of the successful experiments with and without the appearance of Fe-nuggets.

Experiment	T [°C]	P [Gpa]	t [h]	Buffer	FeO [%]	Method	Capsule(s)	Fe-nuggets
LPUM 300-1	1600	3,00	1,5	C	7,62	PCP	Pt / -	
LPUM 285-2	1550	2,10	2	Cr+Cr_2O_3	9,06	PCP	**Fe** / Pt	**X**
LPUM 210-2	1550	2,10	2	Cr+Cr_2O_3	9,67	PCP	**Fe /Fe**	**X**
LPUM 150-1	1440	1,50	24	Cr+Cr_2O_3	9,37	PCP	**Fe** / Pt	**X**
LPUM 150-3	1440	1,50	16	Cr+Cr_2O_3	9,37	PCP	**Fe** / Pt	**X**
LPUM 100-1	1290	1,00	2	Cr+Cr_2O_3	10,75	PCP	**Fe** / Pt	**X**
LPUM 075-1	1230	0,75	3,5	Cr+Cr_2O_3	12,33	PCP	**Fe** / Pt	**X**
LPUM 050-1	1150	0,50	24	Cr+Cr_2O_3	15,53	PCP	**Fe** / Pt	**X**
LPUM 030-1	1050	0,30	24	Cr+Cr_2O_3	22,74	IHPV	Pt / Pt	
LPUM 030-2	1050	0,30	26	Cr+Cr_2O_3	22,74	IHPV	Pt / Pt	
LPUM 020-1	1025	0,20	2	Cr+Cr_2O_3	25,93	IHPV	Pt / Pt	
LPUM-M-120-1	1340	1,20	16	Cr+Cr_2O_3	1,00	PCP	**Fe** / Pt	**X**
LPUM-M-080-1	1220	0,80	6	Cr+Cr_2O_3	0,58	PCP	**Fe** / Pt	**X**

4.2.1 F(O_2) of the pressurising medium

A possible reason for the observations might be a higher, intrinsic oxygen fugacity during experiments in our IHPV. The vessel contains several thousand atmospheres of argon gas, which is in direct contact with the sample capsule and thus, influences the oxygen fugacity more readily than inside the piston-cylinder-press, where all materials surrounding the sample capsule are dense solids. Since those solids are dependent on the used assembly, the oxygen fugacity for piston-cylinder-press experiments varies much more through this and needs to be controlled or the initial f(O_2) of the sample material must be restrained (Matjuschkin et al., 2015).

For the IHPV, the intrinsic oxygen fugacity reported in the literature ranges from 2 to 4 log units above the Ni-NiO buffer (NNO) (Linnen et al., 1996; Schmidt et al., 1997; Wilke & Behrens, 1997). The variations for the piston-cylinder-press shows a much greater range from 0.8 log-units below the C-CO-CO_2 buffer (CCO) (Medard et al., 2008), hematite-magnetite (HM) (Eggler et al., 1974), two log units below the quartz-fayalite-magnetite buffer (QFM) (Patino Douce & Beard, 1995; Truckenbrodt et al.,1997) to 0 - 2.5 log units above the nickle - nickle oxide buffer (Matjuschkin et al., 2015). The latter study used a NaCl-Pyrex assembly, which is therefore closest to the assembly we used in our experiments.

The intrinsic oxygen fugacity of our experiments in the PCP and IHPV before any buffer considered should therefore be similar but slightly more reducing in the PCP (NNO +0 to +2.5, PCP, vs. NNO+2 to +4, IHPV). In any way, If the buffer was not active in both experimental methods, none of the experiments should yield elemental iron.

4.2.2 Dependencies on Iron content, pressure and temperature

The iron content (FeO) of the initial glasses used for the experiments ranges from 0.58 wt% to 25.93 wt%. A correlation between iron content and the occurrence of the spheres is not apparent, since even in sample LPUM-M-80-1 (not described in this study) with the lowest iron content, iron precipitated (Table 11). The process therefore seems to be independent of concentration. Other factors such as pressure, temperature and duration of the experiment seem to be negligible as well

4.2.3 The capsule material as cause - composition of the residual melt

Significant dissolution of capsule material in the sample would have to result in a more iron-rich composition of the residual melts, as iron is hardly incorporated in the most common minerals of the investigated crystallisation sequence. However, by this mechanism the iron content of the melt already changes, as the residual melt is a distillate of the initial composition. Therefore, an increase in the iron content of the residual melt should be

evident from this alone for most experiments, irrespective of the diffusion of iron from the capsule into the sample. The effect of the solid phases on the melt should be smaller at high melt percentages. The most suitable sample for to investigate the process is therefore LPUM 100-1 (93.6% melt content). For this specimen, the iron content of the residual melt remained almost equal indicating no substantial diffusion of iron into the residual melt (Table 12).

Table 12: Initial iron content and iron content of the residual melt (R) of the LPUM and LPUM-M experiments and the corresponding melt fraction (for initial glasses 100%)

LPUM-	300	300-1R	285	285-2R	210	210-2R	150	150-1R	150	150-3R	100	100-1R
FeO	7,62	No data	9,06	12,19	9,67	6,90	9,37	2,00	9,37	13,77	10,75	10,24
Melt %	100	15,3	100	24,7	100	13,5	100	55,7	100	40,5	100	93,6

LPUM-	075	075-1R	050	050-1R	030	030-1R	020	020-1R	M120	M120-1R
FeO	12,37	12,28	15,53	34,35	22,74	7,87	25,93	15,49	1,01	0,04
Melt %	100	57,4	100	32,3	100	41,6	100	27,0	100	54,6

A comparison of iron content in the starting material and the residual melt shows, that a decrease in the iron content can be observed in many runs (LPUM 210-2, 150-1, 075- 1, 030-1, 020-1, M120-1) despite considerably lower melt contents compared to LPUM 100-1 (Table 12).

The greatest losses of iron are shown for sample 150-1 and M-120-1, for which the platinum of the buffer capsule disintegrated to a greater extent in a $Pt_{66}Fe_{33}$ alloy. This composition forms exactly the phase boundary between $FePt_3$ and FePt in the phase diagram of platinum and iron (Figure 143, Ding et al., 2011). For the experimental conditions of these two experiments (1440°C, LPUM 150-1 & 1340°C, LPUM-M120-1), only a disordered FePt compound should be present. However, since the phase diagram shown here does not regard pressure, it is quite possible that equal proportions of $FePt_3$ and FePt structures were formed. A fundamental loss of iron to the platinum capsule of the buffer through the formation of this alloy is therefore possible for all samples. Thus, if the iron content of the sample has indeed been increased by the diffusion of iron into the melt, the effect is either masked by the crystallisation process within the sample or this fraction has precipitated as Fe-nuggets to the same or greater extent lowering the iron content of the residual melt.

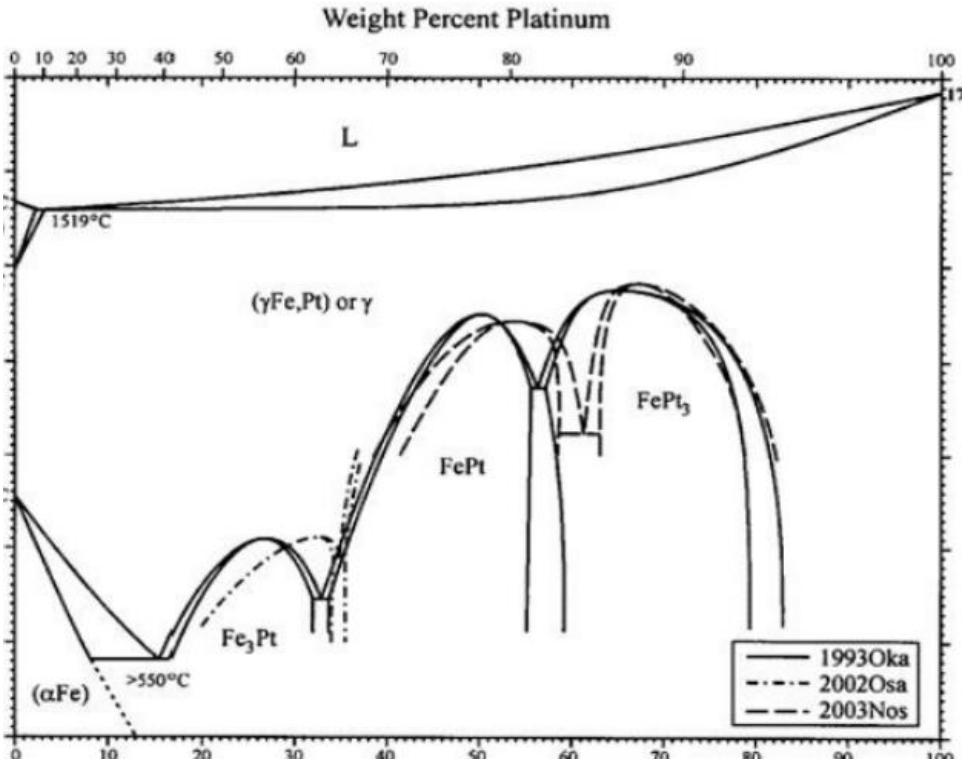


Figure 143: Phase diagram of platinum and iron (Ding et al., 2011)

4.2.4 The capsule material as cause - bulk composition

To include the iron nuggets in the consideration of the overall composition of the samples, point analyses of the melt are not sufficient. Therefore, we performed area measurements including melt, mineral content and Fe-nuggets of the specimens. It is important to ensure that the selected sections cover as much surface area as possible and that they are representative for the entire sample. To check this, we first measured a large area (A) and then divided it again into two areas (e.g. B left, B right) as shown in Figure 144 for sample LPUM 050-1. Assumed the sample is homogeneous, all three areas should show equal results.

The chosen area for specimen LPUM 050-1 shows very similar values compared to the initial composition, although there are larger deviations for some elements such as phosphorus (Table 13). Of particular interest to us is the iron content. This is 0.74% higher in the large area than in the starting material. At the same time, the surface closer to the iron capsule is slightly richer in iron than the one close to platinum.

However, due to an increased amount of aluminium, this finding cannot be clearly attributed to a diffusion of iron into the sample since the EDX-data is normalized to 100%.

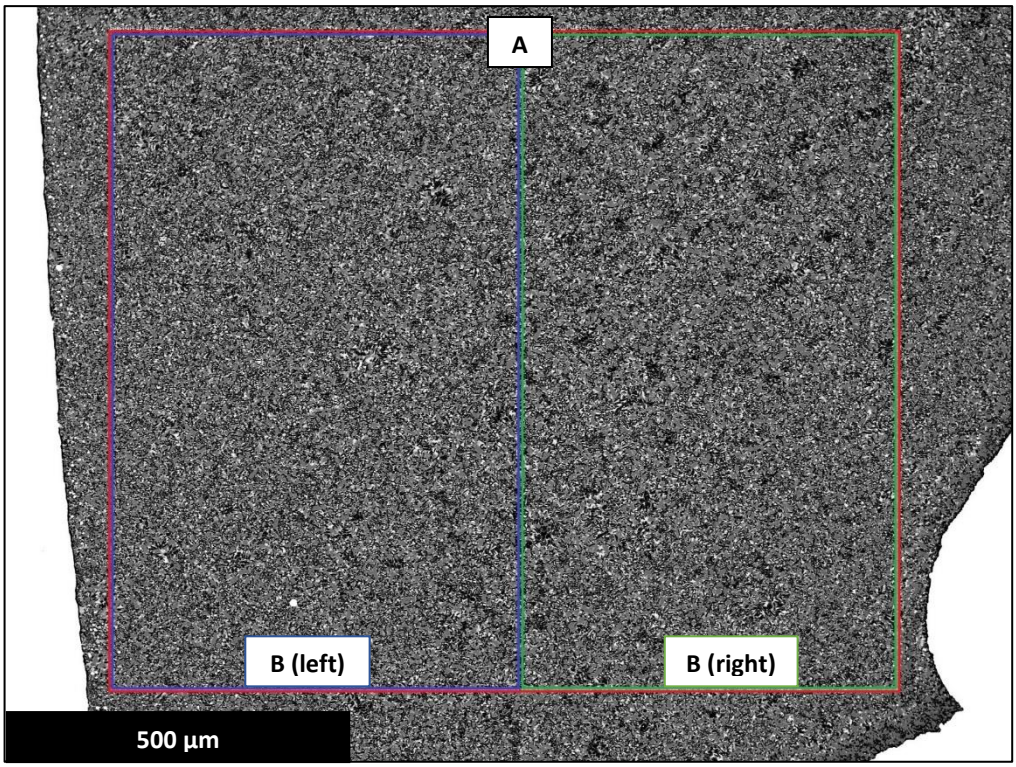


Figure 144: Area measurement on sample LPUM 050-1 with the entire area A (red) and the smaller areas B on the left (blue) and B on the right (green)

Table 13: Composition of area measurements at LPUM 50-1 as shown in Figure 144.

Oxide %	Na_2O	MgO	Al_2O_3	SiO_2	P_2O_5	K_2O	CaO	TiO_2	Cr_2O_3	MnO	FeO	Total
LPUM 050-1 Starting Glas	**1,28**	**6,15**	**15,89**	**47,91**	**0,48**	**0,08**	**11,01**	**1,36**	**0,04**	**0,27**	**15,53**	100
LPUM 50-1 Large Area A	1,42	5,66	17,47	46,42	0,13	0,13	10,93	1,26	0,02	0,30	16,27	100
LPUM 50-1 Small Area B (left)	1,44	5,56	17,41	46,36	0,10	0,13	10,79	1,24	0,01	0,28	16,67	100
LPUM 50-1 Small Area B (right)	1,41	5,77	17,53	46,5	0,15	0,13	11,08	1,27	0,02	0,31	15,83	100

This becomes more notable in sample LPUM-M 120-1 (Figure 145 & Table 14). The area near the capsule wall (right, green area) is more rich in iron (1.86%) than the area on the left (blue, 0.28%) although the iron content of the total area (red) with 1.03% is very close to the starting material with 1.01%.

The iron nuggets already visible in the optical image on the right-hand side of the sample are therefore an addition to the overall composition and are not a $f(O_2)$-related precipitation of elemental iron from the melt itself. The large nuggets in the left area of the sample consist of a $Pt_{66}Fe_{33}$ alloy and originate from the disintegration of the outer parts of the buffer capsule.

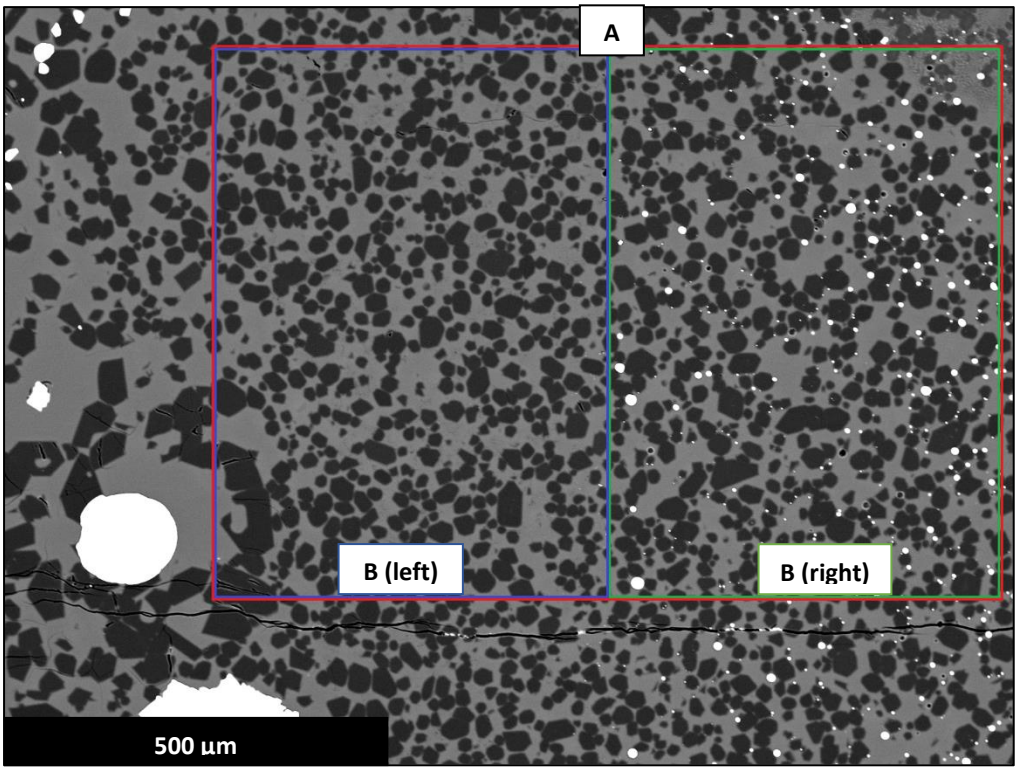


Figure 145: Area measurement on sample LPUM-M 120-1 with large area A (red) and smaller area B on the left (blue) and B on the right (green)

Table 14: Composition of area measurements at LPUM-M-120-1 as shown in Figure 145.

Oxide %	Na_2O	MgO	Al_2O_3	SiO_2	P_2O5	K_2O	CaO	TiO_2	Cr_2O_3	MnO	FeO	Total
LPUM-M-120-1 Starting Glas	**0,27**	**32,08**	**9,36**	**48,31**	**0,03**	**0,03**	**8,07**	**0,40**	**0,18**	**0,25**	**1,01**	100
LPUM-M-120-1 A	0,24	36,10	9,46	45,49	0,00	0,06	7,31	0,08	0,15	0,09	1,03	100
LPUM-M-120-1 B left	0,24	36,42	9,58	45,70	0,00	0,07	7,36	0,09	0,17	0,09	0,28	100
LPUM-M-120-1 B right	0,25	35,76	9,33	45,22	0,00	0,06	7,24	0,07	0,13	0,08	1,86	100

Despite the lower fraction of iron in the left area of the image, the iron content in the right area of the image is already far above the starting composition. Thus, an increase in the iron content due to the iron capsule must have caused the spheres.

To verify this finding, we presaturated the platinum capsules for experiment LPUM 030-2 with iron for 24h in a gas mixing furnace at 1050°C and a gas mixture of 9% CO_2 and 91% H_2 (corresponding to conditions near IW-2) in the same sample composition intended for the later experiment. The capsules were then completely cleaned with hydrofluoric acid and prepared for experiment LPUM-030-2, which is an IHPV experiment identical to LPUM-030-1, but with the iron presaturated platinum capsules for buffer and sample. If the Fe-nuggets really emerge from the iron capsule, this experiment should not contain any. The argument that the precipitated iron was absorbed by the platinum and was, therefore, not visible as nuggets in the sample does not hold due to the pre-saturation.

The comparison between LPUM 030-1 and LPUM 030-2 shows that, apart from a difference in the grain size of the minerals, there were no differences in the formation of the iron nuggets (Figure 146). The spheres observed in the piston-cylinder-press experiments are, therefore, due to the diffusion of capsule iron into the samples. At the same time, the conditions have to be quite reducing, since the iron introduced into the melt forms Fe-nuggets instead of being dissolved as FeO.

Computer simulation of LMO crystallization using MELTs nevertheless predicts precipitation of elemental iron for the runs at an oxygen fugacity of iron-wüstite -2 (compare Chapter 4.3, page 191) This shows that although we see Fe-nuggets originating from the capsule material, our conditions, at least during IHPV-runs, are not sufficiently reducing for the precipitation of iron from the sample. Otherwise, such experiments conducted in platinum capsules would also contain Fe-nuggets, provided the capsule material is presaturated with iron. If the Fe-nuggets found in piston-cylinder-press-experiments are entirely an effect of the capsule or a fraction of it emerges from the sample cannot be told.

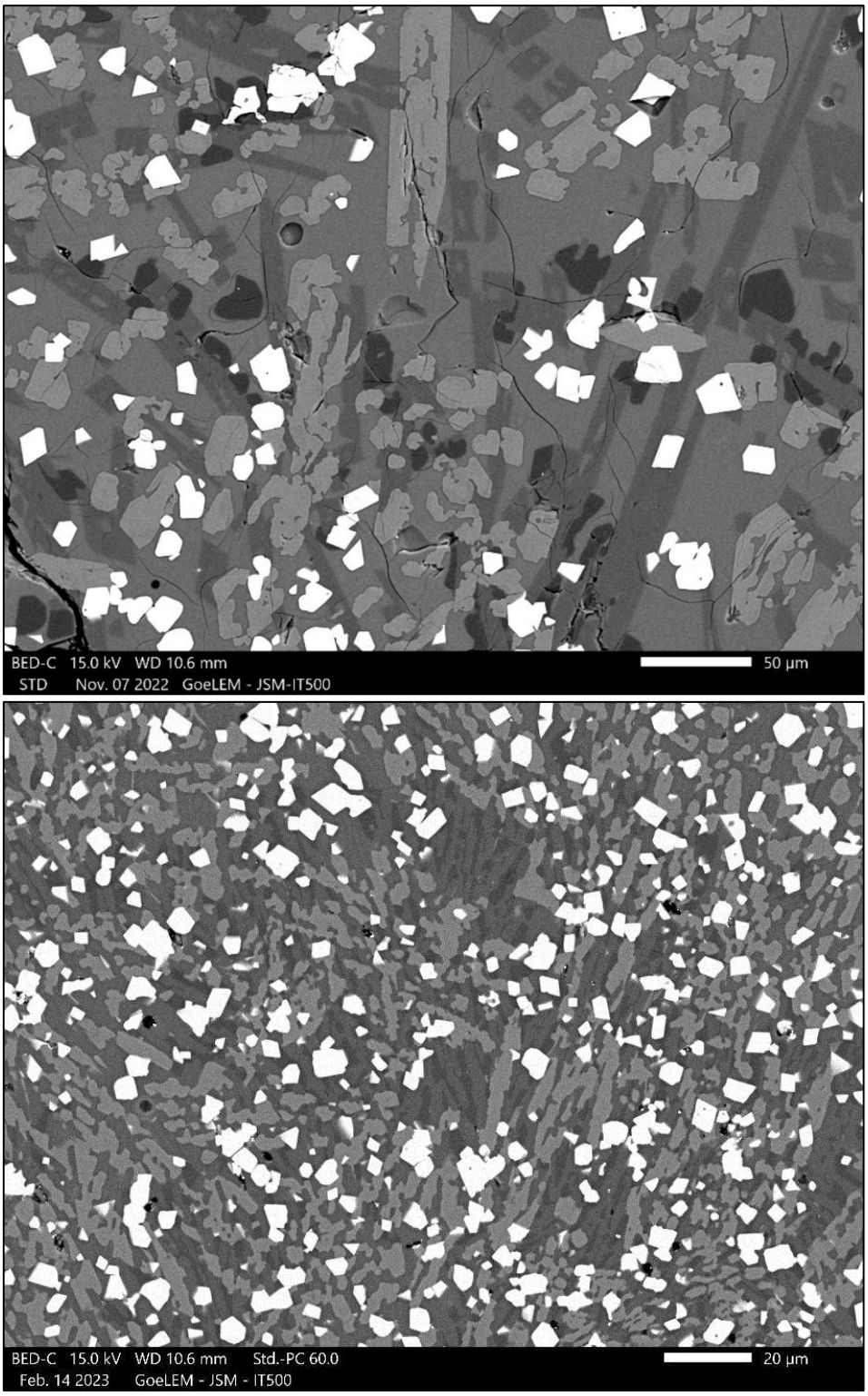


Figure 146: SEM image of the experiments LPUM-30-1 (top) and LPUM 30-2 (bottom)

4.3 Simulation of LMO crystallisation using MELTS

In this chapter we present results on simulations of the LMO crystallisation using the MELTS software package (Ghiorso & Sack, 1995; Asimow & Ghiorso, 1998; Ghiorso et al., 2002; Smith & Asimow, 2005). MELTS was programmed based on experimental thermodynamic data. The model minimises the Gibbs energy, the Helmholtz energy, the enthalpy and the entropy of a system previously defined in terms of chemism, pressure, temperature and oxygen fugacity and returns the phases present at these conditions together with their compositions. Although MELTS has been calibrated with a wide range of compositions, there is always a risk that one's own compositions and conditions will cause the calculation to fail or give faulty results. Therefore, one should be careful when using MELTS.

We used the Excel-based version of MELTS (Gualda & Ghiorso, 2015). This includes the rhyolite-MELTS models v1.0, v1.1 and v1.2 and the p-MELTS version v5.6.1 in its version of 16.12.2020. We chose p-MELTS because it is explicitly calibrated for mantle compositions and the pressure range of 1-4 GPa, which is closest to our conditions.

To analyse the behaviour of the LMO under reducing conditions, two cases were distinguished:

1) The oxygen fugacity is exactly on the iron-wüstite buffer (IW0).

2) The oxygen fugacity is two log units below the iron-wüstite buffer (IW-2).

The same initial composition (LPUM, Table 15) was used for both cases. 100 ppm of water were added to consider the water evolution The degree of crystallisation in our simulations were selected according to the experiments by Rapp and Draper (2018) (Table 16). To this end, significantly higher temperatures were required in the early crystallisation steps than in the experiments of Rapp and Draper (2018).

Table 15: Starting compositon for both of the MELTS simulations

Oxide	SiO_2	MgO	FeO	Al_2O_3	CaO	Cr_2O_3	TiO_2	MnO	Na_2O	K_2O	P_2O_5	H_2O
wt%	46,48	38,88	8,25	4,20	2,99	0,51	0,15	0,12	0,10	0,01	0,01	0,01

Table 16: Most important parameters of the simulations IW0 (top) and IW-2 (bottom) with MELTS

MELTS IW0

PCS [%]	depth [km]	*P [Mpa]*	*T [°C]*	*liquid [%]*	*solids [%]*
25,01	636	4000	1927	74,99	25,01
33,26	529	3000	1876	89,00	11,00
41,27	440	2500	1830	88,01	11,99
51,83	339	2000	1756	82,01	17,99
63,87	239	1600	1636	75,00	25,00
73,99	165	1200	1478	71,99	28,01
88,04	72	800	1291	45,98	54,02
94,26	34	500	1191	47,98	52,02
96,38	21	0.1	1125	63,02	36,98
97,11	17	0.1	1101	79,99	20,01
99,57	3	0.1	1042	14,99	85,01

MELTS IW-2

PCS [%]	depth [km]	*P [Mpa]*	*T [°C]*	*liquid [%]*	*solids [%]*
25,01	636	4000	2044	75,09	24,91
33,26	529	3000	1901	89,05	10,95
41,27	440	2500	1861	88,01	11,99
51,83	339	2000	1798	82,01	17,99
63,87	239	1600	1715	75,00	25,00
73,99	165	1200	1590	72,02	27,98
88,04	72	800	1332	46,03	53,97
94,26	34	500	1264	47,93	52,07
96,38	21	0.1	1213	63,00	37,00
97,11	17	0.1	1194	80,05	19,95
99,57	3	0.1	1025	15,00	85,00

4.3.1 MELTS - LMO composition and mineral stack (1)

The results of each experiment equilibrated in MELTS are depicted in Figure 156 and Figure 157. The melt composition after the run was used as starting material in the following simulation step to be able to observe the development of the LMO independently of the results from Rapp and Draper (2018), unlike in the experiments we conducted in the laboratory.

LPUM IW 0 corresponds most closely to the conditions that prevailed in the experimental work of Rapp and Draper (2018). Nevertheless, major differences are already evident at the beginning of the sequence: the simulations with MELTS all start with orthopyroxene instead of olivine. This observation is by no means new. Schwinger and Breuer (2022) found that pMELTS underestimates olivine in deeper parts of the magma ocean during the crystallisation of magmatic oceans and thus favours OPX. In addition, Schwinger and Breuer (2022) claimed that MELTS provides significantly better results in the shallower regions of magmatic oceans.

To get our own impression in a direct comparison between MELTS and a laboratory experiment, we prepared the composition at 64 PCS of the simulation IW-2 and subjected it to the same conditions as those of the MELTS simulation in a piston-cylinder experiment with an identical set-up like the previously conducted experiments (LPUM-M-120-1, 1.2 GPa, 1340°C, 18h). Since MELTS requires much too high temperatures for a comparable melting fraction, the temperature of the experiment was lowered from 1590°C to 1340°C. Otherwise, the experiment would only contain melt. The results are shown in the following chapter 4.3.2.

4.3.2 LPUM-M-120-1

Method:	PCP	**Pressure**	1,20 GPa	**Temperature**	1340°C
Duration	18h	**f(O_2) Buffer:**	Cr-Cr_2O_3	**Capsule:**	Fe + Pt

Oxide	**SiO_2**	**TiO_2**	**Al_2O_3**	**FeO**	**MnO**	**MgO**	**CaO**	**Na_2O**	**K_2O**	**P_2O_5**	**Cr_2O_3**
wt%	48,30	0,40	9,36	1,00	0,25	32,08	8,07	0,27	0,03	0,03	0,18

Melt fraction: 54,6%	**Crystals:** OPX (64,2%), Olivine (35,3%), Fe-nuggets (0,5%)

LPUM-M-120-1 is used for direct comparison between MELTS and experimental runs in the laboratory. The initial composition corresponds to the result of the MELTS crystallisation step between 51 PCS and 64 PCS. Since a large part of the iron contained in the simulation IW-2 has already been lost in the deep LMO as precipitated iron, the composition is the experiment with the lowest iron content of all runs shown in this study.

The electron microscope image (Figure 147) shows a melt fraction of 54.6%. The crystalline phase consists of 64.2% OPX, 35.3% olivine and 0.5% Fe-nuggets (Figure 154). The minerals have an average size of 20 to 50 µm, single specimens near the platinum capsule reach 150 µm (Figure 148 & Figure 149).

Chemically, the minerals consist of very pure enstatite ($En_{94.8}Fs_{0.5}Wo_{4.7}$) and forsterite ($Fo_{99.8}Fa_{0.2}$) (Figure 152 & Figure 153). This is mainly due to the low iron content of the experiment since the previous simulations predict a strong loss of iron in the deep LMO.

What is striking about LPUM-M-120-1 are the large metal lumps in the sample. This is platinum (Figure 150 & Figure 151), which begins to dissolve under the reducing conditions in combination with the iron capsule forming Pt-Fe-alloys similar to the sample LPUM 150-1. The buffer material has not leaked yet, thus, this has no direct influence on the sample. For the greyscale separation using MATLAB, the platinum components were coloured black and, thus, like the rest of the capsule, were not considered in the separation.

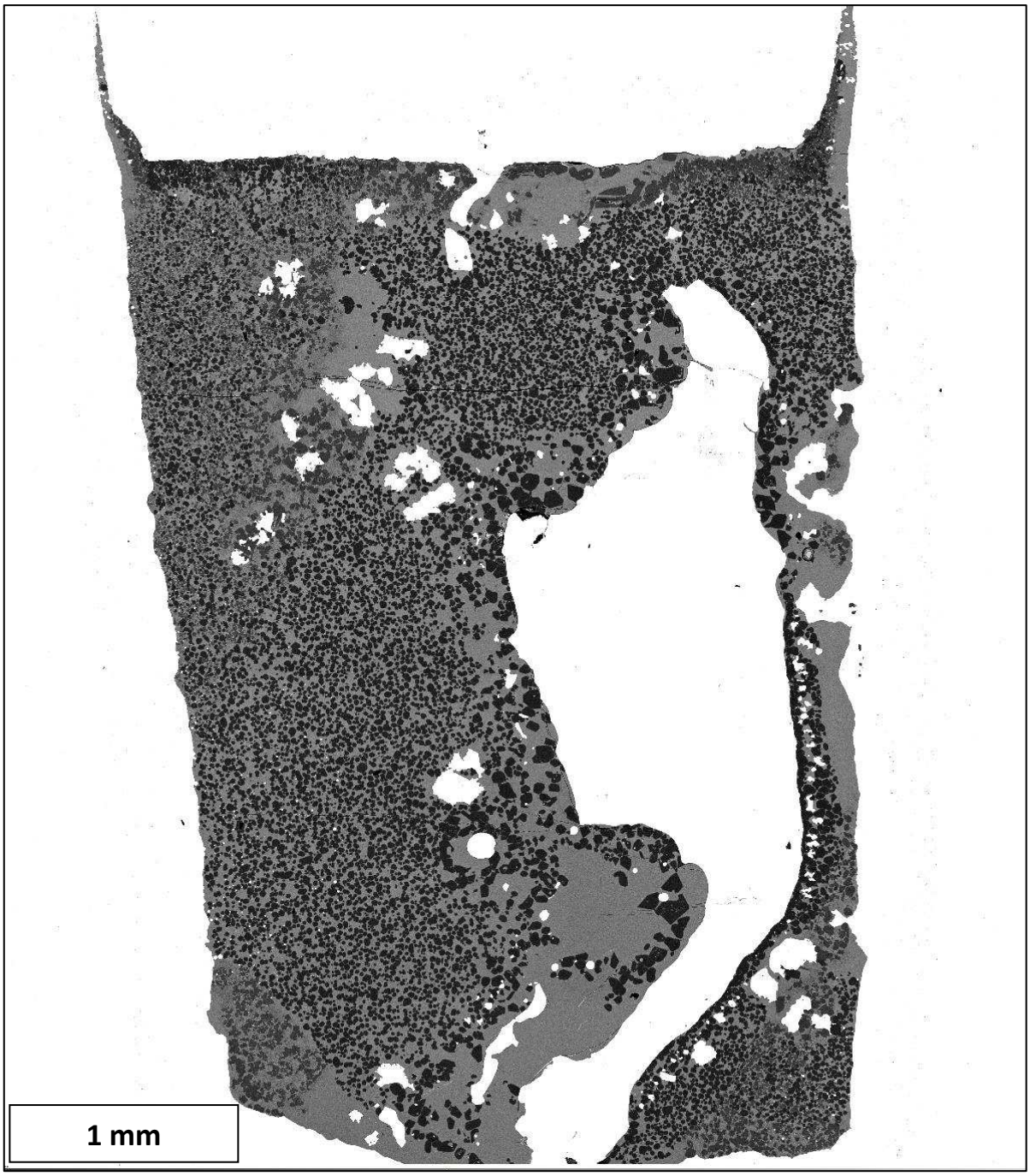


Figure 147: Overview of sample LPUM-M120-1 with capsule materials in white.

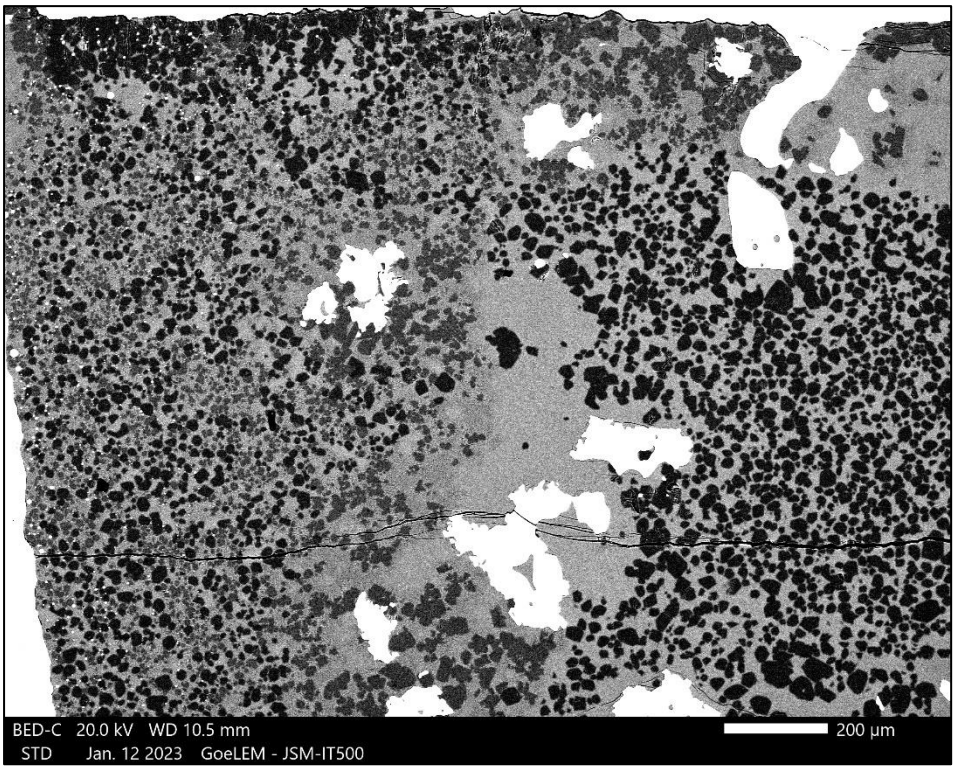


Figure 148: Close-up 1 of sample LPUM-M 120-1 showing orthopyroxene (black), olivine (dark gray), melt (light gray) and the partially dissected platinum capsule (white).

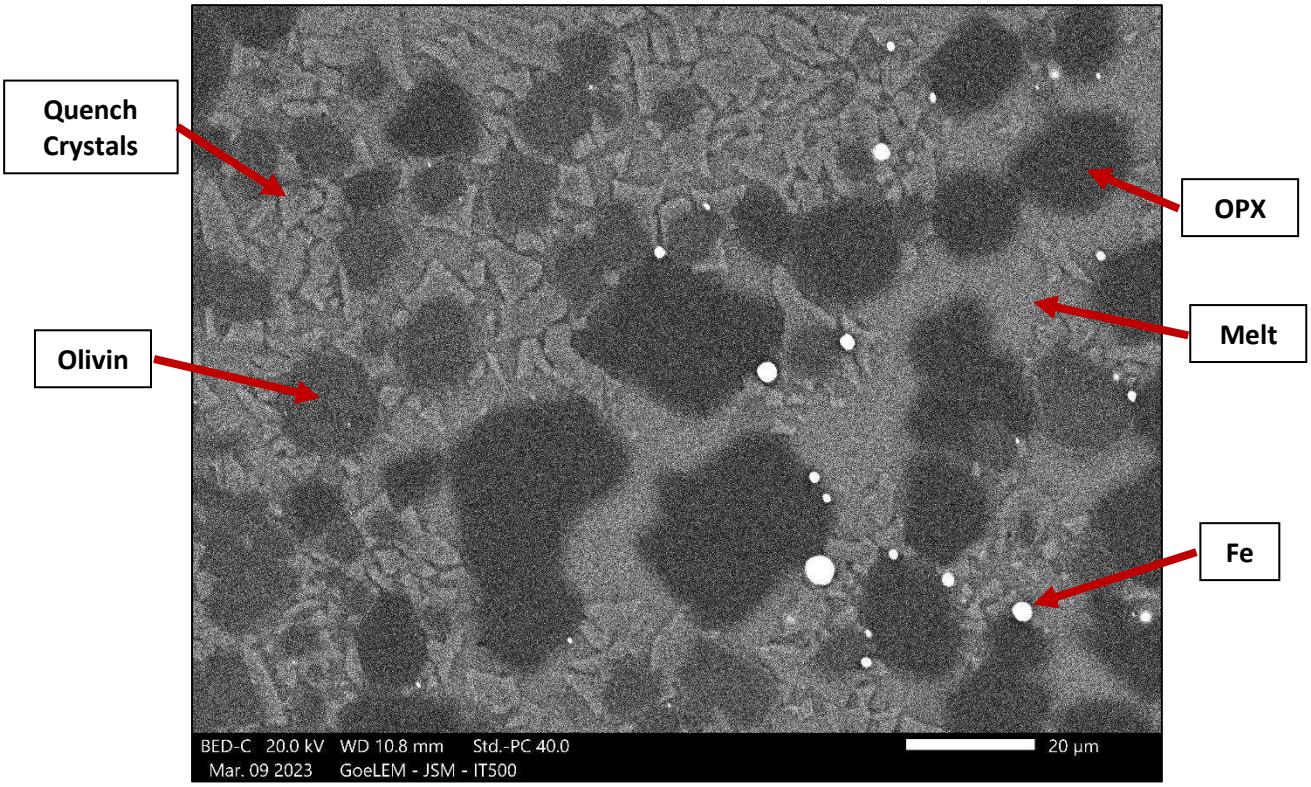


Figure 149: Close-up 2 of sample LPUM-M 120-1 showing orthopyroxene (black), olivine (dark gray), melt (light gray) and Fe-nuggets (white).

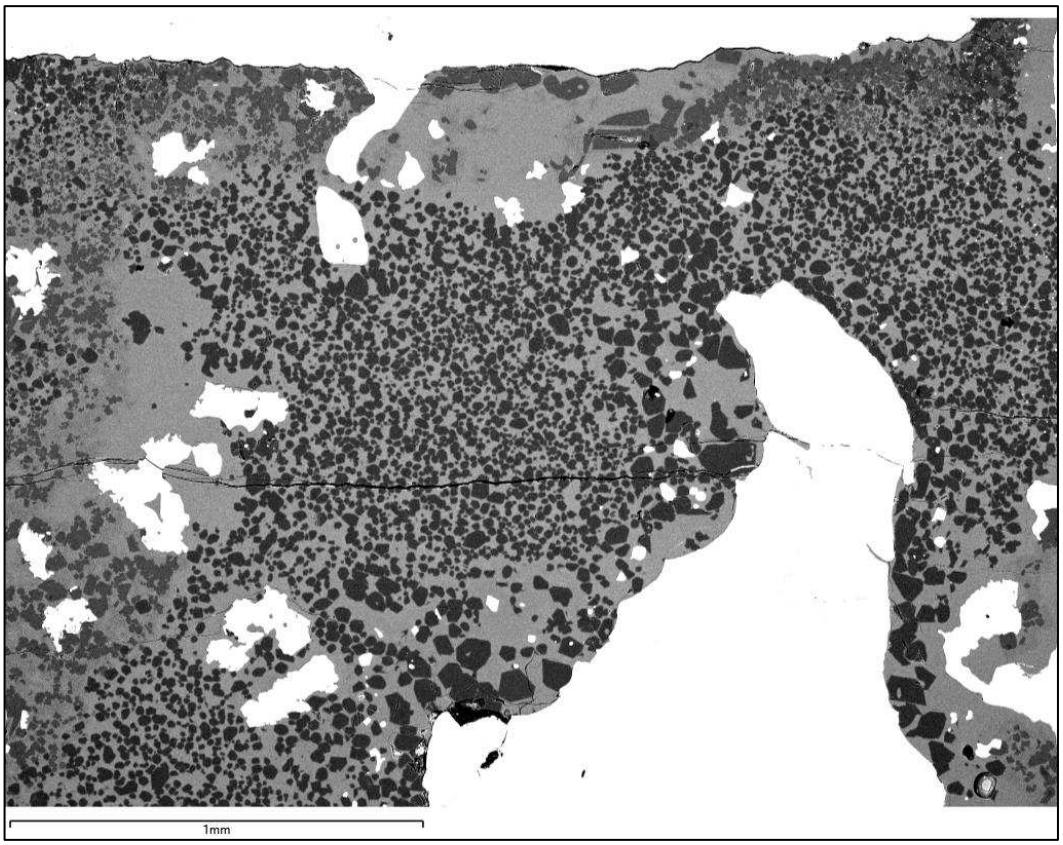


Figure 150: Original Image of sample LPUM-M 120-1 used for mapping the platinum distribution given in Figure 151.

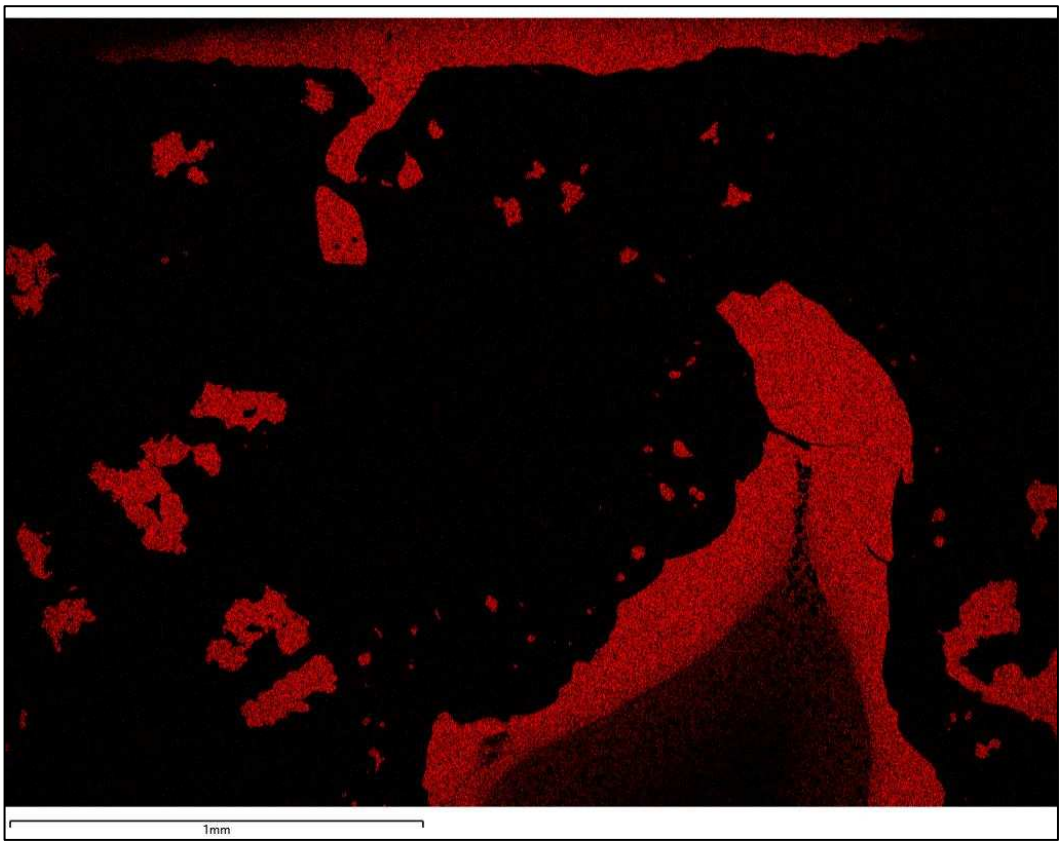


Figure 151: Platinum distribution in sample LPUM-M 120-1 (elemental map).

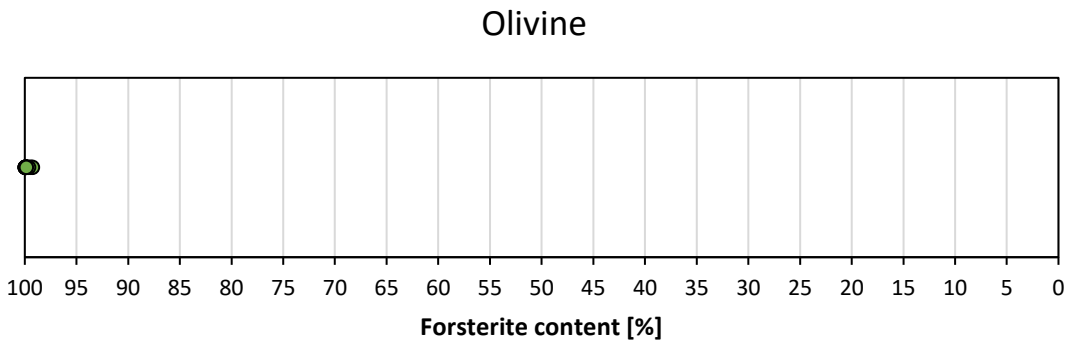


Figure 152: Forsterite content of olivine in sample LPUM-M 120-1.

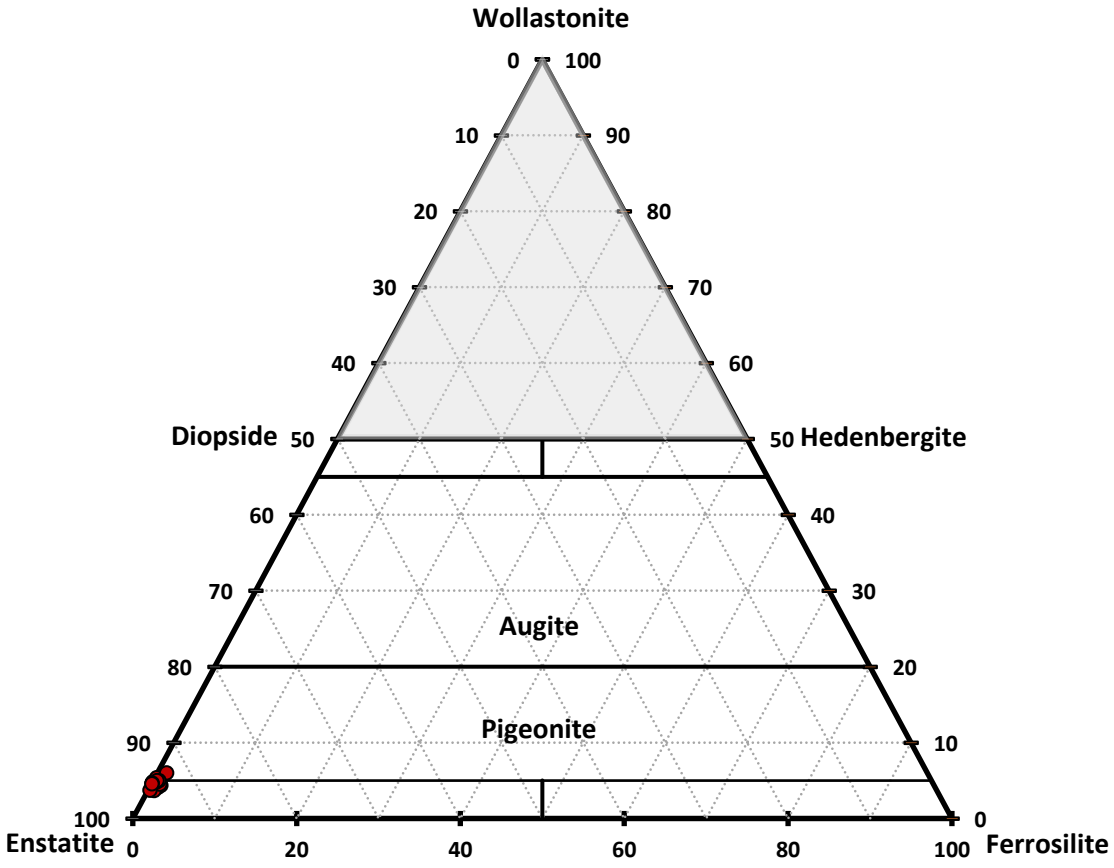


Figure 153: Mineral composition of orthopyroxenes in sample LPUM-M 120-1.

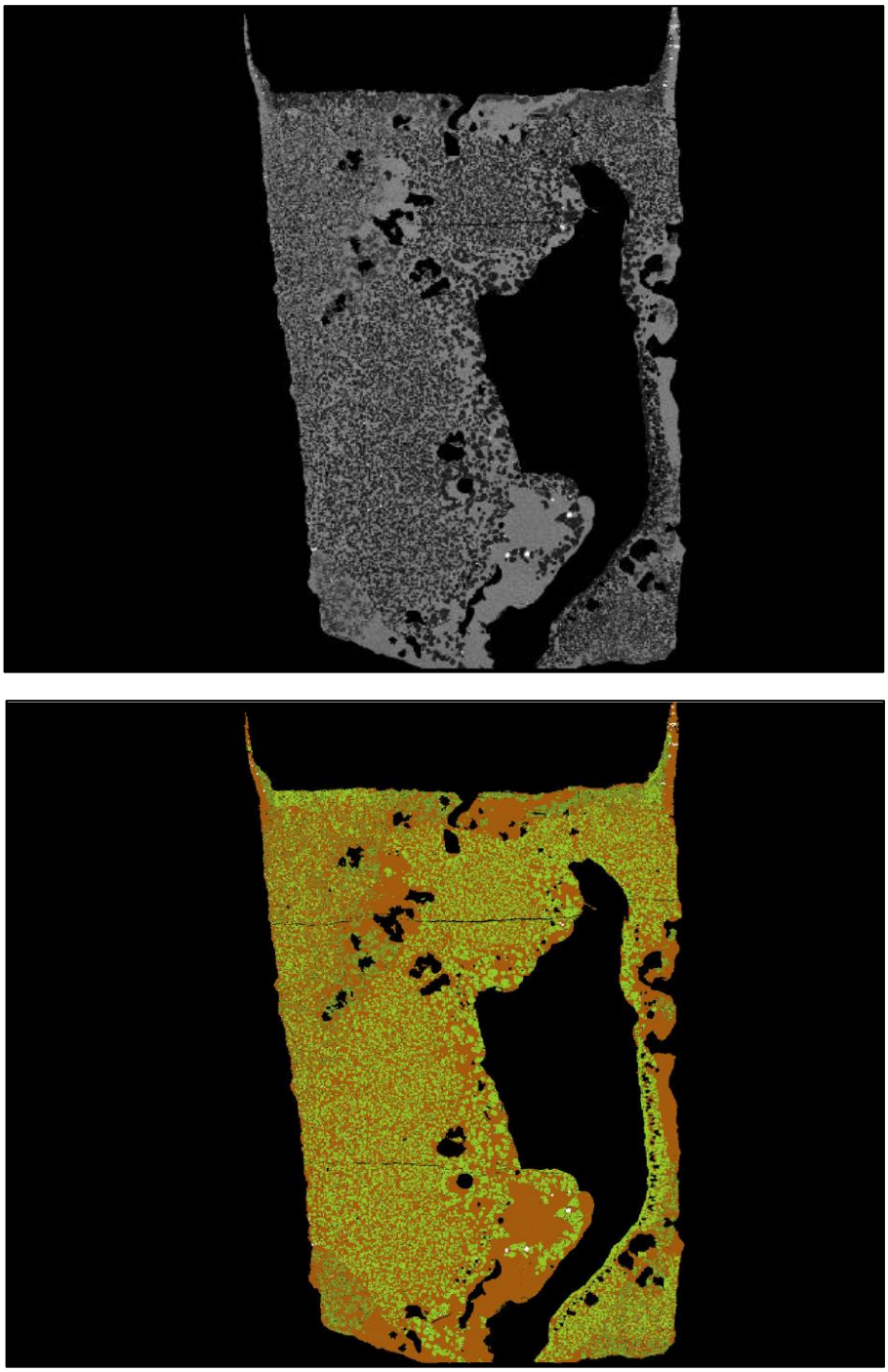


Figure 154: Separation by gray values *of sample 120-1* using MATLAB. Original image (top) and constructed image of the separation (bottom).

Orange: Melt

Dark Green: Olivine

Light Green: OPX

White: Fe-Nuggets

Black: Capsule/Holes

Comparing the results from LPUM-M-120 and the simulation at IW-2 we can conclude that the same minerals (OPX and olivine) are crystallised in both cases, but the modal proportions do not match. Considering the crystal fraction of 54.65% in sample LPUM-M-120-1 obtained via greyscale separation, it clearly exceeds the 29% obtained in the simulation experiment (Figure 154). If the temperature conditions in the MELTS simulation are adjusted to obtain the same degree of crystallisation, the results are much closer to those of the laboratory experiment (Figure 155).

Table 17: Results of the MELTS simulation, the sample LPUM-M-120-1 and the MELTS simulation adjusted in the degree of crystallisation.

	%Solids	*Olivine*	*Orthopyroxene*	*Spinel*
Simulation IW-2	29,00	64,84	34,72	0,44
LPUM-M-120-1	54,65	35,50	64,20	0,50
Simulation IW-2 (adapted)	54,61	42,67	55,79	1,54

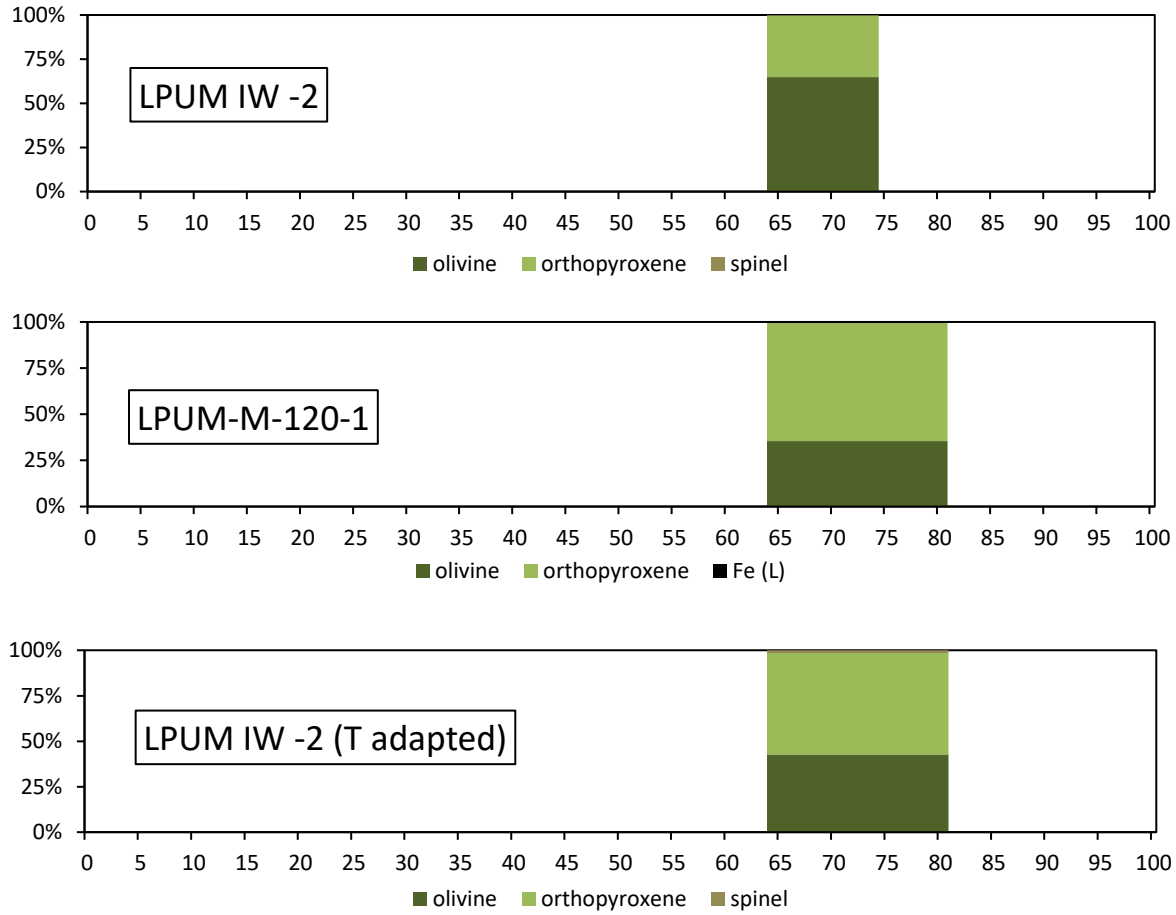


Figure 155: Results of the MELTS simulation (top), the LPUM-M-120-1 sample (middle) and the MELTS simulation adjusted in crystallization degree (bottom).

The modal parts of the laboratory experiment are based on an estimation by the grayscale separation, which has an arbitrary 2D section through the sample as a basis. For this reason, inhomogeneities of the sample, which in reality is three-dimensional, are not taken into account. As a result, the mineral fractions may be even closer or even farther from the simulation. Nevertheless, this experiment shows that simulation and experiment are close enough, at least in this stage of LMO crystallization, to represent a gain in knowledge.

According to the MELTS simulation, Fe-nuggets should not be present in these runs. Instead, it shows a small amount of spinel, mostly consisting of 50% Magnesiochromit ($MgCr_2O_4$) and 50% Magnesiopinel ($MgAl_2O_4$). None of this could be found in the experimental run, showing that even at otherwise close conditions between simulation and reality, the conclusions can be misleading in either way.

4.3.3 MELTS - LMO composition and mineral stack (2)

As mentioned before, the sequence of IW0 starts with orthopyroxene and a small amount of olivine, which has not occurred experimentally in any fractional study yet. Furthermore, spinel is found in our simulations. This has also not been found in the deeper LMO in any experimental study. Only Elardo et al. (2011) report chromium spinel in their experiments, but only from 78 PCS onwards. Chemically, it is a mixture of 60% magnesiochromite ($MgCr_2O_4$), 35% spinel ($MgAl_2O_4$) and 5% chromite ($FeCr_2O_4$). This has a direct influence on the chromium content of the residual melt, which drops from 0.5 wt% to 0.05 wt%. Due to these anomalies in the deep LMO, MELTS is not suitable for direct comparison with experimental studies. Since MELTS provides more credible data for the higher crystallisation range (comparison with LPUM-M-120-1 as well as data in Schwinger and Breuer, 2022) than in the deeper ranges, we nevertheless evaluated the simulations to gain insights from a comparison between them.

LPUM IW 0 – MELTS Simulation

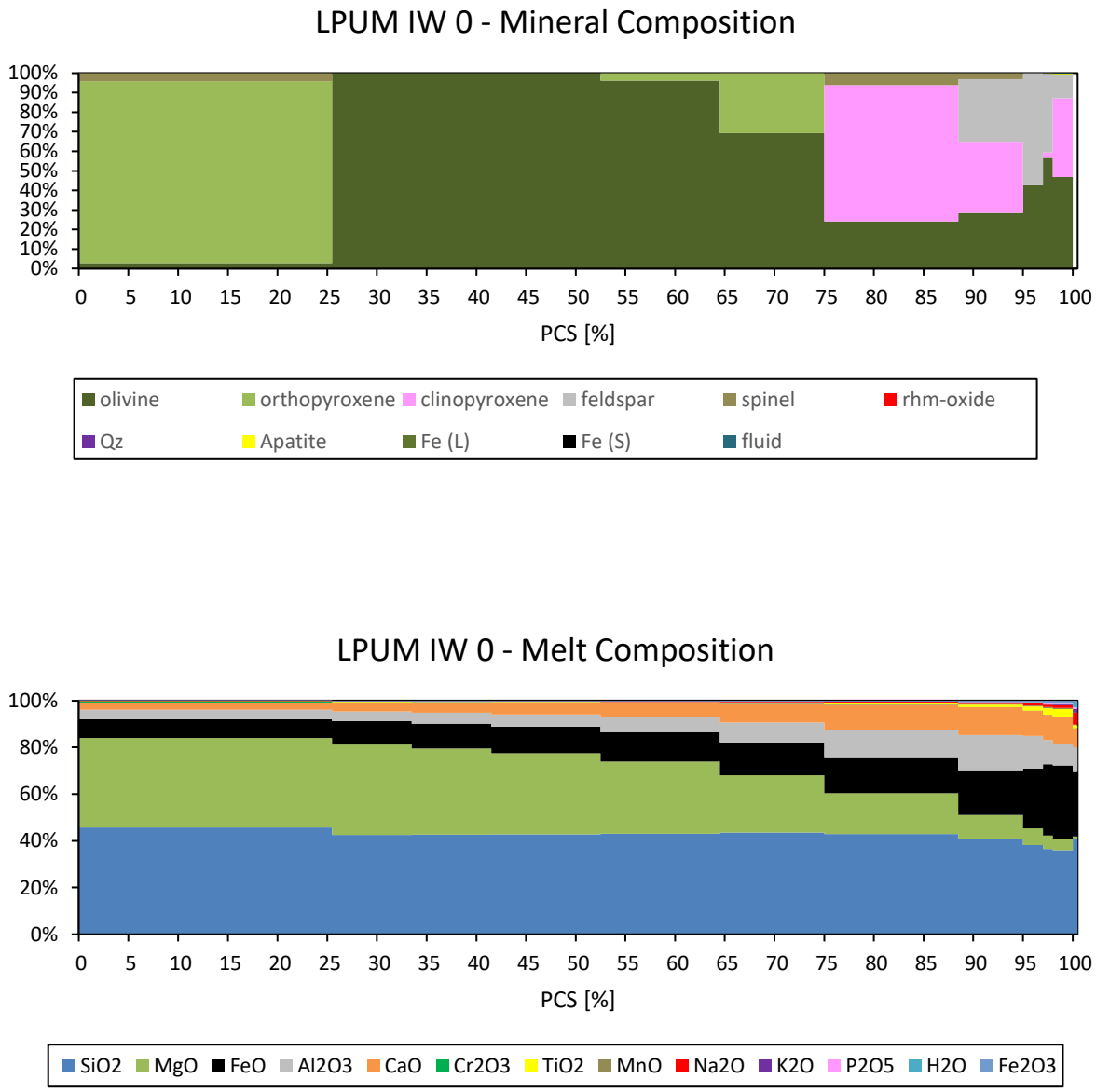


Figure 156: Modal crystal fractions of LMO crystallisation versus degree of crystallisation (PCS) for the MELTS simulation at IW0 (top) as well as the corresponding melt composition (bottom).

LPUM IW -2 – MELTS Simulation

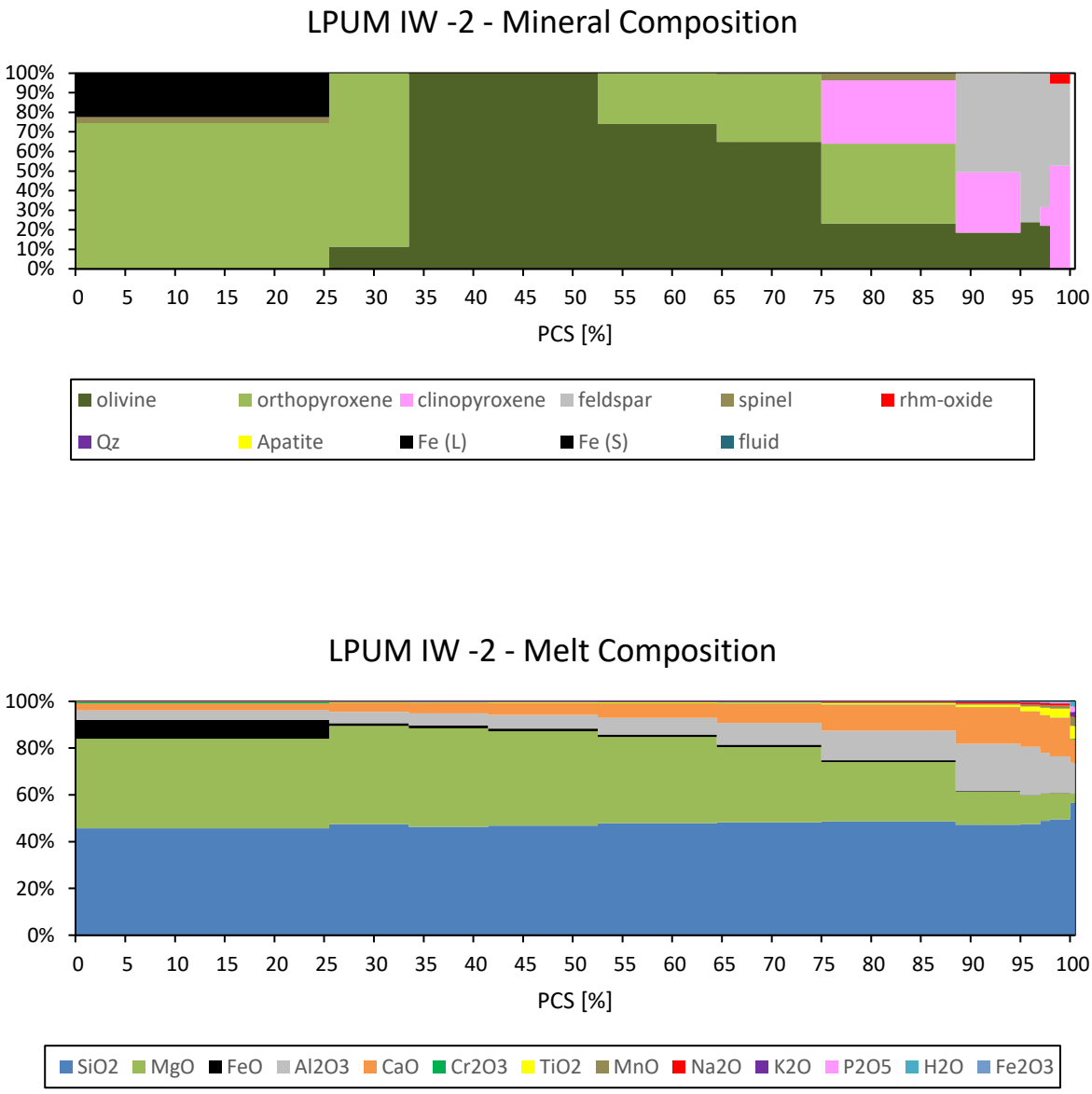


Figure 157: Modal crystal fractions of LMO crystallisation versus degree of crystallisation (PCS) for the MELTS simulation at IW-2 (top) as well as the corresponding melt composition (bottom).

For the series with reducing conditions (IW-2), OPX is also found as the first phase of the sequence. The spinel composition loses magnesiochromite (35.4%) and gains chromite (12.5%). The spinel percentage also increases (51.1%). The remaining percentage is shared by magnetite ($Fe^{2+}Fe^{3+}{}_2O_4$) with 0.75% and ülvospinell (Fe_2TiO_4) with 0.25%. This slightly reduces the loss of chromium for the IW-2 run from 0.5% to 0.88%, but the resulting problem for the later sequence is the same as for IW0.

The fundamental difference between the simulation runs is evident in the formation of elemental iron in the more reduced experiment since a large part of the iron is precipitated from the melt, having a fraction of 22.39% of the corresponding simulation stage. MELTS indicates the density of this phase under the given conditions as 6.97 g/cm^3. This is significantly denser than the melt (2.87g/cm^3) or the minerals (3.07 g/cm^3 for OPX and 4.07 g/cm^3 for spinel). This iron is liquid due to the high ambient temperature but should fractionate due to density since fractionation is also assumed for the less dense minerals.

The iron content of the residual melt decreases from 8.11 wt% to 1.11 wt% in this process. This iron is no longer available in the later LMO crystallisation for the formation of the heavy metal oxides that are necessary for a gravitationally unstable LMO and thus a cumulate overturn. At the same time, spinel occurs significantly earlier in both scenarios (74 PCS) than in the work of Rapp and Draper (2018), where metal containing oxides only occur from 97 PCS onwards.

The formation of feldspar, and thus crust formation, starts at 94 PCS in both scenarios. This is late, compared to the 74 PCS in the experimental work of Rapp and Draper (2018). However, the work of Rapp and Draper is not well comparable due to the deviating sequence in deep areas of the LMO by MELTS.

A potential reason for the later crystallisation of plagioclase could be the loss of aluminium due to the unusual spinel formation in the deep LMO by MELTS. This was already considered as a trigger for reduced crustal thickness by Lin et al. (2017). However, the authors conclude that not enough aluminium is lost through spinel formation. A comparison of the formed volumes in km^3 over the entire sequence in our simulations also indicates that despite roughly equal amounts of spinel in the deep Moon, about 65% more plagioclase was formed in the simulation with IW-2 than in the simulation at IW0 (Figure 158). Therefore, the spinel cannot be the sole trigger.

Another potential reason is the added water in the initial chemistry (100 ppm). Water reduces the liquidus temperature of the system. However, the effect is more pronounced with plagioclase than with olivine or OPX. This increases the crystallised volume of olivine

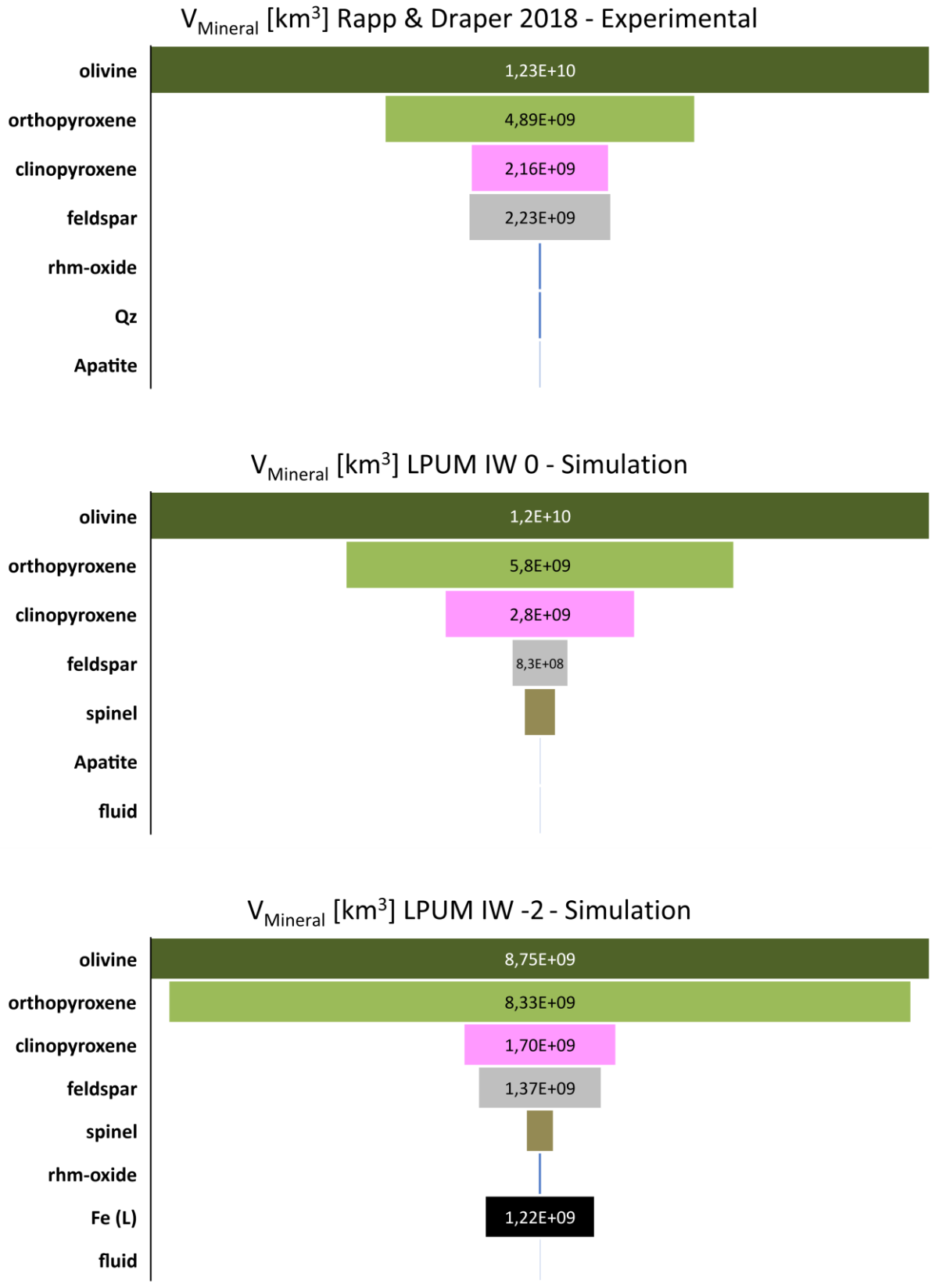


Figure 158: Volume fractions of minerals in Rapp and Draper (2018) and simulations at IW0 and IW-2.

and OPX compared to plagioclase (Yoder, 1965; Sisson & Grove, 1993). Water thus suppresses plagioclase crystallisation in favour of mafic components and thus reduces the crust formation of the LMO (Lin et al., 2017).

Lin et al. (2017) added 0.5% and 1% water to the experiments with the first plagioclase formation (68 PCS at 700 km LMO initial depth). In our simulations, plagioclase does not appear until 94%. The water content at this point in our simulations is 846 ppm (IW0) and 670 ppm (IW-2). The water contents from Lin et al. (2017) are, thus, at least ten times higher than our values but are chosen statically for all experiments. However, our values increase dynamically until the end of the simulated sequence. Thus, 100 ppm of water at the beginning of crystallisation resulted in 0,35 wt% H_2O due to the high incompatibility according to MELTS in the simulations at 99.5 PCS. This is more comparable to the values from Lin et al. (2017).

Converting the volumes from Figure 158 into a crustal thickness in kilometres (assuming the crust is formed of 100% plagioclase) gives the thicknesses shown in Table 18 in comparison with Rapp and Draper (2018) and Lin et al. (2017). For comparison, the calculations from the GRAIL mission are plotted for a crustal thickness of 34 to 43 km (Wieczorek et al., 2013).

Table 18: Plagioclase volume and the crustal thickness calculated from it for Rapp and Draper (2018), Lin et al. (2017) and the simulations at IW0 and IW-2 of this work compared to the GRAIL mission data.

	FSP [km^3]	**Crust [km]**
Wieczorek et al. (2013), GRAIL	-	34 - 43
Rapp and Draper (2018)	2,23E+09	61,0
Lin et al. (2017) - 1% H_2O	-	40,0
Lin et al. (2017) - 0.5% H_2O	-	42,0
LPUM IW 0	8,31E+08	22,2
LPUM IW-2	1,37E+09	36,9
	V_{Moon} [km^3]:	**2,20E+10**

Our simulation at IW-2 fits exactly into the range calculated by Wieczorek et al. (2013), while the simulation at IW+0 underestimates the crustal thickness.

With respect to the results of Lin et al. (2017) (Figure 159), who plotted the crust thickness as a function of the water content at the beginning of the LMO crystallisation, both simulations are inconsistent. Accordingly, our starting composition for the simulation (100 ppm water concentration in the LMO) should produce a significantly higher crust thickness. This again shows the low suitability of the simulated MELTS data for a comparison with

experimental data. Nevertheless, we used the derived mineral compositions to investigate the distribution of water in the present phases in both runs and the study of Rapp and Draper (2018) to investigate the influence of the particular mineral stack.

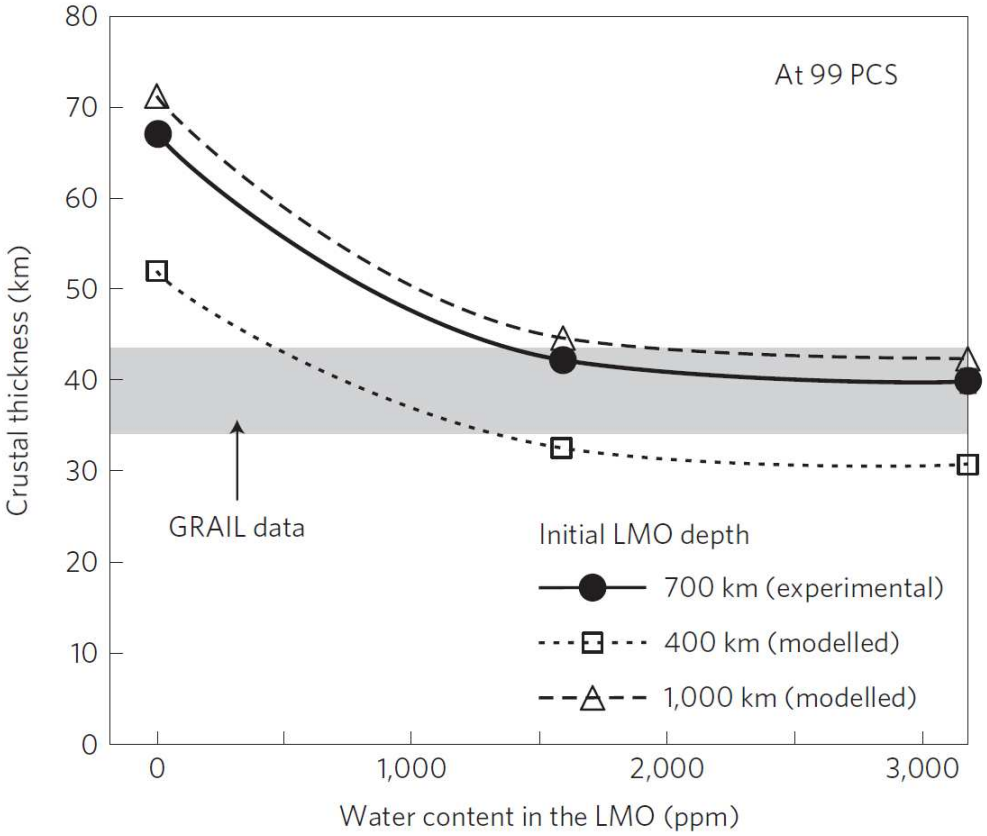


Figure 159: Crust thickness as a result of experimental LMO crystallisation at different water contents and as a function of initial LMO depth at 99 PCS (Lin et al, 2017).

4.4 The distribution of water inside the Moon

Since we have not yet determined the partitioning coefficients for water at realistic lunar conditions at our experiments due to the previously described experimental difficulties, we resort to the data of Potts et al. (2021) for this purpose. These are data obtained under conditions very similar to those that prevailed in our experiments and reflect the lunar conditions very well. They are plotted in Table 19. In addition, we have used data for quartz (Rovetta et al., 1989) and apatite (McCubbin et al., 2015), the latter also obtained at lunar conditions. No data are available for ilmenite or spinel, so we assumed it to be close to 0. The evolution was calculated in 1% steps and takes the mineral compositions of the fully crystallised Moon from Rapp and Draper (2018) and the simulations with IW0 and IW-2 as a basis.

Table 19: Partition coefficients of olivine, OPX, CPX, plagioclase, quartz and apatite to melt. No data are available for ilmenite, which is, thus, assumed almost dry.

$D_{H2O}^{Ol\text{-}Melt}$	**0.001**	*Potts et al. (2021)*
$D_{H2O}^{OPX\text{-}Melt}$	**0.015**	*Potts et al. (2021)*
$D_{H2O}^{CPX\text{-}Melt}$	**0.03**	*Potts et al. (2021)*
$D_{H2O}^{PLAG\text{-}Melt}$	**0.03**	*Potts et al. (2021)*
$D_{H2O}^{Ilm\text{-}Melt}$	**0.000001**	*No data, assumed dry*
$D_{H}^{Qz\text{-}Melt}$	**0.1**	*Rovetta et al. (1989)*
$D_{OH}^{Ap\text{-}Melt}$	**0.07–0.24**	*McCubbin et al. (2015)*

The development of the water content of the melt is shown in Figure 160. This follows the same trend regardless of the composition used. This is due to the very low compatibility of the water in the LMO-relevant minerals. Only minor differences can be seen between 74 PCS and 88 PCS due to the higher plagioclase and CPX content in Rapp and Draper (2018) compared to the simulations.

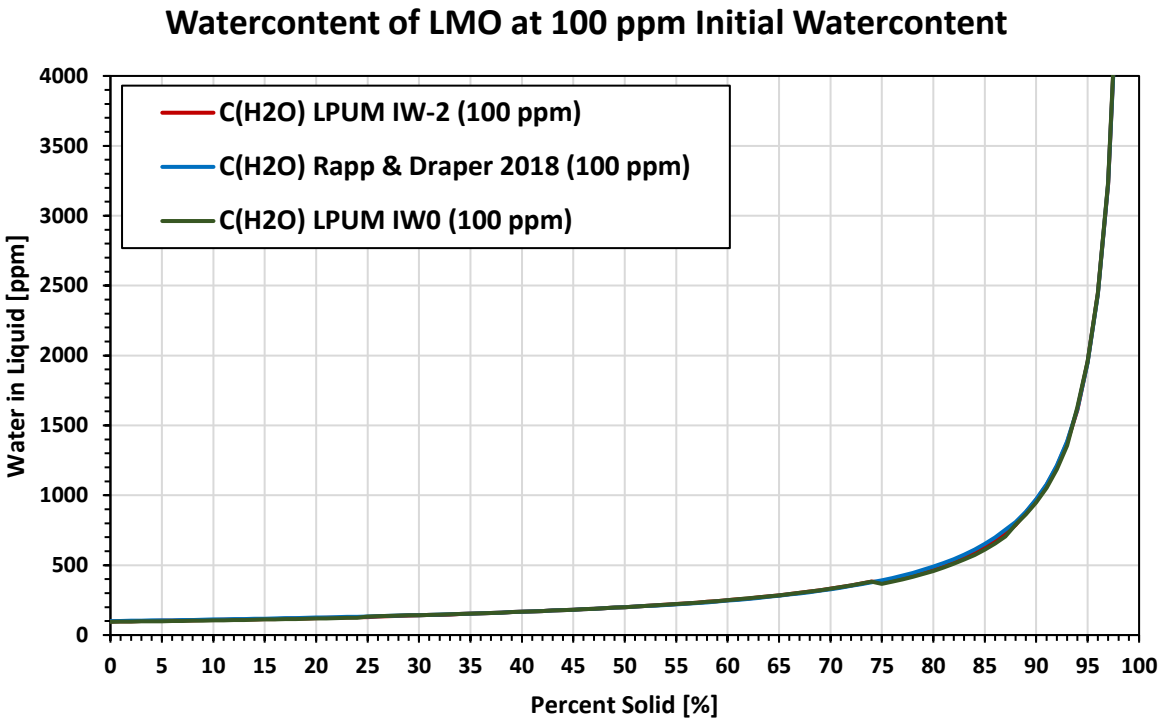


Figure 160: Water content of LMO versus crystallisation progress calculated based on the partition coefficients in Table 19*. Data based on the compositions of Rapp and Draper (2018) and our simulations for IW0 and IW-2.*

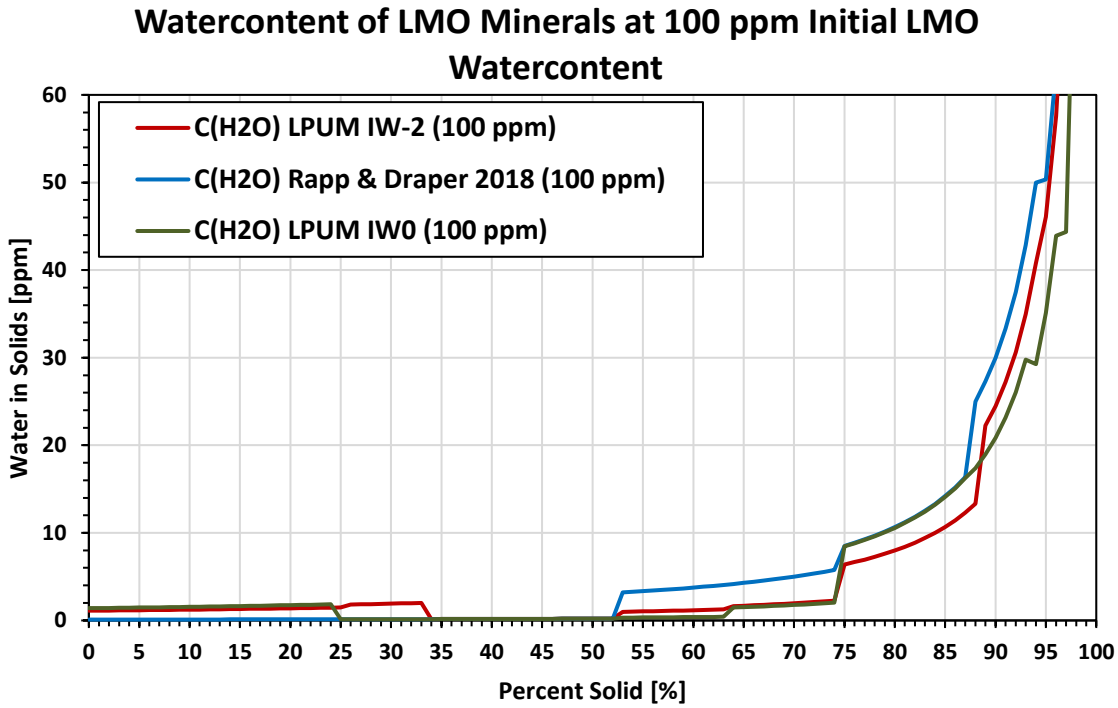


Figure 161: Solid phase water content versus crystallisation progress calculated based on the partition coefficients in Table 19. Data based on the compositions of Rapp and Draper (2018) and our simulations for IW0 and IW-2.

Since the distribution coefficients are directly linked to the water content in the melt, the water content of the minerals is also directly related to the water content of the melt. It is, therefore, not surprising that the water content in the minerals also only increases significantly towards the end of crystallisation. Between 80 PCS and 85 PCS, the contents exceeds 10 ppm for the first time. The range between 34 PCS and 52 PCS is almost free of water in all mineral compositions, as olivine is present here. For Rapp and Draper (2018), this is the case from 0 PCS to 52 PCS. Olivine has a distribution coefficient 15 times smaller than OPX. CPX, and plagioclase even exceeds it by a factor of 30. Since these minerals only appear late in the crystallisation of the LMO while at the same time the concentration of water in the melt increases significantly late, a real increase of water in the minerals is only found in the last 10-15% of the crystallisation (corresponding to 60-90 km depth).

Although the crystallisation sequence of the simulations is flawed by the early OPX formation in the deep LMO and very different from the work of Rapp and Draper (2018), the resulting difference in water content of the solid phase is similar. The distribution of water across the cumulates, thus, depends more on the assumed initial concentration of LMO and the distribution coefficients than on the exact modal proportions of the minerals.

The latest simulation steps predict high water contents of the otherwise nominally dry minerals present and a comparison with the maximum storage capabilities is necessary. Behrens (2021) investigated the solubility of water in plagioclase. They found a maximum water content of 5 ppm (in a 0.001 bar H_2O atmosphere, 1000°C) and 241±31 ppm (in a 2000 bar H_2O atmosphere, 1000°C) at defects in the crystal lattice. Measurements on anorthosites from the Apollo samples gave water contents of around 6 ppm (Hui et al., 2013). This is much lower than our calculation for plagioclase using the mineral composition of Rapp and Draper (2018) (25 - 600 ppm at 88 - 99.5 PCS). This shows that our highest calculated water contents should no longer be soluble in plagioclase and that the real measurements on Apollo-samples even contain less water than the driest plagioclase of our calculations.

Since the obtained water contents depend directly on the initially assumed water content of the LMO, it may have been significantly drier than we assumed in order to bring the water contents of the plagioclase into the range measured by Hui et al. (2013). However, this would result in a significantly thicker crust (Liu et al., 2017), contradicting the GRAIL data (Wieczorek et al., 2013) for a 1400 km deep magma ocean.

When analysing our MELTS simulations again, they show a fluid phase in the last crystallisation steps of the LMO. So, according to MELTS, the water starts to degas at low pressure in the last crystallisation steps. Degassing has already been assumed for the LMO

in other studies (e.g. Liu et al., 2017) and also seems to us to be the more consistent possibility to explain the measured values of the lunar anorthosites.

5 Summary

In this study, we conducted experiments corresponding to the crystallisation of a 1400 km deep lunar magma ocean with the composition of Longhi (2006). We assume complete fractionation of the mineral phases obtained, along the lines of the series of experiments by Rapp and Draper (2018). The aim of the study was to determine the partitioning of water between lunar relevant minerals (olivine, OPX, CPX and plagioclase) at realistic conditions. Subsequently, a model distribution of water in the lunar interior before a possible cumulate overturn should be determined.

Realistic LMO conditions (50 - 100 ppm initial H_2O) require an assembly that limits the diffusion of water into the sample. Boron nitrite meets this requirement well but has been shown to be problematic in the context of thermal sensor stability as well as pressure transfer to the sample at low temperatures. Calibration was finally performed using a NaCl Pyrex assembly with Al_2O_3 around the sample and MgO in the thermocouple region.

For the LMO crystallisation experiments, 9 compositions from Rapp and Draper (2018) were subjected to pressure conditions between 3 and 0.2 GPa, and temperatures between 1600°C and 1025°C. The oxygen fugacity was nominally set to IW-2 via the use of an iron capsule as well as a Cr-Cr_2O_3 buffer.

The experiments show basically the same minerals as in the comparative study. However, they occur in different modal ratios and at different times of the crystallisation sequence. This is due to the temperature limitation of the assembly (1400°C) and the iron capsule (1550°C), which leads to high crystal fractions, especially in experiments in the high P-T range. This directly influences the chemistry of the residual melt, which leads to the deviating mineral phases. A new finding is the appearance of iron spheres. While these should theoretically form at the selected redox conditions of IW-2, we were able to identify them as an artifact of using iron capsules. Due to these issues, we chose to not measure the water content of the problematic experiments with a Secondary Ion Mass Spectrometer (SIMS).

To consider a distribution of water inside the Moon nevertheless, we have resorted to the data published in the meantime by Potts et al. (2021). The experiments in that study have

been conducted under comparable conditions and similar chemistry. As a basis for the modal distribution of minerals in the LMO, we used the data from Rapp and Draper (2018) as well as our own simulations using MELTS at f(O_2) conditions of IW0 and IW-2. MELTS thereby predicts OPX as the liquidus phase for the deeper LMO, contrary to all experimental studies. A comparison experiment showed that the later crystallisation steps agree significantly better with MELTS.

In the case of reducing conditions (IW-2), MELTS predicts that much of the iron in the melt would fractionate in the deep LMO which reflects an unfinished core formation.

The water contained in lunar mineral phases depends mainly on the water content of the melts in equilibrium with these phases while water content of the residual melt depends significantly on the initial water content of the LMO. Therefore, the water content raises for both cases only towards the end of the crystallisation series while the modal mineral proportions have only little effect on the distribution.

5.1.1 Conclusions and future work

Explaining large correlations through small laboratory experiments is the goal of many studies. But as our example shows, success and failure depend on many factors that sometimes only come to the fore during the implementation itself. All too often, one discovers that the processes inside the experiments are not yet fully understood and hinder meaningful interpretations.

In relation to the results of this work, the interaction between buffer material and sample should be mentioned here in particular, since the correct redox conditions during the experiments are of great importance, but their setting is complicated by factors such as the loss of iron to the capsule, the conversion of the buffer material in the reaction or limited communication between buffer and sample.

Also, our specimens show phenomena such as chemical separation, i.e. a different development of different parts of the sample. The interpretation is complicated by such effects or even leads to wrong conclusions. Furthermore, the appearance of iron nuggets in our samples is also subject to an interaction between the capsule and the sample, which we can only explain inadequately. However, it holds the potential for large changes in the crystallisation sequence, especially since MELTS predicts the fundamental presence of the nuggets for the most reduced conditions assumed for the Moon.

These examples show that a better understanding of the processes in the experimental series is essential to be able to draw a real gain in knowledge from the results. Future studies regarding the LMO crystallisation should address the problems.

6 Appendix

6.1.1 LPUM Starting Glasses

LPUM >	300	285	210	150	100	075	050	030	020	M-120	M-80
SiO_2	46,10	47,45	48,68	51,27	48,96	47,53	47,91	46,14	45,83	48,31	49,71
TiO_2	0,17	0,21	0,24	0,35	0,46	0,65	1,36	2,51	3,73	0,40	0,27
Al_2O_3	3,93	5,65	6,78	9,32	11,66	13,13	15,89	11,20	8,73	9,36	16,24
FeO	7,62	9,06	9,67	9,37	10,75	12,37	15,53	22,74	25,93	1,01	0,58
MnO	0,13	0,13	0,14	0,13	0,07	0,06	0,27	0,36	0,42	0,25	0,12
MgO	38,30	32,74	28,82	21,84	17,83	14,58	6,15	4,29	2,59	32,08	18,34
CaO	3,18	4,00	4,78	6,69	9,04	10,22	11,01	10,03	10,01	8,07	13,84
Na_2O	0,05	0,14	0,17	0,24	0,33	0,52	1,28	1,64	1,10	0,27	0,53
K_2O	0,00	0,01	0,02	0,02	0,04	0,05	0,08	0,06	0,06	0,03	0,08
P_2O_5	0,50	0,01	0,02	0,02	0,03	0,10	0,48	1,01	1,57	0,03	0,03
Cr_2O_3	0,02	0,60	0,68	0,75	0,83	0,78	0,04	0,02	0,01	0,18	0,25
Total	**100,00**	**100,00**	**100,00**	**100,00**	**100,00**	**100,00**	**100,00**	**100,00**	**100,00**	**100,00**	**100,00**

6.1.2 LPUM 300-1 OPX and Olivine

LPUM 300-1 OPX	O	Mg	Al	Si	Ca	Cr	Mn	Fe	Total Kat	En	Fs	Wo
OPX 1	6,00	1,90	0,06	1,95	0,02	0,02	0,00	0,06	**4,01**	96,05	3,04	0,91
OPX 2	6,00	1,87	0,09	1,93	0,03	0,02	0,00	0,07	**4,01**	94,91	3,72	1,37
OPX 3	6,00	1,88	0,08	1,94	0,03	0,02	0,00	0,07	**4,01**	95,37	3,30	1,32
OPX 4	6,00	1,90	0,06	1,95	0,02	0,02	0,00	0,06	**4,01**	95,76	3,18	1,06
OPX 5	6,00	1,89	0,06	1,95	0,02	0,02	0,00	0,07	**4,01**	95,69	3,29	1,01
OPX 6	6,00	1,89	0,07	1,94	0,02	0,02	0,00	0,06	**4,01**	95,75	3,24	1,01
OPX 7	6,00	1,90	0,06	1,95	0,02	0,02	0,00	0,07	**4,01**	95,76	3,28	0,96
OPX 8	6,00	1,88	0,10	1,93	0,02	0,02	0,00	0,06	**4,01**	95,71	3,06	1,23
OPX 9	6,00	1,90	0,06	1,95	0,02	0,02	0,00	0,07	**4,01**	95,71	3,33	0,96
OPX 10	6,00	1,87	0,10	1,93	0,02	0,02	0,00	0,07	**4,01**	95,15	3,62	1,23
OPX 11	6,00	1,89	0,07	1,95	0,02	0,02	0,00	0,07	**4,01**	95,69	3,30	1,01
OPX 12	6,00	1,88	0,07	1,95	0,02	0,02	0,00	0,06	**4,01**	95,67	3,26	1,07
OPX 13	6,00	1,89	0,06	1,96	0,02	0,02	0,00	0,06	**4,01**	95,90	3,24	0,86
average	6,00	1,89	0,07	1,94	0,02	0,02	0,00	0,07	**4,01**	95,62	3,30	1,08

LPUM 300-1 Olivine	O	Mg	Al	Si	Ca	Cr	Mn	Fe	Total Kat	Fo	Fa
Olivine 1	4,0	1,95	0,00	0,99	0,00	0,00	0,00	0,06	**3,01**	96,87	3,13
Olivine 2	4,0	1,93	0,00	0,99	0,00	0,00	0,00	0,08	**3,00**	96,15	3,85
Olivine 3	4,0	1,91	0,00	0,99	0,00	0,01	0,00	0,10	**3,01**	95,12	4,88
Olivine 4	4,0	1,92	0,00	0,99	0,00	0,01	0,00	0,09	**3,01**	95,74	4,26
Olivine 5	4,0	1,92	0,03	0,98	0,00	0,00	0,00	0,07	**3,00**	96,71	3,29
Olivine 6	4,0	1,94	0,00	0,99	0,00	0,00	0,00	0,07	**3,01**	96,37	3,63
Olivine 7	4,0	1,94	0,00	0,99	0,00	0,00	0,00	0,07	**3,01**	96,62	3,38
Olivine 8	4,0	1,94	0,00	0,99	0,00	0,00	0,00	0,07	**3,01**	96,52	3,48
Olivine 9	4,0	1,94	0,00	0,99	0,00	0,00	0,00	0,07	**3,01**	96,58	3,42
Olivine 10	4,0	1,90	0,05	0,97	0,00	0,01	0,00	0,07	**3,00**	96,37	3,63
Olivine 11	4,0	1,94	0,00	0,99	0,00	0,00	0,00	0,07	**3,01**	96,72	3,28
Olivine 12	4,0	1,94	0,00	0,99	0,00	0,00	0,00	0,06	**3,01**	96,82	3,18
Olivine 13	4,0	1,94	0,00	0,99	0,00	0,00	0,00	0,06	**3,01**	96,93	3,07
Olivine 14	4,0	1,93	0,00	0,99	0,00	0,00	0,00	0,07	**3,01**	96,43	3,57
Olivine 15	4,0	1,94	0,00	0,99	0,00	0,00	0,00	0,07	**3,01**	96,54	3,46
Olivine 16	4,0	1,93	0,01	0,99	0,00	0,00	0,00	0,08	**3,01**	96,09	3,91
average	**4,00**	**1,93**	**0,01**	**0,99**	**0,00**	**0,00**	**0,00**	**0,07**	3,01	**96,41**	**3,59**

6.1.3 LPUM 285-2 OPX

LPUM 285-2 OPX	O	Mg	Al	Si	Ca	Cr	Mn	Fe	Total Kat	En	Fs	Wo
OPX 1	6,00	1,75	0,10	1,94	0,04	0,01	0,01	0,16	**4,01**	89,78	7,96	2,26
OPX 2	6,00	1,74	0,09	1,95	0,05	0,01	0,02	0,16	**4,01**	89,67	7,97	2,37
OPX 3	6,00	1,74	0,12	1,93	0,04	0,01	0,01	0,15	**4,01**	90,11	7,66	2,23
OPX 4	6,00	1,74	0,13	1,92	0,05	0,01	0,01	0,15	**4,01**	90,01	7,66	2,33
OPX 5	6,00	1,74	0,12	1,93	0,04	0,01	0,02	0,15	**4,01**	89,91	7,92	2,17
OPX 6	6,00	1,74	0,11	1,93	0,05	0,01	0,01	0,17	**4,01**	88,92	8,77	2,31
OPX 7	6,00	1,73	0,17	1,90	0,05	0,02	0,01	0,14	**4,01**	90,29	7,25	2,45
OPX 8	6,00	1,72	0,17	1,89	0,07	0,03	0,00	0,13	**4,01**	89,87	6,58	3,55
OPX 9	6,00	1,72	0,15	1,91	0,06	0,02	0,00	0,13	**4,00**	89,92	6,84	3,24
OPX 10	6,00	1,72	0,16	1,90	0,06	0,02	0,01	0,13	**4,00**	89,98	6,76	3,25
OPX 11	6,00	1,71	0,12	1,92	0,06	0,01	0,03	0,16	**4,01**	88,58	8,35	3,06
OPX 12	6,00	1,70	0,17	1,89	0,06	0,03	0,00	0,15	**4,01**	88,85	7,80	3,35
OPX 13	6,00	1,66	0,15	1,92	0,08	0,01	0,02	0,14	**3,99**	88,12	7,53	4,35
OPX 14	6,00	1,65	0,24	1,86	0,06	0,02	0,01	0,17	**4,01**	87,59	9,11	3,30
OPX 15	6,00	1,72	0,13	1,93	0,05	0,02	0,01	0,15	**4,00**	89,54	7,75	2,71
OPX 16	6,00	1,71	0,15	1,91	0,05	0,02	0,00	0,17	**4,01**	88,73	8,57	2,70
OPX 17	6,00	1,71	0,15	1,90	0,05	0,02	0,01	0,16	**4,01**	88,83	8,37	2,81
OPX 18	6,00	1,73	0,13	1,92	0,05	0,02	0,01	0,15	**4,01**	89,63	7,68	2,70
OPX 19	6,00	1,71	0,15	1,91	0,05	0,02	0,00	0,15	**4,00**	89,21	7,98	2,82
OPX 20	6,00	1,71	0,14	1,91	0,05	0,02	0,01	0,17	**4,01**	88,47	8,88	2,65
OPX 21	6,00	1,74	0,12	1,93	0,05	0,02	0,01	0,15	**4,01**	90,02	7,55	2,43
OPX 22	6,00	1,73	0,12	1,93	0,05	0,02	0,00	0,16	**4,00**	89,36	8,01	2,63
OPX 23	6,00	1,67	0,15	1,91	0,07	0,02	0,00	0,17	**4,00**	87,08	9,07	3,86
OPX 24	6,00	1,68	0,16	1,91	0,07	0,02	0,00	0,16	**4,00**	87,64	8,55	3,81
OPX 25	6,00	1,66	0,21	1,88	0,08	0,02	0,00	0,16	**4,00**	87,62	8,20	4,18
OPX 26	6,00	1,69	0,15	1,91	0,07	0,02	0,00	0,14	**4,00**	88,79	7,33	3,88
OPX 27	6,00	1,70	0,17	1,90	0,07	0,03	0,00	0,13	**4,00**	89,29	6,88	3,83
OPX 28	6,00	1,69	0,20	1,88	0,07	0,04	0,00	0,12	**4,00**	89,86	6,21	3,93
OPX 29	6,00	1,66	0,15	1,92	0,08	0,01	0,00	0,19	**4,00**	86,47	9,63	3,90
OPX 30	6,00	1,66	0,19	1,89	0,08	0,02	0,00	0,16	**4,00**	87,51	8,54	3,95
OPX 31	6,00	1,69	0,16	1,91	0,07	0,02	0,00	0,15	**4,00**	88,46	7,73	3,81
OPX 32	6,00	1,66	0,19	1,89	0,07	0,03	0,00	0,16	**4,00**	87,59	8,56	3,86
average	**6,00**	**1,71**	**0,15**	**1,91**	**0,06**	**0,02**	**0,01**	**0,15**	4,00	**88,93**	**7,93**	**3,15**

6.1.4 LPUM 285-2 Olivine

LPUM 285-2 Olivine	O	Na	Mg	Al	Si	Ca	Cr	Mn	Fe	Total Kat	Fo	Fa
Olivine 1	4,00	0,00	1,83	0,01	0,99	0,01	0,01	0,01	0,15	**3,00**	92,53	7,47
Olivine 2	4,00	0,00	1,83	0,01	0,98	0,01	0,01	0,01	0,15	**3,01**	92,44	7,56
Olivine 3	4,00	0,00	1,88	0,01	0,99	0,01	0,01	0,01	0,10	**3,00**	94,99	5,01
Olivine 4	4,00	0,00	1,89	0,00	1,00	0,01	0,00	0,01	0,10	**3,00**	95,07	4,93
Olivine 5	4,00	0,00	1,88	0,01	0,99	0,01	0,01	0,01	0,10	**3,00**	94,95	5,05
Olivine 6	4,00	0,00	1,91	0,00	0,99	0,01	0,01	0,00	0,09	**3,01**	95,51	4,49
Olivine 7	4,00	0,00	1,88	0,00	0,99	0,01	0,01	0,01	0,12	**3,01**	94,21	5,79
Olivine 8	4,00	0,00	1,86	0,01	0,98	0,01	0,01	0,01	0,12	**3,00**	93,78	6,22
Olivine 9	4,00	0,00	1,89	0,00	0,99	0,01	0,01	0,01	0,11	**3,01**	94,72	5,28
Olivine 10	4,00	0,00	1,90	0,00	0,99	0,01	0,01	0,01	0,09	**3,00**	95,42	4,58
Olivine 11	4,00	0,00	1,89	0,00	0,99	0,01	0,01	0,01	0,11	**3,01**	94,69	5,31
Olivine 12	4,00	0,00	1,89	0,01	0,99	0,01	0,01	0,01	0,09	**3,00**	95,34	4,66
Olivine 13	4,00	0,00	1,89	0,00	0,99	0,01	0,01	0,01	0,10	**3,01**	94,90	5,10
Olivine 14	4,00	0,00	1,88	0,00	1,00	0,01	0,00	0,01	0,11	**3,00**	94,53	5,47
Olivine 15	4,00	0,00	1,85	0,00	1,00	0,01	0,01	0,01	0,14	**3,00**	93,16	6,84
Olivine 16	4,00	0,00	1,84	0,00	1,00	0,01	0,01	0,01	0,14	**3,00**	93,14	6,86
Olivine 17	4,00	0,00	1,84	0,00	1,00	0,01	0,01	0,01	0,14	**3,00**	92,86	7,14
Average	**4,00**	**0,00**	**1,87**	**0,00**	**0,99**	**0,01**	**0,01**	**0,01**	**0,11**	3,00	**94,25**	**5,75**

6.1.5 LPUM 210-2 OPX and CPX

LPUM 210-2 OPX	O	Na	Mg	Al	Si	Ca	Ti	Cr	Mn	Fe	Total Kat	En	Wo	Fs
OPX 1	6,00	0,00	1,69	0,25	1,84	0,09	0,00	0,02	0,01	0,13	**4,03**	88,6	4,5	7,0
OPX 2	6,00	0,00	1,69	0,25	1,83	0,09	0,00	0,02	0,01	0,14	**4,03**	88,1	4,7	7,2
OPX 3	6,00	0,00	1,68	0,27	1,83	0,09	0,01	0,02	0,01	0,13	**4,03**	88,0	4,9	7,1
OPX 4	6,00	0,00	1,68	0,29	1,82	0,08	0,00	0,02	0,00	0,14	**4,03**	88,4	4,3	7,3
OPX 5	6,00	0,00	1,67	0,26	1,83	0,10	0,01	0,02	0,01	0,14	**4,03**	87,6	5,3	7,1
OPX 6	6,00	0,00	1,65	0,28	1,82	0,11	0,01	0,02	0,00	0,13	**4,02**	87,1	5,9	7,0
OPX 7	6,00	0,00	1,65	0,30	1,81	0,11	0,00	0,02	0,01	0,13	**4,03**	87,0	5,9	7,0
OPX 8	6,00	0,00	1,64	0,32	1,80	0,08	0,01	0,02	0,01	0,16	**4,03**	87,4	4,2	8,4
OPX 9	6,00	0,00	1,63	0,22	1,86	0,09	0,00	0,02	0,01	0,20	**4,02**	85,1	4,6	10,3
OPX 10	6,00	0,00	1,62	0,23	1,84	0,09	0,00	0,02	0,01	0,22	**4,03**	83,8	4,5	11,7
OPX 11	6,00	0,00	1,62	0,23	1,85	0,09	0,00	0,02	0,00	0,23	**4,03**	83,5	4,5	12,0
OPX 12	6,00	0,00	1,61	0,33	1,80	0,10	0,01	0,02	0,01	0,16	**4,02**	86,2	5,4	8,4
OPX 13	6,00	0,00	1,58	0,23	1,85	0,09	0,00	0,02	0,01	0,24	**4,03**	82,5	4,8	12,7
OPX 14	6,00	0,00	1,55	0,35	1,80	0,08	0,01	0,02	0,00	0,22	**4,01**	83,9	4,3	11,8
OPX 18	6,00	0,00	1,48	0,31	1,85	0,09	0,00	0,02	0,01	0,21	**3,98**	82,91	5,08	12,00
OPX 19	6,00	0,00	1,49	0,31	1,84	0,09	0,00	0,02	0,01	0,21	**3,98**	83,14	5,12	11,74
OPX 20	6,00	0,00	1,48	0,30	1,86	0,09	0,01	0,02	0,01	0,20	**3,97**	83,28	5,22	11,50
OPX 21	6,00	0,00	1,47	0,32	1,85	0,10	0,00	0,02	0,01	0,20	**3,98**	82,93	5,61	11,45
OPX 22	6,00	0,00	1,53	0,23	1,90	0,10	0,00	0,02	0,01	0,19	**3,98**	83,85	5,75	10,40
OPX 23	6,00	0,00	1,49	0,26	1,88	0,11	0,00	0,02	0,01	0,21	**3,98**	82,48	6,06	11,46
OPX 24	6,00	0,00	1,52	0,24	1,89	0,12	0,00	0,02	0,01	0,18	**3,98**	83,56	6,36	10,08
average	**6,00**	**0,00**	**1,59**	**0,27**	**1,84**	**0,09**	**0,00**	**0,02**	**0,01**	**0,18**	4,01	**85,21**	**5,09**	**9,70**

LPUM 210-2 CPX	O	Na	Mg	Al	Si	Ca	Ti	Cr	Mn	Fe	Total Kat	En	Wo	Fs
CPX 1	6,00	0,00	1,16	0,33	1,85	0,35	0,01	0,02	0,00	0,24	**3,97**	66,27	20,19	13,54
CPX 2	6,00	0,02	1,15	0,33	1,84	0,37	0,01	0,02	0,01	0,23	**3,98**	65,59	21,12	13,29
CPX 3	6,00	0,00	1,20	0,29	1,86	0,39	0,00	0,03	0,00	0,21	**3,98**	66,72	21,41	11,87
CPX 4	6,00	0,02	1,12	0,34	1,84	0,39	0,00	0,02	0,01	0,23	**3,98**	64,43	22,32	13,25
CPX 5	6,00	0,00	1,13	0,34	1,84	0,40	0,01	0,02	0,01	0,23	**3,97**	64,34	22,60	13,06
CPX 6	6,00	0,00	1,13	0,31	1,86	0,41	0,00	0,03	0,00	0,22	**3,97**	64,22	23,08	12,70
CPX 7	6,00	0,00	1,10	0,28	1,86	0,51	0,00	0,03	0,01	0,21	**3,99**	60,77	27,86	11,37
average	**6,00**	**0,00**	**1,40**	**0,29**	**1,85**	**0,20**	**0,00**	**0,02**	**0,01**	**0,21**	3,99	**76,98**	**11,32**	**11,70**

6.1.6 LPUM 150-1 OPX Part 1

LPUM 150-1 OPX-1	O	Mg	Al	Si	Ca	Cr	Mn	Fe	Total Kat	En	Fs	Wo
OPX 1	6,00	1,77	0,15	1,91	0,05	0,06	0,00	0,05	**3,99**	94,56	2,83	2,61
OPX 2	6,00	1,75	0,14	1,92	0,05	0,04	0,00	0,09	**3,99**	92,58	4,88	2,54
OPX 3	6,00	1,76	0,15	1,91	0,05	0,05	0,00	0,07	**3,99**	93,57	3,61	2,81
OPX 4	6,00	1,81	0,09	1,93	0,05	0,06	0,00	0,05	**3,99**	94,71	2,67	2,62
OPX 5	6,00	1,80	0,10	1,93	0,05	0,06	0,00	0,06	**3,99**	94,65	2,94	2,41
OPX 6	6,00	1,81	0,10	1,93	0,05	0,06	0,00	0,06	**4,00**	94,56	2,98	2,46
OPX 7	6,00	1,79	0,11	1,92	0,04	0,06	0,02	0,05	**3,99**	95,06	2,66	2,28
OPX 8	6,00	1,77	0,14	1,91	0,05	0,06	0,02	0,05	**4,00**	94,47	2,82	2,71
OPX 9	6,00	1,77	0,14	1,91	0,05	0,06	0,00	0,05	**3,99**	94,66	2,67	2,67
OPX 10	6,00	1,82	0,09	1,93	0,05	0,06	0,02	0,05	**4,00**	95,08	2,57	2,36
OPX 11	6,00	1,80	0,13	1,92	0,04	0,06	0,00	0,05	**3,99**	94,94	2,74	2,32
OPX 12	6,00	1,82	0,09	1,93	0,05	0,06	0,00	0,04	**3,99**	95,40	2,04	2,56
OPX 13	6,00	1,79	0,12	1,93	0,04	0,06	0,00	0,04	**3,98**	95,48	2,18	2,34
OPX 14	6,00	1,81	0,10	1,93	0,05	0,06	0,00	0,04	**3,99**	95,38	2,10	2,52
OPX 15	6,00	1,80	0,10	1,94	0,04	0,06	0,00	0,04	**3,98**	95,25	2,38	2,38
OPX 16	6,00	1,80	0,12	1,92	0,05	0,05	0,00	0,06	**3,99**	94,34	3,25	2,41
OPX 17	6,00	1,79	0,15	1,89	0,05	0,06	0,02	0,04	**4,00**	95,36	2,13	2,51
OPX 18	6,00	1,72	0,22	1,87	0,05	0,07	0,00	0,04	**3,98**	94,88	2,09	3,03
OPX 19	6,00	1,78	0,11	1,94	0,05	0,06	0,00	0,04	**3,97**	95,60	1,93	2,47
OPX 20	6,00	1,80	0,11	1,93	0,04	0,06	0,00	0,04	**3,98**	95,81	2,02	2,18
OPX 21	6,00	1,75	0,16	1,90	0,05	0,07	0,00	0,06	**3,98**	94,29	3,18	2,53
OPX 22	6,00	1,77	0,11	1,94	0,04	0,05	0,00	0,07	**3,98**	93,96	3,71	2,33
OPX 23	6,00	1,73	0,18	1,88	0,05	0,07	0,00	0,07	**3,99**	93,33	3,87	2,80
OPX 24	6,00	1,71	0,18	1,89	0,05	0,08	0,00	0,06	**3,98**	93,82	3,28	2,90
OPX 25	6,00	1,70	0,18	1,89	0,05	0,09	0,02	0,06	**3,98**	93,77	3,58	2,64
OPX 26	6,00	1,77	0,14	1,90	0,05	0,06	0,01	0,06	**4,00**	94,21	3,19	2,60
OPX 27	6,00	1,79	0,09	1,94	0,04	0,06	0,00	0,07	**3,99**	94,17	3,67	2,15
OPX 28	6,00	1,80	0,09	1,94	0,05	0,06	0,00	0,04	**3,98**	95,25	2,32	2,43
OPX 29	6,00	1,81	0,09	1,93	0,05	0,06	0,00	0,04	**3,99**	95,27	2,31	2,42
OPX 30	6,00	1,81	0,08	1,94	0,04	0,06	0,01	0,07	**4,00**	94,31	3,44	2,24

6.1.7 LPUM 150-1 OPX Part 2

LPUM 150-1 OPX-2	O	Mg	Al	Si	Ca	Cr	Mn	Fe	Total Kat	En	Fs	Wo
OPX 31	6,00	1,79	0,10	1,94	0,04	0,05	0,02	0,05	**3,99**	94,96	2,71	2,33
OPX 32	6,00	1,78	0,11	1,93	0,05	0,05	0,02	0,04	**3,99**	94,94	2,40	2,67
OPX 33	6,00	1,80	0,09	1,94	0,04	0,06	0,00	0,05	**3,99**	94,91	2,89	2,21
OPX 34	6,00	1,78	0,12	1,92	0,04	0,06	0,00	0,07	**3,99**	94,04	3,74	2,21
OPX 35	6,00	1,75	0,17	1,90	0,05	0,06	0,00	0,05	**3,98**	94,75	2,60	2,65
OPX 36	6,00	1,78	0,10	1,94	0,05	0,06	0,00	0,06	**3,99**	94,04	3,38	2,58
OPX 37	6,00	1,80	0,10	1,92	0,05	0,07	0,01	0,06	**4,00**	94,54	2,94	2,52
OPX 38	6,00	1,77	0,10	1,94	0,05	0,06	0,00	0,06	**3,98**	94,22	3,18	2,60
OPX 39	6,00	1,78	0,11	1,93	0,05	0,07	0,00	0,05	**3,99**	94,49	2,81	2,70
OPX 40	6,00	1,79	0,10	1,93	0,05	0,06	0,00	0,06	**3,99**	94,15	3,37	2,48
OPX 41	6,00	1,81	0,09	1,93	0,05	0,06	0,01	0,05	**4,00**	94,60	2,88	2,51
OPX 42	6,00	1,81	0,10	1,92	0,05	0,06	0,02	0,04	**4,00**	95,31	2,05	2,63
OPX 43	6,00	1,78	0,15	1,90	0,05	0,07	0,00	0,04	**3,99**	95,05	2,02	2,93
OPX 44	6,00	1,78	0,12	1,92	0,05	0,06	0,01	0,04	**3,99**	95,09	2,35	2,56
OPX 45	6,00	1,82	0,09	1,93	0,05	0,05	0,00	0,04	**3,99**	95,00	2,24	2,76
OPX 46	6,00	1,78	0,14	1,91	0,05	0,06	0,02	0,04	**3,99**	95,39	2,09	2,52
OPX 47	6,00	1,79	0,10	1,93	0,04	0,06	0,00	0,05	**3,98**	94,88	2,80	2,32
OPX 48	6,00	1,78	0,10	1,94	0,05	0,06	0,00	0,06	**3,99**	94,04	3,27	2,69
OPX 49	6,00	1,79	0,11	1,93	0,04	0,06	0,01	0,05	**3,99**	95,26	2,56	2,18
OPX 50	6,00	1,80	0,10	1,92	0,05	0,06	0,01	0,05	**4,00**	94,99	2,59	2,43
OPX 51	6,00	1,78	0,13	1,92	0,05	0,06	0,00	0,04	**3,99**	95,30	2,03	2,67
OPX 52	6,00	1,79	0,15	1,89	0,04	0,07	0,01	0,04	**4,00**	95,36	2,35	2,29
OPX 53	6,00	1,79	0,09	1,94	0,05	0,05	0,00	0,06	**3,99**	94,43	3,00	2,57
OPX 54	6,00	1,79	0,12	1,91	0,05	0,06	0,01	0,04	**3,99**	95,33	2,12	2,55
OPX 55	6,00	1,80	0,12	1,91	0,05	0,06	0,02	0,04	**4,00**	95,33	1,96	2,70
OPX 56	6,00	1,80	0,13	1,90	0,05	0,06	0,02	0,04	**4,00**	95,33	2,07	2,60
OPX 57	6,00	1,81	0,11	1,93	0,05	0,06	0,00	0,03	**3,99**	95,67	1,74	2,59
OPX 58	6,00	1,79	0,15	1,90	0,05	0,05	0,01	0,04	**4,00**	95,48	2,02	2,50
OPX 59	6,00	1,80	0,14	1,90	0,05	0,06	0,01	0,03	**4,00**	95,53	1,65	2,82
average	**6,00**	**1,78**	**0,12**	**1,92**	**0,05**	**0,06**	**0,01**	**0,05**	3,99	**94,76**	**2,71**	**2,53**

6.1.8 LPUM 150-3 OPX Part 1

LPUM 150-3 OPX	O	Mg	Al	Si	Ca	Cr	Fe	Total Kat	En	Fs	Wo
OPX 1	6,00	1,66	0,13	1,92	0,06	0,02	0,21	**4,00**	85,92	2,98	3,21
OPX 2	6,00	1,64	0,15	1,91	0,07	0,02	0,21	**4,00**	85,51	3,14	3,39
OPX 3	6,00	1,65	0,15	1,91	0,07	0,02	0,20	**4,00**	85,92	3,26	3,49
OPX 4	6,00	1,65	0,14	1,91	0,06	0,02	0,21	**4,00**	85,74	2,94	3,17
OPX 5	6,00	1,64	0,17	1,90	0,06	0,02	0,22	**4,01**	85,38	3,04	3,29
OPX 6	6,00	1,63	0,18	1,89	0,06	0,02	0,22	**4,00**	85,46	3,01	3,25
OPX 7	6,00	1,65	0,15	1,91	0,07	0,02	0,21	**4,01**	85,60	3,14	3,38
OPX 8	6,00	1,66	0,15	1,91	0,07	0,02	0,20	**4,00**	86,21	3,16	3,38
OPX 9	6,00	1,70	0,12	1,93	0,05	0,02	0,19	**4,00**	87,33	2,60	2,78
OPX 10	6,00	1,67	0,12	1,92	0,06	0,02	0,21	**4,00**	86,01	2,92	3,15
OPX 11	6,00	1,60	0,18	1,89	0,07	0,03	0,23	**4,00**	84,17	3,29	3,58
OPX 12	6,00	1,62	0,17	1,89	0,06	0,02	0,23	**4,01**	84,60	3,02	3,29
OPX 13	6,00	1,61	0,18	1,89	0,07	0,03	0,23	**4,00**	84,41	3,14	3,41
OPX 14	6,00	1,64	0,13	1,92	0,06	0,02	0,23	**4,00**	84,85	2,80	3,05
OPX 15	6,00	1,63	0,15	1,91	0,06	0,02	0,23	**4,00**	84,96	2,87	3,12
OPX 16	6,00	1,62	0,16	1,90	0,06	0,02	0,24	**4,00**	84,66	2,77	3,03
OPX 17	6,00	1,64	0,11	1,93	0,06	0,02	0,24	**4,00**	84,61	2,88	3,14
OPX 18	6,00	1,63	0,14	1,91	0,06	0,02	0,24	**4,00**	84,60	2,80	3,06
OPX 19	6,00	1,62	0,15	1,91	0,06	0,02	0,24	**4,00**	84,52	2,86	3,13
OPX 20	6,00	1,65	0,13	1,92	0,06	0,02	0,22	**4,00**	85,51	2,72	2,95

6.1.9 LPUM 150-3 OPX Part 2

LPUM 150-3 OPX	O	Mg	Al	Si	Ca	Cr	Fe	Total Kat	En	Fs	Wo
OPX 21	6,00	1,76	0,10	1,93	0,05	0,02	0,14	**4,00**	90,22	2,50	2,61
OPX 22	6,00	1,69	0,13	1,92	0,06	0,02	0,19	**4,00**	87,31	2,91	3,10
OPX 23	6,00	1,71	0,11	1,93	0,05	0,02	0,19	**4,01**	87,76	2,50	2,67
OPX 24	6,00	1,66	0,16	1,90	0,07	0,02	0,19	**4,01**	86,47	3,33	3,54
OPX 25	6,00	1,66	0,12	1,93	0,06	0,02	0,22	**4,00**	85,80	2,87	3,10
OPX 26	6,00	1,66	0,15	1,91	0,06	0,02	0,20	**4,00**	86,26	3,06	3,28
OPX 27	6,00	1,68	0,12	1,92	0,06	0,02	0,20	**4,01**	86,75	2,64	2,84
OPX 28	6,00	1,65	0,13	1,92	0,06	0,02	0,21	**4,00**	85,66	3,08	3,31
OPX 29	6,00	1,71	0,10	1,93	0,05	0,02	0,19	**4,00**	87,54	2,39	2,56
OPX 30	6,00	1,65	0,16	1,90	0,07	0,02	0,20	**4,00**	86,01	3,27	3,50
OPX 31	6,00	1,66	0,15	1,91	0,07	0,02	0,20	**4,00**	86,26	3,21	3,44
OPX 32	6,00	1,65	0,16	1,90	0,07	0,02	0,20	**4,01**	85,75	3,40	3,64
OPX 33	6,00	1,61	0,15	1,91	0,08	0,02	0,23	**4,00**	84,16	3,73	4,03
OPX 34	6,00	1,64	0,16	1,90	0,06	0,02	0,22	**4,00**	85,54	2,90	3,13
OPX 35	6,00	1,64	0,15	1,91	0,06	0,02	0,22	**4,01**	85,49	3,03	3,28
OPX 36	6,00	1,63	0,17	1,90	0,07	0,02	0,22	**4,00**	85,32	3,15	3,40
OPX 37	6,00	1,70	0,12	1,92	0,06	0,02	0,18	**4,00**	87,71	2,82	2,99
OPX 38	6,00	1,64	0,19	1,88	0,06	0,02	0,20	**4,00**	86,24	3,04	3,26
OPX 39	6,00	1,66	0,13	1,92	0,06	0,02	0,21	**4,00**	85,90	3,04	3,27
OPX 40	6,00	1,65	0,15	1,91	0,06	0,02	0,21	**4,00**	85,97	2,95	3,18
average	**6,00**	**1,65**	**0,14**	**1,91**	**0,06**	**0,02**	**0,21**	4,00	**85,85**	**2,98**	**3,21**

6.1.10 LPUM 100-1 Olivine

LPUM 100-1 Olivine	O	Mg	Si	Ca	Fe	Total Kat	Fo	Fa
Ol 1	4,00	1,72	0,99	0,01	0,28	**3,01**	85,89	14,11
Ol 2	4,00	1,72	0,99	0,01	0,28	**3,00**	85,93	14,07
Ol 3	4,00	1,72	0,99	0,01	0,28	**3,00**	86,00	14,00
Ol 4	4,00	1,54	1,04	0,04	0,27	**2,89**	85,11	14,89
Ol 5	4,00	1,72	0,99	0,01	0,28	**3,00**	86,11	13,89
Ol 6	4,00	1,72	1,00	0,01	0,28	**3,00**	85,78	14,22
Ol 7	4,00	1,74	0,99	0,01	0,26	**3,00**	86,91	13,09
Ol 8	4,00	1,72	0,99	0,01	0,28	**3,00**	86,08	13,92
Ol 9	4,00	1,74	1,00	0,01	0,26	**3,00**	87,11	12,89
Ol 10	4,00	1,78	0,99	0,01	0,22	**3,01**	88,83	11,17
Ol 11	4,00	1,77	0,99	0,01	0,23	**3,00**	88,36	11,64
Ol 12	4,00	1,78	0,99	0,01	0,23	**3,00**	88,71	11,29
Ol 13	4,00	1,81	0,99	0,01	0,20	**3,01**	90,05	9,95
Ol 14	4,00	1,80	0,99	0,01	0,21	**3,00**	89,75	10,25
Ol 15	4,00	1,80	0,99	0,01	0,21	**3,00**	89,59	10,41
Ol 16	4,00	1,76	0,99	0,01	0,24	**3,00**	87,87	12,13
Ol 17	4,00	1,72	0,99	0,01	0,28	**3,00**	85,78	14,22
Ol 18	4,00	1,72	1,00	0,01	0,29	**3,01**	85,70	14,30
Ol 19	4,00	1,76	1,00	0,01	0,24	**3,00**	87,79	12,21
Ol 20	4,00	1,73	0,99	0,01	0,27	**3,00**	86,44	13,56
Ol 21	4,00	1,73	1,00	0,01	0,27	**3,00**	86,45	13,55
Ol 22	4,00	1,74	0,99	0,01	0,26	**3,00**	86,83	13,17
Ol 23	4,00	1,71	0,99	0,01	0,29	**3,00**	85,48	14,52
Ol 24	4,00	1,75	0,99	0,01	0,26	**3,00**	87,13	12,87
Ol 25	4,00	1,72	0,99	0,01	0,28	**3,01**	86,05	13,95
Ol 26	4,00	1,74	0,99	0,01	0,26	**3,01**	86,81	13,19
Ol 27	4,00	1,71	0,99	0,01	0,29	**3,00**	85,45	14,55
Ol 28	4,00	1,74	0,99	0,01	0,26	**3,01**	86,81	13,19
Ol 29	4,00	1,73	0,99	0,01	0,27	**3,00**	86,39	13,61
Ol 30	4,00	1,79	0,99	0,01	0,21	**3,00**	89,72	10,28
Ol 31	4,00	1,79	0,99	0,01	0,21	**3,00**	89,51	10,49
Ol 32	4,00	1,76	0,99	0,01	0,25	**3,00**	87,70	12,30
average	**4,00**	**1,74**	**1,00**	**0,01**	**0,26**	3,00	**87,13**	**12,87**

6.1.11 LPUM 100-1 OPX Part 1

LPUM 100-1 OPX 1	O	Mg	Al	Si	Ca	Ti	Cr	Mn	Fe	Total Kat	En	Fs	Wo
OPX 1	6,00	1,74	0,15	1,91	0,06	0,00	0,00	0,00	0,14	**4,01**	89,76	7,39	2,84
OPX 2	6,00	1,71	0,16	1,91	0,06	0,00	0,00	0,00	0,17	**4,01**	88,61	8,54	2,85
OPX 3	6,00	1,71	0,18	1,90	0,05	0,00	0,00	0,00	0,17	**4,01**	88,52	8,73	2,75
OPX 4	6,00	1,72	0,16	1,91	0,06	0,00	0,00	0,00	0,15	**4,01**	89,21	7,83	2,96
OPX 5	6,00	1,66	0,14	1,91	0,05	0,00	0,00	0,00	0,23	**4,01**	85,41	11,86	2,73
OPX 6	6,00	1,68	0,12	1,93	0,05	0,00	0,00	0,00	0,22	**4,01**	85,93	11,34	2,72
OPX 7	6,00	1,68	0,12	1,93	0,05	0,00	0,00	0,00	0,22	**4,01**	85,82	11,47	2,71
OPX 8	6,00	1,68	0,11	1,93	0,05	0,00	0,00	0,00	0,22	**4,01**	86,00	11,24	2,76
OPX 9	6,00	1,63	0,16	1,91	0,07	0,00	0,00	0,00	0,23	**4,01**	84,74	11,88	3,37
OPX 10	6,00	1,68	0,10	1,94	0,05	0,00	0,00	0,00	0,23	**4,01**	85,50	11,89	2,60
OPX 11	6,00	1,68	0,10	1,94	0,05	0,00	0,00	0,00	0,23	**4,01**	85,50	11,80	2,70
OPX 12	6,00	1,66	0,14	1,92	0,05	0,00	0,00	0,00	0,23	**4,01**	85,22	12,05	2,73
OPX 13	6,00	1,66	0,12	1,93	0,06	0,00	0,00	0,00	0,24	**4,01**	84,98	12,05	2,97
OPX 14	6,00	1,68	0,08	1,95	0,06	0,00	0,00	0,00	0,24	**4,01**	84,88	12,08	3,03
OPX 15	6,00	1,68	0,12	1,93	0,06	0,00	0,00	0,00	0,22	**4,01**	85,77	11,06	3,17
OPX 16	6,00	1,67	0,11	1,93	0,06	0,00	0,00	0,00	0,23	**4,01**	85,17	11,92	2,92
OPX 17	6,00	1,67	0,11	1,93	0,05	0,00	0,00	0,00	0,23	**4,01**	85,44	11,96	2,61
OPX 18	6,00	1,65	0,15	1,91	0,06	0,00	0,00	0,00	0,23	**4,01**	85,28	11,76	2,95
OPX 19	6,00	1,65	0,15	1,92	0,06	0,00	0,00	0,00	0,23	**4,01**	85,10	12,01	2,89
OPX 20	6,00	1,66	0,13	1,92	0,06	0,00	0,00	0,00	0,23	**4,01**	85,24	11,84	2,92
OPX 21	6,00	1,65	0,14	1,91	0,07	0,00	0,00	0,00	0,23	**4,01**	84,76	11,74	3,50
OPX 22	6,00	1,67	0,11	1,93	0,06	0,00	0,00	0,00	0,23	**4,01**	85,31	11,87	2,81
OPX 23	6,00	1,63	0,16	1,91	0,06	0,00	0,00	0,00	0,25	**4,01**	84,26	12,75	2,99
OPX 24	6,00	1,62	0,17	1,90	0,07	0,00	0,00	0,00	0,25	**4,01**	83,83	12,80	3,37
OPX 25	6,00	1,68	0,08	1,95	0,05	0,00	0,00	0,00	0,25	**4,01**	85,01	12,56	2,43
OPX 26	6,00	1,66	0,12	1,92	0,05	0,00	0,00	0,00	0,25	**4,01**	84,74	12,61	2,65
OPX 27	6,00	1,65	0,14	1,92	0,05	0,00	0,00	0,00	0,25	**4,01**	84,54	12,94	2,52
OPX 28	6,00	1,46	0,26	1,85	0,10	0,01	0,00	0,00	0,33	**4,01**	77,39	17,34	5,27
OPX 29	6,00	1,67	0,09	1,95	0,05	0,00	0,00	0,00	0,25	**4,01**	84,88	12,68	2,44
OPX 30	6,00	1,65	0,15	1,91	0,05	0,00	0,00	0,00	0,25	**4,01**	84,69	12,63	2,67

6.1.12 LPUM 100-1 OPX Part 2

LPUM 100-1 OPX 2	O	Mg	Al	Si	Ca	Ti	Cr	Mn	Fe	Total Kat	En	Fs	Wo
OPX 31	6,00	1,46	0,25	1,87	0,11	0,00	0,00	0,00	0,31	**4,00**	77,67	16,69	5,64
OPX 32	6,00	1,67	0,10	1,94	0,05	0,00	0,00	0,00	0,25	**4,01**	84,78	12,73	2,49
OPX 33	6,00	1,68	0,08	1,95	0,05	0,00	0,00	0,00	0,25	**4,01**	84,91	12,66	2,43
OPX 34	6,00	1,66	0,12	1,93	0,05	0,00	0,00	0,00	0,24	**4,01**	84,92	12,47	2,61
OPX 35	6,00	1,66	0,12	1,93	0,05	0,00	0,00	0,00	0,24	**4,01**	84,91	12,53	2,57
OPX 36	6,00	1,65	0,13	1,92	0,05	0,00	0,00	0,00	0,24	**4,00**	84,98	12,50	2,52
OPX 37	6,00	1,67	0,11	1,93	0,05	0,00	0,00	0,00	0,25	**4,01**	84,91	12,60	2,50
OPX 38	6,00	1,66	0,12	1,92	0,05	0,00	0,00	0,00	0,25	**4,01**	84,82	12,52	2,66
OPX 39	6,00	1,64	0,15	1,91	0,05	0,00	0,00	0,00	0,24	**4,01**	84,78	12,44	2,79
OPX 40	6,00	1,67	0,10	1,94	0,05	0,00	0,00	0,00	0,25	**4,01**	84,92	12,70	2,39
OPX 41	6,00	1,68	0,08	1,95	0,05	0,00	0,00	0,00	0,25	**4,01**	85,05	12,42	2,53
OPX 42	6,00	1,66	0,11	1,93	0,05	0,00	0,00	0,00	0,25	**4,01**	84,84	12,61	2,55
OPX 43	6,00	1,66	0,10	1,94	0,05	0,00	0,00	0,00	0,25	**4,01**	84,87	12,52	2,61
OPX 44	6,00	1,65	0,14	1,92	0,06	0,00	0,00	0,00	0,24	**4,01**	84,89	12,23	2,88
OPX 45	6,00	1,75	0,15	1,91	0,06	0,00	0,00	0,00	0,14	**4,01**	89,86	7,31	2,83
OPX 46	6,00	1,74	0,16	1,90	0,06	0,00	0,00	0,00	0,13	**4,01**	90,17	6,93	2,90
OPX 47	6,00	1,75	0,12	1,92	0,06	0,00	0,00	0,00	0,15	**4,01**	89,30	7,73	2,97
OPX 48	6,00	1,71	0,19	1,89	0,05	0,00	0,00	0,00	0,16	**4,01**	88,99	8,19	2,82
OPX 49	6,00	1,75	0,17	1,90	0,06	0,00	0,00	0,00	0,12	**4,01**	90,89	6,14	2,97
OPX 50	6,00	1,76	0,11	1,93	0,08	0,00	0,00	0,00	0,12	**4,01**	89,88	5,98	4,14
OPX 51	6,00	1,74	0,16	1,91	0,06	0,00	0,00	0,00	0,13	**4,01**	90,31	6,48	3,21
OPX 52	6,00	1,64	0,14	1,92	0,07	0,00	0,00	0,00	0,23	**4,00**	84,95	11,69	3,36
OPX 53	6,00	1,71	0,10	1,94	0,05	0,00	0,00	0,00	0,20	**4,01**	87,09	10,15	2,76
OPX 54	6,00	1,73	0,15	1,91	0,06	0,00	0,00	0,00	0,15	**4,01**	89,44	7,56	3,00
OPX 55	6,00	1,68	0,09	1,94	0,05	0,00	0,00	0,00	0,24	**4,01**	85,46	12,00	2,54
OPX 56	6,00	1,67	0,10	1,94	0,05	0,00	0,00	0,00	0,24	**4,01**	85,23	12,28	2,50
OPX 57	6,00	1,69	0,09	1,94	0,05	0,00	0,00	0,00	0,23	**4,01**	85,66	11,90	2,44
OPX 58	6,00	1,69	0,09	1,94	0,05	0,00	0,00	0,00	0,23	**4,01**	85,68	11,83	2,49
OPX 59	6,00	1,73	0,10	1,94	0,06	0,00	0,00	0,00	0,18	**4,01**	87,91	9,28	2,80
OPX 60	6,00	1,65	0,18	1,90	0,07	0,00	0,00	0,00	0,19	**4,00**	86,28	10,16	3,56

6.1.13 LPUM 100-1 OPX Part 3

LPUM 100-1 OPX 3	O	Mg	Al	Si	Ca	Ti	Cr	Mn	Fe	Total Kat	En	Fs	Wo
OPX 61	6,00	1,70	0,10	1,93	0,06	0,00	0,00	0,00	0,22	**4,02**	86,11	11,05	2,84
OPX 62	6,00	1,70	0,12	1,93	0,06	0,00	0,00	0,00	0,19	**4,01**	86,97	9,74	3,28
OPX 63	6,00	1,74	0,19	1,76	0,07	0,00	0,00	0,00	0,37	**4,14**	79,83	16,82	3,35
OPX 64	6,00	1,68	0,14	1,92	0,06	0,00	0,00	0,00	0,20	**4,01**	86,47	10,44	3,09
OPX 65	6,00	1,71	0,11	1,93	0,06	0,00	0,00	0,00	0,20	**4,01**	87,23	9,96	2,81
OPX 66	6,00	1,69	0,15	1,91	0,06	0,00	0,00	0,00	0,19	**4,01**	87,15	9,81	3,05
OPX 67	6,00	1,66	0,17	1,91	0,05	0,00	0,00	0,00	0,21	**4,01**	86,22	11,08	2,70
OPX 68	6,00	1,64	0,16	1,84	0,06	0,00	0,00	0,00	0,34	**4,04**	80,40	16,89	2,72
OPX 69	6,00	1,66	0,16	1,90	0,05	0,00	0,00	0,00	0,23	**4,01**	85,49	11,73	2,79
OPX 70	6,00	1,67	0,15	1,91	0,06	0,00	0,00	0,00	0,21	**4,01**	86,19	10,87	2,94
OPX 71	6,00	1,69	0,13	1,92	0,06	0,00	0,00	0,00	0,20	**4,01**	86,67	10,40	2,93
OPX 72	6,00	1,69	0,15	1,91	0,05	0,00	0,00	0,00	0,19	**4,01**	87,49	9,72	2,79
OPX 73	6,00	1,70	0,12	1,93	0,06	0,00	0,00	0,00	0,19	**4,01**	86,92	9,95	3,13
OPX 74	6,00	1,69	0,12	1,93	0,06	0,00	0,00	0,00	0,21	**4,01**	86,55	10,58	2,86
OPX 75	6,00	1,68	0,14	1,92	0,07	0,00	0,00	0,00	0,20	**4,01**	86,34	10,22	3,44
OPX 76	6,00	1,77	0,00	1,97	0,06	0,00	0,00	0,00	0,20	**4,02**	86,93	10,02	3,05
OPX 77	6,00	1,71	0,12	1,92	0,05	0,00	0,00	0,00	0,20	**4,01**	87,12	10,17	2,71
OPX 78	6,00	1,67	0,12	1,93	0,06	0,00	0,00	0,00	0,22	**4,01**	85,71	11,27	3,02
OPX 79	6,00	1,67	0,14	1,92	0,06	0,00	0,00	0,00	0,22	**4,01**	85,82	11,30	2,88
OPX 80	6,00	1,66	0,15	1,91	0,06	0,00	0,00	0,00	0,22	**4,01**	85,60	11,51	2,89
OPX 81	6,00	1,67	0,12	1,93	0,06	0,00	0,00	0,00	0,23	**4,01**	85,25	11,83	2,92
OPX 82	6,00	1,65	0,15	1,91	0,07	0,00	0,00	0,00	0,20	**4,01**	85,65	10,57	3,78
OPX 83	6,00	1,71	0,12	1,93	0,05	0,00	0,00	0,00	0,19	**4,01**	87,54	9,74	2,72
OPX 84	6,00	1,68	0,11	1,93	0,06	0,00	0,00	0,00	0,21	**4,01**	85,98	10,90	3,12
OPX 85	6,00	1,70	0,12	1,93	0,05	0,00	0,00	0,00	0,21	**4,01**	86,71	10,69	2,61
OPX 86	6,00	1,71	0,12	1,93	0,06	0,00	0,00	0,00	0,19	**4,01**	87,25	9,93	2,82
OPX 87	6,00	1,70	0,11	1,93	0,06	0,00	0,00	0,00	0,21	**4,01**	86,67	10,47	2,86
average	**6,00**	**1,68**	**0,13**	**1,92**	**0,06**	**0,00**	**0,00**	**0,00**	**0,22**	4,01	**85,89**	**11,19**	**2,92**

6.1.14 LPUM 075-1 Olivine

LPUM 075-1 Olivine	O	Mg	Si	Ca	Fe	Total Kat	Fo	Fa
Olivine 1	4,00	1,58	1,02	0,01	0,35	**2,97**	81,95	18,05
Olivine 2	4,00	1,57	1,02	0,01	0,36	**2,97**	81,35	18,65
Olivine 3	4,00	1,59	1,02	0,01	0,35	**2,97**	81,82	18,18
Olivine 4	4,00	1,59	1,02	0,01	0,35	**2,97**	81,97	18,03
Olivine 5	4,00	1,60	1,02	0,01	0,34	**2,97**	82,49	17,51
Olivine 6	4,00	1,60	1,02	0,01	0,34	**2,97**	82,39	17,61
Olivine 7	4,00	1,58	1,02	0,01	0,36	**2,97**	81,64	18,36
Olivine 8	4,00	1,59	1,02	0,01	0,35	**2,97**	81,83	18,17
Olivine 9	4,00	1,59	1,02	0,01	0,35	**2,97**	82,19	17,81
Olivine 10	4,00	1,59	1,02	0,01	0,35	**2,97**	81,89	18,11
Olivine 11	4,00	1,59	1,02	0,01	0,35	**2,97**	82,04	17,96
Olivine 12	4,00	1,61	1,02	0,01	0,34	**2,97**	82,50	17,50
Olivine 13	4,00	1,61	1,02	0,01	0,33	**2,97**	82,76	17,24
Olivine 14	4,00	1,61	1,02	0,01	0,33	**2,97**	82,77	17,23
Olivine 15	4,00	1,61	1,02	0,01	0,33	**2,97**	82,93	17,07
Olivine 16	4,00	1,56	1,02	0,01	0,37	**2,97**	80,71	19,29
Olivine 17	4,00	1,56	1,02	0,01	0,38	**2,97**	80,59	19,41
Olivine 18	4,00	1,57	1,02	0,01	0,37	**2,97**	81,10	18,90
Olivine 19	4,00	1,54	1,02	0,01	0,39	**2,97**	79,67	20,33
Olivine 20	4,00	0,58	1,15	0,20	0,26	**2,19**	68,87	31,13
Olivine 21	4,00	1,51	1,03	0,02	0,36	**2,92**	80,53	19,47
Olivine 22	4,00	1,57	1,02	0,01	0,37	**2,97**	80,95	19,05
Olivine 23	4,00	1,57	1,02	0,01	0,37	**2,98**	80,86	19,14
Olivine 24	4,00	1,56	1,02	0,01	0,38	**2,97**	80,38	19,62
Olivine 25	4,00	1,57	1,02	0,01	0,37	**2,97**	80,82	19,18
Olivine 26	4,00	1,57	1,02	0,01	0,37	**2,97**	80,83	19,17
Olivine 27	4,00	1,57	1,02	0,01	0,38	**2,97**	80,66	19,34
average	**4,00**	**1,54**	**1,03**	**0,02**	**0,35**	2,94	**81,06**	**18,94**

6.1.15 LPUM 075-1 OPX Part 1

LPUM 075-1 OPX 1	O	Na	Mg	Al	Si	Ca	Fe	Total Kat	En	Wo	Fs
Pyroxene 1	6,00	0,00	1,45	0,14	1,94	0,16	0,28	**3,97**	76,72	8,31	14,97
Pyroxene 2	6,00	0,00	1,40	0,13	1,95	0,17	0,30	**3,96**	74,57	9,28	16,15
Pyroxene 3	6,00	0,01	1,30	0,28	1,88	0,20	0,28	**3,94**	73,08	11,22	15,70
Pyroxene 4	6,00	0,00	1,34	0,19	1,92	0,20	0,29	**3,95**	73,00	11,08	15,92
Pyroxene 5	6,00	0,00	1,32	0,28	1,85	0,22	0,29	**3,96**	71,91	12,30	15,79
Pyroxene 6	6,00	0,00	1,30	0,23	1,90	0,22	0,29	**3,95**	71,82	12,27	15,91
Pyroxene 7	6,00	0,00	1,32	0,18	1,93	0,20	0,32	**3,95**	71,60	11,00	17,40
Pyroxene 8	6,00	0,00	1,29	0,24	1,89	0,24	0,28	**3,95**	71,46	13,22	15,32
Pyroxene 9	6,00	0,00	1,30	0,23	1,90	0,21	0,31	**3,95**	71,44	11,65	16,90
Pyroxene 10	6,00	0,00	1,28	0,24	1,90	0,25	0,27	**3,94**	70,95	14,06	14,99
Pyroxene 11	6,00	0,00	1,26	0,32	1,84	0,29	0,24	**3,95**	70,69	16,11	13,20
Pyroxene 12	6,00	0,01	1,27	0,26	1,89	0,28	0,25	**3,95**	70,65	15,68	13,67
Pyroxene 13	6,00	0,01	1,26	0,27	1,89	0,28	0,24	**3,94**	70,56	15,75	13,69
Pyroxene 14	6,00	0,00	1,28	0,24	1,89	0,27	0,27	**3,95**	70,54	14,81	14,65
Pyroxene 15	6,00	0,00	1,27	0,26	1,88	0,28	0,25	**3,95**	70,54	15,42	14,04
Pyroxene 16	6,00	0,00	1,28	0,24	1,90	0,25	0,29	**3,95**	70,33	13,79	15,88
Pyroxene 17	6,00	0,00	1,27	0,25	1,89	0,28	0,25	**3,95**	70,26	15,70	14,04
Pyroxene 18	6,00	0,00	1,24	0,25	1,89	0,25	0,30	**3,95**	69,07	14,08	16,85
Pyroxene 19	6,00	0,01	1,22	0,27	1,89	0,25	0,30	**3,94**	68,82	14,02	17,16
Pyroxene 20	6,00	0,01	1,20	0,30	1,87	0,31	0,25	**3,94**	68,12	17,67	14,21
Pyroxene 21	6,00	0,00	1,20	0,26	1,90	0,34	0,23	**3,94**	67,77	19,11	13,12
Pyroxene 22	6,00	0,01	1,14	0,36	1,86	0,26	0,29	**3,92**	67,49	15,61	16,90
Pyroxene 23	6,00	0,01	1,19	0,30	1,87	0,35	0,23	**3,94**	67,27	19,64	13,09
Pyroxene 24	6,00	0,01	1,19	0,28	1,88	0,35	0,23	**3,94**	67,14	19,84	13,02
Pyroxene 25	6,00	0,01	1,19	0,30	1,87	0,29	0,30	**3,94**	67,12	16,10	16,78
Pyroxene 26	6,00	0,01	1,16	0,32	1,87	0,27	0,30	**3,93**	66,76	15,76	17,48
Pyroxene 27	6,00	0,00	1,17	0,30	1,87	0,35	0,25	**3,94**	66,22	19,90	13,88
Pyroxene 28	6,00	0,00	1,16	0,31	1,86	0,31	0,29	**3,94**	66,01	17,53	16,46
Pyroxene 29	6,00	0,01	1,13	0,38	1,83	0,34	0,24	**3,93**	65,95	19,85	14,20
Pyroxene 30	6,00	0,02	1,06	0,44	1,82	0,28	0,29	**3,92**	64,92	17,33	17,75

6.1.16 LPUM 075-1 OPX Part 2

LPUM 075-1 OPX 2	O	Na	Mg	Al	Si	Ca	Fe	Total Kat	En	Wo	Fs
Pyroxene 31	6,00	0,02	1,06	0,42	1,84	0,31	0,27	**3,91**	64,75	18,75	16,50
Pyroxene 32	6,00	0,02	0,95	0,55	1,79	0,31	0,28	**3,89**	61,68	19,94	18,38
Pyroxene 33	6,00	0,01	0,98	0,54	1,77	0,35	0,27	**3,91**	61,60	21,70	16,71
Pyroxene 34	6,00	0,03	0,93	0,49	1,83	0,30	0,31	**3,90**	60,15	19,67	20,18
Pyroxene 35	6,00	0,02	0,77	0,65	1,75	0,37	0,32	**3,89**	52,88	25,08	22,03
Pyroxene 36	6,00	0,04	0,71	0,63	1,78	0,40	0,33	**3,88**	49,17	27,69	23,14
Pyroxene 37	6,00	0,04	0,68	0,67	1,76	0,37	0,35	**3,87**	48,87	26,38	24,75
Pyroxene 38	6,00	0,04	0,67	0,69	1,75	0,38	0,35	**3,87**	48,19	27,01	24,80
Pyroxene 39	6,00	0,05	0,57	0,69	1,79	0,38	0,36	**3,85**	43,88	28,93	27,19
Pyroxene 40	6,00	0,06	0,58	0,69	1,78	0,40	0,36	**3,86**	43,26	29,85	26,89
Pyroxene 41	6,00	0,05	0,56	0,71	1,77	0,42	0,35	**3,85**	42,00	31,76	26,23
Pyroxene 42	6,00	0,07	0,51	0,73	1,78	0,40	0,37	**3,85**	39,57	31,30	29,13
Pyroxene 43	6,00	0,08	0,44	0,76	1,78	0,39	0,38	**3,83**	36,29	32,55	31,16
Pyroxene 44	6,00	0,07	0,44	0,77	1,77	0,41	0,36	**3,82**	35,96	34,09	29,94
Pyroxene 45	6,00	0,08	0,44	0,71	1,80	0,41	0,41	**3,84**	34,70	32,42	32,89
Pyroxene 46	6,00	0,08	0,42	0,74	1,79	0,42	0,39	**3,84**	34,43	34,19	31,39
Pyroxene 47	6,00	0,08	0,42	0,75	1,78	0,42	0,38	**3,83**	34,22	34,63	31,15
Pyroxene 48	6,00	0,08	0,39	0,81	1,77	0,41	0,36	**3,82**	33,42	35,29	31,29
Pyroxene 49	6,00	0,09	0,33	0,82	1,78	0,43	0,38	**3,82**	28,84	37,79	33,36
average	**6,00**	**0,02**	**1,01**	**0,43**	**1,84**	**0,31**	**0,30**	3,91	**60,14**	**20,35**	**19,52**

6.1.17 LPUM 075-1 Spinel

LPUM 075-1 Spinel	O	Na	Mg	Al	Si	K	Ca	Ti	Cr	Mn	Fe	Total	MgFe	$AlCr_2$
Spinel 1	4,00	0,00	0,68	1,65	0,02	0,00	0,01	0,00	0,32	0,00	0,29	**2,99**	0,98	1,98
Spinel 2	4,00	0,00	0,70	1,59	0,07	0,00	0,01	0,00	0,32	0,00	0,29	**2,98**	0,99	1,91
Spinel 3	4,00	0,00	0,66	1,37	0,26	0,00	0,06	0,01	0,28	0,00	0,27	**2,91**	0,93	1,65
Spinel 4	4,00	0,00	0,67	1,59	0,07	0,00	0,01	0,00	0,33	0,00	0,29	**2,97**	0,96	1,91
Spinel 5	4,00	0,00	0,69	1,65	0,02	0,00	0,01	0,00	0,33	0,00	0,30	**2,99**	0,98	1,98
Spinel 6	4,00	0,00	0,68	1,63	0,14	0,00	0,03	0,00	0,21	0,00	0,24	**2,94**	0,92	1,84
average	**4,00**	**0,00**	**0,68**	**1,58**	**0,10**	**0,00**	**0,02**	**0,00**	**0,30**	**0,00**	**0,28**	2,96	**0,96**	**1,88**

6.1.18 LPUM 050-1 Olivine

LPUM 050-1 Olivine	O	Mg	Si	Ca	Mn	Fe	Total Kat	Fo	Fa
Olivine 1	4,00	1,04	1,00	0,02	0,01	0,92	**2,99**	52,99	47,01
Olivine 2	4,00	1,06	1,00	0,02	0,01	0,91	**3,00**	53,81	46,19
Olivine 3	4,00	1,05	1,02	0,01	0,00	0,90	**2,98**	53,92	46,08
Olivine 4	4,00	1,05	1,01	0,01	0,02	0,91	**2,99**	53,45	46,55
Olivine 5	4,00	1,05	0,97	0,01	0,00	1,00	**3,03**	51,15	48,85
Olivine 6	4,00	1,05	1,01	0,01	0,00	0,91	**2,99**	53,67	46,33
Olivine 7	4,00	1,05	1,01	0,01	0,01	0,90	**2,98**	53,78	46,22
Olivine 8	4,00	1,05	1,00	0,01	0,01	0,91	**2,99**	53,52	46,48
Olivine 9	4,00	1,05	1,01	0,01	0,01	0,91	**2,99**	53,58	46,42
Olivine 10	4,00	1,04	1,01	0,01	0,02	0,91	**2,99**	53,29	46,71
Olivine 11	4,00	1,04	1,01	0,01	0,01	0,92	**2,99**	53,20	46,80
average	**4,00**	**1,05**	**1,00**	**0,01**	**0,01**	**0,92**	2,99	**53,30**	**46,70**

6.1.19 LPUM 050-1 CPX

LPUM 050-1 CPX	O	Mg	Al	Si	Ca	Ti	Mn	Fe	Total Kat	En	Fs	Wo
CPX 1	6,00	1,05	0,12	1,95	0,22	0,00	0,00	0,64	**3,99**	54,99	33,47	11,54
CPX 2	6,00	1,02	0,18	1,93	0,25	0,00	0,00	0,61	**3,99**	53,95	32,63	13,42
CPX 3	6,00	0,96	0,19	1,90	0,31	0,01	0,02	0,59	**3,99**	51,64	31,45	16,91
CPX 4	6,00	1,06	0,11	1,95	0,21	0,01	0,02	0,63	**3,99**	55,75	32,97	11,29
CPX 5	6,00	0,96	0,18	1,91	0,32	0,02	0,02	0,58	**3,99**	51,53	31,12	17,35
CPX 6	6,00	1,01	0,17	1,91	0,29	0,01	0,00	0,59	**3,99**	53,62	31,22	15,16
CPX 7	6,00	1,05	0,16	1,92	0,25	0,01	0,00	0,58	**3,98**	55,56	30,93	13,51
CPX 8	6,00	0,93	0,21	1,89	0,41	0,02	0,02	0,51	**3,98**	50,16	27,52	22,32
CPX 9	6,00	1,07	0,14	1,93	0,24	0,01	0,00	0,59	**3,99**	56,10	31,06	12,83
CPX 10	6,00	1,09	0,13	1,94	0,19	0,01	0,00	0,63	**3,99**	57,13	32,85	10,03
CPX 11	6,00	1,00	0,16	1,94	0,27	0,02	0,02	0,56	**3,96**	54,79	30,41	14,80
CPX 12	6,00	1,02	0,15	1,93	0,28	0,01	0,01	0,58	**3,98**	54,39	30,89	14,73
CPX 13	6,00	1,12	0,09	1,95	0,17	0,01	0,01	0,64	**3,99**	57,94	33,20	8,87
CPX 14	6,00	0,99	0,19	1,89	0,31	0,02	0,01	0,58	**3,99**	52,72	30,72	16,56
CPX 15	6,00	1,02	0,19	1,90	0,27	0,02	0,00	0,58	**3,99**	54,58	31,10	14,32
CPX 16	6,00	1,05	0,16	1,93	0,24	0,00	0,00	0,61	**3,99**	55,14	32,27	12,59
CPX 17	6,00	1,05	0,16	1,91	0,25	0,01	0,02	0,60	**3,99**	55,25	31,47	13,28
CPX 18	6,00	0,97	0,20	1,89	0,33	0,02	0,02	0,56	**3,99**	52,14	29,90	17,95
average	**6,00**	**1,02**	**0,16**	**1,92**	**0,27**	**0,01**	**0,01**	**0,59**	3,99	**54,30**	**31,40**	**14,30**

6.1.20 LPUM 050-1 FSP

LPUM 050-1 FSP	O	Na	Mg	Al	Si	K	Ca	Fe	Total Kat	Ab	An	KFSP
FSP 1	8,00	0,23	0,02	1,68	2,29	0,00	0,72	0,05	**4,99**	24,04	75,96	0,00
FSP 2	8,00	0,22	0,03	1,65	2,29	0,00	0,74	0,06	**4,99**	22,83	77,17	0,00
FSP 3	8,00	0,23	0,05	1,61	2,32	0,00	0,74	0,06	**5,00**	23,62	76,38	0,00
FSP 4	8,00	0,22	0,03	1,65	2,30	0,00	0,72	0,06	**4,99**	23,59	76,41	0,00
FSP 5	8,00	0,23	0,04	1,64	2,29	0,00	0,72	0,09	**5,01**	23,97	76,03	0,00
FSP 6	8,00	0,23	0,02	1,71	2,27	0,00	0,73	0,03	**4,99**	24,23	75,77	0,00
FSP 7	8,00	0,08	0,46	0,78	2,36	0,00	0,50	0,96	**5,13**	14,00	86,00	0,00
FSP 8	8,00	0,10	0,43	0,81	2,36	0,00	0,51	0,90	**5,11**	17,06	82,94	0,00
FSP 9	8,00	0,07	0,48	0,73	2,37	0,00	0,49	0,97	**5,12**	12,65	87,35	0,00
FSP 10	8,00	0,08	0,49	0,71	2,35	0,01	0,50	1,02	**5,16**	13,84	83,93	2,23
FSP 11	8,00	0,22	0,01	1,74	2,25	0,00	0,74	0,03	**4,99**	22,78	77,22	0,00
FSP 12	8,00	0,23	0,01	1,75	2,25	0,00	0,72	0,03	**4,98**	23,87	76,13	0,00
FSP 13	8,00	0,22	0,03	1,73	2,25	0,00	0,72	0,04	**4,99**	23,52	76,48	0,00
FSP 14	8,00	0,23	0,00	1,75	2,25	0,00	0,74	0,04	**5,00**	23,72	76,28	0,00
FSP 15	8,00	0,20	0,02	1,75	2,24	0,00	0,74	0,04	**4,99**	21,58	78,42	0,00
FSP 16	8,00	0,21	0,05	1,69	2,26	0,00	0,73	0,07	**5,00**	22,39	77,61	0,00
FSP 17	8,00	0,24	0,01	1,72	2,27	0,00	0,71	0,04	**4,99**	25,51	74,49	0,00
FSP 18	8,00	0,21	0,02	1,75	2,23	0,00	0,74	0,04	**5,00**	22,47	77,53	0,00
FSP 19	8,00	0,23	0,01	1,71	2,28	0,00	0,71	0,04	**4,98**	24,62	75,38	0,00
FSP 20	8,00	0,21	0,02	1,75	2,21	0,00	0,76	0,07	**5,02**	21,31	78,69	0,00
average	**8,00**	**0,19**	**0,11**	**1,52**	**2,28**	**0,00**	**0,68**	**0,23**	5,02	**21,58**	**78,31**	**0,11**

6.1.21 LPUM 030-1 CPX, FSP and Quartz

LPUM 030-1 CPX	O	Na	Mg	Al	Si	Ca	Ti	Fe	Total Kat	En	Fs	Wo
CPX 1	6,00	0,03	0,64	0,34	1,75	0,80	0,06	0,41	**4,03**	34,56	22,19	43,25
CPX 2	6,00	0,02	0,66	0,32	1,76	0,80	0,05	0,40	**4,02**	35,50	21,37	43,13
CPX 3	6,00	0,03	0,62	0,35	1,74	0,83	0,06	0,40	**4,02**	33,46	21,78	44,76
CPX 4	6,00	0,03	0,63	0,35	1,74	0,81	0,06	0,41	**4,03**	33,91	22,25	43,84
CPX 5	6,00	0,05	0,54	0,34	1,90	0,65	0,04	0,34	**3,86**	35,29	22,04	42,66
CPX 6	6,00	0,14	0,33	0,61	1,90	0,59	0,03	0,20	**3,80**	29,96	17,49	52,55
CPX 7	6,00	0,03	0,64	0,35	1,73	0,81	0,07	0,39	**4,00**	34,68	21,25	44,07
CPX 8	6,00	0,00	0,05	0,02	2,92	0,05	0,01	0,02	**3,06**	40,77	18,46	40,77
CPX 9	6,00	0,13	0,43	0,61	1,82	0,67	0,02	0,23	**3,91**	32,34	17,33	50,34
CPX 10	6,00	0,03	0,65	0,33	1,75	0,81	0,05	0,39	**4,01**	34,98	21,26	43,76
average	**6,00**	**0,05**	**0,52**	**0,36**	**1,90**	**0,68**	**0,04**	**0,32**	3,87	**34,55**	**20,54**	**44,91**

LPUM 030-1 FSP	O	Na	Mg	Al	Si	P	K	Ca	Ti	Mn	Fe	Total Kat	Ab	An	Or
FSP 1	8,00	0,35	0,01	1,51	2,44	0,00	0,00	0,60	0,00	0,00	0,06	**4,97**	36,66	63,34	0,00
FSP 2	8,00	0,36	0,00	1,46	2,48	0,00	0,00	0,58	0,01	0,00	0,06	**4,96**	38,46	61,54	0,00
FSP 3	8,00	0,22	0,18	0,72	2,82	0,04	0,01	0,40	0,09	0,02	0,28	**4,78**	34,35	63,62	2,03
FSP 4	8,00	0,37	0,01	1,47	2,48	0,00	0,00	0,57	0,00	0,00	0,07	**4,97**	39,28	60,72	0,00
FSP 5	8,00	0,20	0,21	0,69	2,77	0,06	0,01	0,43	0,10	0,02	0,31	**4,80**	30,94	66,87	2,20
FSP 6	8,00	0,20	0,22	0,68	2,77	0,06	0,01	0,44	0,10	0,02	0,32	**4,81**	30,39	67,65	1,96
average	**7,50**	**0,22**	**0,22**	**0,90**	**2,43**	**0,21**	**0,02**	**0,47**	**1,02**	**8,70**	**5,36**	**14,75**	**35,01**	**63,95**	**1,03**

LPUM 030-1 QZ	O	Al	Si	Ca	Ti	Fe
Quartz 1	2,00	0,00	0,99	0,00	0,00	0,00
Quartz 2	2,00	0,01	0,99	0,00	0,00	0,00
Quartz 3	2,00	0,00	0,99	0,00	0,00	0,00
Quartz 4	2,00	0,00	0,99	0,00	0,00	0,00
Quartz 5	2,00	0,06	0,89	0,04	0,01	0,03
average	**4,19**	**0,09**	**0,69**	**0,29**	**1,00**	**0,05**

6.1.22 LPUM 030-1 Spinel

LPUM 030-1 Spinel	O	Mg	Al	Ti	Fe2+	Fe3+	Total Kat
Spinel 1	4,00	0,20	0,13	0,17	0,80	1,60	**2,90**
Spinel 2	4,00	0,20	0,13	0,16	0,81	1,62	**2,91**
Spinel 3	4,00	0,20	0,13	0,17	0,80	1,60	**2,90**
Spinel 4	4,00	0,20	0,13	0,18	0,80	1,61	**2,91**
Spinel 5	4,00	0,19	0,13	0,18	0,80	1,60	**2,91**
Spinel 6	4,00	0,19	0,13	0,18	0,80	1,61	**2,91**
Spinel 7	4,00	0,21	0,13	0,18	0,80	1,59	**2,90**
Spinel 8	4,00	0,20	0,13	0,18	0,79	1,57	**2,87**
Spinel 9	4,00	0,20	0,13	0,18	0,80	1,60	**2,91**
Spinel 10	4,00	0,20	0,13	0,18	0,80	1,60	**2,90**
average	**4,00**	**0,20**	**0,13**	**0,18**	**0,80**	**1,60**	**1,60**

6.1.23 LPUM 020-1 FSP

LPUM 020-1 FSP	O	Na	Mg	Al	Si	P	K	Ca	Ti	Mn	Fe	Total Kat	An	Ab	Or
FSP 1	8,00	0,28	0,02	1,39	2,50	0,00	0,00	0,61	0,01	0,00	0,12	**4,94**	68,35	31,65	0,00
FSP 2	8,00	0,26	0,09	1,14	2,61	0,00	0,00	0,61	0,02	0,00	0,21	**4,93**	70,45	29,55	0,00
FSP 3	8,00	0,28	0,02	1,33	2,57	0,00	0,00	0,57	0,01	0,00	0,11	**4,89**	67,18	32,82	0,00
FSP 4	8,00	0,22	0,04	1,00	2,85	0,00	0,00	0,49	0,02	0,00	0,13	**4,74**	68,69	31,31	0,00
FSP 5	8,00	0,23	0,06	1,06	2,73	0,01	0,00	0,55	0,02	0,01	0,16	**4,83**	70,82	29,18	0,00
FSP 6	8,00	0,27	0,04	1,29	2,57	0,00	0,00	0,59	0,01	0,00	0,13	**4,90**	68,76	31,24	0,00
FSP 7	8,00	0,26	0,10	1,21	2,52	0,01	0,00	0,66	0,02	0,00	0,19	**4,97**	71,31	28,27	0,42
FSP 8	8,00	0,27	0,02	1,30	2,61	0,00	0,00	0,56	0,01	0,00	0,09	**4,87**	67,54	32,46	0,00
FSP 9	8,00	0,26	0,12	1,15	2,54	0,01	0,01	0,66	0,02	0,00	0,22	**4,99**	71,59	27,85	0,56
FSP 10	8,00	0,28	0,06	1,24	2,36	0,02	0,01	0,56	0,08	0,00	0,46	**5,06**	65,75	33,18	1,07
FSP 11	8,00	0,25	0,07	1,20	2,47	0,04	0,01	0,67	0,03	0,00	0,24	**4,97**	72,50	26,80	0,71
FSP 12	8,00	0,26	0,04	1,25	2,51	0,01	0,00	0,60	0,03	0,00	0,24	**4,95**	69,42	30,58	0,00
FSP 13	8,00	0,27	0,08	1,25	2,43	0,00	0,00	0,65	0,05	0,00	0,32	**5,04**	70,42	29,58	0,00
FSP 14	8,00	0,24	0,02	1,08	2,80	0,00	0,00	0,48	0,02	0,00	0,12	**4,76**	66,67	33,33	0,00
FSP 15	8,00	0,28	0,04	1,34	2,50	0,00	0,00	0,61	0,02	0,00	0,15	**4,94**	68,94	31,06	0,00
FSP 16	8,00	0,27	0,03	1,24	2,59	0,00	0,00	0,54	0,03	0,00	0,21	**4,90**	66,51	33,49	0,00
FSP 17	8,00	0,29	0,04	1,31	2,55	0,00	0,00	0,60	0,01	0,00	0,12	**4,93**	67,54	32,46	0,00
FSP 18	8,00	0,23	0,02	1,05	2,85	0,00	0,00	0,46	0,01	0,00	0,10	**4,73**	66,85	33,15	0,00
FSP 19	8,00	0,26	0,04	1,15	2,72	0,00	0,00	0,53	0,01	0,00	0,12	**4,83**	67,15	32,85	0,00
FSP 20	8,00	0,25	0,13	1,13	2,55	0,00	0,00	0,67	0,02	0,01	0,24	**5,00**	72,43	27,57	0,00
FSP 21	8,00	0,28	0,04	1,40	2,48	0,00	0,00	0,64	0,01	0,00	0,11	**4,95**	69,65	30,35	0,00
average	**8,00**	**0,26**	**0,05**	**1,21**	**2,59**	**0,00**	**0,00**	**0,59**	**0,02**	**0,00**	**0,18**	4,91	**68,98**	**30,89**	**0,13**

6.1.24 LPUM 020-1 CPX and Quartz

LPUM 020-1 CPX	O	Na	Mg	Al	Si	Ca	Ti	Fe	Total Kat	En	Fs	Wo
CPX 1	6,00	0,04	0,42	0,22	1,93	0,71	0,04	0,56	**3,93**	24,81	33,10	42,10
CPX 2	6,00	0,03	0,45	0,22	1,85	0,67	0,06	0,68	**3,98**	24,96	37,72	37,33
CPX 3	6,00	0,06	0,41	0,32	1,88	0,68	0,04	0,55	**3,95**	24,82	33,33	41,85
CPX 4	6,00	0,05	0,41	0,26	1,91	0,68	0,04	0,54	**3,93**	25,24	33,11	41,65
CPX 5	6,00	0,05	0,40	0,25	1,92	0,68	0,04	0,55	**3,92**	24,70	33,76	41,55
CPX 6	6,00	0,05	0,40	0,24	1,91	0,66	0,05	0,59	**3,93**	24,44	35,86	39,70
CPX 7	6,00	0,05	0,39	0,29	1,94	0,68	0,03	0,49	**3,90**	24,89	31,41	43,70
CPX 8	6,00	0,04	0,43	0,20	1,87	0,69	0,05	0,67	**3,98**	24,01	37,38	38,61
CPX 9	6,00	0,04	0,44	0,22	1,83	0,69	0,07	0,69	**4,01**	24,36	37,90	37,74
CPX 10	6,00	0,03	0,45	0,20	1,93	0,72	0,04	0,56	**3,95**	26,06	32,45	41,48
CPX 11	6,00	0,02	0,48	0,20	1,90	0,76	0,03	0,56	**3,98**	26,69	31,17	42,14
CPX 12	6,00	0,04	0,41	0,23	1,93	0,69	0,04	0,55	**3,93**	24,94	33,31	41,75
average	**6,00**	**0,04**	**0,42**	**0,24**	**1,90**	**0,69**	**0,04**	**0,58**	3,95	**24,99**	**34,21**	**40,80**

LPUM 020-1 QZ	O	Na	Mg	Al	Si	Ca	Ti	Fe
Quartz 1	2,00	0,01	0,01	0,06	0,90	0,04	0,01	0,04
Quartz 2	2,00	0,01	0,00	0,05	0,93	0,02	0,00	0,02
Quartz 3	2,00	0,01	0,02	0,04	0,89	0,07	0,01	0,05
Quartz 4	2,00	0,02	0,00	0,12	0,86	0,06	0,00	0,03
Quartz 5	2,00	0,01	0,02	0,07	0,89	0,06	0,00	0,03
Quartz 6	2,00	0,02	0,01	0,13	0,83	0,07	0,00	0,03
Quartz 7	2,00	0,02	0,01	0,11	0,86	0,06	0,00	0,03
Quartz 8	2,00	0,01	0,02	0,07	0,87	0,06	0,01	0,05

6.1.25 LPUM-M 120-1 OPX and Olivine

LPUM-M 120-1 OPX	O	Mg	Al	Si	Ca	Fe	Total Kat	En	Fs	Wo
OPX 1	6,00	1,82	0,18	1,90	0,08	0,02	**4,00**	94,88	0,99	4,13
OPX 2	6,00	1,80	0,18	1,90	0,08	0,02	**3,99**	94,39	1,21	4,40
OPX 3	6,00	1,86	0,12	1,94	0,07	0,01	**4,00**	95,58	0,72	3,70
OPX 4	6,00	1,77	0,27	1,85	0,09	0,02	**4,00**	94,44	1,02	4,55
OPX 5	6,00	1,89	0,10	1,94	0,07	0,00	**4,01**	96,02	0,20	3,77
OPX 6	6,00	1,84	0,15	1,92	0,10	0,00	**4,01**	95,10	0,00	4,90
OPX 7	6,00	1,79	0,21	1,89	0,10	0,01	**4,01**	94,07	0,52	5,40
OPX 8	6,00	1,80	0,24	1,88	0,09	0,00	**4,01**	95,29	0,00	4,71
OPX 9	6,00	1,78	0,25	1,87	0,09	0,01	**4,00**	94,79	0,43	4,79
OPX 10	6,00	1,79	0,24	1,87	0,10	0,00	**4,00**	94,40	0,21	5,39
OPX 11	6,00	1,79	0,18	1,90	0,12	0,02	**4,01**	92,87	1,09	6,04
OPX 12	6,00	1,79	0,22	1,88	0,10	0,01	**4,00**	94,32	0,68	5,00
OPX 13	6,00	1,83	0,15	1,92	0,10	0,01	**4,00**	94,57	0,41	5,01
OPX 14	6,00	1,83	0,15	1,93	0,09	0,00	**4,00**	95,31	0,00	4,69
OPX 15	6,00	1,83	0,19	1,90	0,09	0,00	**4,01**	95,41	0,00	4,59
average	**6,00**	**1,81**	**0,19**	**1,90**	**0,09**	**0,01**	**4,00**	**94,76**	**0,50**	**4,74**

LPUM-M 120-1 Olivine	O	Mg	Si	Total Kat	Fo	Fa
Olivine 1	4,00	2,00	0,99	**2,99**	99,79	0,21
Olivine 2	4,00	2,00	0,99	**2,99**	99,86	0,14
Olivine 3	4,00	2,00	0,99	**2,99**	99,90	0,10
Olivine 4	4,00	2,00	0,99	**2,99**	99,44	0,56
Olivine 5	4,00	1,99	0,99	**2,98**	99,27	0,73
Olivine 6	4,00	2,00	0,99	**2,99**	100,00	0,00
Olivine 7	4,00	2,00	0,99	**2,99**	99,97	0,03
Olivine 8	4,00	2,00	0,99	**2,99**	99,97	0,03
Olivine 9	4,00	2,00	1,00	**3,00**	99,97	0,03
Olivine 10	4,00	2,00	0,99	**3,00**	99,86	0,14
Olivine 11	4,00	2,00	0,99	**3,00**	99,90	0,10
Olivine 12	4,00	2,00	0,99	**3,00**	99,97	0,03
Olivine 13	4,00	2,00	0,99	**3,00**	99,93	0,07
Olivine 14	4,00	2,00	1,00	**2,99**	99,65	0,35
Olivine 15	4,00	2,00	1,00	**2,99**	99,86	0,14
average	**4,00**	**2,00**	**0,99**	**2,99**	**99,8**	**0,2**

6.1.26 LPUM residual melts – Part 1

LPUM 285-2 Melt Ox%	Na2O	MgO	Al2O3	SiO2	P2O5	K2O	CaO	TiO2	Cr2O3	MnO	FeO	Total
Melt 1	0,89	6,90	18,97	46,08	0,00	0,19	13,65	0,85	0,42	1,04	11,02	**100,0**
Melt 2	1,10	6,12	19,97	45,70	0,00	0,22	13,13	0,83	0,21	0,95	11,76	**100,0**
Melt 3	1,30	5,87	19,61	45,29	0,02	0,26	12,07	0,80	0,06	0,93	13,80	**100,0**
average	**1,10**	**6,30**	**19,52**	**45,69**	**0,01**	**0,22**	**12,95**	**0,83**	**0,23**	**0,97**	**12,19**	100,0
LPUM 210-2 Melt Ox%	**Na2O**	**MgO**	**Al2O3**	**SiO2**	**P2O5**	**K2O**	**CaO**	**TiO2**	**Cr2O3**	**MnO**	**FeO**	**Total**
Melt 1	0,25	22,50	7,68	50,59	0,00	0,00	11,24	0,00	0,73	0,19	6,81	**100,0**
Melt 2	0,31	26,19	8,21	51,01	0,00	0,00	6,57	0,25	0,64	0,26	6,57	**100,0**
Melt 3	0,00	24,39	7,12	51,62	0,00	0,00	9,77	0,00	0,75	0,20	6,15	**100,0**
Melt 4	0,00	24,65	8,10	51,23	0,00	0,00	8,27	0,00	0,86	0,00	6,88	**100,0**
Melt 5	0,24	21,71	8,68	50,08	0,00	0,00	11,16	0,25	0,66	0,25	6,98	**100,0**
Melt 6	0,26	23,70	8,66	50,59	0,00	0,00	9,84	0,36	0,68	0,00	5,92	**100,0**
Melt 7	0,30	23,32	8,77	50,43	0,00	0,00	8,79	0,35	0,64	0,00	7,40	**100,0**
Melt 8	0,31	22,84	8,79	50,30	0,00	0,00	9,30	0,42	0,50	0,22	7,32	**100,0**
Melt 9	0,27	22,49	7,52	50,66	0,00	0,00	10,09	0,25	0,63	0,00	8,08	**100,0**
average	**0,22**	**23,53**	**8,17**	**50,72**	**0,00**	**0,00**	**9,45**	**0,21**	**0,68**	**0,12**	**6,90**	100,0
LPUM 150-1 Melt Ox%	**Na2O**	**MgO**	**Al2O3**	**SiO2**	**P2O5**	**K2O**	**CaO**	**TiO2**	**Cr2O3**	**MnO**	**FeO**	**Total**
Melt 1	0,74	6,68	20,21	52,77	0,18	0,10	13,68	0,62	2,24	0,53	2,24	**100,0**
Melt 2	0,52	8,10	19,45	51,86	0,00	0,22	13,92	0,85	2,27	0,85	1,96	**100,0**
Melt 3	0,51	6,85	19,87	52,06	0,04	0,11	14,31	0,79	2,74	0,80	1,92	**100,0**
Melt 4	0,67	6,45	20,62	53,17	0,00	0,00	13,73	0,58	1,99	0,62	2,17	**100,0**
Melt 5	0,75	6,77	19,48	53,47	0,00	0,02	13,75	0,54	2,62	0,61	2,01	**100,0**
Melt 6	0,48	8,42	19,73	52,22	0,00	0,10	13,38	0,49	2,36	0,65	2,16	**100,0**
Melt 7	0,54	9,66	18,20	52,62	0,15	0,16	12,57	0,63	2,74	0,66	2,06	**100,0**
Melt 8	0,66	11,23	16,53	52,41	0,00	0,07	12,64	0,49	2,60	0,85	2,51	**100,0**
Melt 9	0,56	13,55	14,72	53,35	0,05	0,00	11,58	0,52	2,89	0,49	2,29	**100,0**
Melt 10	0,64	7,47	19,35	52,49	0,01	0,09	14,18	0,65	2,43	0,68	2,02	**100,0**
Melt 11	0,76	9,20	18,64	52,14	0,10	0,20	13,22	0,79	2,68	0,57	1,69	**100,0**
Melt 12	0,79	7,97	19,94	53,32	0,00	0,16	13,24	0,69	2,03	0,66	1,21	**100,0**

6.1.27 LPUM residual melts – Part 2

LPUM 150-1 Melt Ox%	Na2O	MgO	Al2O3	SiO2	P2O5	K2O	CaO	TiO2	Cr2O3	MnO	FeO	Total
Melt 13	0,77	6,85	20,67	52,47	0,00	0,22	14,21	0,36	2,06	0,58	1,80	**100,0**
Melt 14	0,59	8,72	19,07	51,96	0,01	0,17	13,79	0,55	2,49	0,82	1,81	**100,0**
Melt 15	0,65	8,58	19,28	52,07	0,00	0,21	13,47	0,74	2,46	0,95	1,59	**100,0**
Melt 16	0,65	8,22	20,35	51,89	0,03	0,11	13,13	0,73	2,52	0,57	1,80	**100,0**
Melt 17	0,64	8,74	19,00	52,73	0,00	0,13	13,53	0,55	2,59	0,56	1,52	**100,0**
Melt 18	0,51	8,79	19,04	52,89	0,00	0,07	13,53	0,51	2,37	0,59	1,71	**100,0**
Melt 19	0,72	7,10	20,75	52,51	0,13	0,13	13,86	0,58	1,75	0,89	1,58	**100,0**
Melt 20	0,60	8,29	19,72	51,99	0,00	0,18	13,92	0,56	2,46	0,64	1,64	**100,0**
Melt 21	0,64	7,42	20,23	52,77	0,00	0,18	13,19	0,65	2,39	0,93	1,60	**100,0**
Melt 22	0,22	18,21	12,48	53,69	0,00	0,05	8,93	0,57	2,48	1,00	2,37	**100,0**
Melt 23	0,26	18,23	12,71	53,22	0,00	0,12	8,97	0,58	2,71	0,52	2,69	**100,0**
Melt 24	0,31	18,42	12,71	53,16	0,07	0,08	8,98	0,36	2,72	0,51	2,67	**100,0**
Melt 25	0,48	18,39	12,80	52,94	0,02	0,09	8,62	0,57	2,41	0,80	2,87	**100,0**
average	**0,59**	**9,93**	**18,22**	**52,65**	**0,03**	**0,12**	**12,73**	**0,60**	**2,44**	**0,69**	**2,00**	100,0
LPUM 150-3 Melt Ox%	**Na2O**	**MgO**	**Al2O3**	**SiO2**	**P2O5**	**K2O**	**CaO**	**TiO2**	**Cr2O3**	**MnO**	**FeO**	**Total**
Melt 1	0,77	3,73	19,95	49,33	0,00	0,25	11,07	0,67	0,00	0,25	13,97	**100,0**
Melt 2	0,89	2,91	21,00	49,60	0,00	0,32	10,97	0,60	0,00	0,20	13,51	**100,0**
Melt 3	0,82	2,91	20,80	49,30	0,00	0,30	11,32	0,68	0,00	0,23	13,63	**100,0**
Melt 4	0,88	3,39	20,37	48,56	0,00	0,28	11,82	0,72	0,00	0,20	13,79	**100,0**
Melt 5	0,82	3,37	19,99	49,24	0,00	0,28	11,38	0,73	0,00	0,25	13,93	**100,0**
average	**0,84**	**3,26**	**20,42**	**49,21**	**0,00**	**0,29**	**11,31**	**0,68**	**0,00**	**0,23**	**13,77**	100,0
LPUM 100-1 Melt Ox%	**Na2O**	**MgO**	**Al2O3**	**SiO2**	**P2O5**	**K2O**	**CaO**	**TiO2**	**Cr2O3**	**MnO**	**FeO**	**Total**
Melt 1	0,43	16,05	13,97	49,50	0,15	0,10	10,60	0,52	0,00	0,16	8,52	**100,0**
Melt 2	0,41	17,06	12,63	49,04	0,13	0,08	9,57	0,47	0,04	0,15	10,41	**100,0**
Melt 3	0,41	16,40	13,12	49,04	0,15	0,10	9,82	0,48	0,03	0,16	10,29	**100,0**
Melt 4	0,37	16,52	12,47	48,75	0,13	0,07	9,35	0,43	0,03	0,14	11,73	**100,0**
average	**0,41**	**16,51**	**13,05**	**49,08**	**0,14**	**0,09**	**9,84**	**0,48**	**0,03**	**0,15**	**10,24**	100,0
LPUM 075-1 Melt Ox%	**Na2O**	**MgO**	**Al2O3**	**SiO2**	**P2O5**	**K2O**	**CaO**	**TiO2**	**Cr2O3**	**MnO**	**FeO**	**Total**
Melt 1	0,82	11,12	16,69	48,57	0,00	0,14	10,22	0,66	0,29	0,00	11,49	**100,0**
Melt 2	0,82	10,51	16,78	49,25	0,00	0,13	10,45	0,73	0,15	0,00	11,17	**100,0**

6.1.28 LPUM residual melts – Part 3

LPUM 075-1 Melt Ox%	Na2O	MgO	Al2O3	SiO2	P2O5	K2O	CaO	TiO2	Cr2O3	MnO	FeO	Total
Melt 3	0,93	9,50	16,79	49,21	0,00	0,12	10,66	0,69	0,00	0,00	12,10	**100,0**
Melt 4	0,97	9,55	16,81	49,27	0,00	0,15	10,67	0,70	0,11	0,00	11,78	**100,0**
Melt 5	0,82	7,25	18,23	49,88	0,00	0,15	11,53	0,76	0,15	0,00	11,23	**100,0**
Melt 6	0,97	8,45	17,66	49,58	0,00	0,14	10,64	0,70	0,15	0,06	11,67	**100,0**
Melt 7	1,03	6,11	18,77	50,19	0,00	0,16	11,51	0,79	0,16	0,08	11,20	**100,0**
Melt 8	1,59	4,08	19,89	49,84	0,00	0,25	10,54	0,64	0,00	0,04	13,13	**100,0**
Melt 9	1,52	4,38	19,60	49,62	0,00	0,24	10,49	0,70	0,00	0,09	13,36	**100,0**
Melt 10	1,46	4,75	19,13	49,42	0,00	0,23	10,59	0,64	0,00	0,09	13,70	**100,0**
Melt 11	1,58	3,99	19,85	49,66	0,00	0,23	10,40	0,66	0,00	0,05	13,57	**100,0**
Melt 12	1,53	4,39	19,61	49,32	0,00	0,22	10,50	0,64	0,00	0,10	13,68	**100,0**
Melt 13	1,57	4,24	20,05	49,44	0,00	0,24	10,53	0,68	0,00	0,05	13,20	**100,0**
Melt 14	1,52	4,63	19,93	49,14	0,00	0,21	10,69	0,76	0,00	0,04	13,07	**100,0**
Melt 15	1,50	4,56	19,72	49,22	0,00	0,24	10,51	0,68	0,01	0,06	13,49	**100,0**
Melt 16	1,65	3,63	19,89	49,90	0,00	0,25	10,35	0,67	0,00	0,05	13,61	**100,0**
Melt 17	1,76	3,51	20,05	50,10	0,00	0,25	10,22	0,57	0,00	0,09	13,45	**100,0**
Melt 18	1,42	5,13	18,95	50,14	0,00	0,19	10,86	0,73	0,00	0,08	12,50	**100,0**
Melt 19	0,85	8,25	17,51	49,59	0,00	0,15	10,88	0,73	0,12	0,06	11,85	**100,0**
Melt 20	0,81	8,76	17,15	49,41	0,00	0,14	10,59	0,69	0,18	0,03	12,24	**100,0**
Melt 21	1,08	7,28	17,73	49,42	0,00	0,16	10,74	0,69	0,02	0,06	12,81	**100,0**
Melt 22	0,87	9,91	16,55	49,26	0,00	0,14	10,68	0,70	0,07	0,12	11,70	**100,0**
Melt 23	0,94	8,93	16,96	49,24	0,00	0,15	10,77	0,73	0,08	0,09	12,09	**100,0**
Melt 24	0,81	10,22	16,64	49,36	0,00	0,17	10,61	0,70	0,14	0,04	11,32	**100,0**
Melt 25	0,77	10,11	16,91	49,09	0,00	0,14	10,72	0,76	0,12	0,07	11,29	**100,0**
Melt 26	0,91	9,60	17,09	49,30	0,00	0,14	10,86	0,75	0,15	0,07	11,14	**100,0**
Melt 27	0,92	9,66	16,96	49,15	0,00	0,16	10,63	0,73	0,09	0,03	11,67	**100,0**
Melt 28	0,79	10,06	16,75	49,30	0,00	0,15	10,72	0,72	0,14	0,07	11,32	**100,0**
Melt 29	0,86	10,08	16,71	48,93	0,00	0,15	10,50	0,77	0,17	0,12	11,71	**100,0**
Melt 30	0,80	10,14	16,89	49,06	0,00	0,15	10,65	0,72	0,15	0,09	11,35	**100,0**
Melt 31	0,36	27,89	9,21	44,28	0,00	0,10	4,75	0,34	0,13	0,05	12,88	**100,0**
average	**1,10**	**8,09**	**17,79**	**49,26**	**0,00**	**0,18**	**10,47**	**0,69**	**0,08**	**0,06**	**12,28**	**100,0**

6.1.29 LPUM residual melts – Part 4

LPUM 050-1 Melt Ox%	Na2O	MgO	Al2O3	SiO2	P2O5	K2O	CaO	TiO2	Cr2O3	MnO	FeO	Total
Melt 1	0,94	2,13	9,11	37,30	0,79	0,13	10,54	3,32	0,09	0,27	35,38	**100,0**
Melt 2	0,78	2,38	8,21	40,72	0,64	0,33	9,69	2,85	0,04	0,48	33,89	**100,0**
Melt 3	0,90	1,94	8,71	41,09	0,63	0,29	9,60	3,02	0,00	0,51	33,31	**100,0**
Melt 4	0,55	3,08	6,82	39,54	0,91	0,32	8,94	3,20	0,02	0,58	36,01	**100,0**
Melt 5	0,90	2,19	8,62	39,14	0,99	0,33	9,44	2,98	0,00	0,45	34,96	**100,0**
Melt 6	0,80	2,76	9,49	40,30	0,83	0,19	9,71	3,04	0,08	0,49	32,31	**100,0**
Melt 7	0,60	2,69	7,76	39,04	0,88	0,36	9,70	2,93	0,05	0,42	35,57	**100,0**
Melt 8	0,73	2,38	7,33	38,67	0,90	0,37	9,47	3,37	0,03	0,45	36,29	**100,0**
Melt 9	0,78	2,43	9,67	41,01	0,61	0,29	10,10	2,82	0,07	0,40	31,82	**100,0**
Melt 10	0,81	2,34	9,64	40,54	0,80	0,23	9,89	3,09	0,06	0,44	32,16	**100,0**
Melt 11	0,95	1,81	9,05	38,61	0,80	0,32	9,02	2,75	0,03	0,54	36,12	**100,0**
average	**0,79**	**2,38**	**8,58**	**39,63**	**0,80**	**0,29**	**9,65**	**3,03**	**0,04**	**0,46**	**34,35**	100,0
LPUM 030-1 Melt Ox%	**Na2O**	**MgO**	**Al2O3**	**SiO2**	**P2O5**	**K2O**	**CaO**	**TiO2**	**Cr2O3**	**MnO**	**FeO**	**Total**
Melt 1	2,05	2,75	12,73	60,70	1,51	0,22	8,60	2,87	0,04	0,40	8,13	**100,0**
Melt 2	2,08	2,90	12,83	59,90	1,64	0,21	8,69	2,91	0,06	0,44	8,35	**100,0**
Melt 3	2,09	2,63	12,86	62,18	1,24	0,28	8,06	2,54	0,00	0,41	7,71	**100,0**
Melt 4	2,19	2,46	13,00	62,99	1,13	0,25	8,06	2,18	0,00	0,39	7,35	**100,0**
Melt 5	2,23	2,55	12,87	62,18	1,17	0,23	8,10	2,56	0,00	0,55	7,56	**100,0**
Melt 6	2,35	2,61	12,98	62,15	1,11	0,27	8,04	2,57	0,00	0,39	7,53	**100,0**
Melt 7	2,13	2,75	13,00	61,72	1,18	0,25	8,29	2,81	0,00	0,00	7,88	**100,0**
Melt 8	2,19	2,91	12,89	60,15	1,30	0,27	8,58	2,99	0,00	0,31	8,41	**100,0**
Melt 9	2,12	2,72	13,09	60,94	1,24	0,20	8,29	2,79	0,00	0,42	8,18	**100,0**
Melt 10	2,24	2,72	13,05	62,12	0,99	0,23	7,93	2,60	0,00	0,41	7,70	**100,0**
Melt 11	2,22	2,85	12,75	61,50	1,33	0,23	8,28	2,68	0,00	0,45	7,73	**100,0**
average	**2,17**	**2,71**	**12,91**	**61,50**	**1,26**	**0,24**	**8,27**	**2,68**	**0,01**	**0,38**	**7,87**	100,0
LPUM 020-1 Melt Ox%	**Na2O**	**MgO**	**Al2O3**	**SiO2**	**P2O5**	**K2O**	**CaO**	**TiO2**	**Cr2O3**	**MnO**	**FeO**	**Total**
Melt 1	1,59	2,03	10,76	55,29	1,37	0,24	10,91	2,16	0,00	0,60	15,06	**100,0**
Melt 2	1,49	1,81	10,68	55,13	1,46	0,23	11,06	2,30	0,00	0,49	15,35	**100,0**
Melt 3	1,58	1,98	10,52	53,86	1,35	0,22	11,55	2,41	0,00	0,55	15,98	**100,0**
Melt 4	1,50	1,93	10,59	55,24	1,33	0,25	10,70	2,41	0,00	0,49	15,57	**100,0**
average	**1,54**	**1,94**	**10,64**	**54,88**	**1,38**	**0,24**	**11,06**	**2,32**	**0,00**	**0,53**	**15,49**	100,0

6.1.30 LPUM residual melts – Part 5

LPUM-M 120-1 Melt Ox%	Na2O	MgO	Al2O3	SiO2	P2O5	K2O	CaO	TiO2	Cr2O3	MnO	FeO	Total
Melt 1	0,60	18,54	16,22	50,06	0,00	0,06	13,92	0,30	0,17	0,13	0,00	**100,0**
Melt 2	0,54	17,92	16,71	49,84	0,00	0,11	14,12	0,33	0,30	0,11	0,03	**100,0**
Melt 3	0,58	17,93	16,54	49,92	0,00	0,11	14,27	0,31	0,16	0,12	0,06	**100,0**
Melt 4	0,54	18,26	16,22	50,11	0,00	0,08	14,23	0,32	0,10	0,10	0,05	**100,0**
Melt 5	0,52	17,79	17,22	49,71	0,00	0,07	14,05	0,25	0,15	0,13	0,10	**100,0**
Melt 6	0,60	17,67	17,38	49,50	0,00	0,09	14,14	0,24	0,20	0,13	0,04	**100,0**
Melt 7	0,51	17,69	16,35	50,07	0,00	0,11	14,53	0,32	0,21	0,12	0,09	**100,0**
Melt 8	0,56	19,17	15,65	50,12	0,00	0,09	13,76	0,29	0,20	0,07	0,09	**100,0**
Melt 9	0,51	20,43	15,48	49,46	0,00	0,07	13,04	0,25	0,64	0,10	0,03	**100,0**
Melt 10	0,49	20,45	15,54	49,50	0,00	0,07	13,01	0,25	0,51	0,13	0,04	**100,0**
Melt 11	0,53	20,25	15,82	49,43	0,00	0,09	13,32	0,29	0,21	0,04	0,02	**100,0**
Melt 12	0,52	20,30	15,22	50,07	0,00	0,08	13,00	0,27	0,32	0,13	0,09	**100,0**
Melt 13	0,48	17,87	15,93	50,48	0,00	0,08	14,08	0,27	0,18	0,09	0,55	**100,0**
Melt 14	0,51	20,26	15,88	49,21	0,00	0,08	13,22	0,24	0,44	0,09	0,07	**100,0**
Melt 15	0,44	19,74	15,14	50,18	0,00	0,10	13,32	0,19	0,14	0,17	0,58	**100,0**
Melt 16	0,52	20,37	15,58	49,57	0,00	0,05	12,99	0,24	0,48	0,14	0,04	**100,0**
Melt 17	0,48	17,92	15,73	50,61	0,00	0,07	14,14	0,20	0,19	0,12	0,55	**100,0**
Melt 18	0,52	17,61	16,31	50,36	0,00	0,10	14,16	0,24	0,21	0,15	0,33	**100,0**
Melt 19	0,57	18,29	16,62	49,86	0,00	0,09	13,87	0,30	0,21	0,12	0,08	**100,0**
Melt 20	0,54	17,48	16,92	49,92	0,00	0,10	14,28	0,34	0,28	0,13	0,02	**100,0**
Melt 21	0,52	16,03	17,21	50,50	0,00	0,08	14,96	0,31	0,16	0,14	0,08	**100,0**
Melt 22	0,53	18,28	16,32	50,07	0,00	0,07	14,00	0,33	0,24	0,11	0,06	**100,0**
Melt 23	0,58	17,81	17,28	49,54	0,00	0,11	13,97	0,25	0,19	0,18	0,09	**100,0**
Melt 24	0,52	19,32	15,97	50,16	0,00	0,07	13,27	0,20	0,31	0,10	0,09	**100,0**
Melt 25	0,57	17,93	16,49	50,10	0,00	0,09	14,12	0,32	0,15	0,20	0,04	**100,0**
Melt 26	0,57	16,89	17,39	49,95	0,00	0,08	14,45	0,30	0,26	0,11	0,03	**100,0**
Melt 27	0,51	17,69	16,21	50,27	0,00	0,08	14,57	0,30	0,25	0,12	0,00	**100,0**
Melt 28	0,61	16,11	17,71	50,07	0,00	0,09	14,78	0,21	0,20	0,14	0,09	**100,0**
average	**0,57**	**17,16**	**16,95**	**50,10**	**0,00**	**0,09**	**14,48**	**0,28**	**0,22**	**0,14**	**0,04**	100,0

6.1.31 MELTS – IW-2 and IW0 Conditions and Runproducts

MELTS IW-2																
Name	**d(PCS) km**	***PCS***	**P Mpa**	**T °C**	**H_2O input**	***liquid***	***solids***	***olivine***	***OPX***	***CPX***	***plagioclase***	***spinel***	***rhm-oxide***	***Apatite***	***Fe (L)***	***fluid***
IW-2 400	636	24,91	4000	2044	100	75,09	25,01		74,47			3,14			22,39	
IW-2 300	529	33,13	3000	1900,8	133	89,05	10,96	11,36	88,64							
IW-2 250	440	41,14	2500	1861,3	150	88,01	11,99	100,00								
IW-2 200	339	51,73	2000	1798	170	82,01	18,01	100,00								
IW-2 160	239	63,80	1600	1714,6	207	75,00	25,00	74,07	25,93							
IW-2 120	165	73,93	1200	1589,5	277	72,02	28,01	64,84	34,72			0,44				
IW-2 80	72	88,00	800	1332,3	384	46,03	53,98	23,21	40,81	32,21		3,77				
IW-2 50	34	94,25	500	1263,5	853	47,93	52,14	18,47		30,91	50,53	0,10				
IW-2 1bar A	21	96,38	1bar	1213	1743	63,00	37,11	23,75			75,89					0,35
IW-2 1bar B	17	97,10	1bar	1193,5	2764	80,05	19,95	21,79		9,47	67,63					1,10
IW-2 1bar C	3	99,56	1bar	1025	3443	15,00	85,35			52,75	41,87		4,99			0,39
MELTS IW0																
Name	**d(PCS) km**	***PCS***	**Mpa**	**T°C**	**H_2O input**	***liquid***	***solids***	***olivine***	***OPX***	***CPX***	***plagioclase***	***spinel***	***rhm-oxide***	***Apatite***	***Fe (L)***	***fluid***
IW0 400	636	25,01	4000	1927,1	100	74,99	26,59	2,81	93,05			4,14				
IW0 300	529	33,26	3000	1876,3	134	89,00	11,01	100,00								
IW0 250	440	41,27	2500	1830,1	152	88,01	12,00	100,00								
IW0 200	339	51,83	2000	1755,6	172	82,01	18,00	100,00								
IW0 160	239	63,87	1600	1636,1	210	75,00	25,00	96,22	3,78							
IW0 120	165	73,99	1200	1478,2	280	71,99	28,03	69,26	30,73			0,01				
IW0 80	72	88,04	800	1290,6	389	45,98	54,04	24,18		69,63		6,19				
IW0 50	34	94,26	500	1191,4	846	47,98	52,08	28,40		36,47	32,08	3,05				
IW0 1bar A	21	96,38	1bA	1125,3	1765	63,02	37,05	42,49			57,12					0,40
IW0 1bar B	17	97,11	1bB	1100,6	1991	79,99	19,93	55,97		2,70	39,80	0,30				1,22
IW0 1bar C	3	99,57	1bC	1041,6	2531	14,99	85,40	46,94		40,17	11,83			0,66		0,40

6.1.32 MELTS – IW-2 and IW0 Melt Compositions

IW0	IW0 400	IW0 300	IW0 250	IW0 200	IW0 160	IW0 120	IW0 80	IW0 50	IW0 1bar A	IW0 1bar B	IW0 1bar C	IW0 1bar C res.
SiO_2	46,41	42,55	42,64	42,76	43,03	43,48	42,84	40,55	38,21	36,46	35,95	40,83
MgO	38,83	38,68	36,86	34,66	30,84	24,58	17,55	10,46	7,11	5,78	4,72	1,02
FeO	8,24	10,03	10,66	11,41	12,55	14,03	15,45	19,20	25,69	30,47	31,53	27,55
Al_2O_3	4,20	4,13	4,64	5,28	6,43	8,55	11,52	15,05	13,89	10,38	9,39	10,64
CaO	2,98	3,92	4,40	4,99	6,06	8,02	10,90	11,96	10,77	10,84	11,42	8,12
Cr_2O_3	0,51	0,05	0,05	0,06	0,07	0,10	0,13	0,00	0,00	0,00	0,00	0,00
TiO_2	0,15	0,19	0,21	0,24	0,29	0,39	0,54	1,00	1,78	2,83	3,41	1,29
MnO	0,12	0,16	0,17	0,18	0,19	0,20	0,22	0,35	0,47	0,48	0,45	0,22
Na_2O	0,10	0,13	0,15	0,17	0,21	0,27	0,38	0,71	0,94	1,06	1,18	5,12
K_2O	0,01	0,01	0,02	0,02	0,02	0,03	0,04	0,08	0,17	0,25	0,30	1,73
P_2O_5	0,01	0,01	0,02	0,02	0,02	0,03	0,04	0,08	0,18	0,28	0,35	0,59
H_2O	0,01	0,01	0,02	0,02	0,02	0,03	0,04	0,08	0,18	0,28	0,35	1,81
Fe_2O_3	0,00	0,13	0,17	0,20	0,25	0,30	0,36	0,46	0,61	0,89	0,95	1,07

IW-2	IW-2 400	IW-2 300	IW-2 250	IW-2 200	IW-2 160	IW-2 120	IW-2 80	IW-2 50	IW-2 1bar A	IW-2 1bar B	IW-2 1bar C	IW-2 1bar C res.
SiO_2	46,48	47,47	46,33	46,87	47,85	48,30	48,59	47,22	47,50	48,89	49,56	56,55
MgO	38,88	42,00	42,16	40,27	36,85	32,08	25,44	14,22	12,23	11,72	11,18	4,00
FeO	8,25	1,19	1,24	1,21	1,13	1,00	0,76	0,27	0,12	0,05	0,02	0,00
Al_2O_3	4,20	4,76	5,15	5,85	7,14	9,36	12,63	20,15	20,67	17,28	15,66	13,18
CaO	2,99	3,95	4,42	5,02	6,10	8,07	11,06	15,60	15,24	16,11	16,56	10,05
Cr_2O_3	0,51	0,09	0,10	0,11	0,14	0,18	0,17	0,01	0,01	0,02	0,02	0,16
TiO_2	0,15	0,20	0,22	0,25	0,30	0,40	0,56	1,04	1,98	3,14	3,90	5,52
MnO	0,12	0,16	0,18	0,19	0,21	0,25	0,29	0,49	0,83	1,12	1,30	3,90
Na_2O	0,10	0,13	0,15	0,17	0,21	0,27	0,38	0,76	0,89	0,83	0,78	0,24
K_2O	0,01	0,01	0,02	0,02	0,02	0,03	0,04	0,08	0,17	0,26	0,32	1,87
P_2O_5	0,01	0,01	0,02	0,02	0,02	0,03	0,04	0,08	0,18	0,28	0,35	2,28
H_2O	0,01	0,01	0,01	0,02	0,02	0,03	0,04	0,08	0,17	0,28	0,34	2,25
Fe_2O_3	0,00	0,01	0,01	0,01	0,01	0,01	0,01	0,00	0,00	0,00	0,00	0,00

6.2 MATLAB – Source Code used for Image Separation

```
img = double(imread("Name.jpg"));              %read image
img = img(:,:,1);                              %show one channel only
figure,imshow(img,[]);title('Original');       %show original image
figure,histogram(img);title('Histogram');      %show histogram of image

a = input('select lower boundary')             %select boundary a prompt
b = input('select middle boundary')            %select boundary b prompt
c = input('select upper boundary')             %select boundary c prompt
d = input('select upperest boundary')          %select boundary d prompt

BL = bitand(img>-1,img<1);                     %find all px between -1 and 1
    figure,imshow(BL,[]);title('Holes');       %show image of px -1 - 1
BLL = sum(sum(BL))                             %count all px in the image

X = bitand(img>1,img<a);                       %find all px between 3 and a
    figure,imshow(X,[]);title('boundary 1');   %show image of px 1 - a
XX = sum(sum(X))                               %count all px in the image

Y = bitand(img>a,img<b);                       %find all px between a and b
    figure,imshow(Y,[]);title('boundary 2');   %show image of px a-b
YY = sum(sum(Y))                               %count all px in the image

Z = bitand(img>b,img<c);                       %find all px between b and c
    figure,imshow(Z,[]);title('boundary 3');   %show image of px b-c
ZZ = sum(sum(Z))                               %count all px in the image

U = bitand(img>c,img<d);                       %find all px between c and d
    figure,imshow(U,[]);title('boundary 4');   %show image of px c-d
UU = sum(sum(U))                               %count all px in the image

Q = bitand(img>d,img<254);                     %find all px between d and 254
    figure,imshow(Q,[]);title('boundary 5');   %show image of px d-254
QQ = sum(sum(Q))                               %count all white px

W = bitand(img>254,img<256);                   %find all px with value 255
    figure,imshow(W,[]);title('White');        %show image of white px
WW = sum(sum(W))                               %count all white px

reply = input('Close all Figures? (y/n):','s');  %prompt close all open images
if strcmp(reply,'y')                             %to clean up after run
    close all
end
```

6.3 References

Abe, Yutaka, Eiji Ohtani, Takua Okuchi, Kevin Righter, Michael Drake, and R. M. Canup. 2000. *Origin of the Earth and Moon*. *Water in the Early Earth*. Univ. Arizona Press Tuscon.

Albarède, Francis. 2011. 'Oxygen Fugacity'. In *Encyclopedia of Astrobiology*, edited by Muriel Gargaud, Ricardo Amils, José Cernicharo Quintanilla, Henderson James Cleaves, William M. Irvine, Daniele L. Pinti, and Michel Viso, 1196–1196. Berlin, Heidelberg: Springer Berlin Heidelberg. https://doi.org/10.1007/978-3-642-11274-4_4021.

Anderson, Alfred T., and Georgia Gilliland Brown. 1993. 'CO2 Contents and Formation Pressures of Some Kilauean Melt Inclusions'. *American Mineralogist* 78 (7–8): 794–803.

Arnold, James R. 1979. 'Ice in the Lunar Polar Regions'. *Journal of Geophysical Research* 84 (B10): 5659. https://doi.org/10.1029/JB084iB10p05659.

Asimow, Paul D., and Mark S. Ghiorso. 1998. 'Algorithmic Modifications Extending MELTS to Calculate Subsolidus Phase Relations'. *American Mineralogist* 83 (9–10): 1127–32. https://doi.org/10.2138/am-1998-9-1022.

Baker, Don R. 2008. 'The Fidelity of Melt Inclusions as Records of Melt Composition'. *Contributions to Mineralogy and Petrology* 156 (3): 377–95. https://doi.org/10.1007/s00410-008-0291-3.

Barnes, Jessica J., Romain Tartèse, Mahesh Anand, Francis M. McCubbin, Ian A. Franchi, Natalie A. Starkey, and Sara S. Russell. 2014. 'The Origin of Water in the Primitive Moon as Revealed by the Lunar Highlands Samples'. *Earth and Planetary Science Letters* 390 (March): 244–52. https://doi.org/10.1016/j.epsl.2014.01.015.

Behrens, Harald. 2021. 'Hydrogen Defects in Feldspars: Defect Properties and Implications for Water Solubility in Feldspar'. *Physics and Chemistry of Minerals* 48 (2): 8. https://doi.org/10.1007/s00269-020-01128-0.

Behrens, Harald, and Nicole Jantos. 2001. 'The Effect of Anhydrous Composition on Water Solubility in Granitic Melts'. *American Mineralogist* 86 (1–2): 14–20. https://doi.org/10.2138/am-2001-0102.

Bell, David R., and George R. Rossman. 1992. 'Water in Earth's Mantle: The Role of Nominally Anhydrous Minerals'. *Science* 255 (5050): 1391–97. https://doi.org/10.1126/science.255.5050.1391.

Blank, J.G., E.M. Stolper, and M.R. Carroll. 1993. 'Solubilities of Carbon Dioxide and Water in Rhyolitic Melt at 850°C and 750 Bars'. *Earth and Planetary Science Letters* 119 (1–2): 27–36. https://doi.org/10.1016/0012-821X(93)90004-S.

Blundy, J., and K. Cashman. 2008. 'Petrologic Reconstruction of Magmatic System Variables and Processes'. *Reviews in Mineralogy and Geochemistry* 69 (1): 179–239. https://doi.org/10.2138/rmg.2008.69.6.

Bouvier, Audrey, and Meenakshi Wadhwa. 2010. 'The Age of the Solar System Redefined by the Oldest Pb–Pb Age of a Meteoritic Inclusion'. *Nature Geoscience* 3 (9): 637–41. https://doi.org/10.1038/ngeo941.

Boyd, F. R., and J. L. England. 1960. 'Apparatus for Phase-Equilibrium Measurements at Pressures up to 50 Kilobars and Temperatures up to 1750°C'. *Journal of Geophysical Research* 65 (2): 741–48. https://doi.org/10.1029/JZ065i002p00741.

Butler, J., Jr., and C. Meyer Jr. 1976. 'Sulfur Prevails in Coatings on Glass Droplets: Apollo 15 Green and Brown Glasses and Apollo 17 Orange and Black (Devitrified) Glasses.' *Lunar and Planetary Science Conference Proceedings* 2 (April): 1561–81.

Canup, R. M. 2012. 'Forming a Moon with an Earth-like Composition via a Giant Impact'. *Science* 338 (6110): 1052–55. https://doi.org/10.1126/science.1226073.

Canup, R. M. 2014. 'Lunar-Forming Impacts: Processes and Alternatives'. *Philosophical Transactions of the Royal Society A: Mathematical, Physical and Engineering Sciences* 372 (2024): 20130175. https://doi.org/10.1098/rsta.2013.0175.

Canup, R. M. 2004. 'Simulations of a Late Lunar-Forming Impact'. *Icarus* 168 (2): 433–56. https://doi.org/10.1016/j.icarus.2003.09.028.

Canup, R. M., and Erik Asphaug. 2001. 'Origin of the Moon in a Giant Impact near the End of the Earth's Formation'. *Nature* 412 (6848): 708–12. https://doi.org/10.1038/35089010.

Castaing, Bernard, Gemunu Gunaratne, François Heslot, Leo Kadanoff, Albert Libchaber, Stefan Thomae, Xiao-Zhong Wu, Stéphane Zaleski, and Gianluigi Zanetti. 1989. 'Scaling of Hard Thermal Turbulence in Rayleigh-Bénard Convection'. *Journal of Fluid Mechanics* 204 (1): 1. https://doi.org/10.1017/S0022112089001643.

Cates, N.L., and S.J. Mojzsis. 2007. 'Pre-3750 Ma Supracrustal Rocks from the Nuvvuagittuq Supracrustal Belt, Northern Québec'. *Earth and Planetary Science Letters* 255 (1–2): 9–21. https://doi.org/10.1016/j.epsl.2006.11.034.

Chen, Yang, Youxue Zhang, Yang Liu, Yunbin Guan, John Eiler, and Edward M. Stolper. 2015. 'Water, Fluorine, and Sulfur Concentrations in the Lunar Mantle'. *Earth and Planetary Science Letters* 427 (October): 37–46. https://doi.org/10.1016/j.epsl.2015.06.046.

Clark, Roger N. 2009. 'Detection of Adsorbed Water and Hydroxyl on the Moon'. *Science* 326 (5952): 562–64. https://doi.org/10.1126/science.1178105.

Colaprete, Anthony, Peter Schultz, Jennifer Heldmann, Diane Wooden, Mark Shirley, Kimberly Ennico, Brendan Hermalyn, et al. 2010. 'Detection of Water in the LCROSS Ejecta Plume'. *Science* 330 (6003): 463–68. https://doi.org/10.1126/science.1186986.

Daly, Reginald A. 1946. 'Origin of the Moon and Its Topography'. *Proceedings of the American Philosophical Society* 90 (2): 104–19.

Darwin, G. H., and J. W. L. Glaisher. 1879. 'I. On the Bodily Tides of Viscous and Semi-Elastic Spheroids, and on the Ocean Tides upon a Yielding Nucleus'. *Philosophical Transactions of the Royal Society of London* 170 (December): 1–35. https://doi.org/10.1098/rstl.1879.0061.

Dauphas, N., J. H. Chen, and D. A. Papanastassiou. 2015. 'Testing Earth-Moon Isotopic Homogenization with Calcium-48'. In *46th Annual Lunar and Planetary Science Conference*, 2436.

Dauphas, Nicolas, and Edwin A. Schauble. 2016. 'Mass Fractionation Laws, Mass-Independent Effects, and Isotopic Anomalies'. *Annual Review of Earth and Planetary Sciences* 44: 709–83.

DeMeo, F. E., and B. Carry. 2014. 'Solar System Evolution from Compositional Mapping of the Asteroid Belt'. *Nature* 505 (7485): 629–34. https://doi.org/10.1038/nature12908.

Ding, Yinfeng, Xing Zhao, and Emmalau Liu. 2011. 'L10 FePt (001) Thin Films for Perpendicular Magnetic Recording Media'. In *Magnetic Thin Films: Properties, Performance and Applications*, 27.

Dixon, J. E., E. M. Stolper, and J. R. Holloway. 1995. 'An Experimental Study of Water and Carbon Dioxide Solubilities in Mid-Ocean Ridge Basaltic Liquids. Part I: Calibration and Solubility Models'. *Journal of Petrology*, December. https://doi.org/10.1093/oxfordjournals.petrology.a037267.

Drake, Michael J. 2005. 'Origin of Water in the Terrestrial Planets'. *Meteoritics & Planetary Science* 40 (4): 519–27. https://doi.org/10.1111/j.1945-5100.2005.tb00960.x.

Druzhbin, D., and R. Myhill. 2016. 'Generation of Pressures over 40 GPa Using Kawai-Type Multi-Anvil Press with Tungsten Carbide Anvils'. *Review of Scientific Instruments* 87 (2): 024501. https://doi.org/10.1063/1.4941716.

Dubrovinsky, L., N. Dubrovinskaia, E. Bykova, M. Bykov, V. Prakapenka, C. Prescher, K. Glazyrin, et al. 2015. 'The Most Incompressible Metal Osmium at Static Pressures above 750 Gigapascals'. *Nature* 525 (7568): 226–29. https://doi.org/10.1038/nature14681.

Eggler, D. H., B. O. Mysen, and T. C. Hoering. 1974. 'Gas Species in Sealed Capsules in Solid Media, High Pressure Apparatus'. *Carnegie Institution of Washington Yearbook* 73: 228–32.

Eke, V.R., L.F.A. Teodoro, and R.C. Elphic. 2009. 'The Spatial Distribution of Polar Hydrogen Deposits on the Moon'. *Icarus* 200 (1): 12–18. https://doi.org/10.1016/j.icarus.2008.10.013.

Elardo, Stephen M., David S. Draper, and Charles K. Shearer. 2011. 'Lunar Magma Ocean Crystallization Revisited: Bulk Composition, Early Cumulate Mineralogy, and the Source Regions of the Highlands Mg-Suite'. *Geochimica et Cosmochimica Acta* 75 (11): 3024–45. https://doi.org/10.1016/j.gca.2011.02.033.

Elkins Tanton, Linda T., James A. Van Orman, Bradford H. Hager, and Timothy L. Grove. 2002. 'Re-Examination of the Lunar Magma Ocean Cumulate Overturn Hypothesis: Melting or Mixing Is Required'. *Earth and Planetary Science Letters* 196 (3–4): 239–49. https://doi.org/10.1016/S0012-821X(01)00613-6.

Elkins-Tanton, Linda T., Nilanjan Chatterjee, and Timothy L. Grove. 2003. 'Experimental and Petrological Constraints on Lunar Differentiation from the Apollo 15 Green Picritic Glasses'. *Meteoritics & Planetary Science* 38 (4): 515–27. https://doi.org/10.1111/j.1945-5100.2003.tb00024.x.

Elphic, R. C., V. R. Eke, L. F. A. Teodoro, D. J. Lawrence, and D. B. J. Bussey. 2007. 'Models of the Distribution and Abundance of Hydrogen at the Lunar South Pole: HYDROGEN AT THE LUNAR SOUTH POLE'. *Geophysical Research Letters* 34 (13): n/a-n/a. https://doi.org/10.1029/2007GL029954.

Faure, F, and P Schiano. 2005. 'Experimental Investigation of Equilibration Conditions during Forsterite Growth and Melt Inclusion Formation'. *Earth and Planetary Science Letters* 236 (3–4): 882–98. https://doi.org/10.1016/j.epsl.2005.04.050.

Feldman, W. C., D. J. Lawrence, R. C. Elphic, B. L. Barraclough, S. Maurice, I. Genetay, and A. B. Binder. 2000. 'Polar Hydrogen Deposits on the Moon'. *Journal of Geophysical Research: Planets* 105 (E2): 4175–95. https://doi.org/10.1029/1999JE001129.

Feldman, W. C., S. Maurice, A. B. Binder, B. L. Barraclough, R. C. Elphic, and D. J. Lawrence. 1998. 'Fluxes of Fast and Epithermal Neutrons from Lunar Prospector: Evidence for Water Ice at the Lunar Poles'. *Science* 281 (5382): 1496–1500. https://doi.org/10.1126/science.281.5382.1496.

Feldman, W. C., S. Maurice, D. J. Lawrence, R. C. Little, S. L. Lawson, O. Gasnault, R. C. Wiens, et al. 2001. 'Evidence for Water Ice near the Lunar Poles'. *Journal of Geophysical Research: Planets* 106 (E10): 23231–51. https://doi.org/10.1029/2000JE001444.

Flasar, F. Michael, and Francis Birch. 1973. 'Energetics of Core Formation: A Correction'. *Journal of Geophysical Research* 78 (26): 6101–3. https://doi.org/10.1029/JB078i026p06101.

Fogel, Robert A., and Malcolm J. Rutherford. 1995. 'Magmatic Volatiles in Primitive Lunar Glasses: I. FTIR and EPMA Analyses of Apollo 15 Green and Yellow Glasses and Revision of the Volatile-Assisted Fire-Fountain Theory'. *Geochimica et Cosmochimica Acta* 59 (1): 201–15. https://doi.org/10.1016/0016-7037(94)00377-X.

Frost, B. Ronald. 1991. 'Chapter 1.INTRODUCTION TO OXYGEN FUGACITY AND ITS PETROLOGIC IMPORTANCE'. In *Oxide Minerals*, edited by Donald H. Lindsley, 1–10. De Gruyter. https://doi.org/10.1515/9781501508684-004.

Garcia, Raphaël F., Jeannine Gagnepain-Beyneix, Sébastien Chevrot, and Philippe Lognonné. 2011. 'Very Preliminary Reference Moon Model'. *Physics of the Earth and Planetary Interiors* 188 (1–2): 96–113. https://doi.org/10.1016/j.pepi.2011.06.015.

Garcia, Raphaël F., Jeannine Gagnepain-Beyneix, Sébastien Chevrot, and Philippe Lognonné. 2012. 'Erratum to "Very Preliminary Reference Moon Model", by R.F. Garcia, J. Gagnepain-Beyneix, S. Chevrot, P. Lognonné [Phys. Earth Planet. Inter. 188 (2011) 96–113]'. *Physics of the Earth and Planetary Interiors* 202–203 (August): 89–91. https://doi.org/10.1016/j.pepi.2012.03.009.

Georg, R. Bastian, Alex N. Halliday, Edwin A. Schauble, and Ben C. Reynolds. 2007. 'Silicon in the Earth's Core'. *Nature* 447 (7148): 1102–6. https://doi.org/10.1038/nature05927.

Ghiorso, Mark S., Marc M. Hirschmann, Peter W. Reiners, and Victor C. Kress. 2002. 'The PMELTS: A Revision of MELTS for Improved Calculation of Phase Relations and Major Element Partitioning Related to Partial Melting of the Mantle to 3 GPa: PMELTS, A REVISION OF MELTS'. *Geochemistry, Geophysics, Geosystems* 3 (5): 1–35. https://doi.org/10.1029/2001GC000217.

Ghiorso, Mark S., and Richard O. Sack. 1995. 'Chemical Mass Transfer in Magmatic Processes IV. A Revised and Internally Consistent Thermodynamic Model for the Interpolation and Extrapolation of Liquid-Solid Equilibria in Magmatic Systems at Elevated Temperatures and Pressures'. *Contributions to Mineralogy and Petrology* 119 (2–3): 197–212. https://doi.org/10.1007/BF00307281.

Goldberg, R. H., T. A. Tombrello, and D. S. Burnett. 1976. 'Fluorine as a Constituent in Lunar Magnetic Gases.' *Lunar and Planetary Science Conference Proceedings* 2 (April): 1597–1613.

Goldstein, S. B., and R. W. Luth. 2006. 'THE IMPORTANCE OF COOLING REGIME IN THE FORMATION OF MELT INCLUSIONS IN OLIVINE CRYSTALS IN HAPLOBASALTIC MELTS'. *The Canadian Mineralogist* 44 (6): 1543–55. https://doi.org/10.2113/gscanmin.44.6.1543.

Greenwood, James P., Shoichi Itoh, Naoya Sakamoto, Paul Warren, Lawrence Taylor, and Hisayoshi Yurimoto. 2011. 'Hydrogen Isotope Ratios in Lunar Rocks Indicate Delivery of Cometary Water to the Moon'. *Nature Geoscience* 4 (2): 79–82. https://doi.org/10.1038/ngeo1050.

Grossmann, Siegfried, and Detlef Lohse. 1992. 'Scaling in Hard Turbulent Rayleigh-Bénard Flow'. *Physical Review A* 46 (2): 903–17. https://doi.org/10.1103/PhysRevA.46.903.

Gualda, Guilherme A. R., and Mark S. Ghiorso. 2015. 'MELTS_Excel: AMicrosoft Excel-Based MELTS Interface for Research and Teaching of Magma Properties and Evolution'. *Geochemistry, Geophysics, Geosystems* 16 (1): 315–24. https://doi.org/10.1002/2014GC005545.

Gurenko, Andrey A., and Marc Chaussidon. 1995. 'Enriched and Depleted Primitive Melts Included in Olivine from Icelandic Tholeiites: Origin by Continuous Melting of a Single Mantle Column'. *Geochimica et Cosmochimica Acta* 59 (14): 2905–17. https://doi.org/10.1016/0016-7037(95)00184-0.

Halliday, Alex N. 2008. 'A Young Moon-Forming Giant Impact at 70–110 Million Years Accompanied by Late-Stage Mixing, Core Formation and Degassing of the Earth'. *Philosophical Transactions of the Royal Society A: Mathematical, Physical and Engineering Sciences* 366 (1883): 4163–81. https://doi.org/10.1098/rsta.2008.0209.

Hamilton, D. L., C. W. Burnham, and E. F. Osborn. 1964. 'The Solubility of Water and Effects of Oxygen Fugacity and Water Content on Crystallization in Mafic Magmas'. *Journal of Petrology* 5 (1): 21–39. https://doi.org/10.1093/petrology/5.1.21.

Hartmann, Lee, Fred Ciesla, Oliver Gressel, and Richard Alexander. 2017. 'Disk Evolution and the Fate of Water'. *Space Science Reviews* 212 (1–2): 813–34. https://doi.org/10.1007/s11214-017-0406-0.

Haskin, L., and P. Warren. 1991. *Lunar Chemistry*. *Lunar Sourcebook, A User's Guide to the Moon*. https://ui.adsabs.harvard.edu/abs/1991lsug.book..357H.

Hauri, E, G Gaetani, and T Green. 2006. 'Partitioning of Water during Melting of the Earth's Upper Mantle at H2O-Undersaturated Conditions'. *Earth and Planetary Science Letters* 248 (3–4): 715–34. https://doi.org/10.1016/j.epsl.2006.06.014.

Hauri, Erik H., Alberto E. Saal, Malcolm J. Rutherford, and James A. Van Orman. 2015. 'Water in the Moon's Interior: Truth and Consequences'. *Earth and Planetary Science Letters* 409 (January): 252–64. https://doi.org/10.1016/j.epsl.2014.10.053.

Hauri, Erik H., Thomas Weinreich, Alberto E. Saal, Malcolm C. Rutherford, and James A. Van Orman. 2011. 'High Pre-Eruptive Water Contents Preserved in Lunar Melt Inclusions'. *Science* 333 (6039): 213–15. https://doi.org/10.1126/science.1204626.

Hess, P.C., and E.M. Parmentier. 1995. 'A Model for the Thermal and Chemical Evolution of the Moon's Interior: Implications for the Onset of Mare Volcanism'. *Earth and Planetary Science Letters* 134 (3–4): 501–14. https://doi.org/10.1016/0012-821X(95)00138-3.

Hijikata, Ken-ichi, and Kenzo Yagi. 1967. 'Phase Relations of Ca-Tschermak's Molecule at High Pressures and Temperatures'. *Journal of the Faculty of Science, Hokkaido University. Series 4, Geology and Mineralogy* 13 (4): 407–17.

Holland, T. J. B. 1980. 'The Reaction Albite = Jadeite+quartz Determined Experimentally in the Range 600–1200 ° C'. *American Mineralogist* 65 (1–2): 129–34.

Holloway, John R., Vivian Pan, and Gisli Gudmundsson. 1992. 'High-Pressure Fluid-Absent Melting Experiments in the Presence of Graphite: Oxygen Fugacity, Ferric/Ferrous Ratio and Dissolved CO2'. *European Journal of Mineralogy* 4 (1): 105–14. https://doi.org/10.1127/ejm/4/1/0105.

Holzheid, A., and H.St.C. O'Neill. 1995. 'The Cr Cr2O3 Oxygen Buffer and the Free Energy of Formation of Cr2O3 from High-Temperature Electrochemical Measurements'. *Geochimica et Cosmochimica Acta* 59 (3): 475–79. https://doi.org/10.1016/0016-7037(94)00287-V.

Hughes, J. M., B. L. Jolliff, and M. E. Gunter. 2006. 'The Atomic Arrangement of Merrillite from the Fra Mauro Formation, Apollo 14 Lunar Mission: The First Structure of Merrillite from the Moon'. *American Mineralogist* 91 (10): 1547–52. https://doi.org/10.2138/am.2006.2021.

Hui, Hejiu, Anne H. Peslier, Youxue Zhang, and Clive R. Neal. 2013. 'Water in Lunar Anorthosites and Evidence for a Wet Early Moon'. *Nature Geoscience* 6 (3): 177–80. https://doi.org/10.1038/ngeo1735.

Ishii, Takayuki, Daisuke Yamazaki, Noriyoshi Tsujino, Fang Xu, Zhaodong Liu, Takaaki Kawazoe, Takafumi Yamamoto, et al. 2017. 'Pressure Generation to 65 GPa in a Kawai-Type Multi-Anvil Apparatus with Tungsten Carbide Anvils'. *High Pressure Research* 37 (4): 507–15. https://doi.org/10.1080/08957959.2017.1375491.

Javoy, Marc, Edouard Kaminski, François Guyot, Denis Andrault, Chrystèle Sanloup, Manuel Moreira, Stéphane Labrosse, Albert Jambon, P. Agrinier, and Anne Davaille. 2010. 'The Chemical Composition of the Earth: Enstatite Chondrite Models'. *Earth and Planetary Science Letters* 293 (3–4): 259–68.

Jeans, James H. 1928. 'Astronomy and Cosmogony.' *Geological Magazine* 65 (7): 329–30. https://doi.org/10.1017/S0016756800107861.

Johannes, W. 1973. 'A Simplified Piston-Cylinder Apparatus of High Precision'. *Neues Jahrbuch Für Mineralogie - Monatshefte* 1973 (7–8): 337–51. https://doi.org/10.1127/njmm/1973/1973/337.

Jolliff, B. L., J. M. Hughes, J. J. Freeman, and R. A. Zeigler. 2006. 'Crystal Chemistry of Lunar Merrillite and Comparison to Other Meteoritic and Planetary Suites of Whitlockite and Merrillite'. *American Mineralogist* 91 (10): 1583–95. https://doi.org/10.2138/am.2006.2185.

Jolliff, Bradley L., Jeffrey J. Gillis, Larry A. Haskin, Randy L. Korotev, and Mark A. Wieczorek. 2000. 'Major Lunar Crustal Terranes: Surface Expressions and Crust-Mantle Origins'. *Journal of Geophysical Research: Planets* 105 (E2): 4197–4216. https://doi.org/10.1029/1999JE001103.

Jolliff, Bradley L., Larry A. Haskin, Russell O. Colson, and Meenakshi Wadhwa. 1993. 'Partitioning in REE-Saturating Minerals: Theory, Experiment, and Modelling of Whitlockite, Apatite, and Evolution of Lunar Residual Magmas'. *Geochimica et Cosmochimica Acta* 57 (16): 4069–94. https://doi.org/10.1016/0016-7037(93)90354-Y.

Jones, J. H., and L. L. Hood. 1988. 'Does the Moon Have the Same Composition as the Terrestrial Upper Mantle?' 681 (January): 35.

Kagi, R. 2005. 'Piston-Cylinder Experiments on H2O Undersaturated Fe-Bearing Systems: An Experimental Setup Approaching FO2 Conditions of Natural Calc-Alkaline Magmas'. *American Mineralogist* 90 (4): 708–17. https://doi.org/10.2138/am.2005.1663.

Keihm, S. J., and M. G. Langseth. 1977. 'Lunar Thermal Regime to 300 Km.' *Lunar and Planetary Science Conference Proceedings* 1 (January): 499–514.

Kent, A. J.R. 2008. 'Melt Inclusions in Basaltic and Related Volcanic Rocks'. *Reviews in Mineralogy and Geochemistry* 69 (1): 273–331. https://doi.org/10.2138/rmg.2008.69.8.

Khan, A., J. Maclennan, S. R. Taylor, and J. A. D. Connolly. 2006. 'Are the Earth and the Moon Compositionally Alike? Inferences on Lunar Composition and Implications for Lunar Origin and Evolution from Geophysical Modeling'. *Journal of Geophysical Research* 111 (E5): E05005. https://doi.org/10.1029/2005JE002608.

Kohut, Edward, and Roger L. Nielsen. 2004. 'Melt Inclusion Formation Mechanisms and Compositional Effects in High-An Feldspar and High-Fo Olivine in Anhydrous Mafic Silicate Liquids'. *Contributions to Mineralogy and Petrology* 147 (6): 684–704. https://doi.org/10.1007/s00410-004-0576-0.

König, S., C. Münker, S. Hohl, H. Paulick, A.R. Barth, M. Lagos, J. Pfänder, and A. Büchl. 2011. 'The Earth's Tungsten Budget during Mantle Melting and Crust Formation'. *Geochimica et Cosmochimica Acta* 75 (8): 2119–36. https://doi.org/10.1016/j.gca.2011.01.031.

Kuzmin, D. V., and A. V. Sobolev. 2004. 'Boundary Layer Contribution to the Composition of Melt Inclusions in Olivine'. In *Geochimica et Cosmochimica Acta*, 68:A544–A544. PERGAMON-ELSEVIER SCIENCE LTD THE BOULEVARD, LANGFORD LANE, KIDLINGTON ….

Langseth, M. G., S. J. Keihm, and K. Peters. 1976. 'Revised Lunar Heat-Flow Values.' *Lunar and Planetary Science Conference Proceedings* 3 (April): 3143–71.

Lawrence, David J., W. C. Feldman, R. C. Elphic, J. J. Hagerty, S. Maurice, G. W. McKinney, and T. H. Prettyman. 2006. 'Improved Modeling of Lunar Prospector Neutron Spectrometer Data: Implications for Hydrogen Deposits at the Lunar Poles'. *Journal of Geophysical Research* 111 (E8): E08001. https://doi.org/10.1029/2005JE002637.

Li, S., and R. E. Milliken. 2013. 'Quantitative Mapping of Lunar Surface Hydration with Moon Mineralogy Mapper (M^ 3) Data'. In *44th Annual Lunar and Planetary Science Conference*, 1337.

Li, S., and R. E. Milliken. 2014. 'Quantitative Mapping of Hydration in Lunar Pyroclastic Deposits: Insights into Water from the Lunar Interior'. In *45th Annual Lunar and Planetary Science Conference*, 2012.

Libowitzky, E., and A. Beran. 2006. 'The Structure of Hydrous Species in Nominally Anhydrous Minerals: Information from Polarized IR Spectroscopy'. *Reviews in Mineralogy and Geochemistry* 62 (1): 29–52. https://doi.org/10.2138/rmg.2006.62.2.

Lin, Yanhao, Elodie J. Tronche, Edgar S. Steenstra, and Wim van Westrenen. 2017a. 'Evidence for an Early Wet Moon from Experimental Crystallization of the Lunar Magma Ocean'. *Nature Geoscience* 10 (1): 14–18. https://doi.org/10.1038/ngeo2845.

Lin, Yanhao, Elodie J. Tronche, Edgar S. Steenstra, and Wim van Westrenen. 2017b. 'Experimental Constraints on the Solidification of a Nominally Dry Lunar Magma Ocean'. *Earth and Planetary Science Letters* 471 (August): 104–16. https://doi.org/10.1016/j.epsl.2017.04.045.

Linnen, Robert L., Michel Pichavant, and François Holtz. 1996. 'The Combined Effects of FO2 and Melt Composition on SnO2 Solubility and Tin Diffusivity in Haplogranitic Melts'. *Geochimica et Cosmochimica Acta* 60 (24): 4965–76. https://doi.org/10.1016/S0016-7037(96)00295-5.

Liu, Y., Y. Guan, Y. Chen, Y. Zhang, J. M. Eiler, G. R. Rossman, and L. A. Taylor. 2013. 'Hydroxyl in Lunar Regolith: Dependence on Soil Composition and Maturity'. In *44th Annual Lunar and Planetary Science Conference*, 2203.

Lognonné, P., and C.L. Johnson. 2015. 'Planetary Seismology'. In *Treatise on Geophysics*, 65–120. Elsevier. https://doi.org/10.1016/B978-0-444-53802-4.00167-6.

Lognonné, Philippe, Jeannine Gagnepain-Beyneix, and Hugues Chenet. 2003. 'A New Seismic Model of the Moon: Implications for Structure, Thermal Evolution and Formation of the Moon'. *Earth and Planetary Science Letters* 211 (1–2): 27–44. https://doi.org/10.1016/S0012-821X(03)00172-9.

Longhi, John. 1980. 'A Model of Early Lunar Differentiation.' *Lunar and Planetary Science Conference Proceedings* 1 (January): 289–315.

Longhi, John. 1992. 'Experimental Petrology and Petrogenesis of Mare Volcanics'. *Geochimica et Cosmochimica Acta* 56 (6): 2235–51. https://doi.org/10.1016/0016-7037(92)90186-M.

Longhi, John. 2006. 'Petrogenesis of Picritic Mare Magmas: Constraints on the Extent of Early Lunar Differentiation'. *Geochimica et Cosmochimica Acta* 70 (24): 5919–34. https://doi.org/10.1016/j.gca.2006.09.023.

Martin, Rebecca G., and Mario Livio. 2012. 'On the Evolution of the Snow Line in Protoplanetary Discs: Evolution of the Snow Line'. *Monthly Notices of the Royal Astronomical Society: Letters* 425 (1): L6–9. https://doi.org/10.1111/j.1745-3933.2012.01290.x.

Matjuschkin, Vladimir, Richard A. Brooker, Brian Tattitch, Jon D. Blundy, and Charlotte C. Stamper. 2015. 'Control and Monitoring of Oxygen Fugacity in Piston Cylinder Experiments'. *Contributions to Mineralogy and Petrology* 169 (1): 9. https://doi.org/10.1007/s00410-015-1105-z.

McCubbin, F. M., A. Steele, H. Nekvasil, A. Schnieders, T. Rose, M. Fries, P. K. Carpenter, and B. L. Jolliff. 2010. 'Detection of Structurally Bound Hydroxyl in Fluorapatite from Apollo Mare Basalt 15058,128 Using TOF-SIMS'. *American Mineralogist* 95 (8–9): 1141–50. https://doi.org/10.2138/am.2010.3448.

McCubbin, Francis M., Bradley L. Jolliff, Hanna Nekvasil, Paul K. Carpenter, Ryan A. Zeigler, Andrew Steele, Stephen M. Elardo, and Donald H. Lindsley. 2011. 'Fluorine and Chlorine Abundances in Lunar Apatite: Implications for Heterogeneous Distributions of Magmatic Volatiles in the Lunar Interior'. *Geochimica et Cosmochimica Acta* 75 (17): 5073–93. https://doi.org/10.1016/j.gca.2011.06.017.

McCubbin, Francis M., Andrew Steele, Erik H. Hauri, Hanna Nekvasil, Shigeru Yamashita, and Russell J. Hemley. 2010. 'Nominally Hydrous Magmatism on the Moon'. *Proceedings of the National Academy of Sciences* 107 (25): 11223–28. https://doi.org/10.1073/pnas.1006677107.

McCubbin, Francis M., Kathleen E. Vander Kaaden, Romain Tartèse, Jeremy W. Boyce, Sami Mikhail, Eric S. Whitson, Aaron S. Bell, et al. 2015. 'Experimental Investigation of F, Cl, and OH Partitioning between Apatite and Fe-Rich Basaltic Melt at 1.0–1.2 GPa and 950–1000 °C'. *American Mineralogist* 100 (8–9): 1790–1802. https://doi.org/10.2138/am-2015-5233.

McCubbin, Francis M., Kathleen E. Vander Kaaden, Romain Tartèse, Rachel L. Klima, Yang Liu, James Mortimer, Jessica J. Barnes, et al. 2015. 'Magmatic Volatiles (H, C, N, F, S, Cl) in the Lunar Mantle, Crust, and Regolith: Abundances, Distributions, Processes, and Reservoirs'. *American Mineralogist* 100 (8–9): 1668–1707. https://doi.org/10.2138/am-2015-4934CCBYNCND.

Médard, Etienne, Catherine A. McCammon, Jay A. Barr, and Timothy L. Grove. 2008. 'Oxygen Fugacity, Temperature Reproducibility, and H2O Contents of Nominally Anhydrous Piston-Cylinder Experiments Using Graphite Capsules'. *American Mineralogist* 93 (11–12): 1838–44.

Metrich, N., and P. J. Wallace. 2008. 'Volatile Abundances in Basaltic Magmas and Their Degassing Paths Tracked by Melt Inclusions'. *Reviews in Mineralogy and Geochemistry* 69 (1): 363–402. https://doi.org/10.2138/rmg.2008.69.10.

Métrich, Nicole. 2008. '10. Volatile Abundances in Basaltic Magmas and Their Degassing Paths Tracked by Melt Inclusions'. In *Minerals, Inclusions And Volcanic Processes*, edited by Keith D. Putirka and Frank J. Tepley III, 363–402. De Gruyter. https://doi.org/10.1515/9781501508486-011.

Meyer, C., Jr., D. S. McKay, D. H. Anderson, and P. Butler Jr. 1975. 'The Source of Sublimates on the Apollo 15 Green and Apollo 17 Orange Glass Samples.' *Lunar and Planetary Science Conference Proceedings* 2 (January): 1673–99.

Mills, R. D., J. I. Simon, C. M. Alexander, J. Wang, R. Christoffersen, and Z. Rahman. 2014. 'Chemical Zoning of Feldspars in Lunar Granitoids: Implications for the Origins of Lunar Silicic Magmas'. In *Lunar and Planetary Science Conference*.

Mills, R.D., J.I. Simon, C.M.O'D. Alexander, J. Wang, and E.H. Hauri. 2017. 'Water in Alkali Feldspar: The Effect of Rhyolite Generation on the Lunar Hydrogen Budget'. *Geochemical Perspectives Letters*, 115–23. https://doi.org/10.7185/geochemlet.1712.

Moore, Gordon. 2008. '9. Interpreting H_2O and CO_2 Contents in Melt Inclusions: Constraints from Solubility Experiments and Modeling'. In *Minerals, Inclusions And Volcanic Processes*, edited by Keith D. Putirka and Frank J. Tepley III, 333–62. De Gruyter. https://doi.org/10.1515/9781501508486-010.

Morbidelli, A., J. Chambers, J. I. Lunine, J. M. Petit, F. Robert, G. B. Valsecchi, and K. E. Cyr. 2000. 'Source Regions and Timescales for the Delivery of Water to the Earth'. *Meteoritics & Planetary Science* 35 (6): 1309–20. https://doi.org/10.1111/j.1945-5100.2000.tb01518.x.

Mueller, Steve, G. Jeffrey Taylor, and Roger J. Phillips. 1988. 'Lunar Composition: A Geophysical and Petrological Synthesis'. *Journal of Geophysical Research: Solid Earth* 93 (B6): 6338–52.

Myers, J. t, and H. P. Eugster. 1983. 'The System Fe-Si-O: Oxygen Buffer Calibrations to 1,500 K'. *Contributions to Mineralogy and Petrology* 82 (1): 75–90.

Nakajima, Miki, and David J. Stevenson. 2018. 'Inefficient Volatile Loss from the Moon-Forming Disk: Reconciling the Giant Impact Hypothesis and a Wet Moon'. *Earth and Planetary Science Letters* 487 (April): 117–26. https://doi.org/10.1016/j.epsl.2018.01.026.

Nakamura, M., and S. Shimakita. 1998. 'Dissolution Origin and Syn-Entrapment Compositional Change of Melt Inclusion in Plagioclase'. *Earth and Planetary Science Letters* 161 (1–4): 119–33. https://doi.org/10.1016/S0012-821X(98)00144-7.

Nakamura, Y., G. V. Latham, H. J. Dorman, and J.E. Harris. 1981. 'Passive Seismic Experiment Long Period Event Catalog, Final Version, 1969 Day 202 - 1977 Day 273'. UTIG Technical Report No. 18.

Nakamura, Yosio. 1983. 'Seismic Velocity Structure of the Lunar Mantle'. *Journal of Geophysical Research* 88 (B1): 677. https://doi.org/10.1029/JB088iB01p00677.

Neal, Clive R, and Lawrence A Taylor. 1992. 'Petrogenesis of Mare Basalts: A Record of Lunar Volcanism'. *Geochimica et Cosmochimica Acta* 56 (6): 2177–2211. https://doi.org/10.1016/0016-7037(92)90184-K.

Nicholis, Mike G., and Malcolm J. Rutherford. 2009. 'Graphite Oxidation in the Apollo 17 Orange Glass Magma: Implications for the Generation of a Lunar Volcanic Gas Phase'. *Geochimica et Cosmochimica Acta* 73 (19): 5905–17. https://doi.org/10.1016/j.gca.2009.06.022.

Nielsen, R. L., Jennifer Crum, Rene Bourgeois, Kaylea Hascall, Lance M. Forsythe, Martin R. Fisk, and David M. Christie. 1995. 'Melt Inclusions in High-An Plagioclase from the Gorda Ridge: An Example of the Local Diversity of MORB Parent Magmas'. *Contributions to Mineralogy and Petrology* 122 (November): 34–50. https://doi.org/10.1007/s004100050111.

Nielsen, Roger L., Peter J. Michael, and Rachel Sours-Page. 1998. 'Chemical and Physical Indicators of Compromised Melt Inclusions'. *Geochimica et Cosmochimica Acta* 62 (March): 831–39. https://doi.org/10.1016/S0016-7037(98)00024-6.

Norton, O. Richard, and Lawrence A. Chitwood. 2008. *Field Guide to Meteors and Meteorites*. Patrick Moore's Practical Astronomy Series. London: Springer London. https://doi.org/10.1007/978-1-84800-157-2.

Nozette, S., C. L. Lichtenberg, P. Spudis, R. Bonner, W. Ort, E. Malaret, M. Robinson, and E. M. Shoemaker. 1996. 'The Clementine Bistatic Radar Experiment'. *Science* 274 (5292): 1495–98. https://doi.org/10.1126/science.274.5292.1495.

Nunn, Ceri, Raphael F. Garcia, Yosio Nakamura, Angela G. Marusiak, Taichi Kawamura, Daoyuan Sun, Ludovic Margerin, et al. 2020. 'Lunar Seismology: A Data and Instrumentation Review'. *Space Science Reviews* 216 (5): 89. https://doi.org/10.1007/s11214-020-00709-3.

O'Neil, Jonathan, Richard W. Carlson, Jean-Louis Paquette, and Don Francis. 2012. 'Formation Age and Metamorphic History of the Nuvvuagittuq Greenstone Belt'. *Precambrian Research* 220–221 (November): 23–44. https://doi.org/10.1016/j.precamres.2012.07.009.

O'Neill, Hugh St.C., and Stephen M. Eggins. 2002. 'The Effect of Melt Composition on Trace Element Partitioning: An Experimental Investigation of the Activity Coefficients of FeO, NiO, CoO, MoO2 and MoO3 in Silicate Melts'. *Chemical Geology* 186 (1–2): 151–81. https://doi.org/10.1016/S0009-2541(01)00414-4.

Pahlevan, Kaveh, and David J. Stevenson. 2007. 'Equilibration in the Aftermath of the Lunar-Forming Giant Impact'. *Earth and Planetary Science Letters* 262 (3–4): 438–49. https://doi.org/10.1016/j.epsl.2007.07.055.

Papike, James J., Graham Ryder, and Charles K. Shearer. 1998. 'Chapter 5. LUNAR SAMPLES'. In *Planetary Materials*, edited by James J. Papike, 719–952. De Gruyter. https://doi.org/10.1515/9781501508806-020.

PATIÑO DOUCE, ALBERTO E., and JAMES S. BEARD. 1995. 'Dehydration-Melting of Biotite Gneiss and Quartz Amphibolite from 3 to 15 Kbar'. *Journal of Petrology* 36 (3): 707–38.

Peslier, Anne H. 2020. 'The Origins of Water'. *Science* 369 (6507): 1058–1058. https://doi.org/10.1126/science.abc1338.

Peslier, Anne H., Maria Schönbächler, Henner Busemann, and Shun-Ichiro Karato. 2017. 'Water in the Earth's Interior: Distribution and Origin'. *Space Science Reviews* 212 (1–2): 743–810. https://doi.org/10.1007/s11214-017-0387-z.

Piani, Laurette, Yves Marrocchi, Thomas Rigaudier, Lionel G. Vacher, Dorian Thomassin, and Bernard Marty. 2020. 'Earth's Water May Have Been Inherited from Material Similar to Enstatite Chondrite Meteorites'. *Science* 369 (6507): 1110–13. https://doi.org/10.1126/science.aba1948.

Pierazzo, E., A.M. Vickery, and H.J. Melosh. 1997. 'A Reevaluation of Impact Melt Production'. *Icarus* 127 (2): 408–23. https://doi.org/10.1006/icar.1997.5713.

Pieters, C. M., J. N. Goswami, R. N. Clark, M. Annadurai, J. Boardman, B. Buratti, J.-P. Combe, et al. 2009. 'Character and Spatial Distribution of OH/H $_2$ O on the Surface of the Moon Seen by M ^{3} on Chandrayaan-1'. *Science* 326 (5952): 568–72. https://doi.org/10.1126/science.1178658.

Pollack, Henry N., Suzanne J. Hurter, and Jeffrey R. Johnson. 1993. 'Heat Flow from the Earth's Interior: Analysis of the Global Data Set'. *Reviews of Geophysics* 31 (3): 267–80.

Potts, Nicola J., Geoffrey D. Bromiley, and Richard A. Brooker. 2021. 'An Experimental Investigation of F, Cl and H2O Mineral-Melt Partitioning in a Reduced, Model Lunar System'. *Geochimica et Cosmochimica Acta* 294 (February): 232–54. https://doi.org/10.1016/j.gca.2020.12.003.

Potts, Nicola J., Romain Tartèse, Mahesh Anand, Wim van Westrenen, Alexandra A. Griffiths, Thomas J. Barrett, and Ian A. Franchi. 2016. 'Characterization of Mesostasis Regions in Lunar Basalts: Understanding Late-Stage Melt Evolution and Its Influence on Apatite Formation'. *Meteoritics & Planetary Science* 51 (9): 1555–75. https://doi.org/10.1111/maps.12681.

Qin, Liping, Conel MO'D Alexander, Richard W. Carlson, Mary F. Horan, and Tetsuya Yokoyama. 2010. 'Contributors to Chromium Isotope Variation of Meteorites'. *Geochimica et Cosmochimica Acta* 74 (3): 1122–45.

Rapp, J. F., and D. S. Draper. 2018. 'Fractional Crystallization of the Lunar Magma Ocean: Updating the Dominant Paradigm'. *Meteoritics & Planetary Science* 53 (7): 1432–55. https://doi.org/10.1111/maps.13086.

Raymond, Sean N., and Andre Izidoro. 2017. 'Origin of Water in the Inner Solar System: Planetesimals Scattered Inward during Jupiter and Saturn's Rapid Gas Accretion'. *Icarus* 297: 134–48.

Reufer, Andreas, Matthias M.M. Meier, Willy Benz, and Rainer Wieler. 2012. 'A Hit-and-Run Giant Impact Scenario'. *Icarus* 221 (1): 296–99. https://doi.org/10.1016/j.icarus.2012.07.021.

Ringwood, A. E., and S. E. Kesson. 1976. 'A Dynamic Model for Mare Basalt Petrogenesis'. In *Lunar and Planetary Science Conference Proceedings*, 7:1697–1722.

Roedder, Edwin. 1979. 'Origin and Significance of Magmatic Inclusions'. *Bulletin de Mineralogie* 102 (5): 487–510.

Roedder, Edwin. 1984. 'Volume 12: Fluid Inclusions'. *Reviews in Mineralogy* 12: 644.

Rovetta, M. R., J. D. Blacic, R. L. Hervig, and J. R. Holloway. 1989. 'An Experimental Study of Hydroxyl in Quartz Using Infrared Spectroscopy and Ion Microprobe Techniques'. *Journal of Geophysical Research* 94 (B5): 5840. https://doi.org/10.1029/JB094iB05p05840.

Rudge, John F., Thorsten Kleine, and Bernard Bourdon. 2010. 'Broad Bounds on Earth's Accretion and Core Formation Constrained by Geochemical Models'. *Nature Geoscience* 3 (6): 439–43. https://doi.org/10.1038/ngeo872.

Rufu, Raluca, Oded Aharonson, and Hagai B. Perets. 2017. 'A Multiple-Impact Origin for the Moon'. *Nature Geoscience* 10 (2): 89–94. https://doi.org/10.1038/ngeo2866.

Rutherford, M. J., and P. Papale. 2009. 'Origin of Basalt Fire-Fountain Eruptions on Earth versus the Moon'. *Geology* 37 (March): 219–22. https://doi.org/10.1130/G25402A.1.

Ryder, Graham. 1991. 'Lunar Ferroan Anorthosites and Mare Basalt Sources: The Mixed Connection'. *Geophysical Research Letters* 18 (11): 2065–68. https://doi.org/10.1029/91GL02535.

Saal, Alberto E., Erik H. Hauri, Mauro L. Cascio, James A. Van Orman, Malcolm C. Rutherford, and Reid F. Cooper. 2008. 'Volatile Content of Lunar Volcanic Glasses and the Presence of Water in the Moon's Interior'. *Nature* 454 (7201): 192–95. https://doi.org/10.1038/nature07047.

Safronov, V.S. 1964. 'The Primary Inhomogeneities of the Earth's Mantle'. *Tectonophysics* 1 (3): 217–21. https://doi.org/10.1016/0040-1951(64)90003-4.

Safronov , V.S. 1978. 'The Heating of the Earth during Its Formation'. *Icarus* 33 (1): 3–12. https://doi.org/10.1016/0019-1035(78)90019-2.

Salters, Vincent J. M., and Andreas Stracke. 2004. 'Composition of the Depleted Mantle: DEPLETED MANTLE'. *Geochemistry, Geophysics, Geosystems* 5 (5): n/a-n/a. https://doi.org/10.1029/2003GC000597.

Sato, M. 1976. 'Oxygen Fugacity and Other Thermochemical Parameters of Apollo 17 High-Ti Basalts and Their Implications on the Reduction Mechanism.' *Lunar and Planetary Science Conference Proceedings* 2 (April): 1323–44.

Sato. 1979. 'The Driving Mechanism of Lunar Pyroclastic Eruptions Inferred from the Oxygen Fugacity Behaviour of Apollo 17 Orange Glass.' *Lunar and Planetary Science Conference Proceedings* 1 (January): 311–25.

Schilling, Frank, and Bernd Wunder. 2004. 'Temperature Distribution in Piston-Cylinder Assemblies: Numerical Simulations and Laboratory Experiments'. *European Journal of Mineralogy* 16 (1): 7–14. https://doi.org/10.1127/0935-1221/2004/0016-0007.

Schmidt, B. C., François Holtz, Bruno Scaillet, and Michel Pichavant. 1997. 'The Influence of H2O-H2 Fluids and Redox Conditions on Melting Temperatures in the Haplogranite System'. C*ontributions to Mineralogy and Petrology* 126 (4): 386–400. https://doi.org/10.1007/s004100050258.

Schultz, Peter H., Brendan Hermalyn, Anthony Colaprete, Kimberly Ennico, Mark Shirley, and William S. Marshall. 2010. 'The LCROSS Cratering Experiment'. *Science* 330 (6003): 468–72. https://doi.org/10.1126/science.1187454.

Schwinger, Sabrina, and Doris Breuer. 2022. 'Employing Magma Ocean Crystallization Models to Constrain Structure and Composition of the Lunar Interior'. *Physics of the Earth and Planetary Interiors* 322 (January): 106831. https://doi.org/10.1016/j.pepi.2021.106831.

Sharp, Z. D., C. K. Shearer, K. D. McKeegan, J. D. Barnes, and Y. Q. Wang. 2010. 'The Chlorine Isotope Composition of the Moon and Implications for an Anhydrous Mantle'. *Science* 329 (5995): 1050–53. https://doi.org/10.1126/science.1192606.

Sharp, Zachary D., Francis M. McCubbin, and Charles K. Shearer. 2013. 'A Hydrogen-Based Oxidation Mechanism Relevant to Planetary Formation'. *Earth and Planetary Science Letters* 380 (October): 88–97. https://doi.org/10.1016/j.epsl.2013.08.015.

Shearer, C. K. 2006. 'Thermal and Magmatic Evolution of the Moon'. *Reviews in Mineralogy and Geochemistry* 60 (1): 365–518. https://doi.org/10.2138/rmg.2006.60.4.

Shearer, C. K., S. M. Elardo, N. E. Petro, L. E. Borg, and F. M. McCubbin. 2015. 'Origin of the Lunar Highlands Mg-Suite: An Integrated Petrology, Geochemistry, Chronology, and Remote Sensing Perspective'. *American Mineralogist* 100 (1): 294–325. https://doi.org/10.2138/am-2015-4817.

Shearer, Charles K., Paul C. Hess, Mark A. Wieczorek, Matt E. Pritchard, E. Mark Parmentier, Lars E. Borg, John Longhi, Linda T. Elkins-Tanton, Clive R. Neal, and Irene Antonenko. 2006. 'Thermal and Magmatic Evolution of the Moon'. *Reviews in Mineralogy and Geochemistry* 60 (1): 365–518.

Shraiman, Boris I., and Eric D. Siggia. 1990. 'Heat Transport in High-Rayleigh-Number Convection'. *Physical Review A* 42 (6): 3650–53. https://doi.org/10.1103/PhysRevA.42.3650.

Siggia, Eric D. 1994. 'High Rayleigh Number Convection'. *Annual Review of Fluid Mechanics* 26 (1): 137–68.

Silver, Lynn A., Phillip D. Ihinger, and Edward Stolper. 1990. 'The Influence of Bulk Composition on the Speciation of Water in Silicate Glasses'. *Contributions to Mineralogy and Petrology* 104 (2): 142–62. https://doi.org/10.1007/BF00306439.

Sinton, Chris W., David M. Christie, Valerie L. Coombs, Roger L. Nielsen, and Martin R. Fisk. 1993. 'Near-Primary Melt Inclusions in Anorthite Phenocrysts from the Galapagos Platfrom'. *Earth and Planetary Science Letters* 119 (4): 527–37. https://doi.org/10.1016/0012-821X(93)90060-M.

Sisson, T W, and T L Grove. 1993. 'Experimental Investigations of the Role of H20 in Calc-Alkaline Differentiation and Subduction Zone Magmatism'. *Contributions to Mineralogy and Petrology* 113: 143-166.

Sisson, T. W., K. Ratajeski, W. B. Hankins, and A. F. Glazner. 2005. 'Voluminous Granitic Magmas from Common Basaltic Sources'. *Contributions to Mineralogy and Petrology* 148 (February): 635–61. https://doi.org/10.1007/s00410-004-0632-9.

Sleep, N. H., K. Zahnle, and P. S. Neuhoff. 2001. 'Initiation of Clement Surface Conditions on the Earliest Earth'. *Proceedings of the National Academy of Sciences* 98 (7): 3666–72. https://doi.org/10.1073/pnas.071045698.

Smith, J. V., A. T. Anderson, R. C. Newton, E. J. Olsen, A. V. Crewe, M. S. Isaacson, D. Johnson, and P. J. Wyllie. 1970. 'Petrologic History of the Moon Inferred from Petrography, Mineralogy and Petrogenesis of Apollo 11 Rocks'. *Geochimica et Cosmochimica Acta Supplement* 1: 897.

Smith, Paula M., and Paul D. Asimow. 2005. 'Adiabat_1ph: A New Public Front-End to the MELTS, PMELTS, and PHMELTS Models: ADIABAT_1PH FRONT-END'. *Geochemistry, Geophysics, Geosystems* 6 (2). https://doi.org/10.1029/2004GC000816.

Smyth, Joseph R. 2006. 'Hydrogen in High Pressure Silicate and Oxide Mineral Structures'. *Reviews in Mineralogy and Geochemistry* 62 (1): 85–115.

Snyder, Gregory A, Lawrence A Taylor, and Clive R Neal. 1992. 'A Chemical Model for Generating the Sources of Mare Basalts: Combined Equilibrium and Fractional Crystallization of the Lunar Magmasphere'. *Geochimica et Cosmochimica Acta* 56 (10): 3809–23. https://doi.org/10.1016/0016-7037(92)90172-F.

SOBOLEV, A., R. Clocchiatti, and P. Dhamelincourt. 1983. 'Variations of the Temperature, Melt Composition and Water-Pressure during Olivine Crystallization in Oceanitic Rocks from the Piton Fournaise Volcano (Reunion Island, 1966 Eruption)'. *COMPTES RENDUS DE L ACADEMIE DES SCIENCES SERIE II* 296 (4): 275-.

Sobolev, A. V., V. S. Kamenetsky, and N. N. Kononkova. 1991. 'New Data on Petrology of Siberia Meymechites'. *Geokhimiya*, no. 8: 1084–95.

Sobolev, A. V., V. S. Kamenetsky, N. Metrich, R. Clocchiatti, N. N. Kononkova, A. L. Devirts, and V. I. Ustinov. 1990. 'Regime of Volatile Components and Conditions of Crystallization of Hawaiite Lavas of Etna Volcano, Sicily'. *Geokhimiya*, no. 9: 1277–90.

Sobolev, A. V., O. P. Tsamerian, G. S. Zakariadze, and A. J. Shcherbovskii. 1983. 'Compositions and Conditions of the Crystallization of the Lesser Caucasus Ophiolite Volcanogenic Complex Melts According to the Data of Melt Inclusion Study'. *Doklady Akademii Nauk Sssr* 272 (2): 464–68.

Sobolev, ALEXANDER V., and LEONID V. Danyushevsky. 1994. 'Petrology and Geochemistry of Boninites from the North Termination of the Tonga Trench: Constraints on the Generation Conditions of Primary High-Ca Boninite Magmas'. *Journal of Petrology* 35 (5): 1183–1211.

Sorby, H. C. 1858. 'On the Microscopical, Structure of Crystals, Indicating the Origin of Minerals and Rocks'. *Quarterly Journal of the Geological Society* 14 (1–2): 453–500. https://doi.org/10.1144/GSL.JGS.1858.014.01-02.44.

Spudis, P. D., D. B. J. Bussey, S. M. Baloga, B. J. Butler, D. Carl, Lynn M. Carter, M. Chakraborty, R. C. Elphic, J. J. Gillis-Davis, and J. N. Goswami. 2010. 'Initial Results for the North Pole of the Moon from Mini-SAR, Chandrayaan-1 Mission'. *Geophysical Research Letters* 37 (6).

Spudis, P. D., D. B. J. Bussey, S. M. Baloga, J. T. S. Cahill, L. S. Glaze, G. W. Patterson, R. K. Raney, T. W. Thompson, B. J. Thomson, and E. A. Ustinov. 2013. 'Evidence for Water Ice on the Moon: Results for Anomalous Polar Craters from the LRO Mini-RF Imaging Radar'. *Journal of Geophysical Research: Planets* 118 (10): 2016–29.

Stokes, T.N., G.D. Bromiley, N.J. Potts, K.E. Saunders, and A.J. Miles. 2019. 'The Effect of Melt Composition and Oxygen Fugacity on Manganese Partitioning between Apatite and Silicate Melt'. *Chemical Geology* 506 (February): 162–74. https://doi.org/10.1016/j.chemgeo.2018.12.015.

Sunshine, Jessica M., Tony L. Farnham, Lori M. Feaga, Olivier Groussin, Frédéric Merlin, Ralph E. Milliken, and Michael F. A'Hearn. 2009. 'Temporal and Spatial Variability of Lunar Hydration as Observed by the Deep Impact Spacecraft'. *Science* 326 (5952): 565–68.

Tait, Stephen. 1992. 'Selective Preservation of Melt Inclusions in Igneous Phenocrysts'. *American Mineralogist* 77 (1–2): 146–55.

Tamic, Nathalie, Harald Behrens, and François Holtz. 2001. 'The Solubility of H2O and CO2 in Rhyolitic Melts in Equilibrium with a Mixed CO2–H2O Fluid Phase'. *Chemical Geology* 174 (1–3): 333–47. https://doi.org/10.1016/S0009-2541(00)00324-7.

Tartèse, Romain, Mahesh Anand, Jessica J. Barnes, Natalie A. Starkey, Ian A. Franchi, and Yuji Sano. 2013. 'The Abundance, Distribution, and Isotopic Composition of Hydrogen in the Moon as Revealed by Basaltic Lunar Samples: Implications for the Volatile Inventory of the Moon'. *Geochimica et Cosmochimica Acta* 122 (December): 58–74. https://doi.org/10.1016/j.gca.2013.08.014.

Taylor, G. Jeffrey, Mark A. Wieczorek, Gregory A. Neumann, Francis Nimmo, Walter S. Kiefer, H. Jay Melosh, Roger J. Phillips, Sean C. Solomon, Jeffrey C. Andrews-Hanna, and Sami W. Asmar. 2013. 'Revised Thickness of the Lunar Crust from GRAIL Data: Implications for Lunar Bulk Composition'. In *44th Lunar and Planetary Science Conference*.

Taylor, S. Ross, G. Jeffrey Taylor, and L. August Taylor. 2006. 'The Moon: A Taylor Perspective'. *Geochimica et Cosmochimica Acta* 70 (24): 5904–18.

Taylor, S.R., and P. Jakes. 1974. '1974 (Taylor) The Geochemical Evolution of the Moon.Pdf'.

Teodoro, L. F. A., V. R. Eke, and R. C. Elphic. 2010. 'Spatial Distribution of Lunar Polar Hydrogen Deposits after KAGUYA (SELENE)'. *Geophysical Research Letters* 37 (12).

Thompson, R. N., and I. Kushiro. 1972. 'The Oxygen Fugacity within Graphite Capsules in Piston Cylinder Appartur at High Pressure.' *Carnegie Inst. Wash. Yearbook* 71: 615–16.

Thomson, William. 1862. '4. On the Secular Cooling of the Earth'. *Proceedings of the Royal Society of Edinburgh* 4: 610–11.

Tonks, W. Brian, and H. Jay Melosh. 1993. 'Magma Ocean Formation Due to Giant Impacts'. *Journal of Geophysical Research: Planets* 98 (E3): 5319–33.

Touboul, M., T. Kleine, B. Bourdon, H. Palme, and R. Wieler. 2007. 'Late Formation and Prolonged Differentiation of the Moon Inferred from W Isotopes in Lunar Metals'. *Nature* 450 (7173): 1206–9. https://doi.org/10.1038/nature06428.

Treiman, A. H., J. W. Boyce, J. Gross, Y. Guan, J. M. Eiler, and E. M. Stolper. 2014. 'Phosphate-Halogen Metasomatism of Lunar Granulite 79215: Impact-Induced Fractionation of Volatiles and Incompatible Elements'. *American Mineralogist* 99 (10): 1860–70. https://doi.org/10.2138/am-2014-4822.

Truckenbrodt, Juergen, Dieter Ziegenbein, and Wilhelm Johannes. 1997. 'Redox Conditions in Piston-Cylinder Apparatus; the Different Behavior of Boron Nitride and Unfired Pyrophyllite Assemblies'. *American Mineralogist* 82 (3–4): 337–44. https://doi.org/10.2138/am-1997-3-412.

Urey, Harold C. 1952. 'The Planets: Their Origin and Development'. *Mrs. Hepsa Ely Silliman Memorial Lectures*.

Vander Kaaden, Kathleen E., Carl B. Agee, and Francis M. McCubbin. 2015. 'Density and Compressibility of the Molten Lunar Picritic Glasses: Implications for the Roles of Ti and Fe in the Structures of Silicate Melts'. *Geochimica et Cosmochimica Acta* 149: 1–20.

Walsh, Kevin J., Alessandro Morbidelli, Sean N. Raymond, David P. O'Brien, and Avi M. Mandell. 2011. 'A Low Mass for Mars from Jupiter's Early Gas-Driven Migration'. *Nature* 475 (7355): 206–9. https://doi.org/10.1038/nature10201.

Warren, P. H. 1986. 'The Origin of Pristine KREEP: Effects of Mixing between UrKREEP and the Magmas Parental to the Mg-Rich Cumulates'. In *Geology and Petrology of the Apollo 15 Landing Site*, 113.

Warren, P. H. 1988. 'The Origin of Pristine KREEP: Effects of Mixing between UrKREEP and the Magmas Parental to the Mg-Rich Cumulates.' *Lunar and Planetary Science Conference Proceedings* 18 (January): 233–41.

Warren, P. H. 1985. 'The Magma Ocean Concept and Lunar Evolution'. *Annual Review of Earth and Planetary Sciences* 13: 201–40.

Warren, P. H. 1989. 'KREEP: Major-Element Diversity, Trace-Element Uniformity (Almost).' In *Moon in Transition: Apollo 14, KREEP, and Evolved Lunar Rocks*, 149–53.

Warren, P. H. 2011. 'Stable-Isotopic Anomalies and the Accretionary Assemblage of the Earth and Mars: A Subordinate Role for Carbonaceous Chondrites'. *Earth and Planetary Science Letters* 311 (1–2): 93–100.

Warren, P. H., and John T. Wasson. 1979. 'The Origin of KREEP'. *Reviews of Geophysics* 17 (1): 73. https://doi.org/10.1029/RG017i001p00073.

Watson, Kenneth, Bruce Murray, and Harrison Brown. 1961. 'On the Possible Presence of Ice on the Moon'. *Journal of Geophysical Research* 66 (5): 1598–1600.

Weber, Renee C. 2014. 'Interior of the Moon'. In *Encyclopedia of the Solar System*, 539–54. Elsevier. https://doi.org/10.1016/B978-0-12-415845-0.00024-4.

Weber, Renee C., Pei-Ying Lin, Edward J. Garnero, Quentin Williams, and Philippe Lognonné. 2011. 'Seismic Detection of the Lunar Core'. *Science* 331 (6015): 309–12. https://doi.org/10.1126/science.1199375.

Weichert, U. 2001. 'Oxygen Isotopes and the Moon-Forming Event'. *Science* 294: 345–48.

Weidenschilling, S. J., D. Spaute, D. R. Davis, F. Marzari, and K. Ohtsuki. 1997. 'Accretional Evolution of a Planetesimal Swarm'. *Icarus* 128 (2): 429–55.

Wetherill, George W. 1975. 'Radiometric Chronology of the Early Solar System'. *Annual Review of Nuclear Science* 25 (1): 283–328.

Wetherill, George W. 1985. 'Occurrence of Giant Impacts during the Growth of the Terrestrial Planets'. *Science* 228 (4701): 877–79.

Wetherill, George W. 1990. 'Formation of the Earth'. *Annual Review of Earth and Planetary Sciences* 18: 205–56.

Wieczorek, Mark A., Gregory A. Neumann, Francis Nimmo, Walter S. Kiefer, G. Jeffrey Taylor, H. Jay Melosh, Roger J. Phillips, et al. 2013. 'The Crust of the Moon as Seen by GRAIL'. *Science* 339 (6120): 671–75. https://doi.org/10.1126/science.1231530.

Wilke, Max, and Harald Behrens. 1999. 'The Dependence of the Partitioning of Iron and Europium between Plagioclase and Hydrous Tonalitic Melt on Oxygen Fugacity'. *Contributions to Mineralogy and Petrology* 137 (1–2): 102–14. https://doi.org/10.1007/s004100050585.

Wolbeck, John, and H. C. Connolly. 2010. 'Origin of the Moon: Icy Impactor Model (IIM)'. *Meteoritics and Planetary Science Supplement* 73: 5140.

Wood, J. A. 1975. 'Lunar Petrogenesis in a Well-Stirred Magma Ocean'. In *Lunar and Planetary Science Conference Proceedings*, 6:1087–1102.

Wood, John A., John S. Dickey Jr, Ursula B. Marvin, and B. N. Powell. 1970. 'Lunar Anorthosites and a Geophysical Model of the Moon'. *Geochimica et Cosmochimica Acta Supplement* 1: 965.

Wright, John, and David A. Rothery. 1998. *˜Theœ Ocean Basins Their Structure and Evolution*. 2nd ed. Jordan Hill: Elsevier Science.

Wright, Kate. 2006. 'Atomistic Models of OH Defects in Nominally Anhydrous Minerals'. *Reviews in Mineralogy and Geochemistry* 62 (1): 67–83.

Yamashita, S. 1999. 'Experimental Study of the Effect of Temperature on Water Solubility in Natural Rhyolite Melt to 100 MPa'. *Journal of Petrology* 40 (10): 1497–1507. https://doi.org/10.1093/petroj/40.10.1497.

Yoder, H. S. 1965. 'Diopside-Anorthite-Water at Five and Ten Kilobars and Its Bearing on Explosive Volcanism'. *Carnegie Institution of Washington Yearbook* 64: 82–89.

Young, Edward D., Issaku E. Kohl, Paul H. Warren, David C. Rubie, Seth A. Jacobson, and Alessandro Morbidelli. 2016. 'Oxygen Isotopic Evidence for Vigorous Mixing during the Moon-Forming Giant Impact'. *Science* 351 (6272): 493–96.

Zhang, Junjun, Nicolas Dauphas, Andrew M. Davis, Ingo Leya, and Alexei Fedkin. 2012. 'The Proto-Earth as a Significant Source of Lunar Material'. *Nature Geoscience* 5 (4): 251–55.

Zhang, Youxue. 1999. 'H_2O in Rhyolitic Glasses and Melts: Measurement, Speciation, Solubility, and Diffusion'. *Reviews of Geophysics* 37 (4): 493–516. https://doi.org/10.1029/1999RG900012.

6.4 List of Tools

pMELTS – v5.6.1	- Thermodynamic simulations
SigmaPlot	- Regressions
MATLAB	- Image separation
GIMP	- Image construction of separated images
DeepL	- Translation helper
Zotero	- Citation organizer